Compressible Lubrication Theory in Pressurized Gases

Ssu-Ying Chien

Dissertation submitted to the Faculty of the
Virginia Polytechnic Institute and State University
in partial fulfillment of the requirements for the degree of

Doctor of Philosophy
in
Engineering Mechanics

Mark S. Cramer, Chair
Anne E. Staples
Surot Thangjitham
Pengtao Yue
Nicole T. Abaid

March 22, 2019
Blacksburg, Virginia

Keywords: Fluid mechanics, Supercritical fluids, Compressible lubrication, Low Reynolds number

Compressible Lubrication Theory in Pressurized Gases

Ssu-Ying Chien

Abstract

In this dissertation we present theoretical and computational studies of a series of problems intended to extend the classic lubrication theory to include the effects of pressurized gases. The focus of this dissertation is on the canonical equation for nearly all lubrication flows, viz., the Reynolds equation.

This dissertation is composed of five studies. The first study begins with a careful and systematic analysis of the Navier-Stokes-Fourier equations for a two-dimensional flow in a thin gap between a stationary surface and one translating with a constant speed. In order to focus on the most fundamental issues concerning pressurized gases, the flows are taken to be laminar, steady and single-phase. An important contribution of this dissertation is the establishment of the correct form of the Reynolds equation for pressurized gases. Our analysis provides the boundaries on the range of validity of this Reynolds equation when supercritical gases are of interest. Our Reynolds equation was verified by comparing its numerical solutions to those of the full Navier-Stokes-Fourier equations. In contrast with the literature on high-pressure gas lubrication, our work shows that the Reynolds equation is most conveniently cast as a differential equation for density rather than pressure. We also demonstrate that the flow dynamics can be described by a version of the commonly employed speed number and a new parameter characterizing the local stiffness of the lubricant; we termed this parameter the *effective bulk modulus*. A new simplified temperature equation corresponding to our Reynolds equation is also derived and solved.

On the basis of our first study, we apply a perturbation analysis in the next three studies to describe the dynamics and thermal effects associated with our new Reynolds equation for large speed number flows. Our second study provides simple and explicit formulas for the local flow parameters including pressure, temperature and heat flux in terms of the speed numbers, film thickness function and material functions. The third study develops a simplified model for the global flow parameters including the lubricating force, friction loss and attitude angle. Our work demonstrates that the total force scales with the bulk modulus while the loss is controlled by the variation of the viscosity. The fourth study employs a virial, i.e., small density, expansion technique to further simplify the results of the third study. New results include simple, explicit formulas for the total force, friction loss and attitude angle valid for dense and slightly supercritical fluids.

In the last study, we seek to extend the theory to three-dimensional lubrication flows. A systematic analysis similar to that applied to our first study is carried out for a standard model of a thrust bearing. The resulting Reynolds equation is a nonlinear elliptical partial differential equation for density and is solved using the finite difference method. Through a perturbation analysis, we develop the approximate solution to our Reynolds equation for high-speed lubrication flows. We find that the flow structure is composed of five boundary

layers in addition to the relatively simple "core" region. The flow in two of the boundary layers is governed by a nonlinear heat equation and the remaining boundary layers can be described by nonlinear relaxation equations. Finite difference codes are developed to examine the details in each boundary layer. A composite solution was constructed which constitutes a single approximation and has the same accuracy as the individual approximations in each of their respective regions.

Overall, the key contributions are the establishment of the appropriate forms of the Reynolds equation for dense and supercritical flows, analytical solutions for quantities of practical interest, demonstrations of the roles played by various thermodynamic functions, the first detailed discussions of the physics of lubrication in dense and supercritical flows, and the discovery of boundary layer structures in flows associated with thrust bearings.

Compressible Lubrication Theory in Pressurized Gases

Ssu-Ying Chien

General Audience Abstract

Lubrication theory plays a fundamental role in all mechanical design as well as applications to biomechanics. All machinery are composed of moving parts which must be protected against wear and damage. Without effective lubrication, maintenance cycles will be shortened to impractical levels resulting in increased costs and decreased reliability. The focus of the work presented here is on the lubrication of rotating machinery found in advanced power systems and designs involving micro-turbines.

One of the earliest studies of lubrication is due to Osborne Reynolds in 1886 who recorded what is now regarded as the canonical equation governing all lubrication problems; this equation and its extensions have become known as the Reynolds equation. In the past century, Reynolds equation has been extended to include three-dimensional effects, unsteadiness, turbulence, variable material properties, non-newtonian fluids, multi-phase flows, wall slip, and thermal effects. The bulk of these studies have focused on highly viscous liquids, e.g., oils. In recent years there has been increasing interest in power systems using new working fluids, micro-turbines and non-fossil fuel heat sources. In many cases, the design of these systems employs the use of gases rather than liquids. The advantage of gases over liquids include the reduction of weight, the reduction of adverse effects due to fouling, and compatibility with power system working fluids.

Most treatments of gas lubrication are based on the ideal, i.e., low pressure, gas theory and straightforward retro-fitting of the theory of liquid lubrication. However, the 21st Century has seen interest in gas lubrication at high pressures. At pressures and temperatures corresponding to the dense and supercritical gas regime, there is a strong dependence on gas properties and even singular behavior of fundamental transport properties. Simple extrapolations of the intuition and analyses of the ideal gas or liquid phase theory are no longer possible.

The goal of this dissertation is to establish the correct form of the Reynolds equation valid for both low and high pressure gases and to explore the dynamics predicted by this new form of the Reynolds equation. The dissertation addresses five problems involving our new Reynolds equation. In the first, we establish the form appropriate for the simple benchmark problem of two-dimensional journal bearings. It is found that the material response is completely determined by a single thermodynamic parameter referred to as the *effective bulk modulus*. The validity of our new Reynolds equation has been established using solutions to the full Navier-Stokes-Fourier equations. We have also provided analytical estimates for the range of validity of this Reynolds equation and provided a systematic derivation of the energy equation valid whenever the Reynolds equation holds.

The next three problems considered here derive local and global results of interest in high

speed lubrication studies. The results are based on a perturbation analysis of our Reynolds and energy equation resulting in simplified formulas and the explicit dependence of pressure, temperature, friction losses, load capacity, and heat transfer on the thermodynamic state and material properties.

Our last problem examines high pressure gas lubrication in thrust bearings. We again derive the appropriate form of the Reynolds and energy equations for these intrinsically three-dimensional flows. A finite difference scheme is employed to solve the resultant (elliptic) Reynolds equation for both moderate and high-speed flows. This Reynolds equation is then solved using perturbation methods for high-speed flows. It is found that the flow structure is comprised of five boundary layer regions in addition to the main "core" region. The flow in two of these boundary layer regions is governed by a nonlinear heat equation and the flow in three of these boundary layers is governed by nonlinear relaxation equations. Finite difference schemes are employed to obtain detailed solutions in the boundary layers. A composite solution is developed which provides a single solution describing the flow in all six regions to the same accuracy as the individual solutions in their respective regions of validity.

Overall, the key contributions are the establishment of the appropriate forms of the Reynolds equation for dense and supercritical flows, analytical solutions for quantities of practical interest, demonstrations of the roles played by various thermodynamic functions, the first detailed discussions of the physics of lubrication in dense and supercritical flows, and the discovery of boundary layer structures in flows associated with thrust bearings.

Contents

List of Figures

List of Tables

Chapter 1

Introduction

The Reynolds equation plays a central role in a wide variety of applications involving lubrication theory. In the simplest case, this canonical equation can be written as

$$\frac{d}{dx}\left(h^3\,\frac{dp}{dx}\right) = 6\mu U\,\frac{dh}{dx}, \tag{1.1}$$

where h = h(x) is the thickness of the fluid layer, p = p(x) is the fluid pressure, μ is the shear viscosity, U is a measure of the fluid velocity in the main flow direction, and x is the spatial coordinate in the main flow direction. Since first reported by Osborne Reynolds [1], it has been extended to include effects of three-dimensionality, unsteadiness, turbulence, non-newtonian fluids and thermal effects [2, 3, 5, 4].

The theory of compressible lubrication in low-pressure gases, i.e., ideal gases corresponding to the regime seen in Figure 1.1, was developed between 1950 to 1970 [2, 3]. Since then, gas film lubrication has been successfully used in many applications such as machine tools, dental drills, navigation systems and high-precision instruments [3]. The advantages of gases over liquids as lubricants are the obvious reductions in weight for aeronautical and space applications, compatibility with working fluids in gas and micro-turbines, and a reduction in fouling associated with oil leaks.

Because the shear viscosities of gases are considerably smaller than those of oils, significant reductions in the friction losses can be achieved. However, the speeds involved must be relatively large in order to generate the pressures required to support a given load. As a result, the flows in gas bearings also tend to be compressible. In order to account for the compressibility effects, the Reynolds equation is typically coupled with the perfect gas model [2, 3, 5, 4].

Recent studies further extended the theory to supersonic lubrication flows [6], piezoviscous fluids [7, 8, 9] and a variety of bearing designs involving steady and transient films for specific industrial applications [10, 11, 12, 13]. For example, the NASA Glenn Research Center established the oil-free turbomachinery program for the development of foil bearing

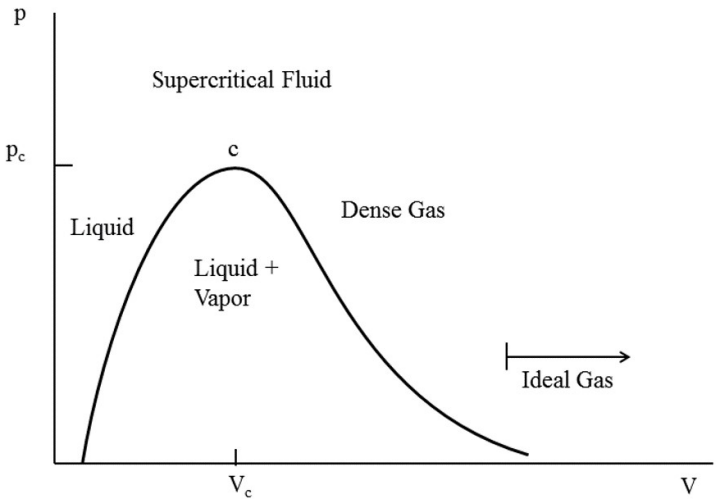

Figure 1.1: Pressure-Volume Diagram for Real Fluid. The state V_c, p_c denotes the thermodynamic critical point. Subscripts c will always denote quantities evaluated at the thermodynamic critical point. $V \equiv 1/\rho$ is the specific volume.

technology with potential applications to aeropropulsion engines [14, 15].

Interest in high-pressure gases as lubricants has been growing due to the development of supercritical CO_2 power cycles in the Sandia National Laboratories (SNL) and Southwest Research Institute (SwRI) in the U.S [16, 17, 18]. The high-pressure gases include those in the supercritical and dense gas regimes depicted in Figure 1.1. The motivation for their study was the potential increases in the efficiency of advanced micro-turbomachinery and lower capital costs [17]. This new energy conversion cycle is expected to be applied in many areas including nuclear [16], geothermal [19] and solar-thermal systems [20, 21].

Supercritical fluids are known to exhibit non-classical behaviors, particularly when the flows are highly compressible. Singularities and rapid variations of properties of supercritical fluids may limit the validity of the Reynolds equation for lubrication problems. As a result, in the supercritical and dense gas regimes, the ideal gas model cannot describe the correct qualitative behavior of the flow, nor can it give accurate quantitative estimates. Unfortunately, previous investigations have not addressed the issue of singular properties and their effects on the validity of the Reynolds equation or the dynamics in the context of lubrication. Therefore, the use of pressurized gases as lubricants presents a new challenge in the field of gas film lubrication.

While the literature on compressible lubrication in low-pressure gases can be dated back

to 1950, little work on high-pressure gases has been carried out until very recently. An important example is a series of experiments in pressurized gases initiated by the SNL. Their experimental results demonstrated the need to consider thermal effects in lubrication flows [17]. Conboy [22], Kim [23], Dousti and Allaire [24] and Qin [25] have presented versions of the Reynolds equation for compressible lubrication flows of pressurized gases. Each has used an equation of state based on the NIST REFPROP database [26]. Guenat and Schiffmann [27] have used the COOLPROP database [28].

Conboy [22] used a Reynolds equation appropriate for compressible pressurized gases in foil-thrust bearings. The equation was cast in terms of both pressure and density. Although the author states that the fluid properties were evaluated based on the local temperature and pressure, no algorithm for the computation of the temperature was presented. Both turbulent and laminar flows were considered and curve-fits for the load and loss, based on the numerical computations, were provided.

Kim [23] has presented a design strategy based on a Reynolds equation for a foil-journal bearing. The Reynolds equation was cast in terms of pressure and a compressibility factor averaged across the gap width. The shear viscosity was taken to be independent of pressure. The pressures were in the dense gas regime, i.e., on the order of half the critical pressure. In spite of the fact that the flow inertia was ignored, the energy equation included energy convection.

Dousti and Allaire [24] presented computational results for supercritical gases. The equation of state was taken to have a linear density-pressure relation. As a result, the Reynolds equation is invalid for even moderate changes in pressure and density. The effects of turbulence were considered but no temperature equation was given. For the purposes of comparison to the incompressible theory, the authors estimated the power loss using the zero eccentricity, i.e., zero load, formula.

The Reynolds equation used by Guenat and Schiffmann [27] resembles the equation developed in [29, 30] in that it is a single equation for the density. Guenat and Schiffmann [27] introduced the bulk modulus in a manner similar to our work. The viscosity was taken to be constant and no temperature equation was given.

Qin [25] evaluated the inertia effects for foil-thrust bearings by comparing the numerical results from the full Navier-Stokes equations to those from the Reynolds equation. The full Navier-Stokes equations were solved by a modified commercial code (referred to as Eilmer) and the Reynolds equation is solved using a finite difference method. The comparison of these two equations were only done for a specific thermodynamic state only and the temperature equation was not considered.

Our review of previous studies has uncovered no detailed justification of the Reynolds equation for pressurized gases nor have we found any discussion of the limitations on the validity of the Reynolds equation. It is highly likely that the singular properties of supercritical fluids would affect the validity of this important canonical equation. In addition, many previous

investigations are inconsistent in their simultaneous flow and thermal modeling, although this may be complicated by their inclusion of turbulence. Finally, we note that there is a need for a clarification of the physics of compressible pressurized lubricants.

The general goals of this dissertation, therefore, are (1) to establish the form and limitations on the Reynolds equation for compressible supercritical flows for two commonly encountered configurations, (2) to examine the flow dynamics and to identify and describe any new physics arising in the supercritical or dense gas regime, and (3) to derive simple, explicit formulas that can illuminate the physics by revealing the dependence of the flow on the key bearing parameters and fluid properties. The approach adopted in this dissertation is through systematic analysis, numerical calculations, and the development of simple, explicit approximate formulas for the dynamics.

The work presented in this dissertation is organized in five standalone manuscripts that appear as five chapters. Starting with Chapter 2, we carry out a systematic derivation of the two-dimensional compressible Reynolds equation and its corresponding temperature equation. We also delineate the restrictions on and regions of validity of these equations for high-pressure gases. We identify the key parameter that controls the behavior of lubrication flows of high-pressure gases; we term this parameter as "effective bulk modulus".

Based on the theory derived in Chapter 2, in Chapter 3-5 we develop a simplified model to examine two-dimensional high-speed lubrication flows of pressurized gases between non-concentric cylinders. In Chapter 3 we derive the approximate solutions to the compressible Reynolds equation and its corresponding simplified temperature equation derived in Chapter 2. These results include the explicit formulas for pressure, density, temperature and heat flux in terms of the speed number, film thickness, and material functions, i.e., bulk modulus, shear viscosity and thermal expansivity.

In Chapter 4 we develop the general expressions for the global parameters including the total lubricating force and friction loss. The effects of pressurization and compressibility on the lubricating force and friction loss are also discussed. In Chapter 5, we employ the virial, i.e., small density, expansions for the bulk modulus and viscosity to derive simple, explicit formulas of the lubricating force and friction loss for pressurized gases.

In Chapter 6, we apply a systematic analysis similar to that applied in Chapter 2-5 to a three-dimensional configuration, i.e., a standard model of a thrust bearing. The resulting compressible Reynolds equation is found to be a nonlinear elliptic partial differential equation for the density. A numerical scheme based on the finite difference method is used to solve this Reynolds equation. We also develop the approximate solutions to the Reynolds equation for high-speed lubrication flows. In the course of derivation we discovered that the boundary layers form on three out of the four edges of the flow domain. The equations that governs these boundary layer flows are derived and compared to solutions of the Reynolds equation. The core and five boundary layer solutions are combined into a single composite solution valid over the whole flow regime.

Bibliography

[1] O. Reynolds. On the theory of lubrication and its application to Mr. Beauchamp Tower's experiments, including an experimental determination of the viscosity of olive oil. *Proceedings of the Royal Society of London*, 40(242-245), 191–203, 1886.

[2] O. Pinkus and B. Sternlicht. *Theory of Hydrodynamic Lubrication*. McGraw-Hill, 1961.

[3] W. A. Gross, L. A. Matsch, V. Castelli, A. Eshel, J. H. Vohr, and M. Wildmann. *Fluid Film Lubrication*. John Wiley and Sons, Inc., 1980.

[4] A. Z. Szeri. *Fluid Film Lubrication*. Cambridge University Press, 2010.

[5] B. J. Hamrock, S. R. Schmidt, and B. O. Jacobson. *Fundamentals of Fluid Film Lubrication*. CRC Press, 2004.

[6] F. Dupuy, B. Bou-Saïd, M. Garcia, G. Grau, J. Rocchi, M. Crespo, J. Tichy. Tribological study of a slider bearing in the supersonic regime. *Journal of Tribology*, 138(4), 041702, 2016.

[7] K. R. Rajagopal and A. Z. Szeri. On an inconsistency in the derivation of the equations of elastohydrodynamic lubrication. In *Proceedings of the Royal Society of London A: Mathematical, Physical and Engineering Sciences*, 459, 2771–2786. The Royal Society, 2003.

[8] G. Bayada, B. Cid, G. García, and C. Vázquez. A new more consistent reynolds model for piezoviscous hydrodynamic lubrication problems in line contact devices. *Applied Mathematical Modelling*, 37(18-19), 8505–8517, 2013.

[9] T. Gustafsson, K. R. Rajagopal, R. Stenberg, and J. Videman. Nonlinear reynolds equation for hydrodynamic lubrication. *Applied Mathematical Modelling*, 39(17), 5299–5309, 2015.

[10] F. Dimofte. Wave journal bearing with compressible lubricant—part i: the wave bearing concept and a comparison to the plain circular bearing. *Tribology Transactions*, 38(1), 153–160, 1995.

[11] G. L. Agrawal. Foil air/gas bearing technology—an overview. In *ASME 1997 international gas turbine and aeroengine congress and exhibition*, pages V001T04A006–V001T04A006. American Society of Mechanical Engineers, 1997.

[12] W. M. Hannon, M. J. Braun, and S. I. Hariharan. Generalized universal reynolds equation for variable properties fluid-film lubrication and variable geometry self-acting bearings. *Tribology Transactions*, 47(2), 171–181, 2004.

[13] I. Temizer and S. Stupkiewicz. Formulation of the reynolds equation on a time-dependent lubrication surface. *Proc. R. Soc. A*, 472(2187), 20160032, 2016.

[14] C. DellaCorte, K. C. Radil, R. J. Bruckner, and S. A. Howard. Design, fabrication, and performance of open source generation I and II compliant hydrodynamic gas foil bearings. *Tribology Transactions*, 51(3), 254–264, 2008.

[15] C. DellaCorte and R. J. Bruckner. Remaining technical challenges and future plans for oil-free turbomachinery. *Journal of Engineering for Gas Turbines and Power*, 133(4), 042502, 2011.

[16] V. Dostal, M. J. Driscoll, and P. Hejzlar. A supercritical carbon dioxide cycle for next generation nuclear reactors. Technical report, MIT-ANP-TR-100, 2004.

[17] S. A. Wright, R. F. Radel, M. E. Vernon, G. E. Robert, and P. S. Pickard. Operation and analysis of a supercritical CO_2 Brayton cycle. *Sandia Report, No. SAND2010-0171*, 2010.

[18] T. M. Conboy, S. A. Wright, J. Pasch, D. Fleming, G. Rochau, and R. Fuller. Performance characteristics of an operating supercritical CO_2 Brayton cycle. *Journal of Engineering for Gas Turbines and Power*, 134(11), 111703, 2012.

[19] H. Chen, D. Y. Goswami and E. K. Stefanakos. A review of thermodynamic cycles and working fluids for the conversion of low-grade heat. *Renewable and Sustainable Energy Reviews*, 14(9), 3059–3067, 2010.

[20] C. S. Turchi, Z. Ma, T. W. Neises, and M. J. Wagner. Thermodynamic study of advanced supercritical carbon dioxide power cycles for concentrating solar power systems. *Journal of Solar Energy Engineering*, 135(4), 041007, 2013.

[21] B. D. Iverson, T. M. Conboy, J. J. Pasch and A. M. Kruizenga. Supercritical CO_2 Brayton cycles for solar-thermal energy. *Applied Energy*, 111, 957–970, 2013.

[22] T. M. Conboy. Real-gas effects in foil thrust bearings operating in the turbulent regime. *Journal of Tribology*, 135(3), 031703, 2013.

[23] D. Kim. Design space of foil bearings for closed-loop supercritical CO_2 power cycles based on three-dimensional thermohydrodynamic analyses. *Journal of Engineering for Gas Turbines and Power*, 138(3), 032504, 2016.

[24] S Dousti and P Allaire. A compressible hydrodynamic analysis of journal bearings lubricated with supercritical carbon dioxide. In *Proceeding of Supercritical* CO_2 *Power Cycle Symposium. San Antonio, TX*, 2016.

[25] K. Qin. *Development and application of multiphysics simulation tools for foil thrust bearings operating with carbon dioxide.* PhD thesis, University of Queensland, 2017.

[26] E. W. Lemmon, M. L. Huber, and M. O. McLinden. NIST Reference fluid thermodynamic and transport properties–REFPROP. *NIST Standard Reference Database*, 23, v7, 2002.

[27] E. Guenat and J. Schiffmann. Real-gas effects on aerodynamic bearings. *Tribology International*, 120, 358–368, 2018.

[28] I. H. Bell, J. Wronski, S. Quoilin, and V. Lemort. Pure and pseudo-pure fluid thermophysical property evaluation and the open-source thermophysical property library CoolProp. *Industrial & Engineering Chemistry Research*, 53(6), 2498–2508, 2014.

[29] S. Y. Chien, M. S. Cramer, and A. Untaroiu. Compressible Reynolds equation for high-pressure gases. *Physics of Fluids*, 29(11), 116101, 2017.

[30] S. Y. Chien, M. S. Cramer, and A. Untaroiu. A compressible thermohydrodynamic analysis of journal bearings lubricated with supercritical CO_2. In *ASME 2017 Fluids Engineering Division Summer Meeting*, pages V01BT09A001–V01BT09A001. American Society of Mechanical Engineers, 2017.

Chapter 2

Compressible Reynolds Equation for High-pressure Gases

The contents of this chapter are reproduced from *S. Y. Chien, M. S. Cramer, and A. Untaroiu. Compressible Reynolds equation for high-pressure gases. Physics of Fluids, 29(11), 116101, 2017*, with the permission of AIP Publishing. The published article can be found at: `https://aip.scitation.org/doi/10.1063/1.5000827`.

Attribution

The work presented in this chapter was primarily carried out by S.Y. Chien. M. S. Cramer conceived of the main idea and contributed to the development and implementation of this work. A. Untaroiu provided access to the commercial code, ANSYS-CFX for the numerical computations discussed in Section 2.7.

Abstract

We derive the Reynolds equation corresponding to steady, laminar, two-dimensional, compressible flows of single-phase Navier-Stokes fluids in a thin gap between a stationary surface and one translating with constant speed. The thermodynamic state of the fluid is taken to be in the dense and supercritical gas regime. The equation of state is a well-known cubic equation, and the shear viscosity and thermal conductivity are taken to depend on density and temperature. Thermal boundary conditions are taken to include those for constant-temperature and adiabatic walls. The flow is seen to be governed by both the speed number and a single thermodynamic parameter referred to as the effective bulk modulus. Numerical solutions to the Reynolds equation are compared to those of the full Navier-Stokes equa-

tions. It is shown that the Reynolds equation breaks down in the vicinity of the thermodynamic critical point. Furthermore, we show that energy convection is negligible whenever the Reynolds equation is valid which enables us to present new explicit solutions for the temperature distributions.

2.1 Introduction

Flows in narrow gaps arise in a wide variety of applications including sealing, lubrication, hydrodynamic scattering of particles, and biomechanics. The canonical equation governing such flows is the Reynolds equation which, in its simplest form, is written as

$$\frac{d}{dx}\left(h^3\,\frac{dp}{dx}\right) = 6\mu U\,\frac{dh}{dx}, \tag{2.1}$$

where h = h(x) is the thickness of the fluid layer, p = p(x) is the fluid pressure, μ is the shear viscosity, U is a measure of the fluid velocities in the main flow direction, and x is the spatial coordinate in the main flow direction. This equation was first reported by Reynolds [1] and forms the foundation of lubrication theory. Since that time (2.1) has been extended to include the effects of three-dimensionality, unsteadiness, non-newtonian fluids, turbulence, and thermal effects [2, 5, 4].

Implicit in the derivation of (2.1) and many of its generalizations are two key restrictions. The first is that the fluid layer be thin compared to the length scales associated with the variations in the main flow direction and the second is that the reduced Reynolds number [6] be small, i.e.,

$$\frac{h_o}{L} \ll 1 \;\text{ and }\; Re\frac{h_o^2}{L^2} \ll 1, \tag{2.2}$$

where h_o is a measure of the thickness of the fluid layer, L is a measure of the length scale of the variations in the main flow direction, and Re is the Reynolds number based on L and U. The second of (2.2) is equivalent to a small Reynolds number approximation and permits the neglect of the effects of inertia relative to the pressure and viscous forces.

Recently there has been considerable interest in the replacement of highly viscous liquids as lubricants by gases. The motivation for this replacement is the obvious reduction in weight for aeronautical and space applications, compatibility with working fluids in gas and micro-turbines, and a reduction in fouling associated with oil leaks. For example, NASA Glenn Research Center has established an oil-free turbomachinery program with potential applications to aeropropulsion engines [12]. In recent years, more studies led by Sandia National Laboratories (SNL) in the U.S. have focused on the development of closed-loop Brayton cycles for nuclear power systems using supercritical carbon dioxide (CO_2) as a working fluid [11, 13, 14]. The motivation for their study was the potential increases in the efficiency of advanced micro-turbomachinery and lower capital costs [13]. Supercritical CO_2

cycles have also been applied in other areas including those involving geothermal [15] and solar-thermal systems [16, 17].

Because the shear viscosities of gases are considerably smaller than those of oils, significant reductions in the friction losses can be achieved. However, the speeds involved must be relatively large in order to generate the pressures required to support a given load. As a result, the flows in gas bearings also tend to be compressible. Many previous studies on low-pressure gas bearings used the perfect gas model. However, in the supercritical and dense gas regime the perfect gas model is no longer valid and, in some cases, can not even provide the correct qualitative behavior.

Experimental studies on gas bearings in the dense gas regime include those carried out at the SNL. These experiments clearly demonstrate the need to consider thermal effects [13] in lubrication flows. Conboy, et al [20] examined the role of turbulence using an isothermal model[19] and an equation of state based on the NIST REFPROP database [18]. Kim [21] and Dousti and Allaire [22] also presented computational results based on a modified Reynolds equation.

The goal of the present study is to provide a detailed derivation of a Reynolds equation valid for compressible flows in most of the supercritical and dense gas regime. In addition, we present new explicit solutions for the temperature distribution; use of the latter can significantly reduce the computational complexity and effort when thermal effects are of interest.

It is shown that the compressible form of the Reynolds equation is no longer valid when the thermodynamic state is in the vicinity of the thermodynamic critical point. In the near-critical region, the singularities in the specific heat at constant pressure, the thermal expansion coefficient and the Prandtl number cause the flow properties to vary across the fluid film and the energy convection to be non-negligible.

In the next section we describe our gas model and illustrate the behavior of these critical parameters. In Sections 2.3-2.5 we outline the derivation of the Reynolds equation and associated temperature equation valid over the bulk of the pressurized gas regime. In Section 2.6 we discuss the breakdown and region of validity of our results. In Section 2.7 we compare our results to detailed numerical solutions to the Navier-Stokes equations.

2.2 Gas Model

In this study we focus on flows which correspond to pressurized, rather than ideal, gases including those occupying the supercritical gas regime. The general regimes of interest are indicated in Fig. 2.1. In all that follows, we consider only single-phase fluids so that the fluid is specified by equation of state

$$p = p(\rho, T), \tag{2.3}$$

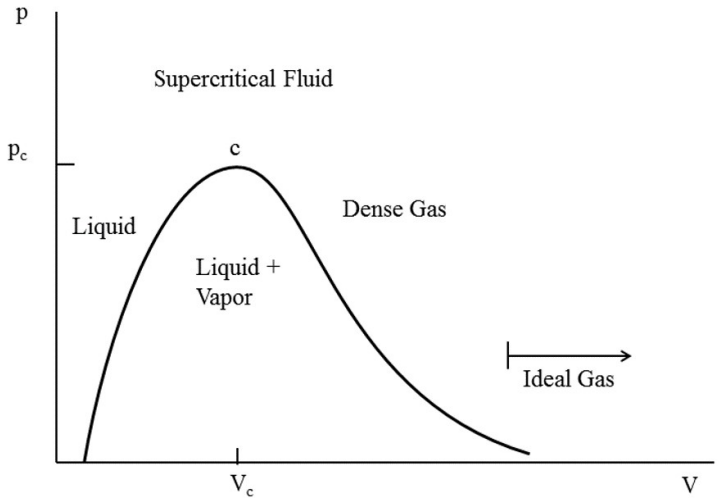

Figure 2.1: Pressure-Volume Diagram for Real Fluid. The state V_c, p_c denotes the thermodynamic critical point. Subscripts c will always denote quantities evaluated at the thermodynamic critical point. $V \equiv 1/\rho$ is the specific volume.

where $\rho > 0$ is the fluid density, $T > 0$ is the absolute temperature, and the ideal gas or zero-pressure specific heat at constant volume, i.e.,

$$c_{v\infty} = c_{v\infty}(T) \equiv \lim_{\rho \to 0} c_v(\rho, T), \tag{2.4}$$

where

$$c_v = c_v(\rho, T) \equiv c_{v\infty}(T) - T \int_0^\rho \left. \frac{\partial^2 p}{\partial T^2} \right|_\rho \frac{d\rho}{\rho^2}, \tag{2.5}$$

is the actual specific heat at constant volume. As $\rho \longrightarrow 0$, the pressure approaches that of an ideal gas. At small values of the specific volume $V \equiv 1/\rho$ and the supercritical temperatures, i.e., $T \geq T_c$, the pressure typically becomes singular, e.g.,

$$p \sim \frac{f(T)}{V - b}, \tag{2.6}$$

where f(T) is some function of temperature and b is a measure of the molecular excluded volume. When $V \approx b$, it can be shown that the fluid becomes stiff with large sound speeds and a vanishingly small thermal expansion coefficient. The focus of the present study is on the supercritical and dense gases regimes. The singularities in the liquid-like regime, i.e., $V \approx b$, will be ignored in all that follows.

At the thermodynamic critical point, pressure is taken to satisfy

$$\left.\frac{\partial p}{\partial V}\right|_T = \left.\frac{\partial^2 p}{\partial V^2}\right|_T = 0, \tag{2.7}$$

although some gas models impose constraints on higher derivatives. In this regime, small isothermal changes in pressure yield large changes in the specific volume and density, i.e., the fluid is extremely compressible. Near the thermodynamic critical point,

$$\left.\frac{T}{p}\frac{\partial p}{\partial T}\right|_\rho = O(1). \tag{2.8}$$

If we expand (2.3) in the vicinity of an arbitrary reference state $\mathrm{V}_* \approx \mathrm{V}_c$, $\mathrm{T}_* \approx \mathrm{T}_c$, we find that the lowest order approximation for $p(\rho, T)$ is

$$\begin{aligned} p = p_* &+ \left.\frac{\partial p}{\partial T}\right|_\rho (T - T_*) + \left.\frac{\partial p}{\partial V}\right|_T (V - V_*) + \frac{1}{2}\left.\frac{\partial^2 p}{\partial V^2}\right|_T (V - V_*)^2 \\ &+ \frac{1}{6}\left.\frac{\partial^3 p}{\partial V^3}\right|_T (V - V_*)^3 + O(V - V_*)^4, \end{aligned} \tag{2.9}$$

where all partial derivatives in (2.9) are evaluated at $(\mathrm{V}_*, \mathrm{T}_*)$ and we have taken (2.8) and

$$\left.\frac{V}{p}\frac{\partial p}{\partial V}\right|_T = O\left(\frac{V - V_c}{V_c}\right)^2 = o(1), \tag{2.10}$$

$$\left.\frac{V^2}{p}\frac{\partial^2 p}{\partial V^2}\right|_T = O\left(\frac{V - V_c}{V_c}\right) = o(1), \tag{2.11}$$

$$\left.\frac{V^3}{p}\frac{\partial^3 p}{\partial V^3}\right|_T = O(1), \tag{2.12}$$

$$\frac{T - T_c}{T_c} = O\left(\frac{V - V_c}{V_c}\right)^3 = o(1) \tag{2.13}$$

in the near-critical regime. Thus, near the critical point, the pressure perturbations can be taken to be linear in the temperature perturbations and cubic in the specific volume or density perturbations.

In the course of our analysis, several thermodynamic parameters play a key role. These parameters include the thermal expansion coefficient or thermal expansivity

$$\beta = \beta(\rho, T) \equiv -\frac{1}{\rho}\left.\frac{\partial \rho}{\partial T}\right|_p, \tag{2.14}$$

and the bulk modulus

$$\kappa_T = \kappa_T(\rho, T) \equiv \rho\left.\frac{\partial p}{\partial \rho}\right|_T = -V\left.\frac{\partial p}{\partial V}\right|_T = \frac{\rho a^2}{\gamma} > 0, \tag{2.15}$$

where

$$a = a(\rho, T) \equiv \sqrt{\left.\frac{\partial p}{\partial \rho}\right|_s} \tag{2.16}$$

is the thermodynamic sound speed and s = fluid entropy. The quantity $\gamma = \gamma\ (\rho,\mathrm{T}) \equiv \mathrm{c}_p/\mathrm{c}_v$ is the ratio of specific heats and $\mathrm{c}_p = \mathrm{c}_p(\rho,\mathrm{T})$ is the specific heat at constant pressure. Because the flow is both viscous and compressible, the Grüneisen parameter

$$G = G(\rho, T) \equiv \frac{\beta a^2}{c_p} = \frac{\kappa_T \beta}{\rho c_v} = \frac{1}{\rho c_v}\left.\frac{\partial p}{\partial T}\right|_\rho = \frac{\gamma - 1}{\beta T} \tag{2.17}$$

will naturally arise. The specific heat at constant pressure is typically calculated from the last of (2.17) combined with (2.5), (2.14), and the equation of state (2.3).

In the limit of $\rho \longrightarrow 0$, it is easily verified that $\beta \longrightarrow 1/\mathrm{T}$, $\kappa_T \longrightarrow \mathrm{p}$, and $\mathrm{G} \longrightarrow \gamma - 1$. When we take the limit $\mathrm{V} \longrightarrow \mathrm{b}$, κ_T, p, and G, all become unbounded. In the near-critical region, both c_v and G are bounded and non-zero, and

$$\kappa_T = p_* \, O\left(\frac{V - V_*}{V_*}\right)^2 \longrightarrow 0, \tag{2.18}$$

$$\beta T = \frac{T}{\kappa_T}\left.\frac{\partial p}{\partial T}\right|_\rho = O\left(\frac{V - V_*}{V_*}\right)^{-2} \longrightarrow \infty, \tag{2.19}$$

$$\frac{c_p}{R} = \frac{c_v}{R} + \left.\frac{\beta T}{\rho R}\frac{\partial p}{\partial T}\right|_\rho \sim \left.\frac{\beta T}{\rho R}\frac{\partial p}{\partial T}\right|_\rho = O\left(\frac{V - V_*}{V_*}\right)^{-2} \longrightarrow \infty, \tag{2.20}$$

where R is the gas constant and the last of (2.17) has been used. Thus, any theory of lubrication involving dense or supercritical fluids must take into account the singularities in the specific heat and the thermal expansion coefficient.

In order to give an explicit illustration of the physics, we employ a well-known cubic equation of state, viz., the Redlich-Kwong-Soave (RKS) equation. While more accurate and significantly more complex models are available, the RKS equation is reasonably accurate for the purposes of the present study and, more importantly, gives the correct qualitative behavior of all real gases. The details of the RKS equation and models for the ideal gas specific heat can be found in Reid et al.[7]. The isotherms of CO_2 corresponding to the RKS equation have been plotted in Fig. 2.2 for temperatures $\mathrm{T} \geq \mathrm{T}_c$. The molecular weight, properties at the thermodynamic critical point, and acentric factor of CO_2 can also be found in Reid et al. [7]. The cubic nature of the isotherms near the critical point and the singularity in the liquid-like region is clearly seen in Fig. 2.2. The specific heat at constant pressure and thermal expansion coefficient are plotted in Fig. 2.3 and Fig. 2.4, respectively. In each plot the $\mathrm{T} = \mathrm{T}_c$ curves become unbounded at $\mathrm{V} = \mathrm{V}_c$. Although $\beta T \ll 1$ in the liquid-like region, i.e., $\mathrm{V} \approx \mathrm{b}$, its value increases rapidly as V increases becoming O(1) over most of the p-V diagram and large near the thermodynamic critical point. Thus, lubrication theories based on the assumption of negligible thermal expansion are strictly only valid for liquids.

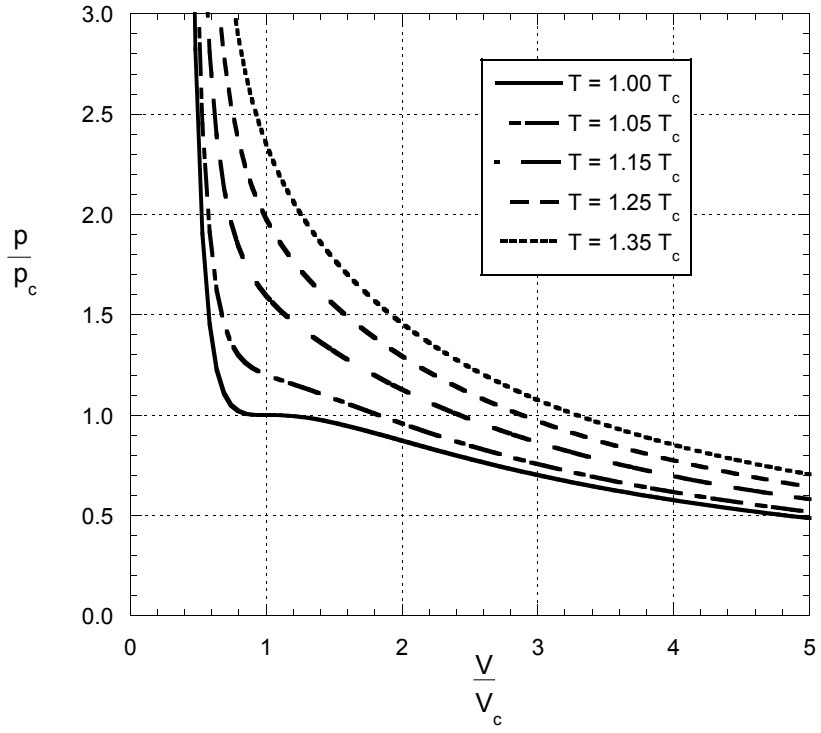

Figure 2.2: Isotherms of CO_2 Using the RKS Equation of State.

The viscosity and thermal conductivity models were taken to be those of Chung et al [24, 25]. The Chung et al.[24, 25] shear viscosity model was found to have excellent agreement with the experimental data recorded by Reid et al.[7]. The shear viscosity using this model is plotted in Fig. 2.5 for CO_2. Near the critical point, the variations of μ with both temperature and specific volume are seen to be mild.

The thermal conductivities are found to have a similar variation and the details are omitted in order to save journal space.

We may now combine our viscosity and thermal conductivity models with the expressions for the specific heat to compute the Prandtl number

$$Pr \equiv \frac{\mu c_p}{k}, \tag{2.21}$$

where k = k(ρ,T) is the thermal conductivity. The Prandtl number is plotted in Fig. 2.6. The shear viscosity and thermal conductivity are bounded and have roughly the same variation with specific volume as each other, even near the critical point. The singularity in Pr is solely due to the singularity in c_p. Thus, the near-critical singularity in the Prandtl number

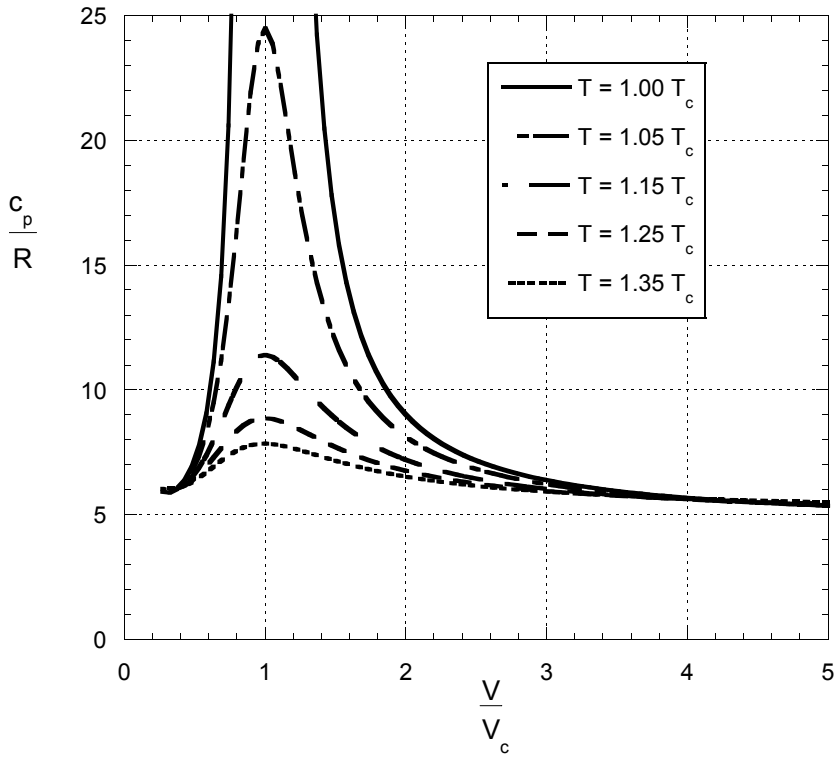

Figure 2.3: Specific Heat at Constant Pressure of CO_2. Equation of state is the RKS equation and R is the gas constant.

is the same as that for c_p and βT, i.e.,

$$Pr = O\left(\frac{V - V_*}{V_*}\right)^{-2}. \tag{2.22}$$

This contrasts with the situation involving liquid oil, where the specific heat takes on values roughly equal to those in the ideal gas limit. In oils, large Prandtl numbers are due to the relatively large values of the shear viscosity.

2.3 Formulation

In order to examine the physical effects in the simplest possible context, we consider a two-dimensional, steady, single-phase, laminar flow in a thin gap corresponding to the configuration sketched in Fig. 2.7. The body force and volumetric energy supplies are taken to be zero. A Navier-Stokes fluid is contained in the region $0 \leq x \leq L$ and $0 \leq y \leq h(x)$. The

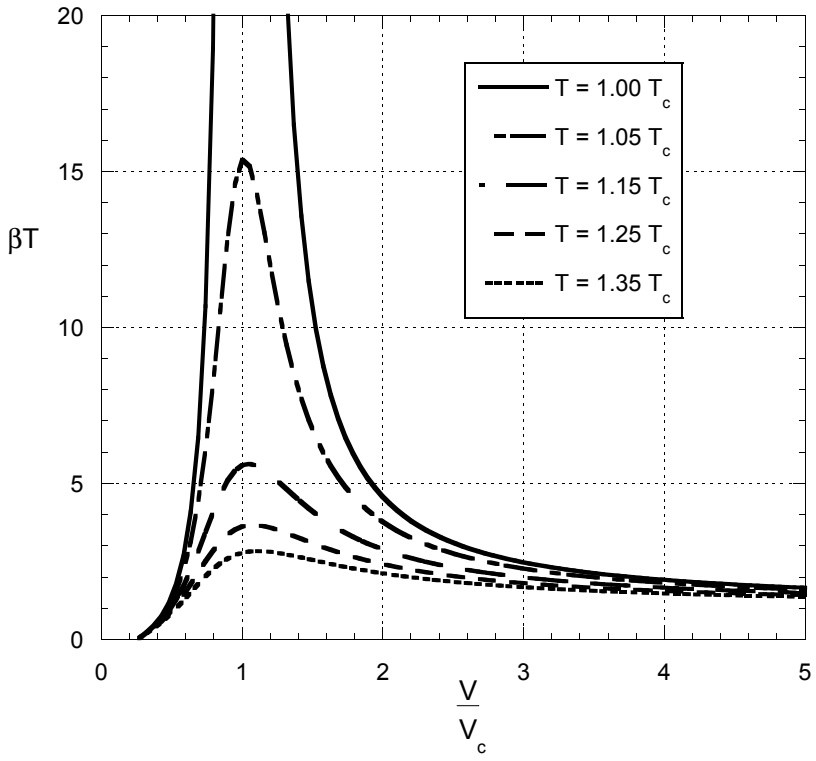

Figure 2.4: Thermal Expansion Coefficient of CO_2. Equation of state is the RKS equation.

function $h(x)$ is selected to correspond to a typical journal bearing,

$$h(x) = h_0 \left[1 + 2\delta sin^2\left(\pi \frac{x}{L}\right)\right], \tag{2.23}$$

where $h_0 = h(0)$ is the minimum value of $h(x)$ and $\delta > 0$ is a nondimensional amplitude which can be associated with the bearing eccentricity. However, the only restrictions relevant to the approximation scheme described here are the first of (2.2). The upper surface, i.e., $y = h(x)$, is at rest and $h(x)$ varies with the length scale L. The lower surface, i.e., $y = 0$, is translating with constant speed U in the positive x-direction. For convenience, we refer to the upper and lower surface as the stator and rotor surfaces, respectively. Thus, the no-slip and kinematic boundary conditions require

$$v_x = U, v_y = 0 \; at \; y = 0, \tag{2.24}$$

$$v_x = v_y = 0 \; at \; y = h(x), \tag{2.25}$$

where v_x and v_y are velocity components in the x and y directions. In Section 2.7, we take all physical variables to have identical values at x = 0 and x = L. Thermal boundary

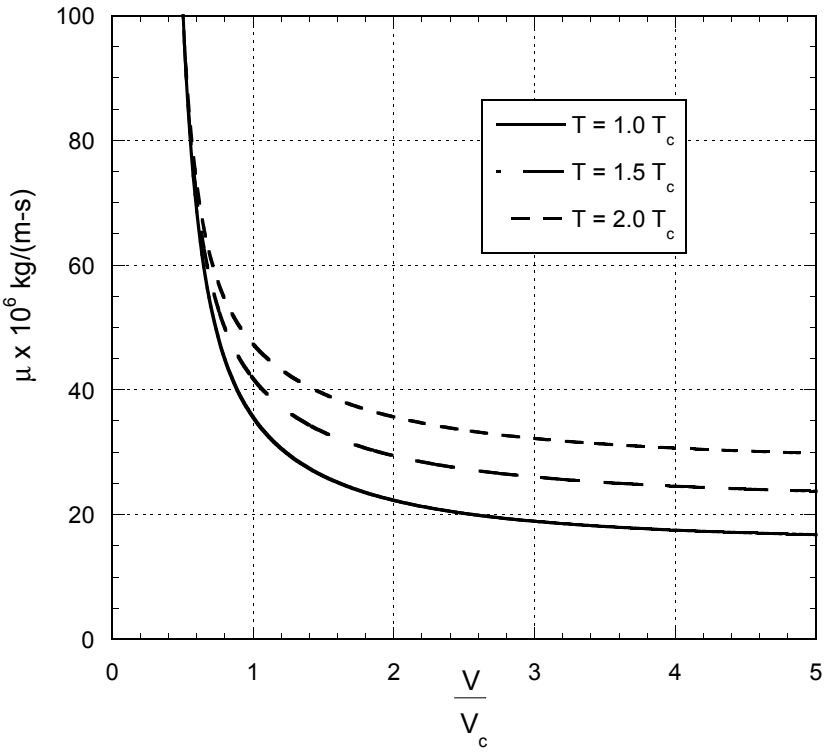

Figure 2.5: Shear Viscosity of CO_2 vs Specific Volume. Viscosity model is that of Chung et al.[24, 25].

conditions will be taken to be those for an adiabatic wall at either y = h(x) or at y = 0 with a fixed known temperature at the non-adiabatic wall. Constant-temperature walls will also be considered. In this case, both upper and lower surfaces are taken to have fixed temperatures.

Under these conditions, the nondimensional Navier-Stokes equations can be written

$$\frac{\partial(u\overline{\rho})}{\partial\overline{x}} + \frac{\partial(v\overline{\rho})}{\partial\overline{y}} = 0, \tag{2.26}$$

$$Re\frac{h_o^2}{L^2}\,\overline{\rho}\,\overline{\mathbf{v}}\cdot\overline{\nabla}u + \frac{\partial\overline{p}}{\partial\overline{x}} = \frac{\partial\overline{T}_{yx}}{\partial\overline{y}} + \frac{h_o^2}{L^2}\frac{\partial\overline{T}_{xx}}{\partial\overline{x}}, \tag{2.27}$$

$$Re\frac{h_o^4}{L^4}\,\overline{\rho}\,\overline{\mathbf{v}}\cdot\overline{\nabla}v + \frac{\partial\overline{p}}{\partial\overline{y}} = \frac{h_o^2}{L^2}\left(\frac{\partial\overline{T}_{xy}}{\partial\overline{x}} + \frac{\partial\overline{T}_{yy}}{\partial\overline{y}}\right), \tag{2.28}$$

$$Re\frac{h_o^2}{L^2}\,Pr\,\overline{\rho}\,\overline{c}_p\,\overline{\mathbf{v}}\cdot\overline{\nabla T} = \frac{\partial}{\partial\overline{y}}\left(\overline{k}\frac{\partial\overline{T}}{\partial\overline{y}}\right) + \frac{h_o^2}{L^2}\frac{\partial}{\partial\overline{x}}\left(\overline{k}\frac{\partial\overline{T}}{\partial\overline{x}}\right) + PrEc(\overline{\Phi} + \beta T\overline{\mathbf{v}}\cdot\overline{\nabla}\overline{p}), \tag{2.29}$$

where $\overline{x} = x/L$, $\overline{y} = y/h_0$, $u = v_x/U$, $v = v_y L/Uh_0$. The thermodynamic pressure, density

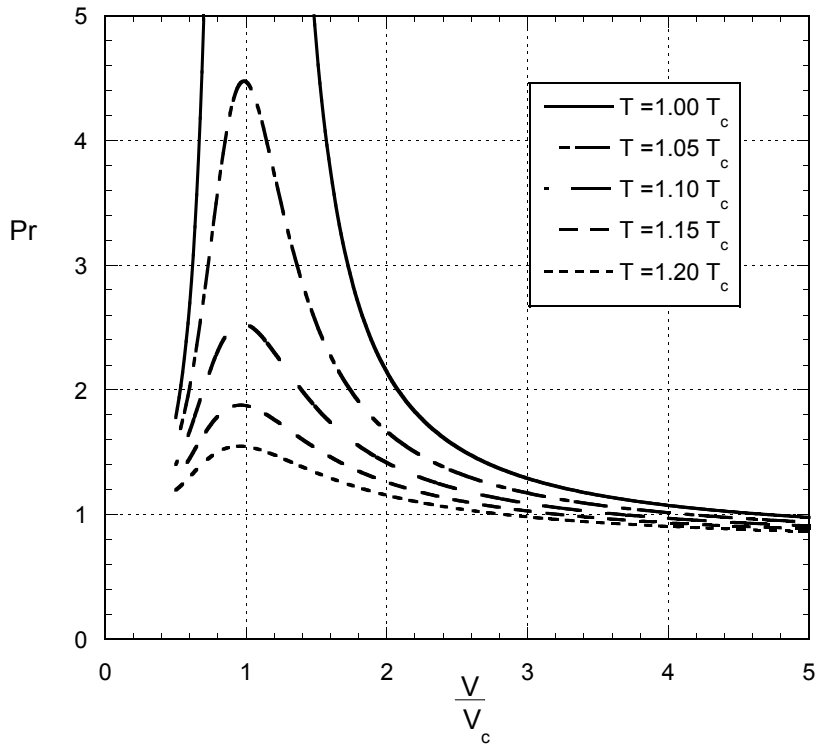

Figure 2.6: Prandtl Number of CO_2 vs Specific Volume. Viscosity model is that of Chung et al. [24, 25] and equation of state is the RKS equation.

and temperature are scaled as follows

$$\overline{p} = (p - p_{ref})\frac{h_0^2}{\mu_{ref} U L},\ \overline{\rho} = \frac{\rho}{\rho_{ref}}, and\ \overline{T} = \frac{T - T_{ref}}{\Delta T}, \tag{2.30}$$

where the quantity ΔT represents a measure of temperature differences occurring in the flow. Throughout this study, the subscript "ref" denotes constant reference values, typically selected to be the values of quantities evaluated at x = 0. The shear and second viscosities, specific heat at constant pressure, and thermal conductivity are scaled as follows:

$$\overline{\mu} = \mu/\mu_{ref},\ \overline{\lambda} = \lambda/\mu_{ref},\ \overline{c}_p = c_p/c_{pref},\ \overline{k} = k/k_{ref} \tag{2.31}$$

where $\overline{\lambda}$ is the dimensionless second viscosity. It is well known [8, 9, 10] that the bulk and therefore second viscosity of CO_2 can be thousands of times larger than the shear viscosity. However, the flow examined here is quasi-parallel and we will require that

$$\overline{\lambda}\frac{h_o^2}{L^2} \ll 1 \tag{2.32}$$

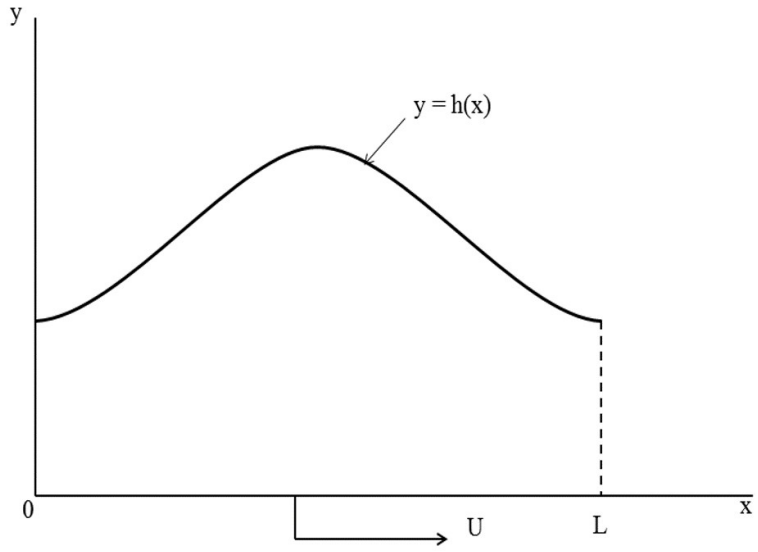

Figure 2.7: Configuration Corresponding to the Reynolds Equation.

which allows us to ignore any effects of a large bulk viscosity.

The Reynolds number Re is based on μ_{ref}, ρ_{ref}, U and L. In all that follows, the Prandtl number Pr is based on the reference values of the shear viscosity, thermal conductivity, and c_p. The Eckert number is given by

$$Ec \equiv \frac{U^2}{c_{pref}\Delta T} = \frac{M_{ref}^2}{\beta \Delta T} G_{ref}, \tag{2.33}$$

where the Mach number is based on U and the reference thermodynamic sound speed a_{ref}. The quantity Φ is the viscous dissipation defined as

$$\Phi \equiv \mathrm{tr}(\mathbf{T}(\nabla \mathbf{v})^T), \tag{2.34}$$

where "tr" denotes the trace, the superscript "T" denotes the transpose, and $\mathbf{T}$ is the stress tensor having Cartesian components T_{xx}, T_{xy}, T_{yy}, etc. The components of the nondimensional stress tensor and the viscous dissipation in (2.27)-(2.29) are related to the physical components T_{xx}, T_{xy}, T_{yy} and Φ by

$$\overline{T}_{xx} = \frac{L}{\mu_{ref} U} T_{xx},\ \overline{T}_{xy} = \frac{h_0}{\mu_{ref} U} T_{xy},\ \overline{T}_{yy} = \frac{L}{\mu_{ref} U} T_{yy}, \tag{2.35}$$

and

$$\overline{\Phi} = \frac{h_0^2}{\mu_{ref} U^2} \Phi. \tag{2.36}$$

The mass, momentum, and energy equations (2.26)-(2.29) are exact. We now regard all quantities with an overbar as being O(1). In many derivations of (2.1), the restrictions (2.2) are regarded as sufficient to guarantee its validity. However, because the flow is compressible, thermal effects and thermal expansion can play a significant role and can lead to a breakdown of the Reynolds equation. The effect of thermal expansion can be measured by the nondimensional product $\beta\Delta$T. When one or the other surface is taken to be adiabatic, the temperature differences are not imposed but are determined by the flow dynamics. In this case, the scaling for the temperature difference ΔT can be taken to be

$$\Delta T = \frac{U^2}{c_{pref}} Pr. \tag{2.37}$$

If the temperature at the upper and lower surfaces are prescribed constants, we will require that the prescribed temperature difference satisfies $\Delta \mathrm{T} = \mathrm{O}(\mathrm{M}_{ref}^2\ \mathrm{T}_{ref})$. In the next section the Mach number will be required to be small so that the temperature difference in this case is required to be

$$\frac{\Delta T}{T_{ref}} = O(M_{ref}^2) \ll 1. \tag{2.38}$$

Thus, when one surface is adiabatic,

$$\beta\Delta T = \frac{\beta a_{ref}^2}{c_{pref}} \frac{U^2}{a_{ref}^2}\, Pr = O(G_{ref}\ M_{ref}^2\ Pr) = O(M_{ref}^2\ Pr), \tag{2.39}$$

everywhere outside of the liquid-like regime. When the wall temperatures are prescribed

$$\beta\Delta T = O(\beta_{ref} T_{ref} M_{ref}^2). \tag{2.40}$$

Because $\mathrm{Pr} = \mathrm{O}(\beta\mathrm{T}) = \mathrm{O}(\gamma)$ and $\mathrm{G} = \mathrm{O}(1)$ at all pressures and temperatures outside of the liquid-like regime, our restriction on the temperature variations can be taken to be

$$\beta\Delta T = O(\beta_{ref}\ T_{ref}\ M_{ref}^2) = O(Pr\ M_{ref}^2) = O(\gamma_{ref}\ M_{ref}^2) \ll 1 \tag{2.41}$$

for both types of boundary conditions used here. We note further that the product Pr Ec appearing in (2.29) can be taken to be 1 when one wall is adiabatic and $\mathrm{O}(\mathrm{G}_{ref}\ \mathrm{Pr}/\beta_{ref}\mathrm{T}_{ref})$ $= \mathrm{O}(1)$ when (2.38) is imposed.

2.4 Compressible Reynolds Equation

In this section, the pressures and temperatures are taken to be outside of the near-critical region so that Pr, c_p, γ, and $\beta\mathrm{T} = \mathrm{O}(1)$. We now apply the restrictions (2.2) to obtain the

following approximations to the momentum equations:

$$\frac{\partial \overline{p}}{\partial \overline{x}} = \frac{\partial}{\partial \overline{y}}\left(\overline{\mu}\frac{\partial u}{\partial \overline{y}}\right) + O\left(Re\frac{h_o^2}{L^2}, \frac{h_o^2}{L^2}\right), \tag{2.42}$$

$$\frac{\partial \overline{p}}{\partial \overline{y}} = O\left(Re\frac{h_o^4}{L^4}, \frac{h_o^2}{L^2}\right) = O\left(\frac{h_o^2}{L^2}\right). \tag{2.43}$$

The solution to (2.43) indicates that the pressure variation across the gap is essentially negligible, i.e, $\overline{p} \approx \overline{p}(x)$, and the x-momentum equation (2.42) can be integrated at least once.

In order to evaluate the density variation in the lubrication flow, we now write $\rho = \rho$(p,T) and we can therefore write

$$\frac{d\overline{\rho}}{\overline{\rho}} = \frac{\gamma}{\overline{\rho}\ \overline{a}^2}\frac{M_{ref}^2}{Re\frac{h_o^2}{L^2}}d\overline{p} - \beta\Delta T d\overline{T}. \tag{2.44}$$

The density changes are due to both pressure and temperature changes. Inspection of (2.44) reveals that changes in density due to pressure will be proportional to $\frac{M_{ref}^2}{Re\frac{h_o^2}{L^2}}$, whereas changes in density due to thermal expansion will be proportional to

$$\beta\Delta T = O(PrM_{ref}^2) \ll \gamma\frac{M_{ref}^2}{Re\frac{h_o^2}{L^2}}, \tag{2.45}$$

where (2.2) and (2.41) have been used. The variation of the density in the main flow direction is

$$\frac{1}{\overline{\rho}}\frac{\partial \overline{\rho}}{\partial \overline{x}} = \frac{\gamma}{\overline{\rho}\ \overline{a}^2}\frac{M_{ref}^2}{Re\frac{h_o^2}{L^2}}\frac{\partial \overline{p}}{\partial \overline{x}} + O(Pr\ M_{ref}^2). \tag{2.46}$$

In order that the flow be compressible we require that

$$M_{ref}^2 = O(Re\frac{h_o^2}{L^2}) = o(1). \tag{2.47}$$

Thus, our constraint on M_{ref} used in (2.38) is seen to be consistent. Because γ = O(Pr), we have

$$\frac{1}{\overline{\rho}}\frac{\partial \overline{\rho}}{\partial \overline{x}} \approx \frac{\gamma}{\overline{\rho}\ \overline{a}^2}\frac{M_{ref}^2}{Re\frac{h_o^2}{L^2}}\frac{\partial \overline{p}}{\partial \overline{x}}, \tag{2.48}$$

even in the near-critical region.

The variation in density across the gap, i.e., in the y-direction, is determined from

$$\frac{1}{\overline{\rho}}\frac{\partial \overline{\rho}}{\partial \overline{y}} = \frac{\gamma}{\overline{\rho}\ \overline{a}^2}\frac{M_{ref}^2}{Re\frac{h_o^2}{L^2}}\frac{\partial \overline{p}}{\partial \overline{y}} - \beta\Delta T\frac{\partial \overline{T}}{\partial \overline{y}}, . \tag{2.49}$$

From (2.43) it is clear that the first term on the right hand side of (2.49) is of $O(\gamma\frac{h_o^2}{L^2}) = O(Pr\frac{h_o^2}{L^2}) \ll 1$ and the second term is of order Pr M_{ref}^2 = O(Pr Re$\frac{h_o^2}{L^2}$). Thus, the density variation across the gap is given by

$$\frac{1}{\overline{\rho}}\frac{\partial\overline{\rho}}{\partial\overline{y}} = O(Pr\frac{h_o^2}{L^2}, PrRe\frac{h_o^2}{L^2}) \ll 1, \tag{2.50}$$

and we can take $\overline{\rho} = \overline{\rho}(\overline{x})$ outside of the near-critical regime. Thus, the mass equation (2.26) can be approximated as

$$\frac{d}{d\overline{x}}\big[\overline{\rho}\int_0^{\overline{h}} u\, d\overline{y}\,\big] \approx 0, \tag{2.51}$$

where the boundary conditions (2.24)-(2.25) have been used and $\overline{h} \equiv h/h_o$. In general, the viscosity, thermal conductivity, and bulk modulus all depend on the density and temperature. We can evaluate changes in the shear viscosity by considering a Taylor series for T $\approx$ T_{ref}. When this is done, we find

$$\frac{\mu(\rho,T)-\mu(\rho,T_{ref})}{\mu_{ref}} = \frac{T_{ref}}{\mu_{ref}}\left.\frac{\partial\mu}{\partial T}\right|_\rho \frac{\Delta T}{T_{ref}}\overline{T} + \cdots = O(M_{ref}^2) \ll 1, \tag{2.52}$$

where we have recognized that

$$\frac{T}{\mu}\left.\frac{\partial\mu}{\partial T}\right|_\rho = O(1) \tag{2.53}$$

and have used (2.41). Thus, $\mu(\rho$,T) $\approx \mu(\rho,\mathrm{T}_{ref})$ and we can regard the variation of viscosity as being due to density only. When the flow remains outside of the near-critical region the density is approximately constant in the y-direction so that the shear viscosity is also approximately constant with respect to y. A similar analysis can be carried out for the thermal conductivity, bulk modulus (2.15), and thermal expansion coefficient (2.14) to show that these quantities are, to the lowest order, constant in the y-direction.

The Reynolds equation may now be derived by integrating the x-momentum equation (2.42) twice and by using the boundary conditions (2.24)-(2.25) we find that

$$u = \frac{1}{2\overline{\mu}}\frac{d\overline{p}}{d\overline{x}}\left(\overline{y}^2 - \overline{h}\overline{y}\right) + 1 - \frac{\overline{y}}{\overline{h}}. \tag{2.54}$$

Substitution of (2.54) into the mass equation (2.51) and integration in $\overline{y}$ yields

$$\frac{d}{d\overline{x}}\left(\frac{\overline{\rho}\overline{h}^3}{\overline{\mu}}\frac{d\overline{p}}{d\overline{x}}\right) \approx 6\frac{d(\overline{\rho}\overline{h})}{d\overline{x}}. \tag{2.55}$$

Examination of (2.46) reveals that we may regard the x-variations of ρ as being proportional to the x-variations of p. Thus, we may write

$$\frac{dp}{d\overline{x}} \approx \frac{\kappa_T(\rho, T_{ref})}{\rho} \frac{d\rho}{d\overline{x}} \left[1 + O(M_{ref}^2)\right]. \tag{2.56}$$

so that the nondimensional form of the Reynolds equation for compressible flows becomes

$$\frac{d}{d\overline{x}}\left(\overline{h}^3 \overline{\kappa}_{Te} \frac{d\overline{\rho}}{d\overline{x}}\right) \approx \Lambda \frac{d(\overline{\rho}\overline{h})}{d\overline{x}}, \tag{2.57}$$

where

$$\kappa_{Te} \equiv \kappa_{Te}(\rho, T_{ref}) \equiv \frac{\kappa_T(\rho, T_{ref})}{\mu(\rho, T_{ref})}, \tag{2.58}$$

$$\overline{\kappa}_{Te} \equiv \frac{\kappa_{Te}(\rho, T_{ref})}{\kappa_{Te}(\rho_{ref}, T_{ref})} \equiv \frac{\kappa_{Te}(\rho, T_{ref})}{\kappa_{Te}\big|_{ref}}, \tag{2.59}$$

$$\Lambda \equiv \frac{6UL}{h_o^2 \kappa_{Te}\big|_{ref}} = 6\frac{\gamma_{ref} M_{ref}^2}{Re\frac{h_o^2}{L^2}}. \tag{2.60}$$

The quantity κ_{Te} will be referred to as the effective bulk modulus and gives a measure of the effective stiffness of the fluid in lubrication flows. Alternatively, it gives a measure of the relative strength of compressibility to the influence of friction on the flow. The quantity Λ is frequently referred to as the speed number and, in the lubrication literature, is regarded as a measure of flow compressibility. This is consistent with the interpretation of the ratio $\mathrm{M}_{ref}^2/\mathrm{Re}\frac{h_o^2}{L^2}$ in Section 2.4. The scaled version of effective bulk modulus has been plotted in Fig. 2.8. As $\mathrm{V} \longrightarrow \infty$, $\kappa_{Te} \longrightarrow \mathrm{p}/\mu(0,\mathrm{T}_{ref})$. At the thermodynamic critical point the bulk modulus (2.15) vanishes and κ_{Te} therefore does as well.

Solutions for compressible lubrication flows are obtained by integrating (2.57) for the density once the equation of state and viscosity model are specified. The pressure is then determined through use of the equation of state. We can recover the results for incompressible flow by setting $\overline{\rho} = \overline{\mu} = 1$ in (2.55). We recover the equation for ideal gases by recognizing that $\kappa_T \longrightarrow \mathrm{p} \longrightarrow \rho\mathrm{RT}$ and $\mu \longrightarrow \mu(\mathrm{T})$ only in the ideal gas limit. If we employ the same approximations found in Section 2.4 we find that (2.57) can be approximated as

$$\frac{d}{d\overline{x}}\left(\overline{h}^3 \overline{\rho} \frac{d\overline{\rho}}{d\overline{x}}\right) \approx \Lambda \frac{d(\overline{\rho}\overline{h})}{d\overline{x}}, \tag{2.61}$$

Thus, in the case of ideal gases, the solution for density and pressure will be independent of the reference thermodynamic state except through the speed number. This fact contrasts with situation for non-ideal gases, e.g., dense gases or supercritical fluids, where the behavior depends both on the thermodynamic state through κ_{Te} and the speed number. Result (2.61) is in complete agreement with the ideal gas formula given by Szeri [4].

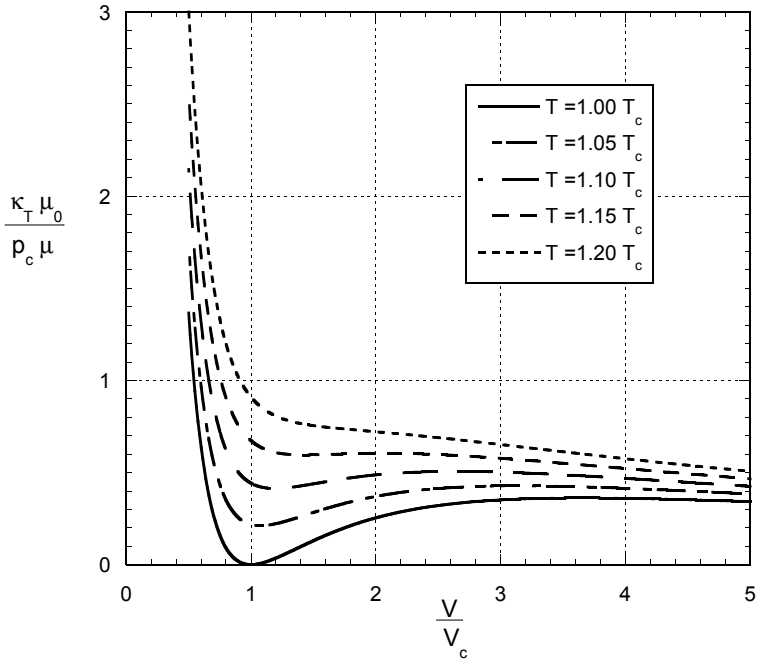

Figure 2.8: Effective Bulk Modulus of CO_2 vs V/V_c. Viscosity model is that of Chung et al.[24, 25] and the gas model is the RKS equation. Here $\mu_0 = \mu_0(T)$ is the ideal gas ($V \longrightarrow \infty$) value of μ.

2.5 Temperature Variation

We now apply the approximations (2.2) to the energy equation (2.29) to obtain the simplified temperature equation:

$$\frac{\partial}{\partial \overline{y}}\left(\overline{k}\frac{\partial \overline{T}}{\partial \overline{y}}\right) = -PrEc(\overline{\Phi} + \beta T u\frac{d\overline{p}}{d\overline{x}}) + O\left(Pr\ Re\frac{h_o^2}{L^2}\ ,\ \frac{h_o^2}{L^2}\right), \tag{2.62}$$

where

$$\overline{\Phi} \approx \overline{\mu}\left(\frac{\partial u}{\partial \overline{y}}\right)^2. \tag{2.63}$$

Inspection of (2.62) reveals that the temperature field is determined by a balance of conduction in the y-direction, viscous dissipation, and flow work. Thus, when Pr = O(1), i.e., outside of the near-critical region, any self-consistent theory must neglect energy convection whenever the inertia is neglected. Result (2.62) is in complete agreement with the simplified temperature equation given by Gross, et al[3].

In Section 2.4 we have already shown that the shear viscosity, thermal conductivity, and thermal expansion coefficient can be taken to be functions of $\rho(\overline{x})$ and T_{ref}. If we also

recognize that T $\approx$ T$_{ref}$, then the simplified temperature equation (2.62) can be integrated explicitly at each value of $\overline{x}$. The only functions of $\overline{y}$ will be those introduced by (2.54) and its derivative.

We first consider the case where both stator and rotor surfaces have a prescribed temperature, i.e., $T = T_R$ = constant at $\overline{y} = 0$ and $T = T_S$ = constant at $\overline{y} = \overline{h}(\overline{x})$. It is easily shown that the resultant solution to (2.62) is

$$\frac{T - T_R}{\Delta T} = Pr\, Ec\, \frac{\overline{y}}{\overline{h}}\, \frac{\overline{\mu}}{\overline{k}} \left[\frac{c_1}{12}(1 - \frac{\overline{y}^3}{\overline{h}^3}) + \frac{c_2}{6}(1 - \frac{\overline{y}^2}{\overline{h}^2}) + \frac{c_3}{2}(1 - \frac{\overline{y}}{\overline{h}}) \right] + \frac{\overline{y}}{\overline{h}}. \tag{2.64}$$

where $\Delta T \equiv$T$_S$ - T$_R$ for this case. We have defined the factors

$$c_0 \equiv \frac{\overline{h}^2}{2\overline{\mu}} \frac{d\overline{p}}{d\overline{x}} = \frac{3\overline{h}^2}{\Lambda} \frac{\overline{\kappa}_{Te}}{\overline{\rho}} \frac{d\overline{\rho}}{d\overline{x}} = c_0(\overline{x}), \tag{2.65}$$

$$c_1 \equiv 2c_0^2(2 + \beta T) = c_1(\overline{x}), \tag{2.66}$$

$$c_2 \equiv -2c_0(1 + c_0)(2 + \beta T) = c_2(\overline{x}), \tag{2.67}$$

$$c_3 \equiv 1 + 2(1 + \beta T)c_0 + c_0^2 = c_3(\overline{x}), \tag{2.68}$$

so that (2.54) is rewritten as

$$u = c_0 \frac{\overline{y}^2}{\overline{h}^2} - (1 + c_0)\frac{\overline{y}}{\overline{h}} + 1. \tag{2.69}$$

We note that the terms that proportional to the factor βT in (2.64)-(2.68) represent the contributions due to flow work while the remaining terms are those due to viscous dissipation.

If the stator surface, i.e., the $\overline{y} = \overline{h}$ surface, is specified as an adiabatic wall and the rotor surface has a fixed temperature T_R, integration of (2.62) yields

$$\frac{T - T_R}{\frac{U^2}{2c_{pref}}} = Pr\, \frac{\overline{\mu}}{\overline{k}}\, \frac{\overline{y}}{\overline{h}} \left[\frac{c_1}{6}(4 - \frac{\overline{y}^3}{\overline{h}^3}) + \frac{c_2}{3}(3 - \frac{\overline{y}^2}{\overline{h}^2}) + a_3(2 - \frac{\overline{y}}{\overline{h}}) \right], \tag{2.70}$$

where we have used (2.37). Finally, if we take the rotor to be adiabatic and $T = T_S$ at $\overline{y} = \overline{h}$, we then find

$$\frac{T - T_S}{\frac{U^2}{2c_{pref}}} = Pr\, \frac{\overline{\mu}}{\overline{k}} \left[\frac{c_1}{6}(1 - \frac{\overline{y}^4}{\overline{h}^4}) + \frac{c_2}{3}(1 - \frac{\overline{y}^3}{\overline{h}^3}) + c_3(1 - \frac{\overline{y}^2}{\overline{h}^2}) \right]. \tag{2.71}$$

We note that the scaled temperature distributions will depend on the material functions

$$Pr\frac{\overline{\mu}}{\overline{k}},\ \overline{\kappa}_{Te},\ \beta T,$$

and, for (2.64), Ec. The first material function is recognized as the local Prandtl number for constant specific heat c$_p$. In many flows where the Reynolds equation (2.57) and our energy equation (2.62) is valid, the variation of the ratio Pr $\overline{\mu}/\overline{k}$ with density is small. For such flows the primary influence of the shear viscosity on the temperature variation is through the effective bulk modulus $\overline{\kappa}_{Te}$.

2.6 Near-Critical Region

In Sections 2.4-2.5 the pressures and temperatures were taken to be sufficiently far from the near-critical region. When $T \approx T_c$ and $V \approx V_c$, the Reynolds equation (2.57) and simplified temperature equation (2.62) are no longer valid due to the singularities in βT, c_p, and Pr. Inspection of (2.28) reveals that the pressure will remain nearly constant across the gap, i.e., in the y-direction. Because $Re(h_0/L)^2$ is independent of the near-critical singularity, the flow inertia can remain negligible in the near-critical region. In the near-critical region $Pr \gg 1$ and inspection of (2.29) reveals that the convection of energy is no longer negligible when

$$PrRe\frac{h_o^2}{L^2} = O(1). \tag{2.72}$$

From (2.49), it can also be shown that the variation in density in the y-direction will no longer be negligible, i.e.,

$$\frac{1}{\overline{\rho}}\frac{\partial \overline{\rho}}{\partial \overline{y}} = O(1). \tag{2.73}$$

Although the dependence of viscosity on temperature remains negligible, the variation of density with y will imply $\mu = \mu(x,y)$ and the simple integration of the x-momentum equation is not possible. Thus, the Reynolds equation (2.57) is expected to give a poor approximation to the flow behavior in the near-critical region.

The region of validity of the theory presented here can be estimated by making use of the expansions (2.9) and (2.22). In particular, (2.72) is satisfied if

$$\frac{V - V_c}{V_c} = O\left(\sqrt{Re\frac{h_o^2}{L^2}}\right), \tag{2.74}$$

$$\frac{T - T_c}{T_c} = O\left(Re\frac{h_o^2}{L^2}\right)^{3/2}. \tag{2.75}$$

2.7 Numerical Results

To solve the compressible Reynolds equation (2.57) we impose boundary conditions $\overline{\rho}(0) = \overline{\rho}(1) = 1$ and employ a two-point boundary value solver coupled with the gas models described in Section 2.2. Once the density and pressure distribution is obtained, we calculate the temperature variations for each thermal boundary condition using (2.64), (2.70), and (2.71).

Numerical solutions to the compressible Reynolds equation (2.57) and simplified temperature equation (2.62) will be compared with the numerical solutions to the exact Navier-Stokes equations and the total energy equation obtained using the commercial code, ANSYS-CFX, in which the velocity-pressure coupling and overall solution procedure are based on the coupled solver. The gas models described in Section 2.2 are employed in the CFD calculation.

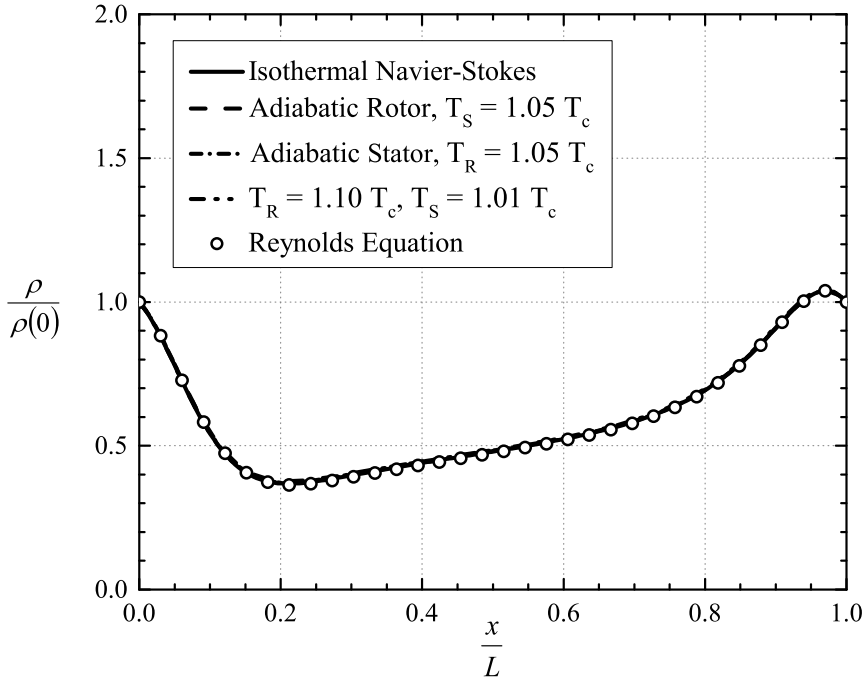

Figure 2.9: Scaled Density vs x/L. Here V(0) = V(L) = 4.8 V_c, T(0) = T(L) = 1.05 T_c.

The fluid domain sketched in Fig. 2.7 is discretized using structured mesh with hexahedral elements. In order to demonstrate grid independence, we compared the simulation results of grids of 10, 15, 20 and 25 elements across the gap with 315, 635, 1250, and 2500 elements in the main flow direction. Grid convergence was achieved with the grid of 15×1250 which results in 0.1% difference in maximum density when compared to the grid of 25×2500. The iteration convergence criteria requires the averaged residuals for mass, momentum, and energy equations to be smaller than 10^{-7} and the variation of the resultant force on the rotor and the maximum temperature inside the flow domain to be less than 1% per 200 iterations.

We first compare solutions of the Reynolds equation (2.57) to those of the isothermal Navier-Stokes equations, i.e., solutions to the mass and momentum equations where the constraint of the energy equation is replaced by the condition of uniform temperature. A re-examination of the discussion of Section 2.4 shows that solutions to the Reynolds equation will agree with the isothermal Navier-Stokes equations if the flow inertia is negligible. We also include the numerical solutions to the full Navier-Stokes equations for each thermal boundary condition discussed in Sections 2.3 and 2.5. In the remainder of this study we take the channel sketched in Fig. 2.7 to be given by h_o/L = 2.251×10^{-5}, $\delta = 2.536$, and U = 62.832 m/s. The fluid will be taken to be CO_2 and the gas models discussed in Section 2.2 are used. Unless stated otherwise, T(0) = T(L) = 1.05 T_c.

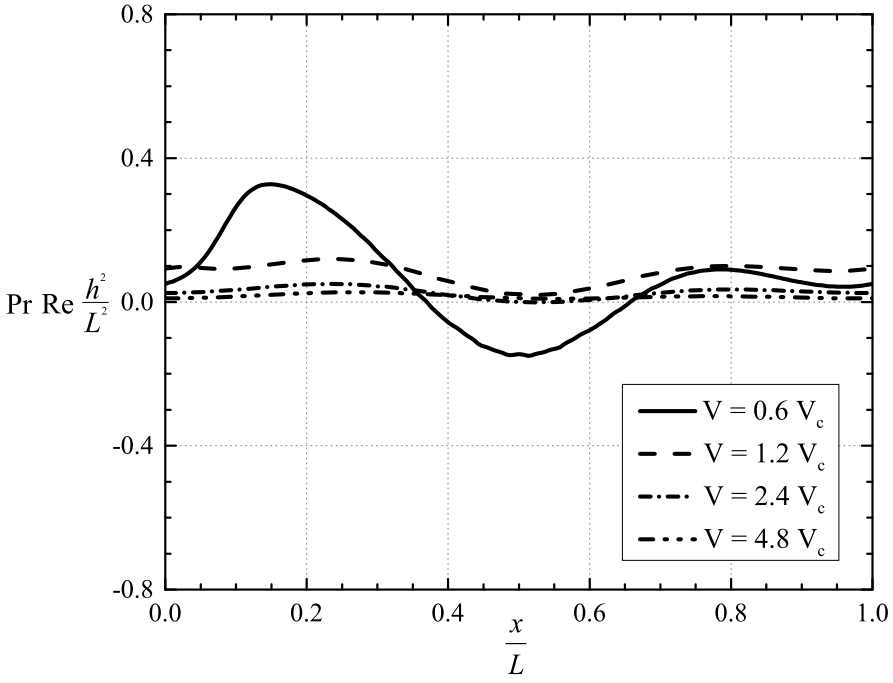

Figure 2.10: Pr Re(h/L)^2 vs x/L for Adiabatic Rotor on y = h(x)/2. Reduced Reynolds number and Pr are based on the local values of ρ, μ, h, v_x and a fixed value of L. T(0) = T(L) = 1.05 T_c.

The first case to be considered is that where the specific volume at the entrance and exit is V(0) = V(L) = 4.8 V_c. The pressure at these points is found to be approximately 40 bar so that the thermodynamic state can be regarded as that of a dense gas or, because T > T_c, a slightly supercritical fluid. The scaled density distribution for this case is plotted in Fig. 2.9. The agreement between the Reynolds equation and each of the Navier-Stokes simulations is excellent.

In Fig. 2.10 we have plotted the local values of Pr Re(h/L)^2 along the mid-surface, i.e., at y = h/2, for an adiabatic rotor. Because Pr $\approx$ 1 for this case, the magnitude of Re(h/L)^2 is roughly the same as that of Pr Re(h/L)^2. Both the reduced Reynolds number and Pr Re(h/L)^2 are small on the centerline. Inspection of the detailed numerical solutions reveal that these parameters remain small everywhere in the flow. These observations are completely consistent with the degree of agreement seen in Fig. 2.9.

The temperature variations for the flow corresponding to the density distribution of Fig. 2.9 are plotted in Fig. 2.11 for thermal boundary conditions corresponding to an adiabatic rotor, an adiabatic stator, and constant-temperature walls. The reference temperature is taken to

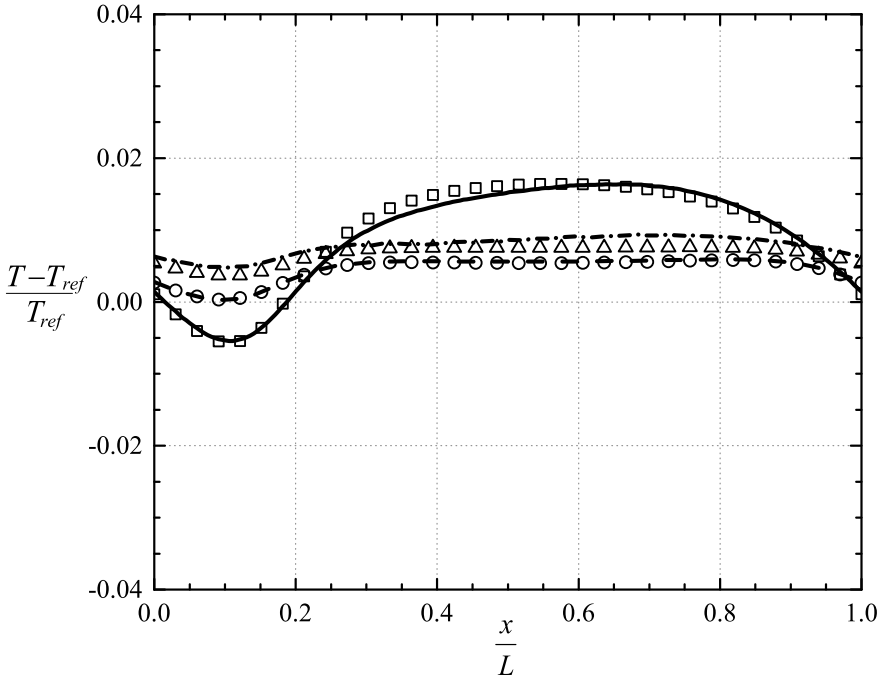

Figure 2.11: Scaled Temperature vs x/L. V(0) = V(L) = 4.8 V_c, T(0) = T(L) = T_{ref} = 1.05 T_c. Lines denote results from the full Navier-Stokes equations and symbols denote the solutions to (2.57) and (2.71), (2.70), and (2.64). Results for the adiabatic rotor are denoted by □ and ———, results for the adiabatic stator are denoted by ◯ and – – – – –, and results for the constant temperature walls T_R = 1.10 T_c, T_S = 1.01 T_c, are denoted by △ and —·—·—·— .

be 1.05 T_{ref}. The temperatures seen in Fig. 2.11 are taken to be those along the centerline so that the curves will not necessarily begin at T = T_{ref}. We compare the temperature variations computed from the Reynolds equation and the solutions to the nonconvective temperature equation discussed in Section 2.5 to those computed using the full Navier-Stokes equations. The agreement is again seen to be very good. The temperature variation is seen to be the strongest for the case of the adiabatic rotor.

The density distributions on the centerline of the channel for the cases of V(0) = V(L) = 2.4 V_c and 1.2 V_c and T = 1.05 T_{ref} are plotted in Fig. 2.12-2.13. For the case depicted in Fig. 2.12, the local values Re(h/L)^2 and Pr Re(h/L)^2 all remain small over nearly all of the flow. The agreement between (2.57) and the exact equations is seen to be quite good. In the case depicted in Fig. 2.13 differences in the density along the centerline are approximately 20.2% for the case of the adiabatic rotor. The values of the reduced Reynolds number remain small over most of the flow. An inspection of Fig. 2.10 reveals that the local values of Pr Re(h/L)^2

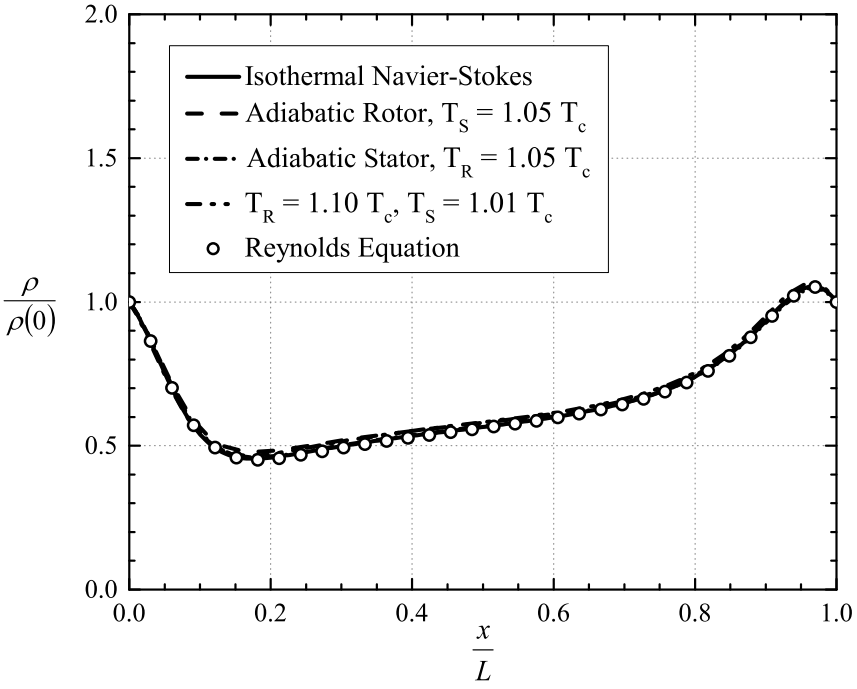

Figure 2.12: Scaled Density vs x/L. Here V(0) = V(L) = 2.4 V_c, T(0) = T(L) = 1.05 T_c.

on the centerline remain small for this case. However, inspection of detailed solutions reveals that the local values of Pr $Re(h/L)^2$ become as large as 1.58 near the y = 0 surface. Thus, the discrepancies seen in Fig. 2.13 are due to fact that near-critical effects are no longer negligible in at least part of the flow regime. The case depicted in Fig. 2.13 represents a boundary of the region of validity of the compressible Reynolds equation.

The scaled density and pressure along the channel centerline for the case V(0) = V(L) = 0.6 V_c are plotted in Fig. 2.14-2.15. The local values of the reduced Reynolds number were found to be small over most of the flow. The solutions to the Reynolds equation and the isothermal Navier-Stokes equations yield pressure and density variations which are in reasonably agreement with each other. Inspection of Fig. 2.10 reveals that the values of Pr $Re(h/L)^2 \ll 1$ for at least the case of the adiabatic rotor. The local values of Pr $Re(h/L)^2$ are also found to be as large as 4.23 on the y = 0 surface. We conclude that both the Reynolds equation (2.57) and the simplified temperature equation (2.62) are no longer valid leading to the significant differences seen in Fig. 2.14-2.15 and the observed strong dependence on the thermal boundary conditions used.

We close this section by comparing solutions to the full Reynolds equation (2.57) to those of the Reynolds equation corresponding to ideal gases (2.61). The case considered is that where

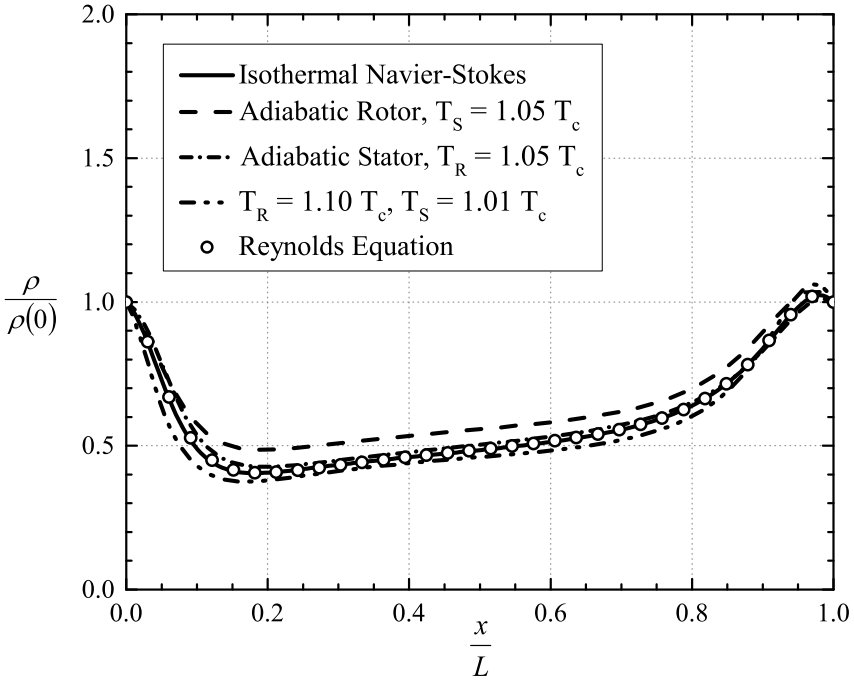

Figure 2.13: Scaled Density vs x/L. Here V(0) = V(L) = 1.2 V_c, T(0) = T(L) = 1.05 T_c.

V(0) = V(L) = 2 V_c and T_{ref} = 1.03 T_c and the same values of h_o, L, and δ as used for Fig. 2.9-2.15. The speed number used in (2.61) is based on the ideal gas viscosity evaluated at T_{ref} and was found to be 8.03. The speed number used in the full Reynolds equation (2.57) was found to be 38.30. The reason for the large difference in the speed number (2.60) is the difference in the numerical value of the bulk modulus which, at a fixed value of V, is proportional to the magnitude of the slope of the isotherm, i.e.,

$$\left| \left. \frac{\partial p}{\partial V} \right|_T \right|.$$

Because the magnitude of the actual slope is considerably less than that of an ideal gas at the same density and temperature, the speed number computed on the basis of the ideal gas theory will be less than the dense gas value. The scaled pressure distributions for the two models are plotted in Fig. 2.16. The maximum difference was found to be approximately 40%. The density variations were found to exhibit even larger differences. The variation of scaled effective bulk modulus (2.59) for the two models is plotted in Fig. 2.17. Because $\kappa_T \longrightarrow$ p and $\mu \longrightarrow \mu_0(T_{ref})$ in the ideal gas limit and the flows are isothermal, the variation in the scaled κ_{Te} of an ideal gas is roughly that of the pressure. For the dense gas, the variation of the scaled κ_{Te} is qualitatively different. The flow follows isotherms similar to those plotted

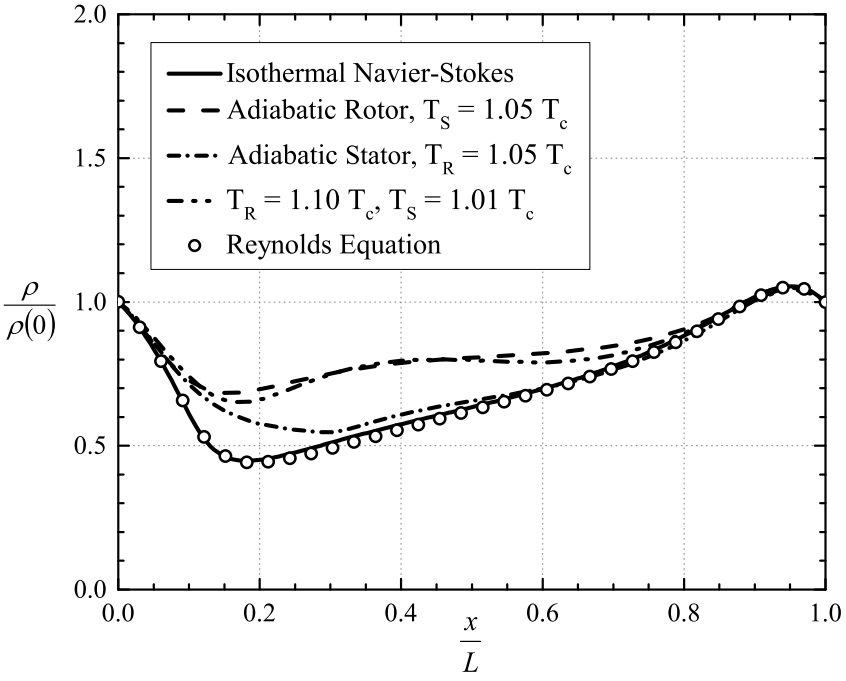

Figure 2.14: Scaled Density vs x/L. Here V(0) = V(L) = 0.6 V_c, T(0) = T(L) = 1.05 T_c.

in Fig. 2.8. At x = 0, the slope of the $\overline{\kappa}_{Te}$ vs V/V_c curve is positive. Thus, the decreasing density causes the value of $\overline{\kappa}_{Te}$ to increase until it attains the local maximum at x $\approx$ 0.08 L. At the minimum value of density and pressure, the value of $\overline{\kappa}_{Te}$ reaches the local minimum value seen in Fig. 2.17. The density and pressure then increase with increasing x/L yielding a mild increase in $\overline{\kappa}_{Te}$ until the local maximum is attained at x $\approx$ 0.67 L. This local maximum in $\overline{\kappa}_{Te}$ is identical to that at x $\approx$ 0.08 L. As the density and pressure increase further, the value $\overline{\kappa}_{Te}$ decreases until the local maximum in pressure and density are attained at x $\approx$ 0.97 L which also corresponds to the second local minimum in $\overline{\kappa}_{Te}$.

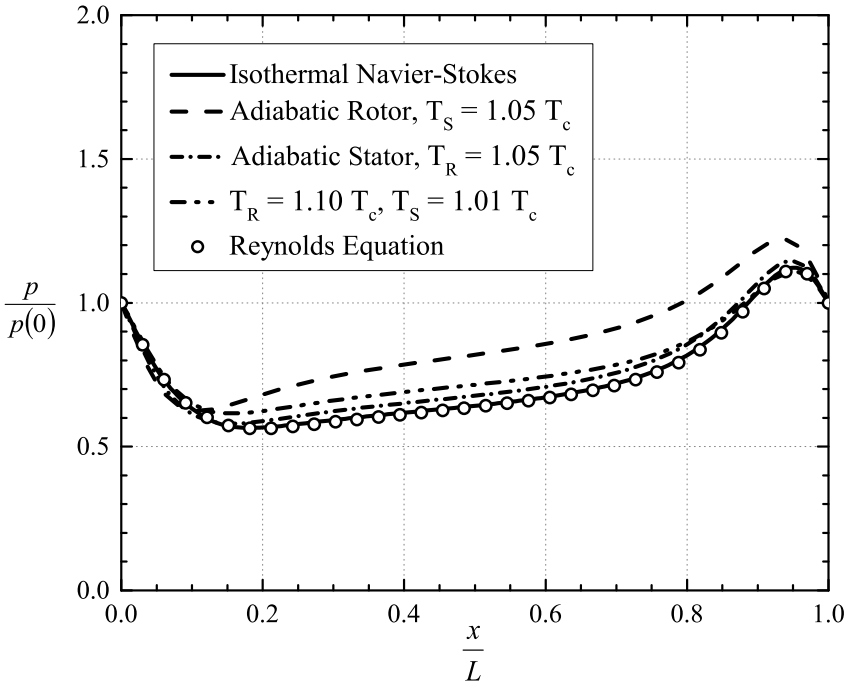

Figure 2.15: Scaled Pressure vs x/L. Here V(0) = V(L) = 0.6 V_c, T(0) = T(L) = 1.05 T_c.

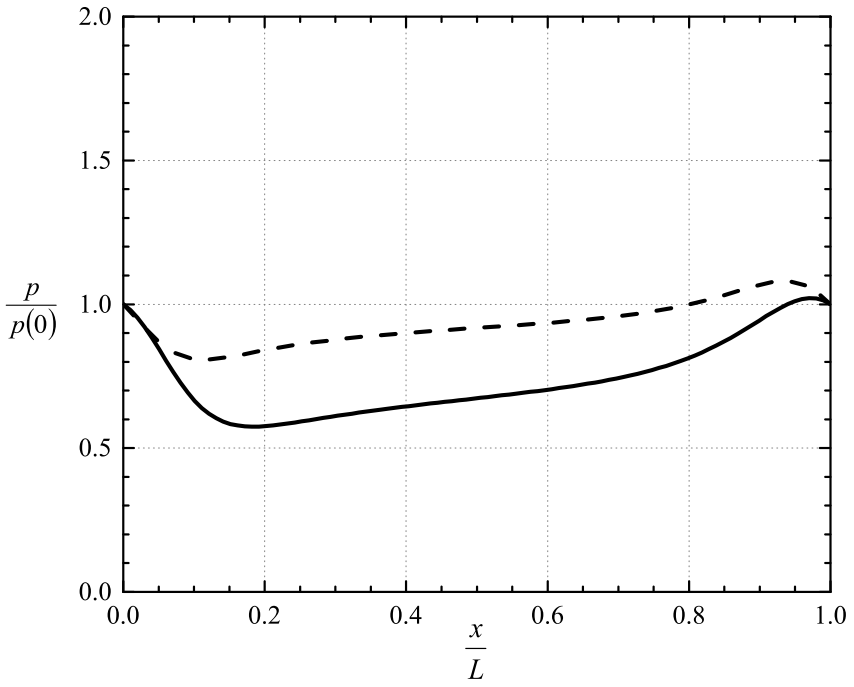

Figure 2.16: Comparison of Scaled Pressures Computed from (2.57) and (2.61). V(0) = V(L) = 2 V_c, T(0) = T(L) = 1.03 T_c. Solid line denotes the solution to the full Reynolds equation and the dashed line denotes the solution to the ideal gas version of Reynolds equation.

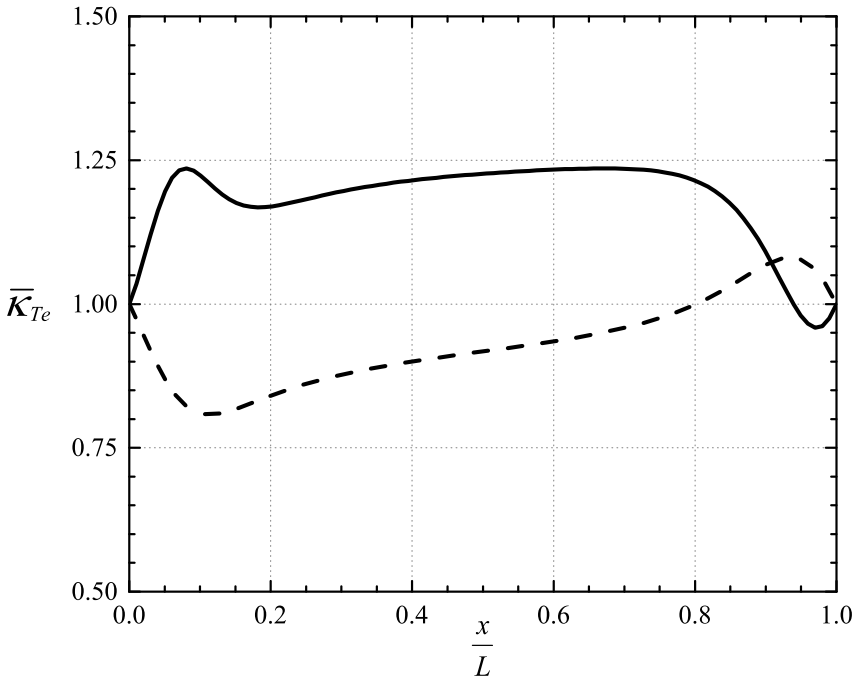

Figure 2.17: Comparison of Scaled Effective Bulk Modulus (2.59) Computed from (2.57) and (2.61). V(0) = V(L) = 2 V_c, T(0) = T(L) = 1.03 T_c. Solid line denotes the solution to the full Reynolds equation and the dashed line denotes the solution to the ideal gas version of Reynolds equation.

2.8 Summary

In this study we have sketched the derivation of the Reynolds equation and the corresponding energy equation for two-dimensional, laminar, steady, compressible flows of single-phase fluids. The viscosity and thermal conductivity are taken to be functions of density and temperature. The Reynolds equation (2.57) is seen to be valid for most pressures and temperatures corresponding to supercritical and dense gases. For a compressible flow, the classical conditions for lubrication flows, i.e., (2.2), are no longer sufficient to guarantee the validity of Reynolds equation. We have shown that we must further require that the temperature changes be sufficiently small as expressed by (2.41). When one of the walls is adiabatic, (2.41) is satisfied automatically provided (2.47) holds. If the walls have fixed temperatures, we must make the additional restriction (2.38).

The results of the present theory are expected to be in very good agreement with the numerical solutions to the exact Navier-Stokes equations in most of the supercritical and dense gas regime. Additionally, we have shown that whenever the Reynolds equation is valid, thermal convection can be neglected. The resultant energy equation can be integrated explicitly for the temperature distribution and recovery temperatures, i.e., the temperatures at adiabatic walls. Our derivation has introduced a single thermodynamic parameter, the effective bulk modulus, that along with the speed number (2.60), governs the flow. The effective bulk modulus (2.58) gives a local measure of the relative importance of the compressibility to the fluid friction. In the simplest flows of ideal gases, the speed number is sufficient to determine the flow details. In dense and supercritical fluids, the flow will strongly depend on the thermodynamic state; this dependence enters the Reynolds equation through the effective bulk modulus.

We have also demonstrated that the compressible Reynolds equation is no longer valid when the thermodynamic states are in the neighborhood of the thermodynamic critical point due to the singularities in the specific heat at constant pressure, thermal expansion coefficient, and Prandtl number discussed in Section 2.2. Near the thermodynamic critical point, convection of energy and variations in the density and viscosity across the gap are no longer negligible. The region in which these near-critical effects occur is given by (2.72) or, equivalently, (2.74)-(2.75).

The estimates given in Section 2.6 are most conveniently computed using known reference values. However, our calculations suggest that near-critical effects can occur locally. These are most likely to first appear near the $y = 0$ surface where the particle speed is the largest and for the case of the adiabatic rotor.

We have also compared solutions of the full Reynolds equation (2.57) to its ideal gas version (2.61). The differences between the solutions seen in Fig. 2.16 are attributed to the large difference in the computed speed number and to the qualitative behavior of the effective bulk modulus (2.58).

The general approximation scheme and restrictions used here are expected to hold for a wide variety of configurations including compressible squeeze films and three dimensional lubrication flows.

Bibliography

[1] O. Reynolds. On the theory of lubrication and its application to Mr. Beauchamp Tower's experiments, including an experimental determination of the viscosity of olive oil. *Proceedings of the Royal Society of London*, 40(242-245), 191–203, 1886.

[2] O. Pinkus and B. Sternlicht. *Theory of Hydrodynamic Lubrication.* McGraw-Hill, 1961.

[3] W. A. Gross, L. A. Matsch, V. Castelli, A. Eshel, J. H. Vohr, and M. Wildmann. *Fluid Film Lubrication.* John Wiley and Sons, Inc., 1980.

[4] A. Z. Szeri. *Fluid Film Lubrication.* Cambridge University Press, 2010.

[5] B. J. Hamrock, S. R. Schmidt, and B. O. Jacobson. *Fundamentals of Fluid Film Lubrication.* CRC press, 2004.

[6] Ockendon, H. and Ockendon, J R. *Viscous Flow.* Cambridge University Press, 1995.

[7] R. C. Reid, J. M. Prausnitz, B. E. Poling. *The Properties of Gases and Liquids.* McGraw-Hill, 1987.

[8] L. Tisza. Supersonic absorption and Stokes' viscosity relation. *Phys.Rev.*, 61, 531–536, 1942.

[9] G. Emanuel. Bulk viscosity of a dilute polyatomic gas. *Physics of Fluids A*, 2(12), 2252–2254, 1990.

[10] M. S. Cramer. Numerical estimates for the bulk viscosity of ideal gases. *Physics of Fluids*, 24, 066102, 2012.

[11] V. Dostal, M. J. Driscoll, and P. Hejzlar. A supercritical carbon dioxide cycle for next generation nuclear reactors. Technical report, MIT-ANP-TR-100, 2004.

[12] C. DellaCorte, K. C. Radil, R. J. Bruckner, and S. A. Howard. Design, fabrication, and performance of open source generation I and II compliant hydrodynamic gas foil bearings. *Tribology Transactions*, 51(3), 254–264, 2008.

[13] S. A. Wright, R. F. Radel, M. E. Vernon, G. E. Robert, and P. S. Pickard. Operation and analysis of a supercritical CO_2 Brayton cycle. *Sandia Report, No. SAND2010-0171*, 2010.

[14] T. M. Conboy, S. A. Wright, J. Pasch, D. Fleming, G. Rochau, and R. Fuller. Performance characteristics of an operating supercritical CO_2 Brayton cycle. *Journal of Engineering for Gas Turbines and Power*, 134(11), 111703, 2012.

[15] H. Chen, D. Y. Goswami and E. K. Stefanakos. A review of thermodynamic cycles and working fluids for the conversion of low-grade heat. *Renewable and Sustainable Energy Reviews*, 14(9), 3059–3067, 2010.

[16] C. S. Turchi, Z. Ma, T. W. Neises, and M. J. Wagner. Thermodynamic study of advanced supercritical carbon dioxide power cycles for concentrating solar power systems. *Journal of Solar Energy Engineering*, 135(4), 041007, 2013.

[17] B. D. Iverson, T. M. Conboy, J. J. Pasch and A. M. Kruizenga. Supercritical CO_2 Brayton cycles for solar-thermal energy. *Applied Energy*, 111, 957–970, 2013.

[18] E. W. Lemmon, M. L. Huber, and M. O. McLinden. NIST Reference fluid thermodynamic and transport properties–REFPROP. *NIST Standard Reference Database*, 23, v7, 2002.

[19] G. G. Hirs. A bulk-flow theory for turbulence in lubricant films. *Journal of Lubrication Technology*, 137–146, 1973.

[20] T. M. Conboy. Real-gas effects in foil thrust bearings operating in the turbulent regime. *Journal of Tribology*, 135(3), 031703, 2013.

[21] D. Kim. Design space of foil bearings for closed-loop supercritical CO_2 power cycles based on three-dimensional thermohydrodynamic analyses. *Journal of Engineering for Gas Turbines and Power*, 138(3), 032504, 2016.

[22] S. Dousti and P. Allaire. A compressible hydrodynamic analysis of journal bearings lubricated with supercritical carbon dioxide. In *Proceeding of Supercritical* CO_2 *Power Cycle Symposium. San Antonio, TX*, 2016.

[23] S. Y. Chien, M. Cramer, A. Untaroiu. A compressible thermohydrodynamic analysis of journal bearings lubricated with supercritical CO_2. In *ASME 2017 Fluids Engineering Division Summer Meeting. Waikoloa, HI*, paper No. FEDSM2017-69310, 2017.

[24] T. H. Chung, L. L. Lee, K. E. Starling. Applications of kinetic gas theories and multiparameter correlation for prediction of dilute gas viscosity and thermal conductivity. *Industrial & Engineering Chemistry Fundamentals*, 23(1), 8–13, 1984.

[25] T. H. Chung, M. Ajlan, L. L. Lee, K. E. Starling. Generalized multiparameter correlation for nonpolar and polar fluid transport properties. *Industrial & Engineering Chemistry Research*, 27(4), 671–679, 1988.

Chapter 3

Pressure, temperature, and heat flux in high speed lubrication flows of pressurized gases

The contents of this chapter are reproduced from *S. Y. Chien and M. S. Cramer. Pressure, temperature, and heat flux in high speed lubrication flows of pressurized gases. Tribology International, 129, 468–475, 2019* , with the permission of Elsevier. The published article can be found at: `https://www.sciencedirect.com/science/article/pii/S0301679X18304262`.

Attribution

The work presented in this chapter was primarily carried out by S. Y. Chien. M. S. Cramer conceived of the main idea and contributed to the development and implementation of this work.

Abstract

We present approximate solutions to the compressible Reynolds equation and the corresponding temperature equation which are valid for large speed numbers in the dense and supercritical gas regime. The flows are taken to be two-dimensional, steady, compressible, single-phase and laminar. New results include explicit formulas for pressure, density, temperature and heat flux in terms of the speed number, film thickness function, and the material functions. We have found that the first correction for finite speed number will depend on the local values of the effective bulk modulus and thermal expansion coefficient. Our approx-

imations are compared to numerical solutions to the exact Reynolds theory. It was found that the first order approximation is necessary to obtain realistic pressure and temperature distributions.

3.1 Introduction

In many applications involving lubrication theory, the Reynolds equation plays a central role. Since first stated by Osborne Reynolds in 1886 [1], the Reynolds equation has been extended to include the effects of unsteadiness, turbulence, three-dimensionality, non-newtonian fluids and thermal effects [2, 5, 4, 3]. While the conditions leading to the Reynolds approximation are frequently satisfied in many applications, see, e.g., [6, 7, 8, 9, 10], further motivation for studies of the Reynolds equation is that it provides valuable insights into more complex lubrication flows while in a relatively simple context.

Historically, large viscosity liquids are employed as lubricating fluids. In recent years there has been considerable interest in the use of both low and high pressure gases as working fluids [11, 12, 13, 14, 15]. The advantage of gases over large viscosity liquids include significant weight reduction, elimination of fouling and complications due to phase changes and the incompatibility with working fluids in power systems. Because the viscosities of gases tend to be smaller than those of liquid lubricants, lubricating gas flows require larger shear strains and are frequently compressible.

The theory of low pressure gas lubrication is well established in the literature where the perfect gas model is coupled with the Reynolds equation to account for compressibility effects [2, 5, 4, 3]. The resulting Reynolds equation in these studies is typically cast as a nonlinear differential equation for pressure [2, 5, 4, 3]. Both numerical and perturbation techniques are commonly employed to obtain solutions to the Reynolds equation. One of the first to derive perturbation solutions for low pressure gas films for high and low speed flows, i.e., large and small speed numbers (or bearing numbers) was Gross [3]. Peng and Khonsari [16] applied similar approach to estimate the lowest order hydrodynamic pressure for foil bearings with large speed numbers and ideal gases.

When the thermodynamic state is such that the lubricating fluids are no longer ideal, i.e., are in the dense or supercritical gas regimes, one must account for a strong dependence of material properties on the thermodynamic state and on rapid changes and singularities in the flow variables. In fact, even the validity of the Reynolds equation must be questioned in the supercritical gas regime, see, e.g., Chien, et al [17, 18]. Previous investigations such as [19, 21, 20, 22, 23] apply pure numerical schemes to different versions of the Reynolds equation. These studies account for the real-gas behavior of the lubricating gas through use of digital table look-ups. For example, studies [19, 21, 20] employed the NIST REFPROP database [24] and Guenat and Schiffmann [22] used the COOLPROP database [25]. Dousti and Allaire [23] have modeled the real gas behavior with a linear pressure-density relation,

but this model is not expected to be valid over the full range of pressures and temperatures corresponding to the dense and supercritical regimes [26].

Because of the well known singularities in the supercritical gas regime, Chien, et al [17] have carried out a detailed justification of the Reynolds equation. Limitations on the Reynolds equation were given. The corresponding simplified temperature equation was also derived. Even when the traditional thin film and lubrication approximations are valid, it was shown that the Reynolds equation and its corresponding temperature equation break down simultaneously in the vicinity of the thermodynamic critical point. Solutions to Chien, et al's [17, 18] Reynolds and temperature equation were compared to solutions of the full Navier-Stokes equations revealing excellent agreement in the stated range of validity of the theory.

The goal of the present study is to develop explicit analytical solutions for density, pressure, temperature, and wall heat flux for high speed lubrication flows corresponding to a simple journal bearing. We follow the approach of [19, 21, 20, 22] in that we analyze the Reynolds equation. In particular, we base our calculations on the Reynolds and temperature equation derived by [17]. We take the speed (or bearing) number to be large and present the first correction to the lowest order theory; here the term "lowest order" will typically refer to the approximation corresponding to an infinite speed number. The advantage of this work is that the dependence on speed number and thermodynamic state is explicit. The present work complements the extensive, but purely numerical, previous studies of pressurized gases [19, 21, 20, 22] and the perturbation analysis of ideal gases by Gross [3].

In the next section we describe the specific configuration and thermal boundary conditions to be considered. We take the flow to be sufficiently far from the near-critical regime so that Chien et al's [17] Reynolds equation and its corresponding simplified temperature equation can be regarded as valid. Exact solutions to Chien, et al.'s [17] temperature equation are also presented in Section 3.2. In Section 3.3 we present the approximate solutions for density, pressure, temperature and heat flux valid for large speed numbers. In Section 3.4 we compare these approximate solutions to numerical solutions of the Reynolds equation and the corresponding temperature equation. The numerical solutions are generated using realistic and explicit models for the equation of state, viscosity, and thermal conductivity.

3.2 Formulation

We consider a two-dimensional flow in a thin gap corresponding to the configuration sketched in Figure 3.1. This representation is a reasonable representation of a (two-dimensional) journal bearing if the clearance is small. The flow contained in the region $0 \leq x \leq L$ and $0 \leq y \leq h(x)$ is taken to be steady, single-phase, compressible, and laminar. All physical variables are taken to have identical values at x = 0 and x = L. The film thickness h(x) is

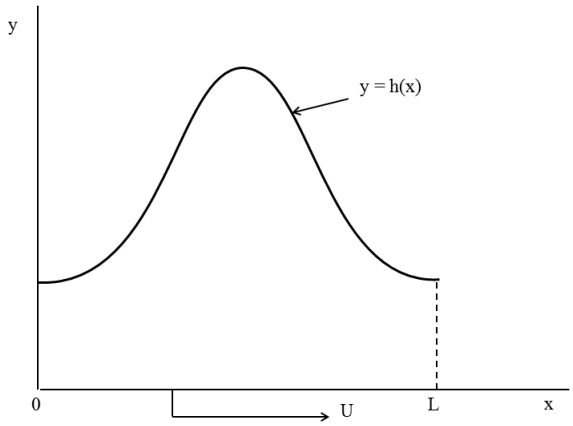

Figure 3.1: Unwrapped Configuration of a Journal Bearing. The y = 0 axis corresponds to the surface of the rotor and y = h(x) denotes the approximate position of the stator. The value of x is the distance measured along the rotor surface from the point of minimum film thickness. The quantity L denotes the circumference of the rotor and U denotes the constant speed of the surface of the rotor. The fluid is contained in the space $0 \leq$ y $\leq$ h(x), $0 \leq$ x $\leq$ L. Only x and y variations are considered and all velocity vectors will lie in the x-y plane.

any sufficiently smooth function that satisfies

$$h(0) = h(L) \text{ and } \frac{dh}{dx}(0) = \frac{dh}{dx}(L) = 0. \tag{3.1}$$

A specific form of h(x) which corresponds to a two-dimensional journal bearing having a thin gap is provided in Section 3.4. Axial flow is not considered so that solutions are expected to be valid near the center plane of a long bearing. The upper surface, i.e., $y = h(x)$, is at rest and varies with the length scale L. The lower surface, i.e., $y = 0$, is translating with constant speed U in the positive x-direction. For convenience, we will refer to the upper and lower surfaces as the stator and rotor surfaces, respectively. Thus, the no-slip and kinematic boundary conditions require

$$\mathrm{v}_x = U, \mathrm{v}_y = 0 \; at \; y = 0, \tag{3.2}$$

$$\mathrm{v}_x = \mathrm{v}_y = 0 \; at \; y = h(x), \tag{3.3}$$

where v_x and v_y represent the velocity components in the x and y directions. Thermal boundary conditions include constant temperature walls where we specify both upper and lower surfaces with fixed temperatures. We will also consider boundary conditions corresponding to an adiabatic wall at either $y = h(x)$ or at $y = 0$ with a fixed known temperature at the non-adiabatic wall.

The Reynolds equation derived by Chien, et al [17] can be written in non-dimensional form

as

$$\frac{d}{d\overline{x}}\left(\overline{h}^3\overline{\kappa}_{Te}\,\frac{d\overline{\rho}}{d\overline{x}}\right)=\Lambda\,\frac{d(\overline{\rho}\overline{h})}{d\overline{x}}, \tag{3.4}$$

where $\overline{x}=x/L$ and $\overline{h}=h(x)/h_0$; here $h_o\equiv$ h(0) and is the measure of the thickness of the fluid film. We take values of quantities evaluated at $\overline{x}=0$ as the constant reference values and denote these values by the subscript "ref". We denote the fluid density by ρ so that $\overline{\rho}\equiv\rho/\rho_{ref}$ is the scaled density. The bulk modulus of the fluid is

$$\kappa_T\equiv\kappa_T(\rho,T)=\rho\,\frac{\partial p}{\partial\rho}\bigg|_T, \tag{3.5}$$

where p = p(ρ,T) is the thermodynamic, i.e., absolute, pressure and T is the absolute temperature. Chien, et al [17] have defined

$$\kappa_{Te}=\kappa_{Te}(\rho,T)\equiv\frac{\kappa_T(\rho,T)}{\mu(\rho,T)} \tag{3.6}$$

as the effective bulk modulus. Here μ(ρ,T) is the shear viscosity. The scaled version of the effective bulk modulus appearing in (3.4) is defined as $\overline{\kappa}_{Te}\equiv\kappa_{Te}/\kappa_{Te}|_{ref}$. In [17], Chien, et al have shown that T $\approx$ T_{ref} for the purposes of solving (3.4) so that

$$\overline{\kappa}_{Te}\approx\frac{\kappa_{Te}(\rho,T_{ref})}{\kappa_{Te}(\rho_{ref},T_{ref})} \tag{3.7}$$

whenever (3.4) is valid.

The quantity Λ is the speed number introduced by Chien, et al [17] and is given by

$$\Lambda\equiv 6\frac{UL}{h_o^2\kappa_{Te}|_{ref}}. \tag{3.8}$$

This version of the speed number is found to be the most natural and convenient form of the speed number for studies of dense and supercritical fluids. The speed number gives a measure of either the speed or the overall compressibility of the flow. The effective bulk modulus, on the other hand, gives a measure of the local fluid stiffness to the local fluid friction.

Chien, et al [17] have shown that the Reynolds equation (3.4) is valid when the thin film and lubrication approximations are valid, i.e., when

$$h_o\ll L\ \text{ and }\ Re\frac{h_o^2}{L^2}\ll 1,$$

where Re $\equiv\rho_{ref}UL/\mu_{ref}$ is the Reynolds number. When the temperature is fixed at the surface of rotor and stator, the product of the temperature difference and thermal expansivity is required to be sufficiently small. The Reynolds equation is then valid for all thermodynamic

states in the single-phase regime except those very near thermodynamic critical point. For the present purposes, the near-critical region was found to be

$$\left|\frac{\rho-\rho_c}{\rho_c}\right| = O\left(Re\frac{h_o^2}{L^2}\right)^{1/2} \ll 1,$$
$$\left|\frac{T-T_c}{T_c}\right| = O\left(Re\frac{h_o^2}{L^2}\right)^{3/2} \ll 1.$$

Here the subscript "c" denotes quantities evaluated at the thermodynamic critical point.

The density distribution is found by solving (3.4) subject to the boundary conditions

$$\overline{\rho}(0) = \overline{\rho}(1) = 1 \tag{3.9}$$

once the models for the shear viscosity $\mu(\rho,\mathrm{T})$ and thermodynamic pressure $\mathrm{p} = \mathrm{p}(\rho,\mathrm{T})$ are specified. This two-point boundary value problem is solved for $\overline{\rho}(\overline{x})$ through use of a straightforward shooting method. The pressure distribution is then determined by substitution into the equation of state, i.e., $\mathrm{p} = \mathrm{p}(\rho,\mathrm{T}_{ref})$.

The first integral of (3.4) subject to (3.9) will be convenient later in this study. This first integral is found to be

$$\overline{\rho}\overline{h} = 1 + \frac{1}{\Lambda}\left(\overline{h}^3\overline{\kappa}_{Te}\frac{d\overline{\rho}}{d\overline{x}} - \frac{d\overline{\rho}}{d\overline{x}}(0)\right). \tag{3.10}$$

Here we have used (3.1), (3.9), and the fact that $\overline{\kappa}_{Te}(1) \equiv 1$.

The temperature perturbations are determined from the energy equation. Chien, et al [17] have shown that energy convection in gases is negligible whenever (3.4) is valid. The nondimensional form of the resultant temperature equation can be written:

$$\frac{\partial^2\overline{T}}{\partial\overline{y}^2} = -\frac{PrEc}{\overline{k}}\left[\overline{\mu}\left(\frac{\partial u}{\partial\overline{y}}\right)^2 + \beta T\, u\frac{d\overline{p}}{d\overline{x}}\right], \tag{3.11}$$

where $\overline{T} = (T - T_{ref})/\Delta T$, $\overline{k} = k/k_{ref}$, and $\mathrm{Ec} = U^2/c_{pref}\Delta T$ is the Eckert number. The quantity ΔT represents a measure of temperature differences occurring in the flow and will depend on the specific boundary conditions used. The quantity $\mathrm{k} = \mathrm{k}(\rho,\mathrm{T})$ is the thermal conductivity, $\mathrm{c}_p = \mathrm{c}_p(\rho,\mathrm{T})$ is the specific heat at constant pressure,

$$Pr \equiv \frac{\mu_{ref}c_{pref}}{k_{ref}}, \tag{3.12}$$

is the Prandtl number evaluated at the reference state, β is the thermal expansion coefficient, and u is the scaled x-component of the particle velocity found to be

$$u(\overline{x},\overline{y}) = \frac{\mathrm{v}_x}{U} = \left(1 - A\overline{h}\overline{y}\right)\left(1 - \frac{\overline{y}}{\overline{h}}\right), \tag{3.13}$$

where the factor A is defined as

$$A(\overline{x}) \equiv \frac{1}{2\overline{\mu}}\frac{d\overline{p}}{d\overline{x}} = \frac{3}{\Lambda}\frac{\overline{\kappa}_{Te}}{\overline{\rho}}\frac{d\overline{\rho}}{d\overline{x}}. \tag{3.14}$$

We note that T $\approx$ T_{ref} for the validity of (3.4) and (3.11) and $\overline{\mu}$, $\overline{k}$ and βT were shown to be functions of $\rho(\overline{x})$ and T_{ref} only whenever (3.4) and (3.11) are valid in [17]. As a result, we can integrate (3.11) explicitly at each value of $\overline{x}$ and the only functions of $\overline{y}$ on the right hand side of (3.11) will be those introduced by u and its derivatives. Inspection of (3.11) reveals that the temperature perturbations are determined by a balance of conduction, viscous dissipation, and flow work.

We have obtained solutions to (3.11) for three commonly encountered thermal boundary conditions. When both stator and rotor surfaces have prescribed temperatures, i.e., $T = T_R$ = constant at $\overline{y} = 0$ and $T = T_S$ = constant at $\overline{y} = \overline{h}(\overline{x})$, the temperature variation is then found to be

$$\frac{T - T_R}{\Delta T} = \overline{y}\,\frac{PrEc}{2\overline{k}}\left[\alpha_1(\overline{h}^3 - \overline{y}^3) + \alpha_2(\overline{h}^2 - \overline{y}^2) + \alpha_3(\overline{h} - \overline{y})\right] + \frac{\overline{y}}{\overline{h}}, \tag{3.15}$$

where $\Delta T \equiv$ T_S - T_R for this case, and the factors

$$\alpha_1 \equiv \frac{1}{3}A^2\overline{\mu}(\beta T + 2), \tag{3.16}$$

$$\alpha_2 \equiv -\frac{2}{3}\frac{A\overline{\mu}}{\overline{h}}(\beta T + 2)(A\overline{h}^2 + 1), \tag{3.17}$$

$$\alpha_3 \equiv \frac{\overline{\mu}}{\overline{h}^2} + A\overline{\mu}\left[A\overline{h}^2 + 2\beta T + 2\right]. \tag{3.18}$$

We now differentiate (3.15) to obtain the scaled heat flux at the rotor and stator surfaces. The results are

$$\overline{q}_y\Big|_{\overline{y}=0} = -\frac{PrEc}{2}\left[\alpha_1\overline{h}^3 + \alpha_2\overline{h}^2 + \alpha_3\overline{h}\right] - \frac{\overline{k}}{\overline{h}}, \tag{3.19}$$

$$\overline{q}_y\Big|_{\overline{y}=\overline{h}} = \frac{PrEc}{2}\left[3\alpha_1\overline{h}^3 + 2\alpha_2\overline{h}^2 + \alpha_3\overline{h}\right] - \frac{\overline{k}}{\overline{h}}, \tag{3.20}$$

where

$$\overline{q}_y \equiv -\,\overline{k}\,\frac{\partial\overline{T}}{\partial\overline{y}} = \frac{h_o}{k_{ref}\Delta T}q_y, \tag{3.21}$$

and q_y is the dimensional y-component of the Fourier heat flux vector.

If we take the stator surface, i.e., $\overline{y} = \overline{h}$, to be adiabatic and the rotor surface to have a fixed temperature T_R, we then find

$$\frac{T - T_R}{\frac{U^2}{2c_{pref}}} = \frac{Pr}{\overline{k}}\left[\alpha_1(4\overline{h}^3\overline{y} - \overline{y}^4) + \alpha_2(3\overline{h}^2\overline{y} - \overline{y}^3) + \alpha_3(2\overline{h}\overline{y} - \overline{y}^2)\right]. \tag{3.22}$$

At the stator, i.e., $\overline{y} = \overline{h}$, the temperature is defined as the adiabatic wall temperature T_{ad} and is given by

$$r_f \equiv \frac{T_{ad} - T_R}{\frac{U^2}{2c_{pref}}} = \frac{Pr}{\overline{k}} \left(3\alpha_1 \overline{h}^4 + 2\alpha_2 \overline{h}^3 + \alpha_3 \overline{h}^2 \right). \tag{3.23}$$

where r_f is referred to as the recovery factor, i.e., a non-dimensional version of the temperature at an adiabatic wall. At the rotor, i.e., $\overline{y} = 0$, the scaled heat flux is

$$\overline{q}_y \Big|_{\overline{y}=0} = -\left(2\alpha_1 \overline{h}^3 + \frac{3}{2}\alpha_2 \overline{h}^2 + \alpha_3 \overline{h} \right), \tag{3.24}$$

where we have used (3.22) and taken the temperature scaling to be $\Delta T = U^2 Pr / c_{pref}$.

Finally, when the rotor surface, i.e., $\overline{y} = 0$, is taken to be adiabatic and $T = T_S$ at $\overline{y} = \overline{h}$, the temperature variation becomes

$$\frac{T - T_S}{\frac{U^2}{2c_{pref}}} = \frac{Pr}{\overline{k}} \left[\alpha_1 (\overline{h}^4 - \overline{y}^4) + \alpha_2 (\overline{h}^3 - \overline{y}^3) + \alpha_3 (\overline{h}^2 - \overline{y}^2) \right]. \tag{3.25}$$

The temperature at the rotor, i.e., $\overline{y} = 0$, is given by

$$r_f \equiv \frac{T_{ad} - T_S}{\frac{U^2}{2c_{pref}}} = \frac{Pr}{\overline{k}} \left(\alpha_1 \overline{h}^4 + \alpha_2 \overline{h}^3 + \alpha_3 \overline{h}^2 \right). \tag{3.26}$$

At the upper surface, i.e., $\overline{y} = \overline{h}$, the scaled heat flux is

$$\overline{q}_y \Big|_{\overline{y}=\overline{h}} = 2\alpha_1 \overline{h}^3 + \frac{3}{2}\alpha_2 \overline{h}^2 + \alpha_3 \overline{h}. \tag{3.27}$$

Comparison of (3.24) and (3.27) reveals that the magnitude of the heat flux at $\overline{y} = 0$ for the case of the adiabatic stator and the magnitude of the heat flux at $\overline{y} = \overline{h}$ for the case of the adiabatic rotor are identical. The magnitude of each of these heat fluxes is also identical to the magnitude of the net heat flux given by the difference between (3.19) and (3.20).

3.3 Approximate Solutions

We now determine solutions to the Reynolds equation (3.4) valid for flows with large speed number Λ. The first order approximation is found to be

$$\overline{\rho} \approx \frac{1}{\overline{h}} - \frac{1}{\Lambda} \overline{\kappa}_{Teo} \frac{d\overline{h}}{d\overline{x}} + O(\frac{1}{\Lambda^2}), \tag{3.28}$$

where the subscript "o" will always represent the quantities evaluated at the lowest order density, i.e.,

$$\overline{\kappa}_{Teo}(\overline{\rho}) \equiv \overline{\kappa}_{Te}(\frac{1}{\overline{h}}). \tag{3.29}$$

It is easily verified that the equation (3.28) satisfies boundary conditions (3.1) and (3.9). Previous studies [3, 16] typically considered the lowest order approximation, i.e, $\overline{\rho} = 1/\overline{h}$, at most. Here we see that the first correction to the lowest order approximation is proportional to the rate of variation of the gap function and the effective bulk modulus. The comparison between the lowest order and the first order approximations will be presented in Section 3.4.

From (3.28) and (3.1) we find that the approximate slope of $\overline{\rho}$ at $\overline{x} = 0$ and 1 is

$$\frac{d\overline{\rho}}{d\overline{x}}(0) \approx -\frac{1}{\Lambda}\frac{d^2\overline{h}}{d\overline{x}^2}(0) + O(\frac{1}{\Lambda^2}). \tag{3.30}$$

If $\hbar$ is a minimum at $\overline{x} = 0$,1, then the slope of $\overline{\rho}$ is always negative at $\overline{x} = 0$,1. Result (3.30) is particularly useful in the development of numerical solutions to (3.4). For example, we have used (3.30) in [17] and the present study as a first guess in the two point boundary value problem scheme applied to the Reynolds equation (3.4). Because of (3.30) and (3.9) we must have at least one maximum and one minimum in $\overline{\rho}$.

The pressure distribution is obtained by expanding the reduced pressure $p_r = p/p_c$ in a simple Taylor series for $\overline{\rho}$ near $1/\overline{h}$. When this is done, we find

$$p_r(\overline{\rho}) \approx p_r(\frac{1}{\overline{h}}) - \frac{1}{\Lambda}\frac{\kappa_T|_{ref}}{p_c}\overline{\mu}_o\,\overline{\kappa}_{Teo}^2\overline{h}\,\frac{d\overline{h}}{d\overline{x}} + O(\frac{1}{\Lambda^2}). \tag{3.31}$$

From (3.31) it is clear that the first correction to the pressure will be proportional to the product of the bulk modulus, the effective bulk modulus, and the slope of $\overline{h}^2$.

The values of (3.16)-(3.18) accurate to $O(\Lambda^{-1})$ were found to be

$$\alpha_1 = O(\frac{1}{\Lambda^2}) \tag{3.32}$$

$$\alpha_2 \approx -\frac{2}{3}\frac{\overline{\mu}}{\overline{h}}A(\beta_o T_{ref} + 2) + O(\frac{1}{\Lambda^2}), \tag{3.33}$$

$$\alpha_3 \approx \frac{\overline{\mu}}{\overline{h}^2} + 2\overline{\mu}A(\beta_o T_{ref} + 1) + O(\frac{1}{\Lambda^2}), \tag{3.34}$$

where (3.14) can now be approximated as

$$A \approx -\frac{3}{\Lambda}\frac{\overline{\kappa}_{Teo}}{\overline{h}}\frac{d\overline{h}}{d\overline{x}} + O(\frac{1}{\Lambda^2}). \tag{3.35}$$

Thus, the first order approximate solutions to (3.11) for each thermal boundary condition can be derived by taking $\alpha_1 \approx 0$ and substituting (3.33)-(3.34) in (3.15), (3.22) and (3.25).

For the case of constant temperature walls, we find that the temperature (3.15) becomes

$$\frac{T - T_R}{\Delta T} \approx \frac{\overline{y}}{\overline{h}}(1 - \frac{\overline{y}}{\overline{h}})\frac{PrEc}{2}\frac{\overline{\mu}}{\overline{k}}\Bigg[1 - \frac{2}{\Lambda}\overline{\kappa}_{Teo}\,\overline{h}\frac{d\overline{h}}{d\overline{x}}\big(3(\beta_o T_{ref} + 1) - (\beta_o T_{ref} + 2)(1 + \frac{\overline{y}}{\overline{h}})\big)\Bigg] + \frac{\overline{y}}{\overline{h}} + O(\frac{1}{\Lambda^2}). \tag{3.36}$$

From (3.36) we find that (3.19)-(3.20) become

$$\overline{q}_y\Big|_{\overline{y}=0} \approx -\frac{PrEc}{2}\frac{\overline{\mu}}{\overline{h}}\left[1-\frac{2}{\Lambda}\overline{\kappa}_{Teo}\,\overline{h}\frac{d\overline{h}}{d\overline{x}}\,(2\beta_o T_{ref}+1)\right]-\frac{\overline{k}}{\overline{h}}+O(\frac{1}{\Lambda^2}), \tag{3.37}$$

$$\overline{q}_y\Big|_{\overline{y}=\overline{h}} \approx \frac{PrEc}{2}\frac{\overline{\mu}}{\overline{h}}\left[1-\frac{2}{\Lambda}\overline{\kappa}_{Teo}\,\overline{h}\frac{d\overline{h}}{d\overline{x}}(\beta_o T_{ref}-1)\right]-\frac{\overline{k}}{\overline{h}}+O(\frac{1}{\Lambda^2}). \tag{3.38}$$

In (3.36)-(3.38) the values of $\overline{\mu}$ and $\overline{k}$ have been left as their exact values. However, to be consistent, the shear viscosity and thermal conductivity appearing explicitly in (3.36)-(3.38) should be evaluated at the first order scaled density (3.28). Alternatively, the shear viscosity could be expanded in a Taylor series to yield

$$\overline{\mu}(\overline{\rho},T_{ref})=\overline{\mu}_o-\frac{\overline{\kappa}_{Teo}}{\Lambda}\left.\frac{\partial\overline{\mu}}{\partial\overline{\rho}}\right|_o\frac{d\overline{h}}{d\overline{x}}+O\big(\frac{1}{\Lambda^2}\big), \tag{3.39}$$

where

$$\left.\frac{\partial\overline{\mu}}{\partial\overline{\rho}}\right|_o\equiv\frac{\partial\overline{\mu}}{\partial\overline{\rho}}(\frac{1}{\overline{h}},T_{ref}) \tag{3.40}$$

is the lowest order value of the rate of change of $\overline{\mu}$. The expression for the first order correction to $\overline{k}$ takes a form similar to (3.39)-(3.40).

When the stator surface, i.e., $\overline{y}=\overline{h}$, is taken to be adiabatic, the temperature (3.22) is found to be

$$\frac{T-T_R}{Pr\frac{U^2}{2c_{pref}}}\approx\frac{\overline{\mu}}{\overline{k}}\frac{\overline{y}}{\overline{h}}\left[2-\frac{\overline{y}}{\overline{h}}+\frac{2}{\Lambda}\overline{\kappa}_{Teo}\,\overline{h}\frac{d\overline{h}}{d\overline{x}}\big((\beta_o T_{ref}+2)(3-\frac{\overline{y}^2}{\overline{h}^2})-3(\beta_o T_{ref}+1)(2-\frac{\overline{y}}{\overline{h}})\big)\right]+O(\frac{1}{\Lambda^2}). \tag{3.41}$$

From (3.41) we obtain the approximation for the recovery factor,

$$r_f\approx Pr\,\frac{\overline{\mu}}{\overline{k}}\left[1-\frac{2}{\Lambda}\overline{\kappa}_{Teo}\,\overline{h}\frac{d\overline{h}}{d\overline{x}}(\beta_o T_{ref}-1)\right]+O(\frac{1}{\Lambda^2}), \tag{3.42}$$

and that for the scaled heat flux at the rotor, i.e., $\overline{y}=0$,

$$\overline{q}_y\Big|_{\overline{y}=0}\approx-\frac{\overline{\mu}}{\overline{h}}(1-\frac{2}{\Lambda}\overline{\kappa}_{Teo}\,\overline{h}\frac{d\overline{h}}{d\overline{x}}\,\beta_o T_{ref})+O(\frac{1}{\Lambda^2}). \tag{3.43}$$

If we take the rotor, i.e., $\overline{y}=0$, to be adiabatic, the temperature (3.25) becomes

$$\frac{T-T_S}{Pr\frac{U^2}{2c_{pref}}}\approx\frac{\overline{\mu}}{\overline{k}}\left[1-\frac{\overline{y}^2}{\overline{h}^2}+\frac{2}{\Lambda}\overline{\kappa}_{Teo}\,\overline{h}\frac{d\overline{h}}{d\overline{x}}\big((\beta_o T_{ref}+2)(1-\frac{\overline{y}^3}{\overline{h}^3})-3(\beta_o T_{ref}+1)(1-\frac{\overline{y}^2}{\overline{h}^2})\big)\right]+O(\frac{1}{\Lambda^2}). \tag{3.44}$$

and the recovery factor (3.26) at $\overline{y} = 0$ is approximated as

$$r_f \approx Pr\frac{\overline{\mu}}{\overline{k}}\left[1 - \frac{2}{\Lambda}\overline{\kappa}_{Teo}\,\overline{h}\frac{d\overline{h}}{d\overline{x}}\,(2\beta_o T_{ref} + 1)\right] + O(\frac{1}{\Lambda^2}). \tag{3.45}$$

At the stator, i.e, $\overline{y} = \overline{h}$, the scaled heat flux (3.27) becomes

$$\overline{q}_y\Big|_{\overline{y}=\overline{h}} \approx \frac{\overline{\mu}}{\overline{h}}(1 - \frac{2}{\Lambda}\overline{\kappa}_{Teo}\,\overline{h}\frac{d\overline{h}}{d\overline{x}}\,\beta_o T_{ref}) + O(\frac{1}{\Lambda^2}). \tag{3.46}$$

In (3.41)-(3.46) the quantities $\overline{\mu}$ and $\overline{k}$ should either be evaluated using (3.28) or expanded in a first order Taylor series.

At large speed number the first corrections to the temperature and local heat flux are due to three physical effects. The first effect is that due to the variation of the shear viscosity and thermal conductivity with density; this effect vanishes in the ideal gas limit. The second physical effect is associated with the terms proportional to βT which is recognized as the heating due to flow work. The remaining terms represent heating due to viscous dissipation. In the case of adiabatic walls, all three effects play a role in the temperature distributions, but the local heat fluxes at the non-adiabatic walls will not depend directly on the viscous dissipation, at least to the first order in large Λ.

3.4 Comparison with Exact Solutions

To demonstrate the accuracy of the large Λ approximation derived in Section 3.3, we compare the approximate solutions for density, pressure, and recovery factor to the exact solutions of the Reynolds equation (3.4) and the corresponding simplified temperature equation (3.11). For the purpose of illustration, we employ a well known Redlich-Kwong-Soave (RKS) equation of state, which is reasonably accurate and, more importantly, gives the correct qualitative behavior of all real gases. The details of the RKS equation and models for the ideal gas specific heat can be found in Reid, et al [27]. The viscosity and thermal conductivity models were taken to be those of Chung, et al [28, 29]. The choice of fluid is carbon dioxide (CO_2); physical parameters for CO_2 are taken from [27].

For all the cases presented here, we take the channel to be that corresponding to a typical journal bearing. We therefore take

$$h(x) \approx \frac{h_0}{1-\epsilon}\left[1 - \epsilon cos\left(\frac{2\pi x}{L}\right)\right], \tag{3.47}$$

with $h_0/L = 2.623 \times 10^{-5}$ and $\epsilon = 0.3$ where h_0 = h(0) = c(1-ϵ) is the minimum value of h(x), c is the radial clearance and ϵ is the eccentricity ratio. The specific volume, i.e.,V

$\equiv 1/\rho$, and the temperature at the entrance and exit are taken to be V(0) = V(L) = 5.0 V_c and T(0) = T(L) = 1.05 T_c, respectively. The pressure at these points is approximately 38.7 bar so that the thermodynamic state can be regarded as that of a dense gas or a slightly supercritical fluid.

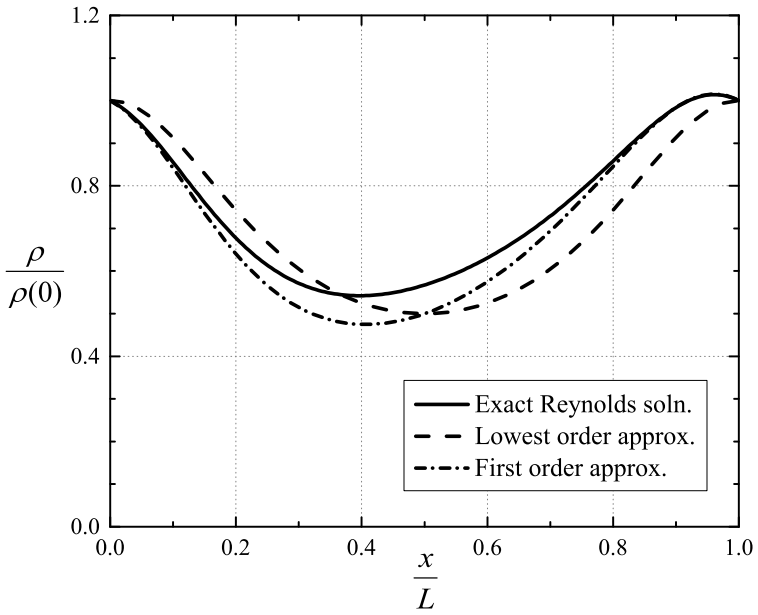

Figure 3.2: Scaled Density vs x/L at V(0) = V(L) = 5.0 V_c, T(0) = T(L) = 1.05 T_c, $\epsilon = 0.3$, $\Lambda = 25$. The solid line corresponds to the exact solutions to the Reynolds equation (3.4); the dashed line denotes the lowest order solutions, i.e., $\overline{\rho} = 1/\overline{h}$; the dash-dot line represents the first order solutions for the scaled density (3.28).

We first consider the case where the speed number $\Lambda = 25$. The variations of the scaled density and pressure for this case are plotted in Figure 3.2 and Figure 3.3. The difference between the dashed and dash-dot lines gives a measure of the influence of the first order correction terms in (3.28) and (3.31) on the distributions of density and pressure. The maximum error of the first order density is found to be 12.6%, which is smaller than that of the lowest order density.

Observation of Figure 3.2 and Figure 3.3 also reveals that the first order approximation gives better prediction of the slope of the curves near both ends of the channel. This is due to the fact that the lowest order density and pressure are independent of Λ whereas the first order approximation to the slope is given by (3.30). We also note that the local minima of the density calculated by the exact and first order theory are located approximately at x/L = 0.4 whereas the lowest order approximation will always have a local minimum at x/L = 0.5. Thus, the density and pressure distribution are better approximated by the first order approximation. We note that the factor $d\overline{h}/d\overline{x}$ in (3.28) and (3.31) vanishes at $x/L = 0.5$. As a result, the dashed line and the dash-dot line will always intersect at $x/L = 0.5$ as seen

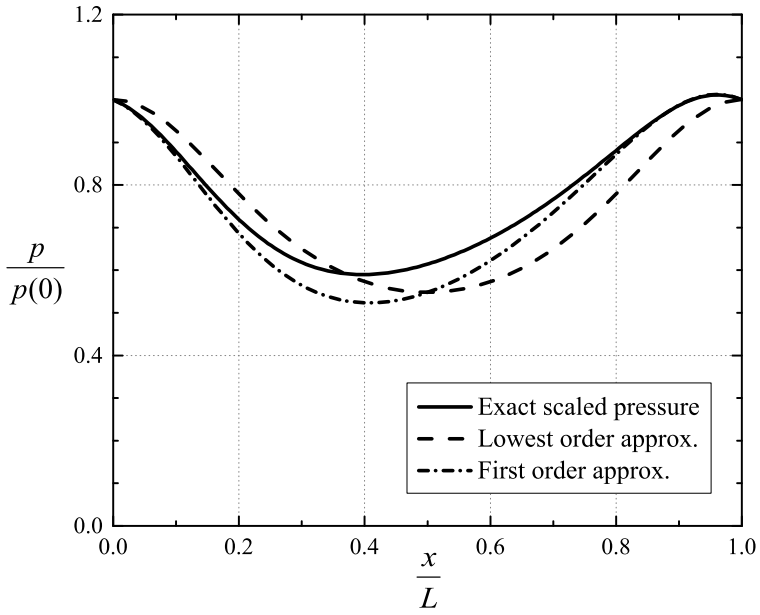

Figure 3.3: Scaled Pressure vs x/L at V(0) = V(L) = 5.0 V_c, T(0) = T(L) = 1.05 T_c, ϵ = 0.3, $\Lambda = 25$. The solid line corresponds to the exact pressure calculated by substituting the exact density to the equation of state; the dashed line represents the lowest order pressure obtained by substituting the lowest order density, i.e., $\overline{\rho} = 1/\overline{h}$, to the equation of state; the dash-dot line denotes the first order pressure computed directly from (3.31).

in Figure 3.2 and Figure 3.3.

The accuracy of our approximation is expected to increase as $\Lambda \to \infty$. To verify this we have presented the variations of density and pressure for the case of $\Lambda = 100$ in Figure 3.4 and Figure 3.5. The agreement between the approximate and exact solutions is excellent. Because of the larger value of Λ for this case, the first order correction terms in (3.28) and (3.31) become smaller, resulting in the smaller differences between the dashed and dash-dot lines seen in Figure 3.4 and Figure 3.5. However, the first order approximation still gives higher accuracy as compared to the lowest order approximation. The maximum relative errors of the lowest order and first order density are found to be approximately 4% and 0.9%, respectively.

As a further indication of the accuracy of the large Λ approximation, the maximum difference between the approximations and the results of the numerical solutions to (3.4) and (3.9) have been plotted as a function of Λ in Figure 3.6. At the chosen reference state and eccentricity, the error in the frequently employed lowest order approximation is below 5% at $\Lambda \approx 100$ but decreases slowly for larger speed numbers. As expected, the first order approximation consistently provides a better estimate of the exact solution. The error in the first order approximation is below 5% by $\Lambda = 50$ and drops below 1% for $\Lambda > 100$.

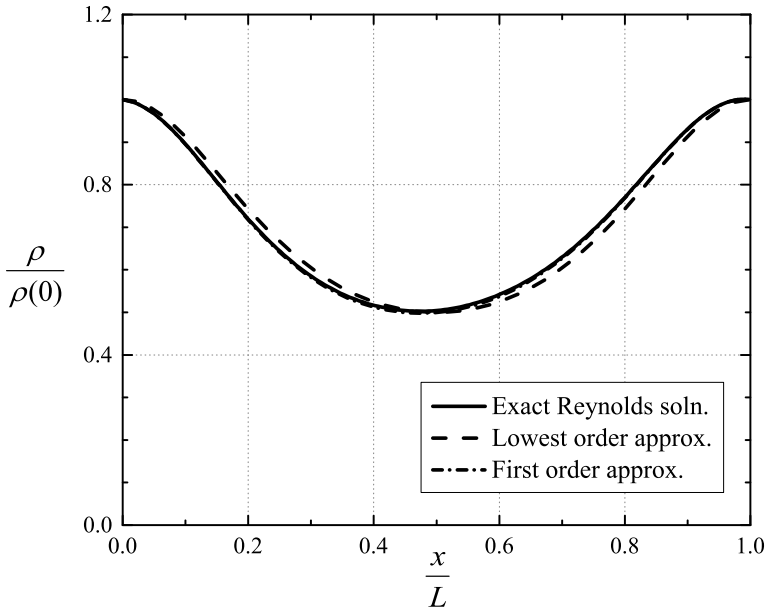

Figure 3.4: Scaled Density vs x/L at V(0) = V(L) = 5.0 V_c, T(0) = T(L) = 1.05 T_c, $\epsilon = 0.3$, $\Lambda = 100$. The solid line corresponds to the exact solutions to the Reynolds equation (3.4); the dashed line denotes the lowest order solutions, i.e., $\overline{\rho} = 1/\overline{h}$; the dash-dot line represents the first order solutions for the scaled density (3.28).

We now compare the approximations for temperature with the solutions to the simplified temperature equation (3.11). Here we only present results from the case of an adiabatic rotor due to the fact that the temperature variations for this case are always seen to be larger than those corresponding to other boundary conditions [17]. The variations of the recovery factor, i.e., (3.45), at $\Lambda = 25$ are plotted in Figure 3.7. The values of the lowest order r_f are approximately constant along the main flow direction. This is due to the fact that the values of the lowest order r_f depend only on the ratio of $\overline{\mu}$ and $\overline{k}$ and, as pointed out by Chien, et al [17], the variations of $\overline{\mu}$ for CO_2 with density at a given temperature are mild and are similar to those of $\overline{k}$. As a result, the lowest order approximation is seen to be in poor agreement with the exact solutions to (3.11). On the other hand, the variation of the first order approximation to r_f has qualitative behavior more closely resembling that of the exact solutions. However, the maximum error between the first order approximation for r_f and the exact solution is found to be approximately 45% at $x/L = 0.43$. The discrepancy in r_f is seen to decrease as Λ increases and the overall approximation becomes better.

We have also plotted the distribution of r_f at $\Lambda = 100$ for the case of an adiabatic rotor in Figure 3.8. Comparison of Figure 3.7 to Figure 3.8 reveals that the variation of r_f becomes smaller at the higher value of Λ due to the fact that the first order correction to r_f is proportional to $1/\Lambda$. Examination of Figure 3.8 also reveals that the variation of the lowest order r_f is still nearly constant whereas the first order approximation is in very good agreement with the exact simplified temperature equation. The maximum differences between the solid

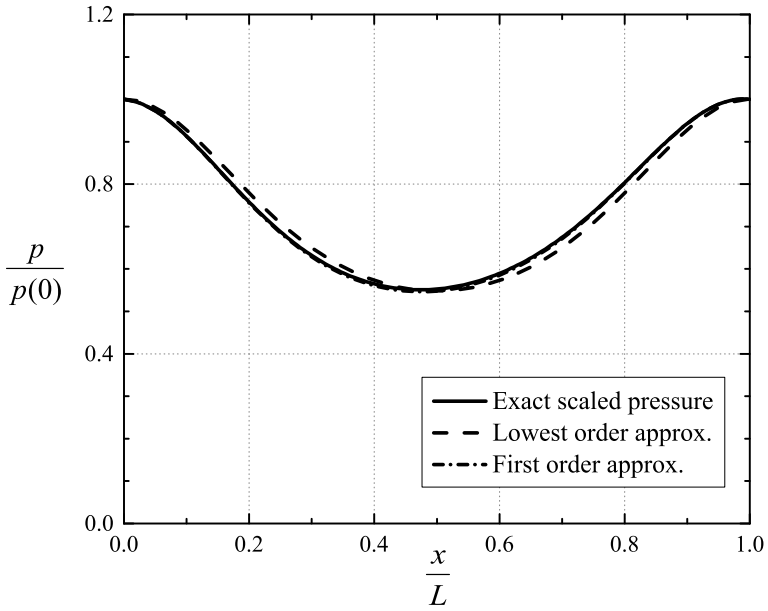

Figure 3.5: Scaled Pressure vs x/L at V(0) = V(L) = 5.0 V_c, T(0) = T(L) = 1.05 T_c, $\epsilon = 0.3$, $\Lambda = 100$. The solid line corresponds to the exact pressure calculated by substituting the exact density to the equation of state; the dashed line represents the lowest order pressure obtained by substituting the lowest order density, i.e., $\overline{\rho} = 1/\overline{h}$, to the equation of state; the dash-dot line denotes the first order pressure computed directly from (3.31).

line and the dash-dot line is found to be approximately 2% at $x/L = 0.5$.

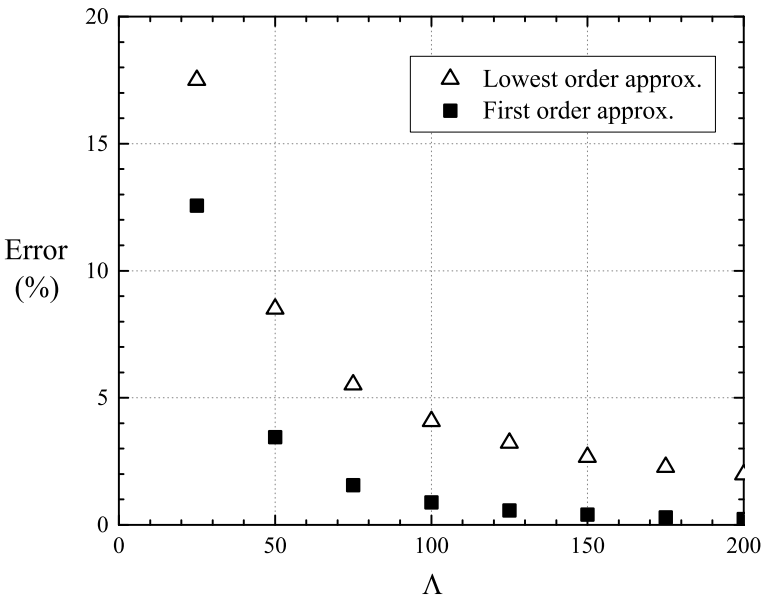

Figure 3.6: Maximum Relative Error between the Approximate and Exact Density vs Λ at V(0) = V(L) = 5.0 V_c, T(0) = T(L) = 1.05 T_c. The symbol $\triangle$ denotes errors of the lowest order approximation; the symbol ■ represents errors of the first order approximation.

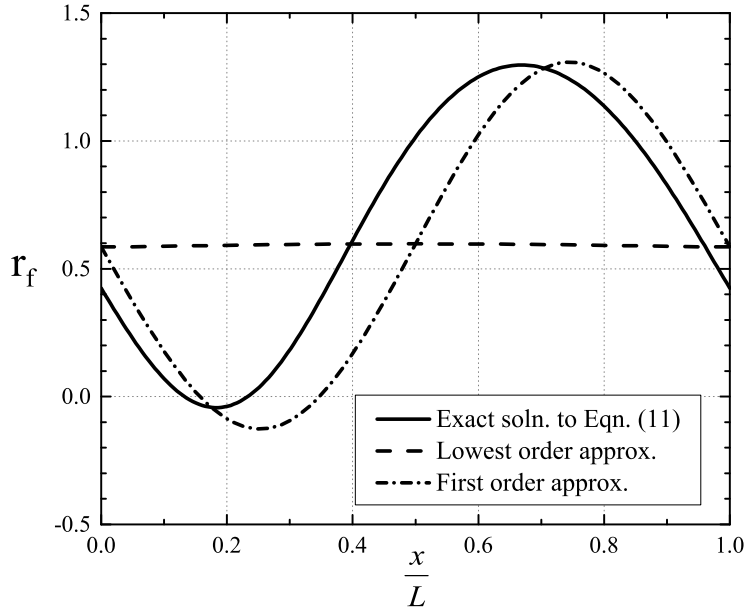

Figure 3.7: Recovery Factor r_f vs x/L at V(0) = V(L) = 5.0 V_c, T(0) = T(L) = 1.05 T_c, ϵ = 0.3, Λ = 25. The solid line denotes the exact r_f computed from (3.26). The dashed line represents the lowest order approximation for r_f, i.e., the first term in (3.45) where $\overline{\mu}$ and $\overline{k}$ are evaluated at $\overline{\rho} = 1/\overline{h}$; the dash-dot line corresponds to the first order approximation for r_f obtained using (3.45).

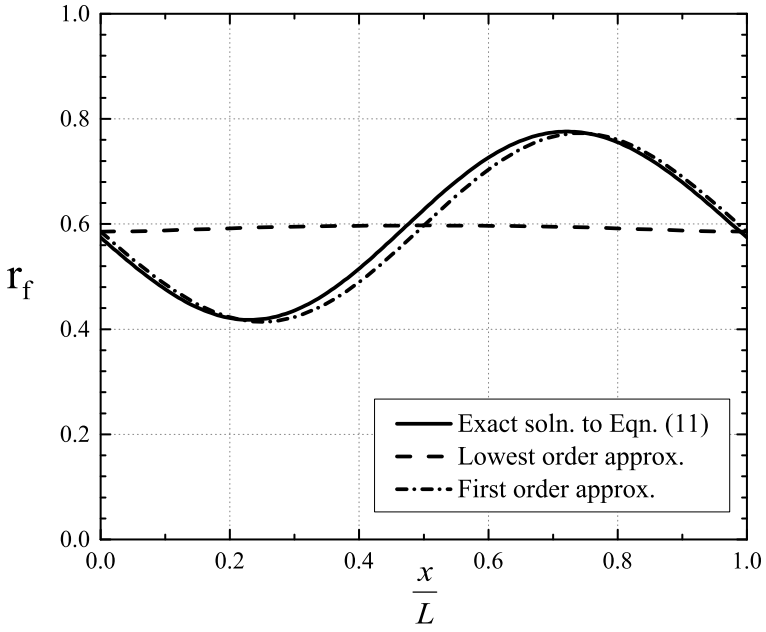

Figure 3.8: Recovery Factor r_f vs x/L at V(0) = V(L) = 5.0 V_c, T(0) = T(L) = 1.05 T_c, ϵ = 0.3, Λ= 100. The solid line denotes the exact r_f computed from (3.26). The dashed line represents the lowest order approximation for r_f, i.e., the first term in (3.45) where $\overline{\mu}$ and $\overline{k}$ are evaluated at $\overline{\rho} = 1/\overline{h}$; the dash-dot line corresponds to the first order approximation for r_f obtained using (3.45).

3.5 Conclusion

We have presented approximate solutions to the Reynolds equation (3.4) and the corresponding temperature equation (3.11) valid for single-phase, steady, two-dimensional, compressible, and laminar flows for large speed number (3.8). The results of Section 3.3 are valid for general gas models and for most pressures and temperatures corresponding to supercritical, dense, and ideal gases. Within this scope, our results reveal the dependence of density, pressure, temperature and wall heat flux on the material functions, i.e., the viscosity, thermal conductivity, effective bulk modulus (3.6) and coefficient of thermal expansion, and the global constants such as the speed, Prandtl, and Eckert number. In the lowest order theory, the density, pressure, temperature and heat flux depend only on the viscosity, thermal conductivity, and Prandtl number. We have shown that local values of the effective bulk modulus and thermal expansion coefficient must also be considered when accounting for the first correction for finite speed number.

The first correction presented in Section 3.3 also provides a qualitative and quantitative measure of the asymmetry in the density and pressure distributions about the $\overline{x} = 1/2$ point, i.e., the point of maximum film thickness. As the fluid is pressurized from an ideal to a dense gas state at constant temperature, the effective bulk modulus, viscosity, and thermal expansion coefficient all increase. As a result, the coefficients of Λ^{-1} will increase and the effect of finite speed number on all parameters will also increase. If the pressure is further increased, the non-monotone variation of the bulk modulus can result in a decrease in the coefficients of Λ^{-1} resulting in a relative weakening of the effect of the speed number.

In Section 3.4 we have compared the lowest and first order approximations to numerical solutions to the exact Reynolds model (3.4) and (3.11). The first order theory was seen to give a more realistic pressure distribution than that obtained by the lowest order theory, both with respect to the values near the minimum gap width and the shift in the local minimum of the density and pressure distributions. The strength of the asymmetry is seen to be directly related to the effective bulk modulus (3.6). Larger differences are observed in the temperature distributions. The lowest order approximation predicts a nearly constant temperature at adiabatic walls with a single local maximum. On the other hand, the exact and first order theory predict significant variation in the flow direction with a local maximum and minimum. Thus, the resultant thermal expansion of either the rotor or stator will have a stronger $\overline{x}$-variation than that predicted by the lowest order theory.

Although the case considered here is relatively simple, the basic approach can be extended by including more complex configurations and turbulence. Material functions such as the effective bulk modulus and the thermal expansion coefficient are expected to play a significant role in both extensions of the present analysis and the interpretation of pure numerical studies. Further extensions include the computation of global parameters such as the load, loss, and net heat transfer and a study of the breakdown of the current theory at high loading; both studies are currently under way by the authors.

Bibliography

[1] O. Reynolds. On the theory of lubrication and its application to Mr. Beauchamp Tower's experiments, including an experimental determination of the viscosity of olive oil. *Proceedings of the Royal Society of London*, 40(242-245), 191–203, 1886.

[2] O. Pinkus and B. Sternlicht. *Theory of Hydrodynamic Lubrication.* McGraw-Hill, 1961.

[3] W. A. Gross, L. A. Matsch, V. Castelli, A. Eshel, J. H. Vohr, and M. Wildmann. *Fluid Film Lubrication.* John Wiley and Sons, Inc., 1980.

[4] A. Z. Szeri. *Fluid Film Lubrication.* Cambridge University Press, 2010.

[5] B. J. Hamrock, S. R. Schmidt, and B. O. Jacobson. *Fundamentals of Fluid Film Lubrication.* CRC press, 2004.

[6] P. Johansen, D. B. Roemer, T. O. Andersen, H. C. Pedersen. On the application of Reynolds theory to thermo-piezo-viscous lubrication in oil hydraulics, In *Fluid Power and Mechatronics, 2015 IEEE International Conference. Harbin, China*, 58–62, 2015.

[7] D. Gropper, L. Wang, T. J. Harvey. Hydrodynamic lubrication of textured surfaces: A review of modeling techniques and key findings. *Tribology International*, 94, 509–529, 2016.

[8] F. Dupuy, B. Bou-Saïd, J. Tichy. High-speed subsonic compressible lubrication. *Journal of Tribology*, 137(4), 041702, 2015.

[9] F. Dupuy, B. Bou-Saïd, M. Garcia, G. Grau, J. Rocchi, M. Crespo, J. Tichy. Tribological study of a slider bearing in the supersonic regime. *Journal of Tribology*, 138(4), 041702, 2016.

[10] Q. Chao, J. Zhang, B. Xu, Q. Wang. Discussion on the Reynolds equation for the slipper bearing modeling in axial piston pumps. *Tribology International*, 118, 140–147 2018.

[11] V. Dostal, M. J. Driscoll, and P. Hejzlar. A supercritical carbon dioxide cycle for next generation nuclear reactors. Technical report, MIT-ANP-TR-100, 2004.

[12] C. DellaCorte, K. C. Radil, R. J. Bruckner, and S. A. Howard. Design, fabrication, and performance of open source generation I and II compliant hydrodynamic gas foil bearings. *Tribology Transactions*, 51(3), 254–264, 2008.

[13] S. A. Wright, R. F. Radel, M. E. Vernon, G. E. Robert, and P. S. Pickard. Operation and analysis of a supercritical CO_2 Brayton cycle. *Sandia Report, No. SAND2010-0171*, 2010.

[14] T. M. Conboy, S. A. Wright, J. Pasch, D. Fleming, G. Rochau, and R. Fuller. Performance characteristics of an operating supercritical CO_2 Brayton cycle. *Journal of Engineering for Gas Turbines and Power*, 134(11), 111703, 2012.

[15] F. Crespi, G. Gavagnin, D. Sánchez, and G. S. Martínez. Supercritical carbon dioxide cycles for power generation: A review. *Applied Energy*, 195, 152–183, 2017.

[16] Z. C. Peng and M. M. Khonsari. On the limiting load-carrying capacity of foil bearings. *Journal of Tribology*, 126(4), 817–818, 2004.

[17] S. Y. Chien, M. S. Cramer, and A. Untaroiu. Compressible Reynolds equation for high-pressure gases. *Physics of Fluids*, 29(11), 116101, 2017.

[18] S. Y. Chien, M. Cramer, A. Untaroiu. A compressible thermohydrodynamic analysis of journal bearings lubricated with supercritical CO_2. In *ASME 2017 Fluids Engineering Division Summer Meeting. Waikoloa, HI*, paper No. FEDSM2017-69310, 2017.

[19] T. M. Conboy. Real-gas effects in foil thrust bearings operating in the turbulent regime. *Journal of Tribology*, 135(3), 031703, 2013.

[20] D. Kim. Design space of foil bearings for closed-loop supercritical CO_2 power cycles based on three-dimensional thermohydrodynamic analyses. *Journal of Engineering for Gas Turbines and Power*, 138(3), 032504, 2016.

[21] K. Qin. *Development and application of multiphysics simulation tools for foil thrust bearings operating with carbon dioxide.* PhD thesis, University of Queensland, 2017.

[22] E. Guenat and J. Schiffmann. Real-gas effects on aerodynamic bearings. *Tribology International*, 120, 358–368, 2018.

[23] S. Dousti, P. Allaire. A compressible hydrodynamic analysis of journal bearings lubricated with supercritical carbon dioxide. In *Proceeding of Supercritical* CO_2 *Power Cycle Symposium, San Antonio, TX*, 2016.

[24] E. W. Lemmon, M. L. Huber, and M. O. McLinden. NIST Reference fluid thermodynamic and transport properties–REFPROP. *NIST Standard Reference Database*, 23, v7, 2002.

[25] I. H. Bell, J. Wronski, S. Quoilin, and V. Lemort. Pure and pseudo-pure fluid thermophysical property evaluation and the open-source thermophysical property library CoolProp. *Industrial & Engineering Chemistry Research*, 53(6), 2498–2508, 2014.

[26] H. Heshmat, J. F. Walton, J. L. Cordova. Technology readiness of 5^{th} and 6^{th} generation compliant foil bearing for 10 MWE s-CO_2 turbomachiery systems. In *Proceeding of the* 6^{th} *International Supercritical* CO_2 *Power Cycles Symposium, Pittsburg, PA,* 2018.

[27] R. C. Reid, J. M. Prausnitz, B. E. Poling. *The Properties of Gases and Liquids*. McGraw-Hill, 1987.

[28] T. H. Chung, L. L. Lee, K. E. Starling. Applications of kinetic gas theories and multiparameter correlation for prediction of dilute gas viscosity and thermal conductivity. *Industrial & Engineering Chemistry Fundamentals*, 23(1), 8–13, 1984.

[29] T. H. Chung, M. Ajlan, L. L. Lee, K. E. Starling. Generalized multiparameter correlation for nonpolar and polar fluid transport properties. *Industrial & Engineering Chemistry Research*, 27(4), 671–679, 1988.

Chapter 4

Load and loss for high speed lubrication flows of pressurized gases between non-concentric cylinders

Attribution

The work presented in this chapter was primarily carried out by S. Y. Chien. M. S. Cramer conceived of the main idea and contributed to the development and implementation of this work.

Abstract

We examine the high-speed flow of pressurized gases between non-concentric cylinders where the inner cylinder rotates at constant speed while the outer cylinder is stationary. The flow is taken to be steady, two-dimensional, compressible, laminar, single-phase and governed by a Reynolds lubrication equation. Approximations for the lubricating force and friction loss are derived using a perturbation expansion for large speed numbers. The present theory is valid for general Navier-Stokes fluids at nearly all states corresponding to ideal, dense, and supercritical gases. Results of interest are the observation that pressurization gives rise to large increases in the lubricating force and decreases in the fluid friction. The lubrication force is found to scale with the bulk modulus. Within the context of the Reynolds equation an exact relation between total heat transfer and power loss is developed.

4.1 Introduction

Thin viscous films arise in a wide variety of applications including those concerned with rotating machinery, tribology, the spreading of droplets or coatings, particle-particle interaction, and bio-lubrication. In such films, inertia is typically ignored and shear forces must be balanced by pressure forces. In lubrication applications, the pressure variations provide the force required to maintain the separation between solid surfaces, i.e., in order to maintain a load. Perhaps the earliest study of such thin film flows was carried out by Osborne Reynolds [1] who stated that the pressure in a steady, incompressible, laminar two-dimensional thin film satisfies

$$h^3(x)\,\frac{dp}{dx} = 6\mu U h(x) + \text{ constant}, \tag{4.1}$$

where h(x) is the film thickness, x is the spatial variable in the main flow direction, $\mu > 0$ is a constant shear viscosity, and U is a measure of the relative speed of the solid surfaces being lubricated. Both (4.1) and its first derivative with respect to x are known as the Reynolds equation. In the time since the publication of Reynolds' study, the Reynolds equation has been extended to include the effects of unsteadiness, turbulence, property variations, and more complex configurations. In recent years, there has been increasing interest in the use of gases rather than liquids as lubricating fluids; see, e.g., [2], [3], [4], [5], and [6]. The advantages of gases over liquids are compatibility with working fluids in power systems and turbomachinery, the reduction of weight, the reduction of fouling due to leaks, and the reduction of complications due to phase changes. Because the viscosity of gases is smaller than that of high viscosity oils, gas lubrication requires considerably higher speeds than those used in applications involving liquids and the resultant flows are typically taken to be compressible.

Most of the previous investigations of compressible gas lubrication have focused on the behavior of ideal, i.e., low pressure, gases. Examples include the discussions of Pinkus and Sternlicht[7], Gross et al.[8], Szeri[9], Hamrock et al.[10], Peng and Khonsari[11], and DellaCorte et al.[3]. Recent studies have examined the behavior of pressurized gases, i.e., gases corresponding to pressures and temperatures on the order of that of the thermodynamic critical point. Studies of lubrication with pressurized gases include those of Conboy[12], Kim[13], Dousti and Allaire[14], Qin[15], Heshmat et al.[16], and Guenat and Schiffmann[19] who applied pure numerical schemes to different versions of the Reynolds equation. The behavior of pressurized gases in these studies was evaluated using a digital table look-up such as the NIST REFPROP database [20] used by [12], [13], [15] and the CoolProp database [21] used by [19]. Dousti and Allaire[14] have employed a gas model based on a linear pressure-density relation, but this model is not expected to be valid over the full range of pressures and temperatures corresponding to the dense and supercritical regimes [16].

Important differences between pressurized gases and ideal gases are the strong dependence on the thermodynamic state and the rapid and sometimes singular dependence of material properties on the density and temperature. Chien et al.[22] have examined the approxima-

tions leading to the Reynolds equation for compressible flows of pressurized gases. A general form of the Reynolds equation was derived and its range of validity was delineated. In addition to the well known thin film and lubrication limitations on the film thickness and mild conditions on the imposed temperature difference between isothermal walls, it was shown that the Reynolds equation breaks down in the vicinity of the thermodynamic critical point. It was also shown that the temperature equation can be simplified whenever the Reynolds equation is valid.

In the case of ideal gases governed by the Reynolds equation, the simplest flows are governed by a single parameter referred to as the speed or bearing number [7, 8, 9, 10]. The speed number gives a measure of either the flow speed or the overall compressibility of the flow. In the case of pressurized gases, computations must take into account the local thermodynamic state. Chien et al.[22] have shown that the local thermodynamic state enters the problem solely through the effective bulk modulus

$$\kappa_{Te} = \kappa_{Te}(\rho, T) \equiv \frac{\kappa_T(\rho, T)}{\mu(\rho, T)}, \tag{4.2}$$

where ρ and T are the fluid density and absolute temperature,

$$\kappa_T \equiv \rho \left.\frac{\partial p}{\partial \rho}\right|_T, \tag{4.3}$$

is the bulk modulus of the fluid, and p = p(ρ,T) is the thermodynamic pressure. The effective bulk modulus (4.2) is recognized as a measure of the local fluid stiffness to the local shear forces.

In the limit of ideal gases, the effective bulk modulus (4.2) increases monotonically with pressure or density at constant temperatures. In the case of pressurized gases, the variation of κ_{Te} is no longer monotone and can take on relatively small values in the general neighborhood of the thermodynamic critical point. To illustrate this variation we have plotted the variation of a scaled version of (4.2) along isotherms in Figure 4.1.

A non-dimensional measure of the flow speed or the overall compressibility of the flow is the speed or bearing number defined as

$$\Lambda \equiv 6\, \frac{UL}{h_o^2 \kappa_{Te}\big|_{ref}} \tag{4.4}$$

where U, L, and h_o are measures of the flow speed, length scale in the general flow direction, and the gap width, respectively, and are defined more precisely in the next section. The quantity $\kappa_{Te}|_{ref}$ is the effective bulk modulus (4.3) evaluated at a reference thermodynamic state. The form (4.4) is that given by [22, 23] and arises naturally when pressurized gases are considered.

In many applications the speed number (4.4) is relatively large partly due to the need to generate sufficiently large lubrication forces and partly to avoid thermal runaway instabilities. Such instabilities will result in excessive heating of the solid components of the device

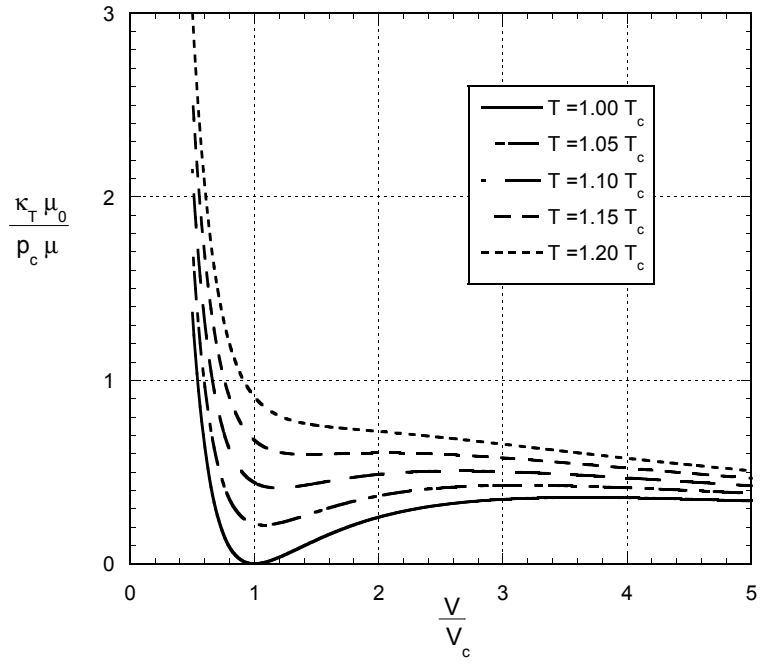

Figure 4.1: Effective Bulk Modulus of Carbon Dioxide (CO_2) vs V/V_c. Viscosity model is that of Chung et al.[26, 27] and the gas model is the Redlich-Kwong-Soave (RKS) equation. Here $V \equiv 1/\rho$ is the specific volume and $\mu_0 = \mu_0(T)$ is the ideal gas ($V \longrightarrow \infty$) value of μ. The subscript "c" denotes values at the thermodynamic critical point.

resulting in thermal expansion which in turn can lead to metal-on-metal contact and failure of the bearing; see, e.g., the discussions of Howard et al.[17] and Briggs et al.[18]. Gross et al.[8] was one of the first to derive the analytical solutions to the Reynolds equation for lubrication flows with large speed numbers. Peng and Khonsari[11] adopted a similar approach to evaluate the lowest-order load generated by different configurations. However, the approximate solutions provided by Gross et al.[8] and Peng and Khonsari[11] are valid for low pressure gases only and thermal effects were not considered.

Chien and Cramer [24] have presented approximate solutions to the Reynolds and corresponding temperature equation for the local values of the density, pressure, temperature, and heat flux valid for flows of pressurized gases with large speed numbers. These solutions reveal the role played by material functions, e.g., the effective bulk modulus and thermal expansivity, in the variation of the fundamental local quantities. The goal of the present study is to develop approximations for the total force and total friction loss valid for large speed numbers. The results will be valid everywhere the Reynolds equation of [22] is, i.e., at all pressures and temperatures in the ideal, dense, and supercritical gas regimes except sufficiently close to the thermodynamic critical point. Although the first-order theory described by Chien and Cramer [24] is sufficient to find the first corrections to the density, pressure, and temperature distributions, we have found that the first corrections to global parameters

such as load, loss, and net heat transfer require expansions which are second-order in Λ^{-1}.

Because our primary interest is to examine the effects of pressurization and finite speed number (4.4), we follow previous investigators in restricting attention to a simple canonical lubrication model, i.e., that of [22], which is the simplest model for compressible thin film flows of high-pressure gases. In addition to requiring the usual thin film conditions of a small lubrication Reynolds number and small layer thickness, Chien et al. [22] have required that the thermodynamic states be sufficiently far from those of the thermodynamic critical point; order of magnitude estimates for the size of the near-critical condition in the context of thin films were given by [22]. The particular form of the Reynolds and temperature equation used here is valid for steady, laminar, two-dimensional, and single-phase gas flows. Here we focus on supercritical temperatures so that multiphase flows will not be relevant. The motivation for the restriction to two-dimensional steady flows is done in order to focus attention on the new behavior arising from pressurization. The condition of two-dimensional flow will to be approximately satisfied for long bearings near the plane of symmetry. As demonstrated by Szeri [9], a Reynolds equation for turbulent flows can be developed, but its form is essentially the same as that used here with a Reynolds number dependent turbulent viscosity and other average properties replacing the local values used here.

In order to present concrete results, we examine the simple case of non-concentric cylinders: the details of this configuration are described in the next section. The large speed number approximations are developed in Section 4.3. We compare our approximations to numerical solutions of the compressible Reynolds equation in Section 4.4. A short derivation of the relation between power loss and heat transfer leaving the fluid film is given in the appendix A. The latter result is exact within the context of the Reynolds equation.

4.2 Formulation

The physical configuration is that sketched in Figure 4.2. The flow is taken to be contained between the inner and outer cylinders depicted there. The inner cylinder has a radius R_i and the outer cylinder has a radius R_o. The origin of the stationary x'-y' coordinate system is located at the center of the inner cylinder. The center of the outer cylinder is located at $x' = -e$, $y' = 0$. The inner cylinder rotates at a constant rate ω while the outer cylinder is stationary. For convenience, we refer to the inner cylinder as the rotor and the outer cylinder as the stator.

Throughout this work we apply the thin film approximation so that we compute the flow details using the "unwrapped" configuration sketched in Figure 4.3. When $R_o \approx R_i$ the fluid can be taken to be contained in the region $0 \leq y \leq h(x)$, where the variable y is recognized as a distance measured normal to the inner cylinder and $x \equiv \theta R_i$ is distance measured along the inner cylinder. The curve $y = h(x)$ in Figure 4.3 approximately corresponds to the surface of the stator. We can now define $L \equiv 2\pi R_i$ which is just the circumference of the

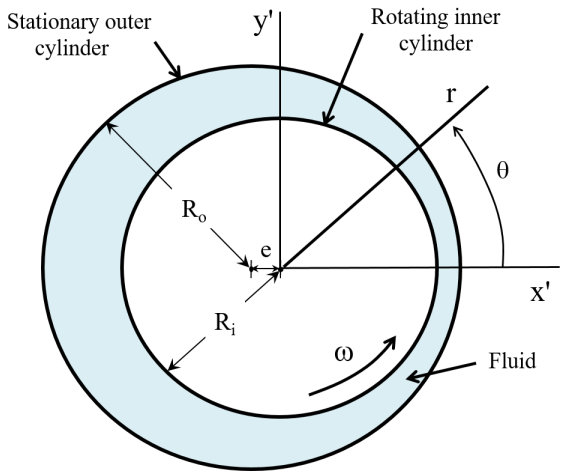

Figure 4.2: Sketch of Physical Configuration.

inner cylinder and $h_o \equiv \mathrm{h}(0)$ which is the minimum gap width; we take h_o to be a measure of the film thickness. For the non-concentric cylinders sketched in Figure 4.2, the thickness of the fluid layer can be approximated by

$$\overline{h} \equiv \frac{h(x)}{h_o} \approx 1 + \delta - \delta \cos(\theta), \tag{4.5}$$

where

$$\delta \equiv \frac{1}{2}(\overline{h}_m - 1) = \frac{\epsilon}{1-\epsilon}. \tag{4.6}$$

The quantity $\overline{h}_m \equiv \overline{h}(\overline{x} = 1/2) = \overline{h}(\theta = \pi)$ is the maximum value of $\overline{h}$. The factor δ has been related to the eccentricity ratio $\epsilon \equiv \mathrm{e/c}$ where $\mathrm{c} \equiv \mathrm{R}_o\text{-}\mathrm{R}_i$ is called the radial clearance; the eccentricity ϵ is commonly used in the lubrication literature; see, e.g., [7], [8], [10], or [9].

In our detailed calculations we will employ (4.5). However, many of our results are also valid under the weaker condition that $\overline{h}$ be symmetric about $\theta = \pi$, i.e.,

$$\overline{h}(\pi - \theta) \equiv \overline{h}(\theta - \pi). \tag{4.7}$$

As a result, the derivatives of $\overline{h}(\theta)$ will satisfy

$$\frac{d\overline{h}}{d\theta}(\pi - \theta) = -\frac{d\overline{h}}{d\theta}(-(\pi - \theta)). \tag{4.8}$$

In order to ensure that $\overline{h}$ is a minimum at $\overline{x} = 0,\ 1$ or $\theta = 0,\ 2\pi$, we require that

$$\begin{aligned} \frac{d\overline{h}}{d\theta} &\geq 0 \ \text{ if } 0 \leq \theta \leq \pi \\ &\leq 0 \ \text{ if } \pi \leq \theta \leq 2\pi. \end{aligned} \tag{4.9}$$

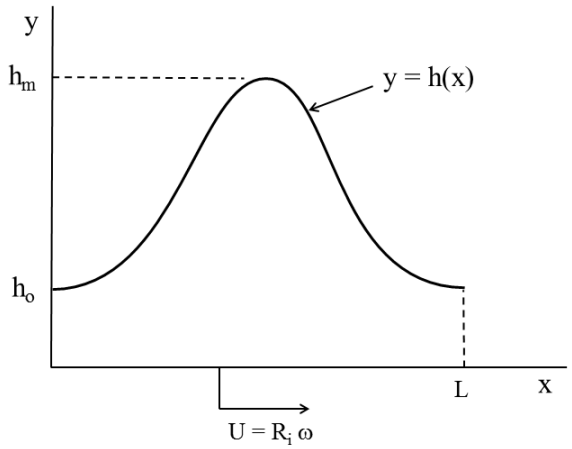

Figure 4.3: Unwrapped Configuration: The stationary outer cylinder of Figure 4.2 is approximated by the y = h(x) surface and the rotating inner cylinder is approximated by the y = 0 surface. The minimum gap width is $h_o \equiv$ h(0) and the maximum value of h(x) is $h_m \equiv$ h(L/2).

The flow will be taken to be steady, two-dimensional, compressible, single-phase and laminar. The physical flow is required to satisfy the usual thin film and lubrication restrictions, i.e.,

$$\frac{h_o}{L} \ll 1, \tag{4.10}$$

$$Re\frac{h_o^2}{L^2} \ll 1, \tag{4.11}$$

where Re is the Reynolds number based on L, U $\equiv$ $R_i\,\omega$, μ_{ref}, and ρ_{ref}. The subscript "ref" will always refer to quantities evaluated at a given reference thermodynamic state. Here we take that reference state to be that at x = 0 and L. As discussed by [22] we also need to require that the flow be sufficiently far from the thermodynamic critical point. If the rotor and stator are both isothermal, we must also require that the product of the fixed, known temperature difference and the thermal expansion coefficient defined by (A.6) be small. Under these conditions, the flow will satisfy the Reynolds equation of [22] which can be written in non-dimensional form as

$$\frac{d}{d\overline{x}}\left(\overline{h}^3\overline{\kappa}_{Te}\frac{d\overline{\rho}}{d\overline{x}}\right) = \Lambda\frac{d(\overline{\rho}\overline{h})}{d\overline{x}}, \tag{4.12}$$

where $\overline{\rho} \equiv \rho/\rho_{ref}$ is the non-dimensional density. Here $\overline{x} \equiv$ x/L and

$$\overline{\kappa}_{Te} = \overline{\kappa}_{Te}(\overline{\rho}) \equiv \frac{\kappa_{Te}(\rho, T_{ref})}{\kappa_{Te}|_{ref}} = \frac{\kappa_{Te}(\rho, T_{ref})}{\kappa_{Te}(\rho_{ref}, T_{ref})} \tag{4.13}$$

is the scaled effective bulk modulus. For the present purposes, the Reynolds equation (4.12) will be integrated subject to the periodicity conditions

$$\overline{\rho}(0) = \overline{\rho}(1) = 1. \tag{4.14}$$

The solution for the fluid density is generally obtained by integrating (4.12) subject to (4.14) to yield $\overline{\rho} = \overline{\rho}(\overline{x}; \Lambda)$ once the reference thermodynamic state (ρ_{ref},T_{ref}) and gas models are specified. The pressure is then found by substitution in the equation of state.

In the following discussion, a convenient first integral of (4.12) is

$$\overline{\rho} = \frac{1}{\overline{h}} + \frac{1}{\Lambda}\left(\overline{h}^2 \overline{\kappa}_{Te} \frac{d\overline{\rho}}{d\overline{x}} - \frac{1}{\overline{h}} \frac{d\overline{\rho}}{d\overline{x}}(0)\right), \tag{4.15}$$

where we have used the fact that $\overline{h} = \overline{\kappa}_{Te} = 1$ at $\overline{x} = 0$. In the limit of incompressible flow with constant viscosity (4.15) reduces to Reynolds' original formula (4.1) with

$$\frac{d\overline{\rho}}{d\overline{x}}(0)$$

playing the role of the integration constant.

With the thin film approximation (4.10) we can write the x′ and y′ components of the forces on the rotor from the fluid as

$$\overline{F}_{x'} \approx \int_0^{2\pi} \overline{p}\cos(\theta) d\theta = -\frac{1}{2\pi}\int_0^{2\pi} \frac{d\overline{p}}{d\overline{x}} \sin(\theta) d\theta, \tag{4.16}$$

$$\overline{F}_{y'} \approx \int_0^{2\pi} \overline{p}\sin(\theta) d\theta = \frac{1}{2\pi}\int_0^{2\pi} \frac{d\overline{p}}{d\overline{x}} \cos(\theta) d\theta, \tag{4.17}$$

where

$$\overline{\mathbf{F}} \equiv -\frac{h_o^2}{\mu_{ref} U 2\pi R_i^2 b}\mathbf{F}', \tag{4.18}$$

b is the length of the cylinders in the z′-direction, and $\mathbf{F}'$ is the dimensional force on the rotor. The quantity $\overline{p}$ is the scaled pressure and is related to the dimensional pressure p by

$$\overline{p} \equiv \frac{h_o^2}{\mu_{ref} U L}(p - p_{ref}). \tag{4.19}$$

The power loss is the work per time done on the rotor, i.e., the y = 0 surface in Figure 4.3. In the thin film approximation, this can be written

$$P = b\,U \int_0^L T_{yx}\, dx \approx \frac{bLU^2\mu_{ref}}{h_o}\overline{P}, \tag{4.20}$$

where the scaled loss is

$$\overline{P} \equiv \int_0^1 \left(\overline{\mu} \frac{\partial u}{\partial \overline{y}} \right) \Big|_{\overline{y}=0} d\overline{x}, \tag{4.21}$$

$\overline{\mu} \equiv \mu/\mu_{ref}$ is a scaled version of the viscosity, and $\overline{y} \equiv \mathrm{y}/h_o$ is the scaled y-coordinate. The x-component of the fluid velocity, denoted by u, is scaled with U and its expression is given in Appendix A.

4.3 General Results

We now determine the approximate solutions to the Reynolds equation (4.12) for lubrication flows with large speed numbers. We first consider the second-order expansion for density, i.e.,

$$\overline{\rho} = \rho_0 + \frac{\rho_1}{\Lambda} + \frac{\rho_2}{\Lambda^2} + O(\frac{1}{\Lambda^3}). \tag{4.22}$$

If we substitute (4.22) and its derivative in (4.15), we then obtain the functions

$$\rho_0 = \frac{1}{\overline{h}}, \tag{4.23}$$

$$\rho_1 = -\overline{\kappa}_{Teo} \frac{d\overline{h}}{d\overline{x}}, \tag{4.24}$$

$$\rho_2 = -\overline{h}^2 \frac{d}{d\overline{x}} \left(\overline{\kappa}_{Te}^2 \frac{d\overline{h}}{d\overline{x}} \right) \Big|_o + \frac{1}{\overline{h}} \frac{d^2\overline{h}}{d\overline{x}^2}(0), \tag{4.25}$$

where the subscript "o" will always refer to quantities evaluated at the lowest-order density, $\overline{\rho} \approx 1/\overline{h}$. For example,

$$\overline{\kappa}_{Teo}(\overline{\rho}) \equiv \overline{\kappa}_{Te}(\frac{1}{\overline{h}}). \tag{4.26}$$

It is easily verified that (4.22)-(4.25) satisfy the boundary conditions (4.14) and the equation for $\overline{h}$, i.e., (4.5), to the appropriate order.

To demonstrate the accuracy of (4.22)-(4.25), we have plotted a comparison of the approximate density (4.22) and the numerical solution to the exact Reynolds equation (4.12) at Λ = 40 in Figures 4.4-4.5. Here we take the channel sketched in Figure 4.3 to be given by h_o/L = 1.989 $\times 10^{-5}$, and δ = 0.5. The gas models are taken to be those described in Section 4.4. The temperature at the entrance and exit is taken to be T(0) = T(L) = 1.05 T_c. In Figure 4.4 the specific volume, i.e., $\mathrm{V} \equiv 1/\rho$, is taken to satisfy V(0) = V(L) = 10 V_c. The pressure at this state is approximately 21.2 bar $\approx$ 0.29 p_c, so that the thermodynamic state can be regarded as that of a dense gas. In Figure 4.5 we consider the case of a slightly supercritical fluid in which the reference specific volume is taken to be V(0) = V(L) = 2V_c and the corresponding pressure is approximately 78.2 bar $\approx$ 1.06 p_c.

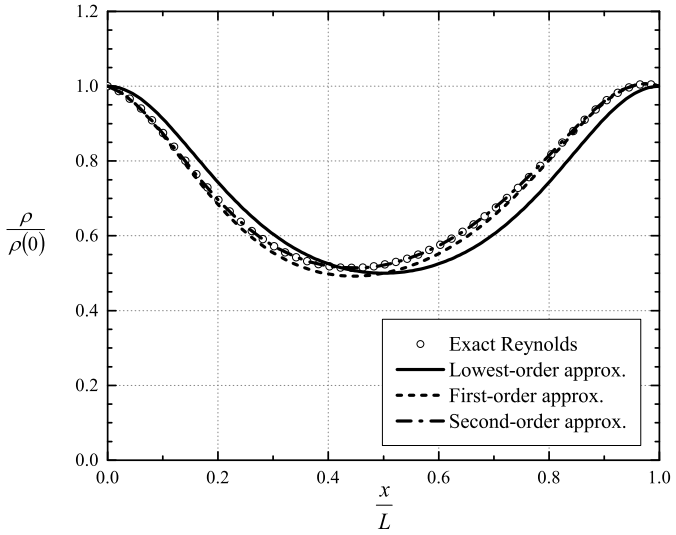

Figure 4.4: Scaled Density vs x/L at V(0) = V(L) = 10 V_c, T(0) = T(L) = 1.05 T_c, $\delta = 0.5$, $\Lambda = 40$. The symbols ○ denote the exact solutions to the Reynolds equation (4.12). The solid line denotes the lowest-order solutions, i.e., $\overline{\rho} = 1/\overline{h}$. The dashed and dash-dot lines represent the first- and second-order solutions of the scaled density (4.22), respectively.

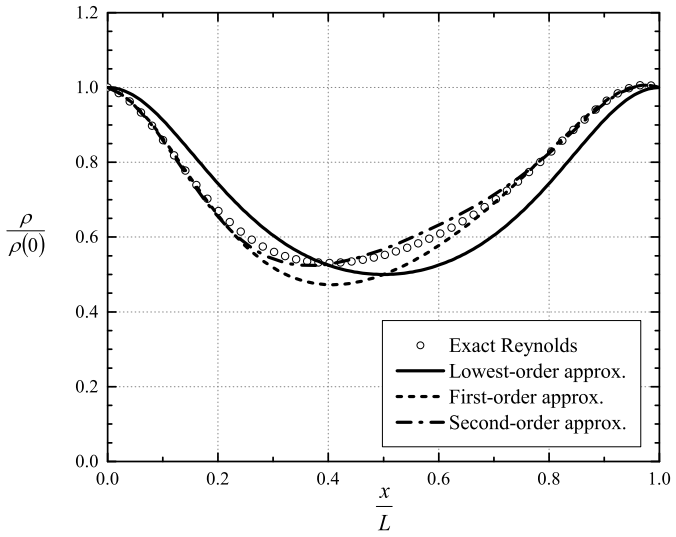

Figure 4.5: Scaled Density vs x/L at V(0) = V(L) = 2 V_c, T(0) = T(L) = 1.05 T_c, $\delta = 0.5$, $\Lambda = 40$. The symbols ○ denote the exact solutions to the Reynolds equation (4.12). The solid line denotes the lowest-order solutions, i.e., $\overline{\rho} = 1/\overline{h}$. The dashed and dash-dot lines represent the first- and second-order solutions of the scaled density (4.22), respectively.

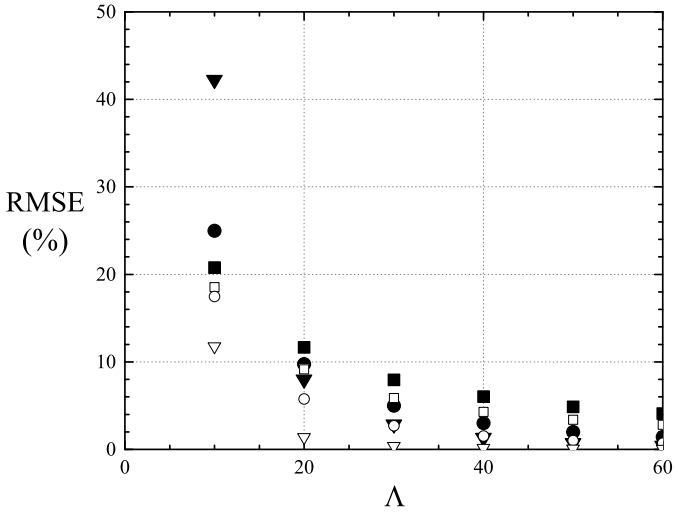

Figure 4.6: Root-Mean-Square Error (RMSE) Between the Approximate and Exact Density vs Λ at $T(0) = T(L) = 1.05\ T_c$ and $\delta = 0.5$. The symbols ■, ● and ▼ represent the lowest-, first- and second-order approximations, respectively, at $V(0) = V(L) = 2\ V_c$. The symbols □, ○ and ▽ represent the lowest-, first- and second-order approximations, respectively, at $V(0) = V(L) = 10\ V_c$.

Inspection of Figure 4.4 and 4.5 reveals that the second-order approximation is in excellent agreement with the exact solutions. As compared to the lowest-order approximation, the first-order term corrects the slope of the curves near both ends of the channel whereas the second-order correction term further improves the prediction of the position and magnitude of the local minimum.

The accuracy of our approximation for both cases increases as $\Lambda \longrightarrow \infty$. In order to illustrate the accuracy of the approximation, we have also plotted the root-mean-square error (RMSE) between the approximate density (4.22) and the exact solution to the Reynolds equation (4.12) as a function of Λ in Figure 4.6. It was found that the second-order approximation can provide reasonable accuracy when $\Lambda \geq 20$. When $\Lambda = 20$, the RMSEs of the second-order approximation for cases of $V(0) = V(L) = 10\ V_c$ and $2\ V_c$ are approximately 1.4% and 8%, respectively.

We now turn to the determination of the large Λ approximation for the forces, i.e., (4.16) and (4.17), on the rotor. If we use (4.3), (4.4) and (4.19), the expressions for the exact force components (4.16) and (4.17) can be rewritten as

$$-\frac{\Lambda}{6}\overline{F}_{x'} = \frac{1}{2\pi}\int_0^{2\pi} \mathscr{R}\frac{d\overline{\rho}}{d\overline{x}}\sin(\theta)d\theta, \tag{4.27}$$

$$\frac{\Lambda}{6}\overline{F}_{y'} = \frac{1}{2\pi}\int_0^{2\pi} \mathscr{R}\frac{d\overline{\rho}}{d\overline{x}}\cos(\theta)d\theta. \tag{4.28}$$

where the factor

$$\mathscr{R} = \mathscr{R}(\overline{\rho}, T_{ref}) \equiv \frac{\overline{\kappa}_T}{\overline{\rho}}, \tag{4.29}$$

can be expanded in a Taylor series for $\overline{\rho}$ near $1/\overline{h}$ yielding

$$\mathscr{R}(\overline{\rho}, T_{ref}) = \mathscr{R}_o + \frac{d\mathscr{R}}{d\overline{\rho}}\bigg|_o (\overline{\rho} - \frac{1}{\overline{h}}) + \frac{1}{2}\frac{d^2\mathscr{R}}{d\overline{\rho}^2}\bigg|_o (\overline{\rho} - \frac{1}{\overline{h}})^2 + O(\frac{1}{\Lambda^3}). \tag{4.30}$$

If we combine (4.30) with (4.22), and multiply the result by the derivative of (4.22), we find

$$\mathscr{R}\frac{d\overline{\rho}}{d\overline{x}} = \mathscr{R}_o\frac{d\rho_0}{d\overline{x}} + \frac{1}{\Lambda}\frac{d(\mathscr{R}_o\rho_1)}{d\overline{x}} + \frac{1}{\Lambda^2}\frac{d}{d\overline{x}}\left[\mathscr{R}_o\rho_2 + \frac{1}{2}\frac{d\mathscr{R}}{d\overline{\rho}}\bigg|_o \rho_1^2\right] + O(\frac{1}{\Lambda^3}). \tag{4.31}$$

Through substitution of (4.23)-(4.25) and (4.31) in (4.27) and straightforward manipulation we then obtain

$$-\frac{\pi\Lambda}{3}\overline{F}_{x'} = I_{x1} + \frac{I_{x2}}{\Lambda} + \frac{I_{x3}}{\Lambda^2} + O(\frac{1}{\Lambda^3}), \tag{4.32}$$

where the quantities

$$I_{x1} \equiv -2\pi\int_0^{2\pi}\frac{\overline{\kappa}_{To}}{\overline{h}}\frac{d\overline{h}}{d\theta}\sin(\theta)d\theta, \tag{4.33}$$

$$I_{x2} \equiv 4\pi^2\int_0^{2\pi}\overline{\kappa}_{To}\overline{\kappa}_{Teo}\overline{h}\frac{d\overline{h}}{d\theta}\cos(\theta)d\theta, \tag{4.34}$$

$$\begin{aligned} I_{x3} \equiv & -8\pi^3\int_0^{2\pi}\left[\frac{1}{2}\overline{\kappa}_{Teo}^2\frac{d}{d\overline{\rho}}\left(\frac{\overline{\kappa}_T}{\overline{\rho}}\right)\bigg|_o + \overline{h}\overline{\kappa}_{To}\frac{d\overline{\kappa}_{Te}^2}{d\overline{\rho}}\bigg|_o\right]\left(\frac{d\overline{h}}{d\theta}\right)^2\cos(\theta)d\theta \\ & + 8\pi^3\int_0^{2\pi}\overline{\kappa}_{To}\overline{\kappa}_{Teo}^2\overline{h}^3\frac{d^2\overline{h}}{d\theta^2}\cos(\theta)d\theta \\ & - 8\pi^3\frac{d^2\overline{h}}{d\theta^2}(0)\int_0^{2\pi}\overline{\kappa}_{To}\cos(\theta)d\theta. \end{aligned} \tag{4.35}$$

We note that $\overline{\kappa}_T > 0$ for all fluids due to the Gibbs stability condition and both $\mathrm{d}\overline{h}/\mathrm{d}\theta$ and $\sin(\theta)$ are antisymmetric with respect to $\theta = \pi$. Thus, the quantity I_{x1} will always be non-zero. From conditions (4.9) we can also show that $\mathrm{I}_{x1} < 0$ for all fluids. That is, the lowest order $\overline{F}_{x'} > 0$ so that the x′-component of the dimensional force on the rotor will point to the left in Figure 4.2. On the other hand, the quantity $\mathrm{I}_{x2} = 0$, because each term in the integrand of I_{x2} is symmetric with respect to $\theta = \pi$ except for $\mathrm{d}\overline{h}/\mathrm{d}\theta$ which is antisymmetric. In (4.35) the integrand of each integral is symmetric about $\theta = \pi$. As a result, each term of I_{x3} is seen to be non-zero.

If we substitute (4.22)-(4.25), (4.31) in (4.28), we then find

$$\frac{\pi\Lambda}{3}\overline{F}_{y'} = I_{y1} + \frac{I_{y2}}{\Lambda} + O(\frac{1}{\Lambda^2}), \tag{4.36}$$

where

$$I_{y1} = -2\pi \int_0^{2\pi} \frac{\overline{\kappa}_{To}}{\overline{h}} \frac{d\overline{h}}{d\theta} \cos(\theta) d\theta, \tag{4.37}$$

$$I_{y2} = -4\pi^2 \int_0^{2\pi} \overline{\kappa}_{To} \overline{\kappa}_{Teo} \overline{h} \frac{d\overline{h}}{d\theta} \sin(\theta) d\theta. \tag{4.38}$$

We note that $\overline{\kappa}_{To}$, $\overline{h}$, and $\cos(\theta)$ are symmetric about $\theta = \pi$ while the derivative $\mathrm{d}\overline{h}/\mathrm{d}\theta$ is antisymmetric. Hence $\mathrm{I}_{y1} = 0$ for all fluids. In like manner, it is easily demonstrated that $\mathrm{I}_{y2} \neq 0$ in general. If we further require that the conditions (4.9) hold, the y′-component of the dimensional force on the rotor will be positive in Figure 4.2.

From (4.32)-(4.38) we can obtain the approximation for the magnitude of the scaled load

$$\Lambda|\overline{\mathbf{F}}| = \frac{3|I_{x1}|}{\pi} \left[1 + \frac{1}{\Lambda^2} \left(\frac{I_{x3}}{I_{x1}} + \frac{1}{2} \frac{I_{y2}^2}{I_{x1}^2} \right) + O(\frac{1}{\Lambda^3}) \right], \tag{4.39}$$

and the angle of the load, i.e., attitude angle

$$\varphi \equiv \tan^{-1} \left(\frac{\overline{F}_{y'}}{\overline{F}_{x'}} \right) \approx \pi - \frac{1}{\Lambda} \frac{I_{y2}}{I_{x1}} + O(\frac{1}{\Lambda^2}), \tag{4.40}$$

where we have used the expansion of the tangent function for $\varphi \approx \pi$ in (4.40). Given the conditions (4.9), it is easily verified that

$$\frac{\pi}{2} \leq \varphi \leq \pi. \tag{4.41}$$

In order to obtain the expression for the approximate loss, we substitute the derivative of u, as given by (A.9), and the exact solution (4.15) in (4.21) yielding

$$\begin{aligned} -\overline{P} = \int_0^1 \frac{\overline{\mu}}{\overline{h}} d\overline{x} + \frac{3}{\Lambda} \left(1 - \frac{1}{\Lambda} \frac{d\overline{\rho}}{d\overline{x}}(0) \right) \int_0^1 \frac{\overline{\kappa}_T}{\overline{\rho}^2} \frac{d\overline{\rho}}{d\overline{x}} d\overline{x} + \frac{3}{\Lambda^2} \int_0^1 \frac{\overline{\mu}\, \overline{\kappa}_{Te}^2}{\overline{\rho}^5} \left(\frac{d\overline{\rho}}{d\overline{x}} \right)^2 d\overline{x} \\ + \frac{3}{\Lambda^2} \int_0^1 \frac{\overline{\mu}\, \overline{\kappa}_{Te}^2}{\overline{\rho}^5} \left(\frac{d\overline{\rho}}{d\overline{x}} \right)^2 \left(\overline{\rho}^3 \overline{h}^3 - 1 \right) d\overline{x}. \end{aligned} \tag{4.42}$$

We note that the second integral is identically zero and the last integral is seen to be $O(\Lambda^{-3})$. As a result, the second-order approximation for loss is found to be

$$-\overline{P} = \int_0^1 \frac{\overline{\mu}}{\overline{h}} d\overline{x} + \frac{3}{\Lambda^2} \int_0^1 \overline{\kappa}_{Teo} \overline{\kappa}_{To} \overline{h} \left(\frac{d\overline{h}}{d\overline{x}} \right)^2 d\overline{x} + O(\frac{1}{\Lambda^3}). \tag{4.43}$$

In (4.43) the values of $\overline{\mu}$ in the first integral have been left as their exact values. However, to be consistent, the shear viscosity in (4.43) should be expanded in a Taylor series for $\overline{\rho} \approx$

$1/\overline{h}$ in a manner similar to that done for (4.30). Alternatively, to simplify the computations, we evaluate the viscosity in the first integral of (4.43) by substituting the $O(\Lambda^{-2})$ density expansion (4.22) in the viscosity model. Errors in this approach will be on the order of terms already neglected.

In the ideal gas limit, i.e., $\kappa_T \longrightarrow p \longrightarrow \rho RT$ and $\mu \longrightarrow \mu(T_{ref})$, we can take $\overline{\kappa}_T = \overline{\rho}$ and $\overline{\mu}$ = 1 so that all the integrals in (4.39), i.e., (4.33)-(4.35) and (4.37)-(4.38), and (4.43) can be integrated explicitly. As a result, the expression of the scaled load can be written as

$$\Lambda|\overline{\mathbf{F}}| = \frac{12\pi(1+\delta-\sqrt{1+2\delta})}{\delta\sqrt{1+2\delta}}\left[1+\frac{2\pi^2}{\Lambda^2}(1+\delta)(\sqrt{1+2\delta}-2)\right]+O(\frac{1}{\Lambda^3}), \tag{4.44}$$

and the attitude angle (4.40) becomes

$$\varphi \approx \pi - \frac{2\pi\sqrt{1+2\delta}}{\Lambda} + O(\frac{1}{\Lambda^2}). \tag{4.45}$$

The expression for the scaled loss can also be written as

$$-\overline{P} = \frac{1}{\sqrt{1+2\delta}} + \frac{12\pi^2}{\Lambda^2}(1+\delta-\sqrt{1+2\delta}) + O(\frac{1}{\Lambda^3}). \tag{4.46}$$

Our lowest-order load and loss, i.e., the first terms of (4.44) and (4.46), the expression of the attitude angle and the fact that the first corrections for the load and loss are $O(\Lambda^{-2})$ are consistent with the ideal gas results by Gross et al.[8]. The work here indicates that this ordering of the large Λ expansion also holds for general fluids. Examination of (4.39), (4.40) and (4.43)-(4.46) reveals that the lowest-order approximation of the scaled load and loss and attitude angle are dependent on δ and Λ alone when the gas is ideal. However, for pressurized gases, the lowest-order scaled load also depends on the variation of the scaled bulk modulus $\overline{\kappa}_T$; the lowest-order scaled loss depends on the variation of the scaled shear viscosity $\overline{\mu}$; the attitude angle depends on the variation of both $\overline{\kappa}_T$ and $\overline{\mu}$ in addition to δ and Λ.

4.4 Numerical Results

In this section, we compare the approximation for the scaled load (4.39), scaled loss (4.43), and the attitude angle (4.40) to their exact values based on the density variation obtained from the exact Reynolds equation (4.12). More specifically, the exact Reynolds equation (4.12) was solved through the use of a straightforward shooting method. Once the pressure distribution was determined by substituting the resulting density variation in the equation of state, the exact scaled load was then computed using (4.16)-(4.18). The exact scaled loss was calculated using (4.21). The exact attitude angle was computed by taking the ratio of (4.17) to (4.16).

As described in Section 4.3, the viscosity in the first integral of (4.43) was evaluated using the second-order density and the reference temperature. In the remaining integrals of our approximation, i.e., (4.33)-(4.35) and (4.38), the bulk modulus (4.3) and shear viscosity were computed based on the lowest-order density and the reference temperature. Derivatives of the bulk modulus and viscosity seen in (4.35) were estimated numerically. All numerical integrations of (4.16)-(4.17), (4.21), (4.33) and (4.35), (4.38), and (4.43) were computed using Simpson's rule. Discretization errors were checked for all computations presented here. For example, the difference in $\overline{\rho}$ between 200 and 300 points distributed over the interval $0 \leq \overline{x} \leq 1$ was less than 0.006%. The tolerance for the value of $\overline{\rho}(1)$ for the shooting method was set to be 10^{-8}.

For the purpose of illustration, we use the Redlich-Kwong-Soave equation of state and the polynomial curve-fit for the ideal gas specific heat provided in Reid et al.[25]. The fluid was chosen to be carbon dioxide (CO_2). The physical properties of CO_2 were taken from Reid et al.[25]; the critical pressure and temperature of CO_2 are p_c = 73.77 bar and T_c = 304 °K, respectively. The acentric factor for CO_2 was given by [25] to be 0.239. The viscosity model is that of [26, 27]. Parameters required for the application of the model of Chung et al.[26, 27] were taken from [25]. We take the channel sketched in Figure 4.3 to be given by $h_o/L = 1.989 \times 10^{-5}$. Unless stated otherwise, $\delta = 0.5$.

We first consider the effect of pressurization on the load. In Figure 4.7 we have plotted the variation of the lowest-order scaled load, i.e., the first term in (4.39), with the reference specific volume for a range of reference temperatures. At $T_{ref} = 1.05\ T_c$ pressurization can increase the scaled load by 56% over the scaled load attained at low pressure. The physical reason for this increase can be seen by an examination of Figure 4.8, in which the variation of $\overline{\kappa}_T$ with $\overline{x}$ is plotted for various thermodynamic states. At the lowest pressure, i.e., for $V(0) = 10\ V_c$, $\overline{\kappa}_T$ is < 1 over much of the range of $\overline{x}$. As the pressure is increased, the variation of $\overline{\kappa}_T$ from 1 decreases. At $V(0) = 2\ V_c$ and $1\ V_c$, it is seen that the values of $\overline{\kappa}_T$ are approximately one. As a result, the scaled load will be larger than that at low pressure. The observation that $\overline{\kappa}_T$ does not decrease significantly at high pressures is due to the non-monotone variation of the bulk modulus. At higher temperatures, the variation of the bulk modulus is a monotone decreasing function of the specific volume. As a result, $\overline{\kappa}_T < 1$ over most of the bearing resulting in an insignificant increase in the scaled load.

We note that the scaled load in Figure 4.7 remains nearly constant as the reference specific volume is varied in the range $V(0) > 4\ V_c$. This observation suggests that the load scales with the reference bulk modulus $\kappa_T\big|_{ref}$. This fact becomes obvious if we multiply (4.39) by

$$\frac{\kappa_T\big|_{ref}}{p_c},$$

and use (4.18). The resultant scaled load is

$$\frac{6|\mathbf{F}'|}{p_c R_i b}. \tag{4.47}$$

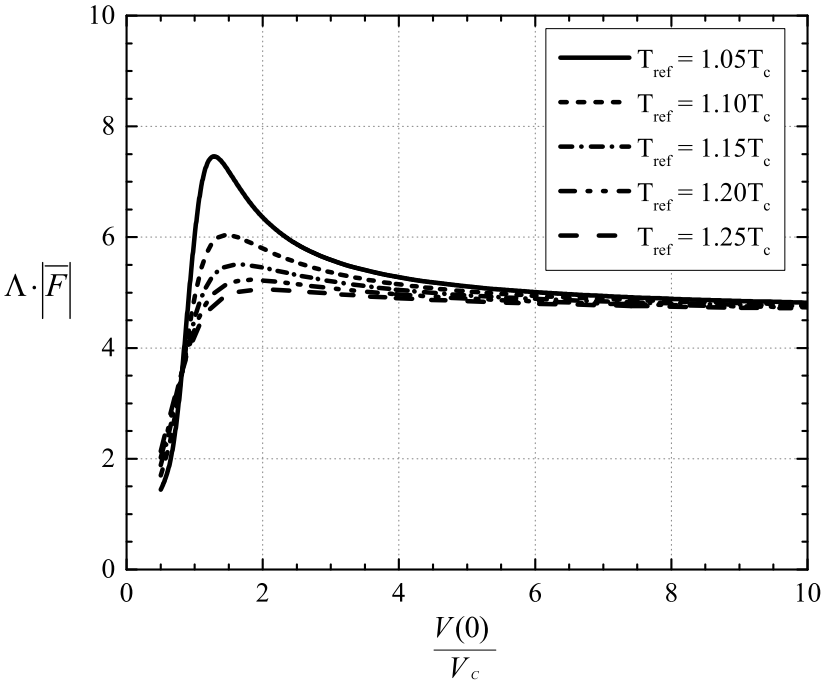

Figure 4.7: Lowest-Order Scaled Load vs Reference Specific Volume. The parameter $\delta = 0.5$.

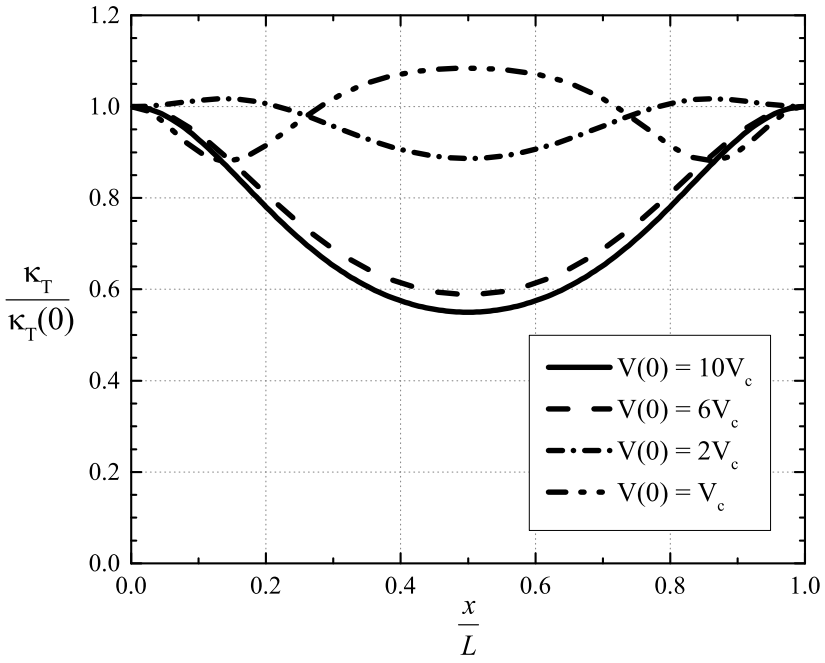

Figure 4.8: Scaled Bulk Modulus vs x/L for $T_{ref} = 1.05\ T_c$. The parameter $\delta = 0.5$.

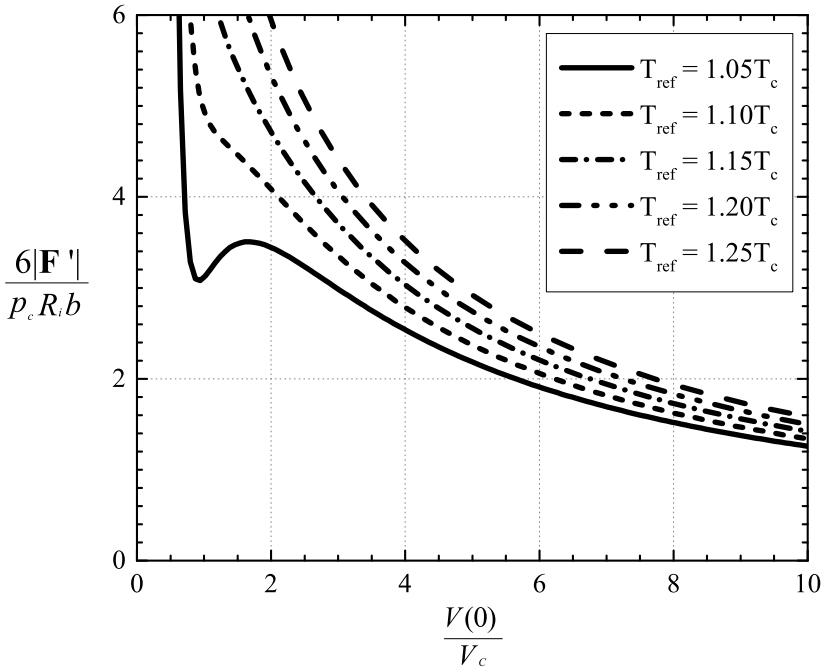

Figure 4.9: Rescaled Load vs Reference Specific Volume. The parameter $\delta = 0.5$.

The scaled force (4.47) gives a measure of the physical force which is independent of the reference states. The variation of the lowest-order load (4.47) with reference thermodynamic state is plotted in Figure 4.9. This version of the load is seen to increase significantly with pressurization at most temperatures and pressures. In the general vicinity of the thermodynamic critical point, the non-monotone variation of the bulk modulus will give rise to a corresponding non-monotone variation in the load.

We next consider the lowest-order loss, i.e., the first term of (4.43), where $\overline{\mu}$ is evaluated at the lowest-order density. Following the conventional scaling used in the lubrication literature where the film thickness is scaled with the radial clearance, we have multiplied (4.43) by $1+\delta$ and have plotted this version of the scaled loss in Figure 4.10 for various reference thermodynamic states. Inspection of Figure 4.10 reveals that the reference temperature has an insignificant effect on the scaled loss. This is due to the fact that the shear viscosity roughly scales with the ideal gas shear viscosity, at least for the purposes of computing the temperature dependence. To illustrate this point, we have plotted the variation of the ratio of the shear viscosity to the ideal gas viscosity at the same temperatures in Figure 4.11.

As indicated in the discussion of (4.46), the scaled loss for low pressure gases will depend only on δ due to the fact that $\overline{\mu} = 1$ in the ideal gas limit. Thus, each curve in Figure 4.10 will approach the same low pressure asymptote for fixed δ. We note that the loss has been scaled with the loss found when the load is zero, i.e., when $\delta \equiv 0$. As a result, the scaled loss will always be larger than 1 as we approach the ideal gas limit. However, observation of Figure 4.11 reveals that the viscosity will depend on the local density as the reference

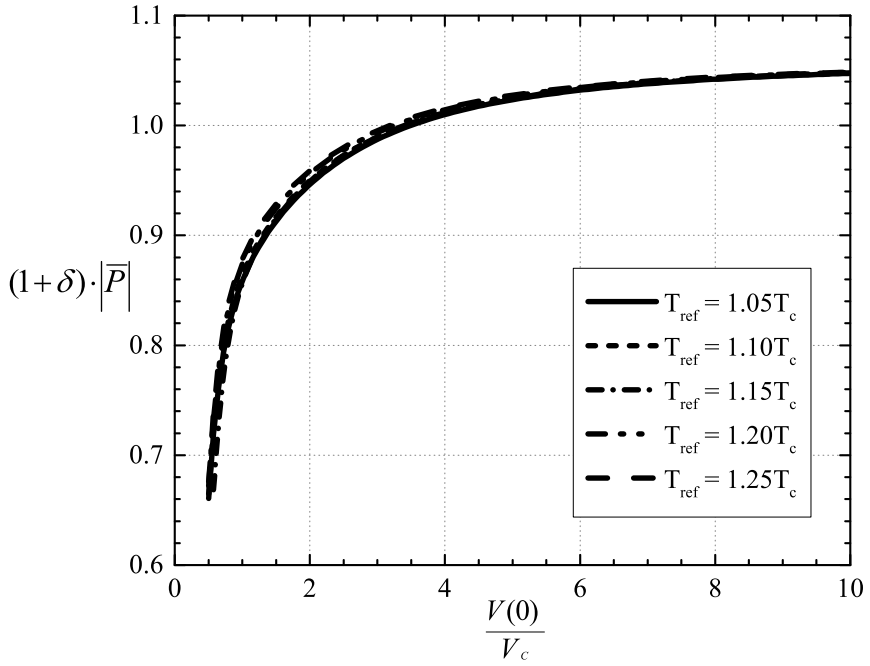

Figure 4.10: Lowest-Order Scaled Loss vs Reference Specific Volume. The parameter $\delta = 0.5$.

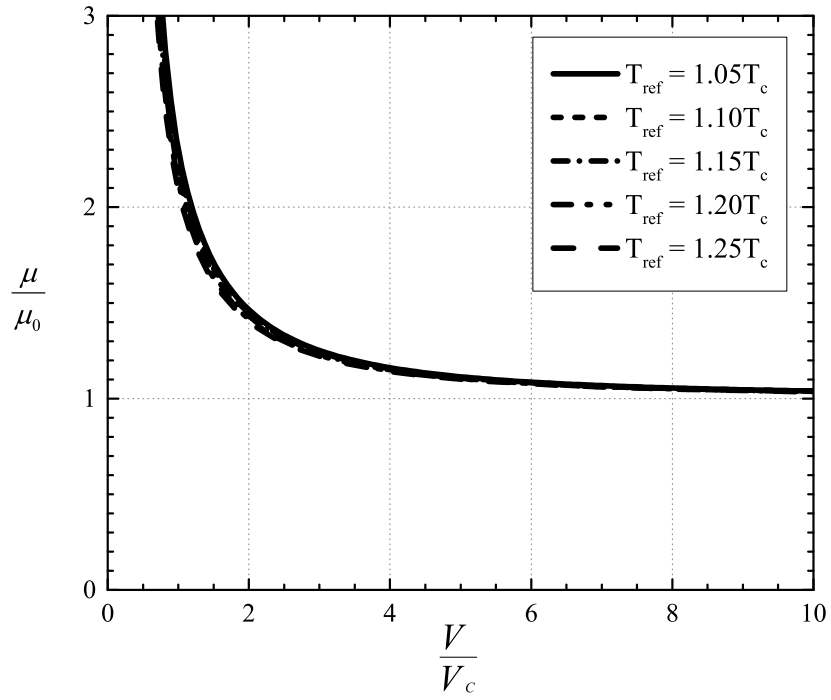

Figure 4.11: Scaled Shear Viscosity of CO_2 vs V/V_c. The viscosity model is that of [26, 27].

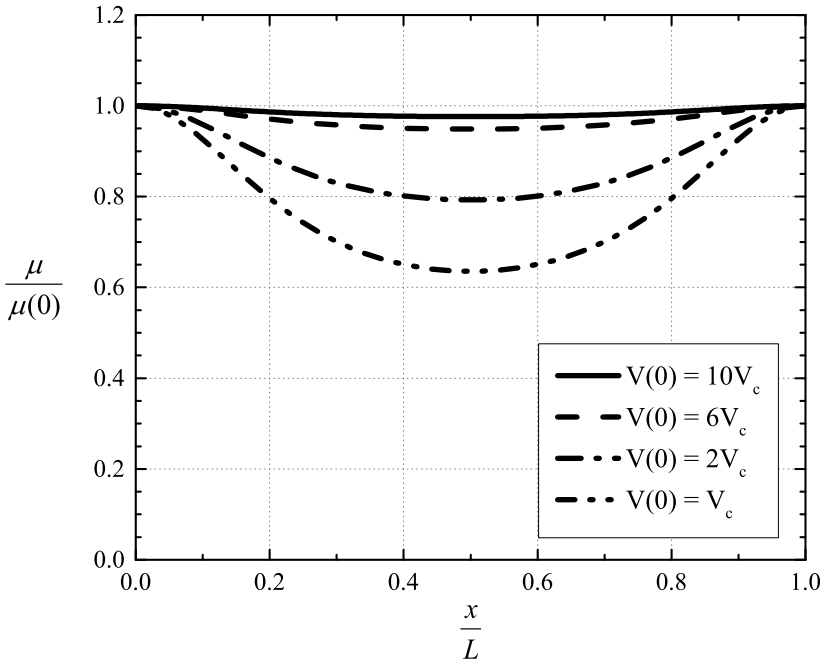

Figure 4.12: Variation of Scaled Viscosity with x/L for $T_{ref} = 1.05\ T_c$. The parameter $\delta = 0.5$.

pressure is increased. Because the viscosity increases monotonically with increasing density, $\overline{\mu} < 1$ over most of the fluid domain. An example of the viscosity variation with $\overline{x}$ is plotted for various thermodynamic states in Figure 4.12. As result, the scaled loss will decrease and even become less than 1 as the reference pressure is increased. That is, for pressurized gases the scaled loss generated by non-concentric cylinders can be smaller than that corresponding to concentric cylinders.

The effects of pressurization on the attitude angle are displayed in Figure 4.13 for various reference temperatures at $\Lambda = 50$. Here we used the associated attitude angle $\psi \equiv \pi - \varphi$, i.e., the angle between the direction of the total force and the negative x′ axis seen in Figure 4.2. Inspection of Figure 4.13 reveals that ψ increases with pressurization for a fixed reference temperature. At $T_{ref} = 1.05\ T_c$ pressurization results in 25.5% increase of ψ over the value of ψ obtained at low pressure. The reason for this increase is due to the non-monotone variation of both $\overline{\kappa}_T$ and $\overline{\kappa}_{Te}$ leading to a smaller decrease in the size of the integrand in (4.38). At higher temperatures both $\overline{\kappa}_T$ and $\overline{\mu}$ undergo a monotone increase as the pressure is increases. Thus, the integrands in (4.40) will be smaller and the increase in ψ will be smaller at higher temperatures.

A comparison of the approximate and the exact scaled load was plotted as a function of δ at $\Lambda = 20$, 30, 40, 50 and ∞ with various reference thermodynamic states in Figure 4.14. The reference temperature is taken to be $T_{ref} = 1.15\ T_c$. The range of the speed numbers is selected to be within the general operating range described by previous investigators [12, 13].

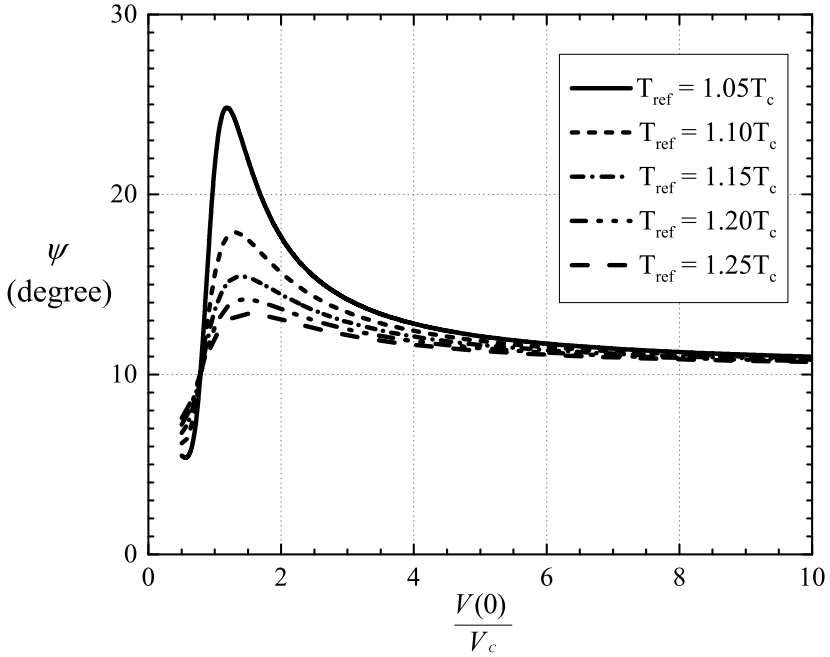

Figure 4.13: Attitude Angle (ψ) vs Reference Specific Volume. The parameter $\delta = 0.5$ and the speed number $\Lambda = 50$.

From (4.4) the rotational speeds corresponding to $\Lambda = 20$ at $V(0) = 12\ V_c$, $6\ V_c$ and $3\ V_c$ are found to be 8432 rpm, 14221 rpm and 19660 rpm, respectively. The solid lines denote the lowest-order theory and the broken lines represent the second-order approximation (4.39). At $V(0) = 12\ V_c$ there is little variation of the load with Λ and it is reasonable to suggest that the lowest-order approximation is sufficient to predict the scaled load for this range of δ. As the reference pressure increases, the scaled load increases as expected, and more importantly, the effect of Λ on the scaled load is seen to become more significant. As a result, the second-order approximation is seen to be necessary to evaluate the load generated by pressurized gases. Even at $\Lambda = 20$ it was found that the maximum discrepancy between the second-order approximation and the exact scaled load for the case of $V(0) = 3V_c$ is 4.7%.

In order to illustrate the effect of Λ on the loss, we have plotted the approximate and exact scaled loss as a function of δ at $V(0) = 12\ V_c$ and $3\ V_c$ in Figure 4.15 and Figure 4.16, respectively. The speed number $\Lambda = 20$, 30, 40, 50 and ∞, and the reference temperature was taken to be $T_{ref} = 1.15\ T_c$. Examination of Figure 4.15 indicates that the agreement between the approximate and exact scaled loss is excellent for each Λ at $V(0) = 12\ V_c$. The maximum difference between the second-order approximation and the exact scaled loss is found to be 2.5% at $\Lambda = 20$. The scaled loss is seen to decrease with the increase of Λ and to increase monotonically as δ increases. At higher pressures, the rate of increase of the viscosity with increasing density is larger than in the low pressure case so that the loss for the case $V(0) = 3\ V_c$ has a local minimum located at $\delta \approx 0.2$. At these higher pressures the

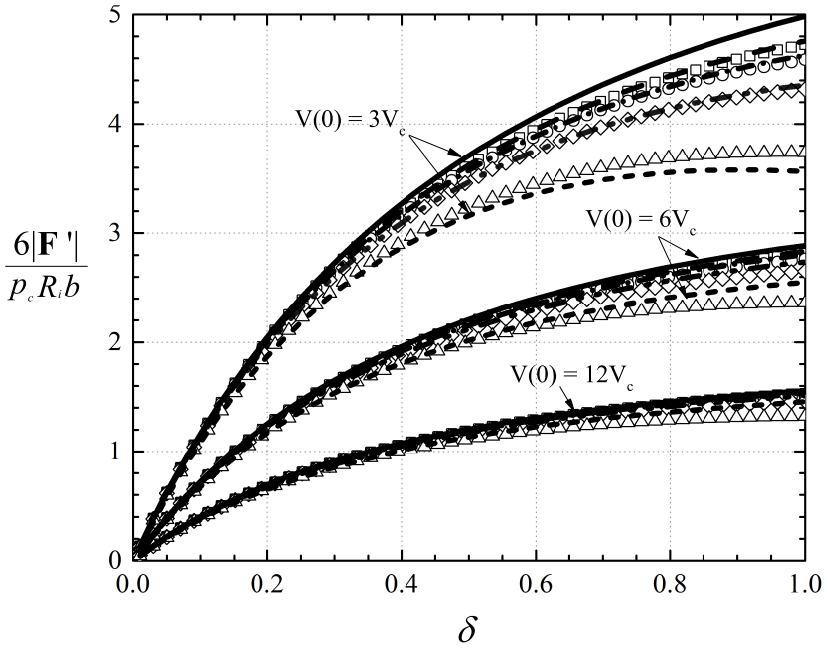

Figure 4.14: Scaled Load vs δ at V(0) = 3 V_c, 6 V_c, and 12 V_c. The speed numbers were taken to be Λ = 20, 30, 40, 50, ∞ and the reference temperature T_{ref} = 1.15 T_c. Symbols represent the exact scaled load computed from (4.16)-(4.18) in which the pressure variation was obtained from the Reynolds equation (4.12) and the equation of state. Lines denote the approximation of the scaled load (4.39). The lowest-order results, i.e., $\Lambda = \infty$, are represented by ——————. Results for Λ = 50 are denoted by □ and — — — — — —, results for Λ = 40 are denoted by ○ and —·—·—·—·—, results for Λ = 30 are represented by ◇ and —··—··—··, and results for Λ = 20 are denoted by △ and - - - - - - - -.

difference between the exact and approximate solutions is larger than in the low pressure examples. Nevertheless, the maximum difference between the exact solution and the Λ = 20 approximation is less that 10% for the chosen values of δ and V(0).

The attitude angle ψ is plotted as a function of δ at T_{ref} = 1.15 T_c for V(0) = 12 V_c and 3 V_c in Figure 4.17 and Figure 4.18, respectively. The speed numbers were taken to be Λ = 20, 30, 40, and 50. Observation of Figure 4.17 reveals that the agreement between the exact ψ and the first-order approximate ψ is seen to be very good for each Λ at V(0) = 12 V_c where the maximum discrepancy is found to be 4% at Λ = 20. The scaled attitude angle decreases with the increase of Λ and the decrease in δ. At V(0) = 3 V_c, the first-order approximation of ψ still has reasonable agreement with the exact ψ when $\Lambda > 30$. At Λ = 20, the maximum difference between the exact ψ and approximate ψ is found to be 10.6%. We note that the non-zero attitude angle at $\delta = 0$ is due to the fact that both $\overline{F}_{x'}$ and $\overline{F}_{y'} \longrightarrow 0$ at the same rate as $\delta \longrightarrow 0$. The limiting value of ψ can be found by taking $\delta \longrightarrow 0$ in (4.40), (4.33) and

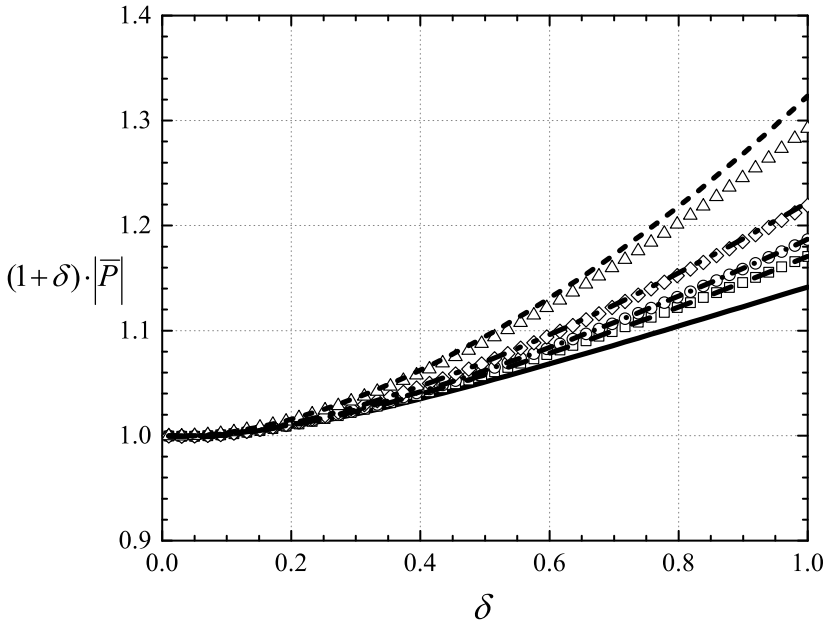

Figure 4.15: Scaled Loss vs δ at V(0) = 12 V_c. The speed numbers are taken to be $\Lambda = 20$, 30, 40, 50, ∞ and the reference temperature $T_{ref} = 1.15\ T_c$. Symbols represent the exact scaled loss computed from (4.21). Lines denote the approximation of the scaled loss (4.43). The lowest-order results, i.e., $\Lambda = \infty$, are represented by ——————. Results for $\Lambda = 50$ are denoted by □ and — — — — — —, results for $\Lambda = 40$ are denoted by ○ and —·—·—·—·—, results for $\Lambda = 30$ are denoted by ◇ and —··—··—··—, and results for $\Lambda = 20$ are denoted by △ and - - - - - - - - .

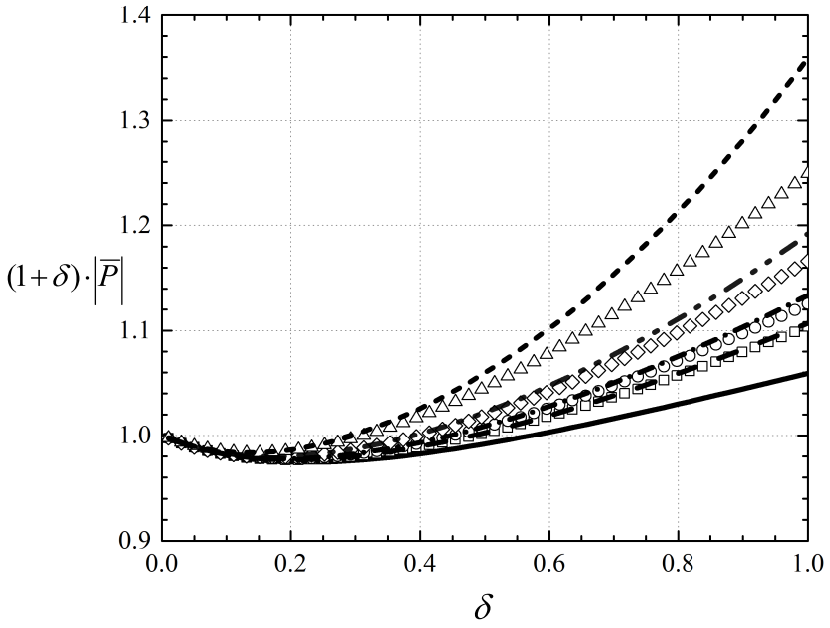

Figure 4.16: Scaled Loss vs δ at V(0) = 3 V_c. The speed numbers are taken to be Λ = 20, 30, 40, 50, ∞ and the reference temperature T_{ref} = 1.15 T_c. Symbols represent the exact scaled loss computed from (4.21). Lines denote the approximation of the scaled loss (4.43). The lowest-order results, i.e., $\Lambda = \infty$, are represented by ——————. Results for Λ = 50 are denoted by □ and — — — — , results for Λ = 40 are denoted by ○ and —·—·—·— , results for Λ = 30 are denoted by ◇ and —··—··—··, and results for Λ = 20 are denoted by △ and - - - - - - - - .

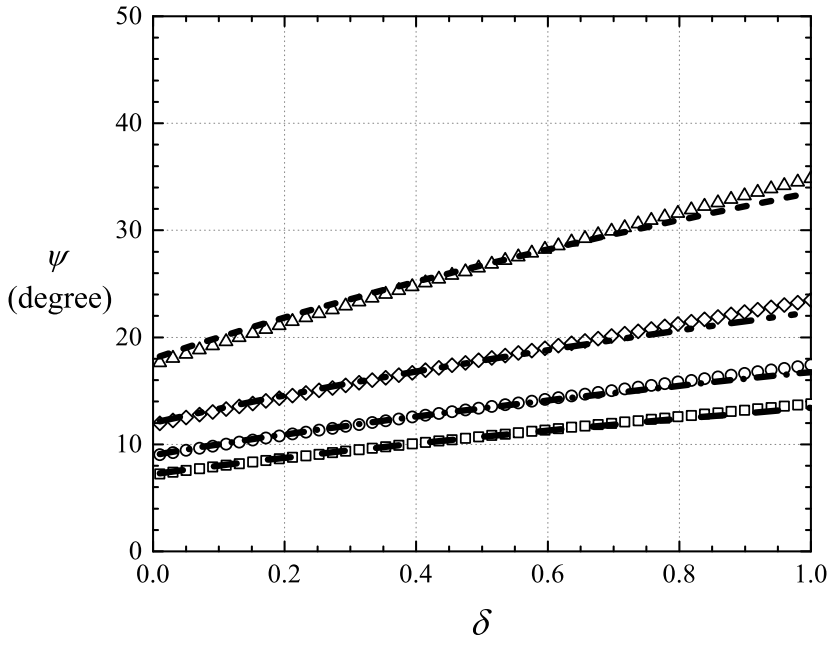

Figure 4.17: Attitude Angle vs δ at V(0) = 12 V_c. The speed numbers are taken to be Λ = 20, 30, 40 and 50 and the reference temperature T_{ref} = 1.15 T_c. The scaled attitude angle is defined as $\psi \equiv \pi - \varphi$, i.e., the angle between the direction of the load and the negative x′ axis seen in Figure 4.2. Symbols represent the exact scaled attitude angle computed from (4.16) and (4.17). Lines denote the approximation of the scaled attitude angle obtained from (4.40). Results for Λ = 50 are denoted by □ and ▬▬▬▬ , results for Λ = 40 are denoted by ○ and ▬·▬·▬·▬ , results for Λ = 30 are denoted by ◇ and ▬··▬··▬·· , and results for Λ = 20 are denoted by △ and - - - - - - - - .

(4.38) yielding

$$\psi \sim \frac{2\pi}{\Lambda} \quad \text{as} \quad \delta \longrightarrow 0. \tag{4.48}$$

Thus, ψ at $\delta = 0$ will be independent of the reference thermodynamic state. For Λ = 20, 30, 40, and 50, the values of ψ at $\delta = 0$ will be 18°, 12°, 9°, and 7.2°, respectively. This non-zero limit of ψ as δ vanishes is consistent with the finding of [8] for ideal gases.

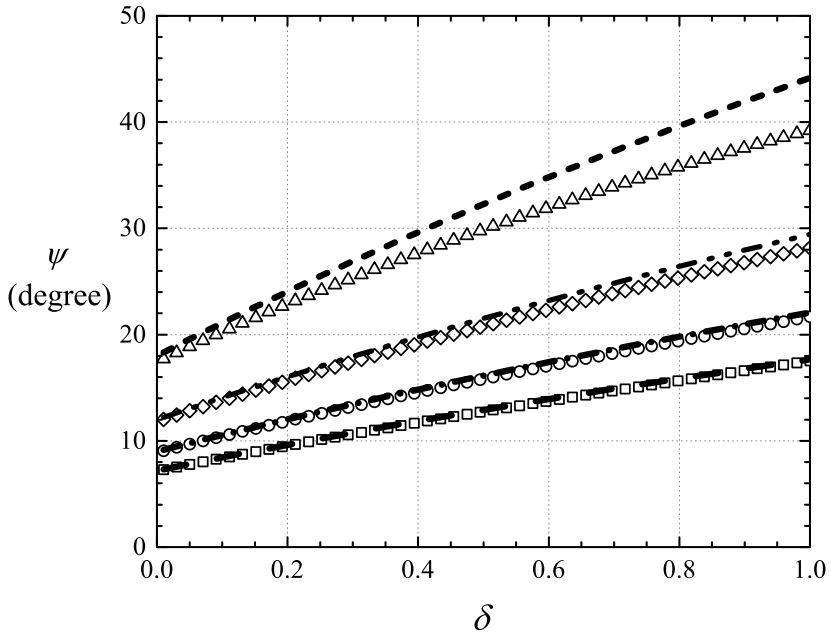

Figure 4.18: Attitude Angle vs δ at V(0) = $3V_c$. The speed numbers Λ = 20, 30, 40 and 50 and the reference temperature T_{ref} = 1.15 T_c. The scaled attitude angle is defined as $\psi \equiv \pi - \varphi$, i.e., the angle between the direction of the load and the negative x′ axis seen in Figure 4.2. Symbols represent the exact scaled attitude angle computed from (4.16) and (4.17). Lines denote the approximation of the scaled attitude angle obtained from (4.40). Results for Λ = 50 are denoted by □ and ▬▬▬▬, results for Λ = 40 are denoted by ○ and ▬·▬·▬·▬, results for Λ = 30 are denoted by ◇ and ▬··▬··▬··, and results for Λ = 20 are denoted by △ and ▬▬▬▬ .

4.5 Summary

We have obtained approximate solutions for the load and loss of a two-dimensional, steady, compressible, laminar, and single-phase flow between two non-concentric cylinders. Solutions are based on large Λ expansions of the Reynolds equation (4.12) and are therefore valid at most pressures and temperatures in the single-phase regime and for all Navier-Stokes fluids; the primary exception is the neighborhood of the thermodynamic critical point where (4.12) breaks down. In Appendix A we have given the connection between the friction loss and the net heat flux so that the heat transfer is determined once the friction loss is.

In the limit of ideal gases, the work of [8] suggests that the first corrections to the load and loss are $O(\Lambda^{-2})$. The present study demonstrates that this ordering holds for general fluids, i.e., for both low and high pressure gases, as well.

The effects of pressurization and non-ideal gas behavior have been illustrated primarily through the use of the lowest-order theory. Pressurization affects the load through the bulk modulus and it affects the loss through the density dependence of the shear viscosity. We found that the load scales with the reference bulk modulus $\kappa_T|_{ref}$ so that the non-monotone variations of the bulk modulus can result in a non-monotone variation of the load. Isothermal pressurization is seen to result in significant increases in the load.

At moderate pressures, inspection of Figures 4.7 and 4.10 suggests that $\Lambda\,|\overline{\mathbf{F}}|$ and $(1+\delta)\,|\overline{P}|$ can be regarded as nearly constant for reference specific volumes of $\mathrm{V}(0) > 6\ \mathrm{V}_c$. At higher pressures, the dependence of the density on the bulk modulus and viscosity becomes more noticeable. As a result, the strong decrease in the loss and the increase in the load will require the use of pure numerical solutions or the approximations given here.

The second-order approximations for load and loss are compared to the exact values obtained based on the solutions to the Reynolds equation (4.12) for a range of δ in Figures 4.14-4.16. These examples illustrate the dependence of the load and loss on the eccentricity parameter (4.6) and the speed number.

The lowest-order attitude angle ($\psi \equiv \pi - \varphi$)has been computed and is found to decrease with increasing Λ. At constant Λ and a fixed reference thermodynamic state, the attitude angle is seen to approximately increase linearly with δ, at least for the cases shown. The values of ψ at $\delta = 0$ are given by (4.48) and are seen to be independent of thermodynamic state.

In order to focus on the physical effects of pressurization and the structure of the approximation scheme, we have restricted attention to the relatively simple flow model of [22]; this model has been validated against numerical solutions to the full Navier-Stokes solutions in [22, 23]. Many of the observed features here are due to the density dependence of the material functions and will be present, to greater or lesser degrees, in more complex flows, including those involving turbulent and three dimensional flows.

Bibliography

[1] O. Reynolds. On the theory of lubrication and its application to Mr. Beauchamp Tower's experiments, including an experimental determination of the viscosity of olive oil. *Proceedings of the Royal Society of London*, 40(242-245), 191–203, 1886.

[2] V. Dostal, M. J. Driscoll, and P. Hejzlar. A supercritical carbon dioxide cycle for next generation nuclear reactors. Technical report, MIT-ANP-TR-100, 2004.

[3] C. DellaCorte, K. C. Radil, R. J. Bruckner, and S. A. Howard. Design, fabrication, and performance of open source generation I and II compliant hydrodynamic gas foil bearings. *Tribology Transactions*, 51(3), 254–264, 2008.

[4] S. A. Wright, R. F. Radel, M. E. Vernon, G. E. Robert, and P. S. Pickard. Operation and analysis of a supercritical CO_2 Brayton cycle. *Sandia Report, No. SAND2010-0171*, 2010.

[5] T. M. Conboy, S. A. Wright, J. Pasch, D. Fleming, G. Rochau, and R. Fuller. Performance characteristics of an operating supercritical CO_2 Brayton cycle. *Journal of Engineering for Gas Turbines and Power*, 134(11), 111703, 2012.

[6] F. Crespi, G. Gavagnin, D. Sánchez, and G. S. Martínez. Supercritical carbon dioxide cycles for power generation: A review. *Applied Energy*, 195, 152–183, 2017.

[7] O. Pinkus and B. Sternlicht. *Theory of Hydrodynamic Lubrication.* McGraw-Hill, 1961.

[8] W. A. Gross, L. A. Matsch, V. Castelli, A. Eshel, J. H. Vohr, and M. Wildmann. *Fluid Film Lubrication.* John Wiley and Sons, Inc., 1980.

[9] A. Z. Szeri. *Fluid Film Lubrication.* Cambridge University Press, 2010.

[10] B. J. Hamrock, S. R. Schmidt, and B. O. Jacobson. *Fundamentals of Fluid Film Lubrication.* CRC Press, 2004.

[11] Z. C. Peng and M. M. Khonsari. On the limiting load-carrying capacity of foil bearings. *Journal of Tribology*, 126(4), 817–818, 2004.

[12] T. M. Conboy. Real-gas effects in foil thrust bearings operating in the turbulent regime. *Journal of Tribology*, 135(3), 031703, 2013.

[13] D. Kim. Design space of foil bearings for closed-loop supercritical CO_2 power cycles based on three-dimensional thermohydrodynamic analyses. *Journal of Engineering for Gas Turbines and Power*, 138(3), 032504, 2016.

[14] S. Dousti and P. Allaire. A compressible hydrodynamic analysis of journal bearings lubricated with supercritical carbon dioxide. In *Proceeding of Supercritical* CO_2 *Power Cycle Symposium. San Antonio, TX*, 2016.

[15] K. Qin. *Development and application of multiphysics simulation tools for foil thrust bearings operating with carbon dioxide*. PhD thesis, University of Queensland, 2017.

[16] H. Heshmat, J. F. Walton, and J. L. Cordova. Technology readiness of 5^{th} and 6^{th} generation compliant foil bearing for 10 MWE s-CO_2 turbomachiery systems. In *Proceeding of the 6^{th} International Supercritical CO_2 Power Cycles Symposium. Pittsburg, PA*, 2018.

[17] S. A Howard, R. J. Bruckner, C. DellaCorte and K. C. Radil. Gas foil bearing technology advancements for closed Brayton cycle turbines. *AIP Conference Proceedings*, 880(1), 668–680, 2007.

[18] M. H. Briggs, J. M. Prahl, R. Bruckner and B. Dykas. High pressure performance of foil journal bearings in various gases. *STLE/ASME 2008 International Joint Tribology Conference*, 403–405. American Society of Mechanical Engineers, 2008.

[19] E. Guenat and J. Schiffmann. Real-gas effects on aerodynamic bearings. *Tribology International*, 120, 358–368, 2018.

[20] E. W. Lemmon, M. L. Huber, and M. O. McLinden. NIST Reference fluid thermodynamic and transport properties–REFPROP. *NIST Standard Reference Database*, 23, v7, 2002.

[21] I. H. Bell, J. Wronski, S. Quoilin, and V. Lemort. Pure and pseudo-pure fluid thermophysical property evaluation and the open-source thermophysical property library CoolProp. *Industrial & Engineering Chemistry Research*, 53(6), 2498–2508, 2014.

[22] S. Y. Chien, M. S. Cramer, and A. Untaroiu. Compressible Reynolds equation for high-pressure gases. *Physics of Fluids*, 29(11), 116101, 2017.

[23] S. Y. Chien, M. Cramer, A. Untaroiu. A compressible thermohydrodynamic analysis of journal bearings lubricated with supercritical CO_2. In *ASME 2017 Fluids Engineering Division Summer Meeting. Waikoloa, HI*, paper No. FEDSM2017-69310, 2017.

[24] S. Y. Chien and M. S. Cramer. Pressure, temperature, and heat flux in high speed lubrication flows of pressurized gases. *Tribology International*, 129, 468–475, 2019.

[25] R. C. Reid, J. M. Prausnitz, B. E. Poling. *The Properties of Gases and Liquids*. McGraw-Hill, 1987.

[26] T. H. Chung, L. L. Lee, K. E. Starling. Applications of kinetic gas theories and multiparameter correlation for prediction of dilute gas viscosity and thermal conductivity. *Industrial & Engineering Chemistry Fundamentals*, 23(1), 8–13, 1984.

[27] T. H. Chung, M. Ajlan, L. L. Lee, K. E. Starling. Generalized multiparameter correlation for nonpolar and polar fluid transport properties. *Industrial & Engineering Chemistry Research*, 27(4), 671–679, 1988.

Chapter 5

Virial Approximation for Load and Loss in High-Speed Journal Bearings using Pressurized Gases

The contents of this chapter have appeared as an open access article in the Fluids, volume 4, issue 1, 2019. The published article can be found at: https://www.mdpi.com/2311-5521/4/1/27.

Attribution

The work presented in this chapter was primarily carried out by S. Y. Chien. M. S. Cramer conceived of the main idea and contributed to the development and implementation of this work.

Abstract

We consider steady, laminar, compressible lubrication flows in a high-speed two-dimensional journal bearing governed by the appropriate Reynolds equation. The thermodynamic states correspond to pressurized gases and are in the single-phase regime. Simple explicit formulas for the load capacity, power loss and attitude angle are derived by applying the virial (or small density) expansions of pressure and shear viscosity to results developed in previous studies. The present virial approximation was compared to the exact numerical solutions to the Reynolds equation. It was shown that the results based on our virial expansions are quite accurate at thermodynamic states corresponding to dense and supercritical gases. The first virial correction is seen to significantly improve predictions based on the ideal gas theory.

5.1 Introduction

The canonical equation governing many lubrication flows is the Reynolds equation [1]. Since its introduction in the late 19^{th} century, it has been generalized to include the effects of three-dimensional unsteady flow, turbulence, non-newtonian constitutive laws, two-phase flow, and wall slip [2, 3, 4, 5]. Conditions under which the Reynolds equation is valid are satisfied in many devices [6, 7, 8, 9, 10]. An important motivation for the use of the Reynolds equation is that it provides a relatively simple, computationally efficient, and easily reproducible context in which to examine physical effects and mathematical models.

Recent interest in novel power systems have motivated the use of gases rather than highly viscous oils [12, 11, 13, 14, 15]. The advantages of gases over liquids include weight reduction, elimination of complications associated with fouling due to leaks and complications due to phase changes, and the compatibility with working fluids of the parent power system.

Because the viscosity of gases is smaller than that of oils, gas lubrication requires high speeds to support reasonable loads and the resultant flows are very often compressible. The overall compressibility of the flow is usually characterized by the speed or bearing number defined as a non-dimensional measure of the flow speed; a precise definition of the version of the speed number used here will be given in the next section.

In most of the previous investigations of gas lubrication the ideal gas model was employed [3, 12, 16]. One of the first analytical studies is due to Gross et al. [3] who developed approximations to the Reynolds equation valid for large speed numbers and ideal gases. It was shown that the first correction for finite speed number to the lowest-order, i.e., that corresponding to an infinite speed number, load and loss of a simple journal bearing is of order of the inverse square of the speed number. For journal bearings lubricated with ideal gases, Gross et al. [3] provided explicit formulas for load and loss in terms of the speed number and eccentricity.

When the pressures are on the order of those of the thermodynamic critical point, the gas can no longer be regarded as ideal, and more complex gas models must be employed. In order to investigate the effects of pressurized gases on bearing performance, previous studies [17, 18, 19, 20] have numerically solved the Reynolds equation along with digital table look-ups to capture the real-gas behavior. Conboy [17], Kim [18] and Qin [19] used the NIST REFPROP database [21] while Guenat and Schiffmann [20] employed the COOLPROP database [22].

At the thermodynamic critical point, properties such as the specific heat at constant pressure and the thermal expansivity are singular; as a result, the Prandtl number is also singular at the thermodynamic critical point. Additionally, the bulk modulus

$$\kappa_T = \kappa_T(\rho, T) \equiv \rho \left.\frac{\partial p}{\partial \rho}\right|_T \geq 0, \tag{5.1}$$

where $\rho > 0$, T > 0, and p = p(ρ,T) are the fluid density, absolute temperature, and

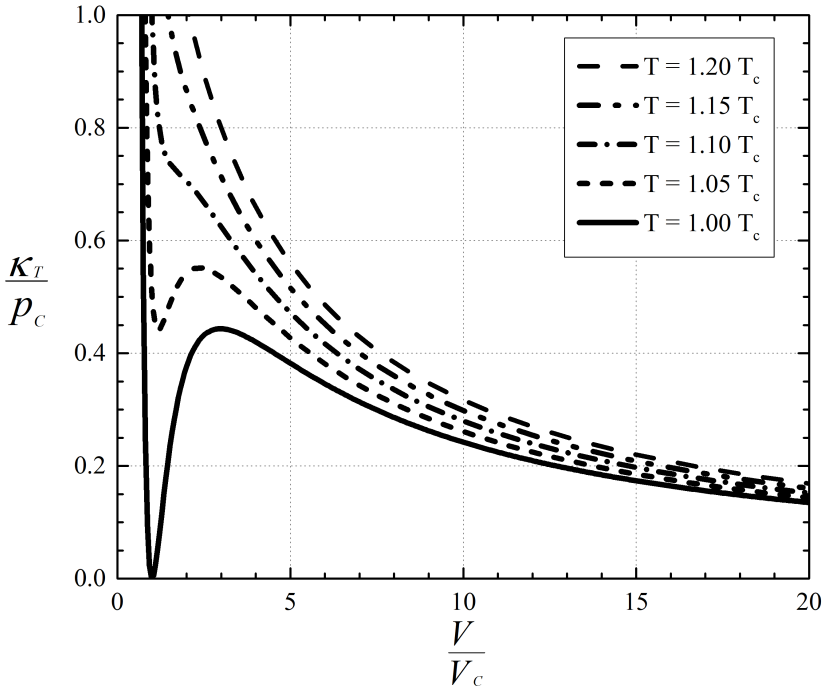

Figure 5.1: Variation of the Scaled Bulk Modulus with Reduced Specific Volume for CO_2. Subscripts "c" will always denote quantities evaluated at the thermodynamic critical point and V $\equiv \rho^{-1}$ = the specific volume. The curves were generated using the Redlich-Kwong-Soave (RKS) equation of state. Details of the RKS equation are given in [23] along with the physical constants for CO_2.

thermodynamic pressure, is seen to be zero at the thermodynamic critical point and has a non-monotone variation with density at constant temperature. A plot of a scaled version of (5.1) is provided in Figure 5.1. Recognition of the singular behavior of high pressure gases has led [24] to examine the validity of the Reynolds equation in the general single-phase regime. These authors have given a careful derivation of the Reynolds equation and corresponding temperature equation valid for compressible flows of pressurized gases. The usual constraints of a thin fluid layer and small lubrication Reynolds number were imposed along with mild conditions on any imposed temperature differences. The resultant form of their Reynolds equation is given in the next section. The Reynolds and temperature equations of [24] were found to be valid over most of thermodynamic states corresponding to ideal, dense, and supercritical fluids, but were seen to break down simultaneously in the near-critical regime. The size of this near-critical region was given in terms of the lubrication Reynolds number; see, e.g., Section IV of [24]. It was shown by [25] and [24] that, within the stated region of validity, the solutions to the Reynolds and temperature equation of [24] were found to be in excellent agreement with the Navier-Stokes equations.

Chien and Cramer [26] have derived approximate solutions to the Reynolds and temperature equation of [24] valid for pressurized gases and large speed numbers. Explicit expressions

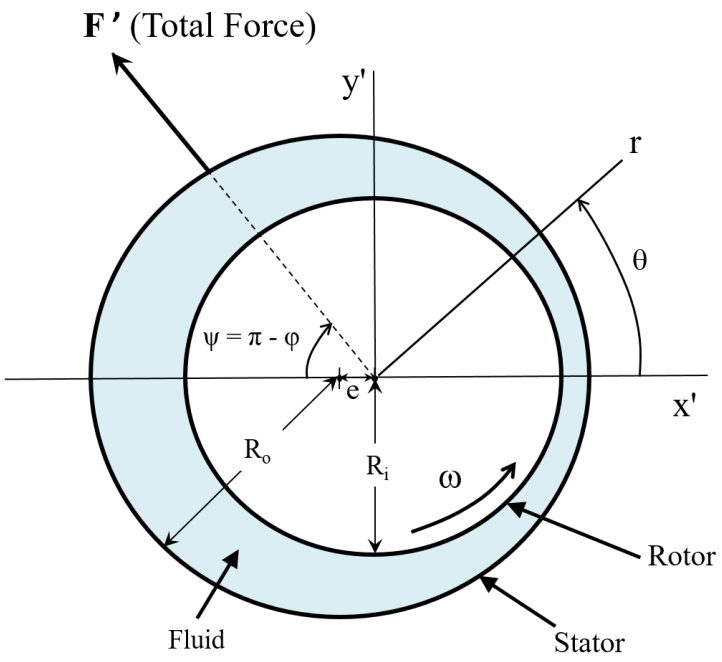

Figure 5.2: Sketch of Two-Dimensional Journal Bearing. The angular velocity of the rotor ω = constant. The angle φ is the angle between the force $\mathbf{F}'$ and the positive x′ axis. The angle $\psi \equiv \pi - \varphi$.

for the local density, pressure, temperature and heat flux were given in terms of the bulk modulus, shear viscosity, thermal conductivity, thermal expansivity, Prandtl number, speed number, and the film thickness. In [27] Chien and Cramer have used approximations which are second order in the speed number to derive general expressions for the load, loss and attitude angle for a two-dimensional journal bearing. For convenience, the relevant results of [27] are recorded in the next section. While the results are explicit, the results require the numerical evaluation of a number of integrals if the gas model is more complicated than that of an ideal gas. Numerical integration will also be required if the fluid properties are supplied by digital table look-ups.

The goal of the present investigation is to develop a simplified model for the load, loss and attitude angle based on virial, i.e., small density, expansions of the pressure and shear viscosity. The resultant expressions will obviate the need for numerical evaluations of the integrals and provide explicit expressions for the load, loss and attitude angle in terms of the first virial coefficient for pressure and a reference viscosity.

5.2 General Formulas

We begin with the general formulas for the load, loss, and attitude angle derived in [27] for large speed number. These formulas were derived by finding the second-order approximations to the Reynolds equation of [24]-[25] and then integrating the results for pressure over the journal bearing configuration sketched in Figure 5.2. The Reynolds equation is valid for steady, two-dimensional, compressible, laminar, single-phase flows at thermodynamic states sufficiently far from those of the thermodynamic critical point. Again, we refer the reader to [24] and [27] for details, derivations, and validation of these results. In the following, we summarize the principal results of [27] which form the basis for the present study.

The configuration considered in this study is a two-dimensional infinitely long journal bearing as sketched in Figure 5.2. The inner cylinder corresponds to the rotor, which has radius R_i and is centered at $\mathrm{x}' = 0$ and $\mathrm{y}' = 0$. The rotor rotates at a rate $\omega = \mathrm{U}/\mathrm{R}_i$, where the constant U is the speed of the surface of the inner cylinder. The outer cylinder represents a stator, which is stationary and has a radius $= \mathrm{R}_o > \mathrm{R}_i$. The center of the stator is located at $\mathrm{x}' = -\,\mathrm{e} \equiv -\,\epsilon\,(\mathrm{R}_o - \mathrm{R}_i)$, $\mathrm{y}' = 0$. Here ϵ is the eccentricity.

We take the gap between the rotor and stator to be sufficiently small compared to their radii. We can then approximate the flow using the unwrapped configuration sketched in Figure 5.3. The film thickness is given by the function h(x), the surface of the stator is taken to be y = h(x) and the surface of the rotor to be given by y = 0. The coordinate x is the distance taken along the inner cylinder, i.e., the rotor, and is related to the angle θ by $\theta \equiv 2\pi\mathrm{x}/\mathrm{L}$ where $\mathrm{L} \equiv 2\pi\mathrm{R}_i$ is the circumference of the rotor. The coordinate y is taken to be normal to the rotor. The minimum film thickness occurs at the origin and is given by $h_o \equiv \mathrm{h}(0)$ and the maximum thickness is $\mathrm{h}_m \equiv \mathrm{h}(\mathrm{x} = \mathrm{L}/2) = \mathrm{h}(\theta = 2\pi)$. Because of the periodicity of the physical configuration and the choice of the coordinate system,

$$h(0) = h(L) = h_o, \tag{5.2}$$

$$\frac{dh}{dx}(0) = \frac{dh}{dx}(0) = 0, \tag{5.3}$$

$$\frac{d^2h}{dx^2}(0) = \frac{d^2h}{dx^2}(L) > 0. \tag{5.4}$$

The general results of [27] were obtained using the relatively weak condition on h(x) that it is symmetric about $\mathrm{x} = \mathrm{L}/2$ or $\theta = \pi$, i.e.,

$$h(\pi - \theta) = h(\theta - \pi) \quad \text{or} \quad h(L/2 - x) = h(x - L/2). \tag{5.5}$$

The formulas derived in Section 5.5 use an explicit form of h(x) corresponding to a two-dimensional journal bearing sketched in Figure 5.2. When the gap width is small compared to the radii of the rotor and stator, we find that h(x) can be approximated by

$$\overline{h} = \overline{h}(\overline{x}) \equiv \frac{h(x)}{h_o} \approx 1 + \delta - \delta\cos(\theta), \tag{5.6}$$

$$= 1 + \delta - \delta\cos(2\,\pi\,\overline{x}), \tag{5.7}$$

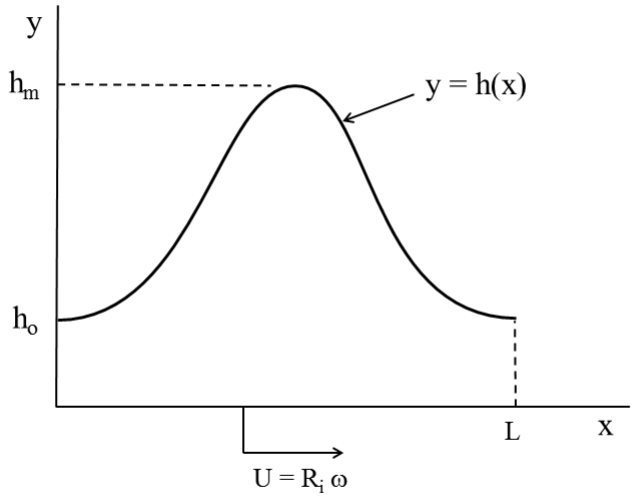

Figure 5.3: Unwrapped Configuration: The surface y = 0 corresponds to the surface of the inner cylinder, i.e., the rotor. The surface y = h(x) corresponds to the surface of the outer cylinder, i.e., the stator. The minimum film thickness is taken to be $h_o \equiv$ h(0) and the maximum film thickness is taken to be $h_m \equiv$ h(L/2).

where $\overline{x} \equiv$ x/L $= \theta/2\pi$ and the parameter δ is related to the eccentricity by $\delta \equiv \epsilon/(1-\epsilon)$.

In terms of the unwrapped configuration of Figure 5.3, the non-dimensional form of the Reynolds equation derived by Chien and Cramer [24] is

$$\frac{d}{d\overline{x}}\left(\overline{h}^3 \overline{\kappa}_{Te} \frac{d\overline{\rho}}{d\overline{x}}\right) = \Lambda \frac{d(\overline{\rho}\overline{h})}{d\overline{x}}, \tag{5.8}$$

subjected to the periodicity condition

$$\overline{\rho} = 1 \quad \text{at} \quad \overline{x} = 0,\ 1. \tag{5.9}$$

Here $\overline{x} \equiv x/L = \theta/2\pi$, and

$$\overline{\rho} \equiv \frac{\rho}{\rho_{ref}} \tag{5.10}$$

is the scaled fluid density. The subscript "ref" will always refer to a reference thermodynamic state; throughout this study we take this reference state to be that at the minimum gap thickness, i.e., at $\overline{x} = 0,\ 1$ or, equivalently, $\theta = 0,\ 2\pi$. The thermodynamic function

$$\kappa_{Te} = \kappa_{Te}(\rho, T) \equiv \frac{\kappa_T(\rho, T)}{\mu(\rho, T)}, \tag{5.11}$$

is the effective bulk modulus which gives a measure of the relative strength of the local fluid stiffness to the fluid friction. The quantity $\mu = \mu(\rho$,T$) > 0$ is the shear viscosity. The scaled

version of the effective bulk modulus (5.11) is

$$\overline{\kappa}_{Te} \equiv \frac{\kappa_{Te}(\rho, T_{ref})}{\kappa_{Te}(\rho_{ref}, T_{ref})} = \frac{\kappa_{Te}(\rho, T_{ref})}{\kappa_{Te}|_{ref}}. \tag{5.12}$$

As in the classical lubrication theory the flow may be regarded as isothermal for the purposes of computing the density and pressure. The temperature is therefore taken to be T_{ref} throughout this calculation. The constant

$$\Lambda \equiv \frac{6UL}{h_o^2 \kappa_{Te}|_{ref}} \tag{5.13}$$

is the speed number. This form is the one that arises naturally during the non-dimensionalization process when pressurized gases are of interest.

For $\Lambda \gg 1$, [27] have shown that the net force on the rotor seen in Figure 5.2 can be written as

$$\frac{6|\mathbf{F}'|}{p_c R_i b} = -\frac{3\kappa_T|_{ref}}{\pi p_c} I_{x1} \left[1 + \frac{1}{\Lambda^2}\left(\frac{I_{x3}}{I_{x1}} + \frac{1}{2}\frac{I_{y2}^2}{I_{x1}^2}\right)\right] + O(\frac{1}{\Lambda^3}), \tag{5.14}$$

where $\mathbf{F}'$ is the dimensional force, p_c is the pressure at the thermodynamic critical point, and b is the length of the bearing in the axial direction, i.e., the direction orthogonal to the diagrams of Figures 5.2-5.3. The quantities I_{x1}, I_{x3}, and I_{y2} arise naturally in the course of the derivation of [27] and are defined

$$I_{x1} \equiv -2\pi \int_0^{2\pi} \frac{\overline{\kappa}_{To}}{\overline{h}} \frac{d\overline{h}}{d\theta} \sin(\theta) d\theta, \tag{5.15}$$

$$\begin{aligned} I_{x3} \equiv & -8\pi^3 \int_0^{2\pi} \left[\frac{1}{2}\overline{\kappa}_{Teo}^2 \frac{\partial}{\partial \overline{\rho}}\left(\frac{\overline{\kappa}_T}{\overline{\rho}}\right)\Big|_o + \overline{h}\overline{\kappa}_{To}\frac{\partial \overline{\kappa}_{Te}^2}{\partial \overline{\rho}}\Big|_o\right]\left(\frac{d\overline{h}}{d\theta}\right)^2 \cos(\theta) d\theta \\ & + 8\pi^3 \int_0^{2\pi} \overline{\kappa}_{To}\overline{\kappa}_{Teo}^2 \overline{h}^3 \frac{d^2\overline{h}}{d\theta^2} \cos(\theta) d\theta \\ & - 8\pi^3 \frac{d^2\overline{h}}{d\theta^2}(0) \int_0^{2\pi} \overline{\kappa}_{To} \cos(\theta) d\theta, \end{aligned} \tag{5.16}$$

$$I_{y2} = -4\pi^2 \int_0^{2\pi} \overline{\kappa}_{To}\overline{\kappa}_{Teo}\, \overline{h}\, \frac{d\overline{h}}{d\theta} \sin(\theta) d\theta, \tag{5.17}$$

where

$$\overline{\kappa}_T \equiv \frac{\kappa_T(\rho, T_{ref})}{\kappa_T(\rho_{ref}, T_{ref})}. \tag{5.18}$$

The subscripts "o" denote quantities evaluated at the lowest-order density $\overline{\rho} \approx 1/\overline{h}$, e.g.,

$$\overline{\kappa}_{To} \equiv \overline{\kappa}_T(\frac{1}{\overline{h}}, T_{ref}). \tag{5.19}$$

The attitude angle (φ) is defined as the angle between $\mathbf{F}'$ and the positive x′ axis seen in Figure 5.2, and was found to be

$$\varphi \equiv \tan^{-1}\left(\frac{F_{y'}}{F_{x'}}\right) \approx \pi - \frac{1}{\Lambda}\frac{I_{y2}}{I_{x1}} + O(\frac{1}{\Lambda^2}). \tag{5.20}$$

Because both I_{x1} and I_{y2} are always < 0, the force on the rotor will always lie in the second quadrant of the x′-y′ plane sketched in Figure 5.2. It will therefore be convenient to define the associated acute angle $\psi \equiv \pi - \varphi$.

Under the same conditions, [27] have shown that the scaled power loss can be written

$$-\overline{P} = -\frac{h_o}{bLU^2\mu_{ref}}P = \int_0^1 \frac{\overline{\mu}}{\overline{h}}d\overline{x} + \frac{3}{\Lambda^2}\int_0^1 \overline{\kappa}_{Teo}\,\overline{\kappa}_{To}\,\overline{h}\left(\frac{d\overline{h}}{d\overline{x}}\right)^2 d\overline{x} + O(\frac{1}{\Lambda^3}), \tag{5.21}$$

where P is the dimensional power loss having units of energy per time, and is negative if fluid friction opposes the motion of the rotor. The quantity

$$\overline{\mu} = \overline{\mu}(\overline{\rho}, T_{ref}) = \frac{\mu(\rho, T_{ref})}{\mu(\rho_{ref}, T_{ref})} \tag{5.22}$$

is the shear viscosity scaled with the reference value. The evaluation of the scaled viscosity in the first integral on the right hand side of (5.21) can be done by using the second-order expression for density derived by [27] or by expanding $\overline{\mu}(\overline{\rho},\mathrm{T}_{ref})$ in a Taylor series. In [27], the first approach was used in detailed numerical examples. Each approach will give approximations which are consistent with the accuracy of [27]. Here it will be convenient to use the second approach. We first expand $\overline{\mu}$ in a Taylor series for densities near the lowest-order density distribution, i.e., near $\overline{\rho} = 1/\overline{h}$. This expansion reads

$$\overline{\mu} = \overline{\mu}_o + \left.\frac{\partial\overline{\mu}}{\partial\overline{\rho}}\right|_o (\overline{\rho} - \frac{1}{\overline{h}}) + \frac{1}{2}\left.\frac{\partial^2\overline{\mu}}{\partial\overline{\rho}^2}\right|_o \left(\overline{\rho} - \frac{1}{\overline{h}}\right)^2 + O(\frac{1}{\Lambda^3}), \tag{5.23}$$

where, as pointed out above,

$$\overline{\mu}_o \equiv \overline{\mu}(\frac{1}{\overline{h}}, T_{ref}). \tag{5.24}$$

and the derivatives are to be evaluated at $\overline{\rho} = 1/\overline{h}$ and $\mathrm{T} = \mathrm{T}_{ref}$. If we further use the second-order expansion for the density, we have

$$\overline{\rho} = \frac{1}{\overline{h}} + \frac{1}{\Lambda}\rho_1 + \frac{1}{\Lambda^2}\rho_2 + O(\frac{1}{\Lambda^3}), \tag{5.25}$$

where ρ_1 and ρ_2 are O(1) expressions given in [27]. Substitution in (5.23) and the first integral on the right hand side of (5.21) yields

$$\int_0^1 \frac{\overline{\mu}}{\overline{h}}\,d\overline{x} = \int_0^1 \frac{\overline{\mu}_o}{\overline{h}}\,d\overline{x} + \frac{1}{\Lambda^2}\int_0^1 \left[\left.\frac{\partial\overline{\mu}}{\partial\overline{\rho}}\right|_o \rho_2 + \frac{1}{2}\left.\frac{\partial^2\overline{\mu}}{\partial\overline{\rho}^2}\right|_o \rho_1^2\right]\frac{d\overline{x}}{\overline{h}} + O(\frac{1}{\Lambda^3}), \tag{5.26}$$

where the symmetry condition (5.5) has been used to show that the $O(\Lambda^{-1})$ contribution is identically zero.

5.3 Virial Expansion of Pressure and Bulk Modulus

The ideal gas theory is valid at low pressures. In particular, the densities are taken to be small compared to those at the thermodynamic critical point, i.e., when

$$\rho \ll \rho_c, \tag{5.27}$$

where the subscript "c" will always denote quantities evaluated at the thermodynamic critical point. Thus, the expansion of pressure in a power series for small density and constant temperature can be written

$$p = \rho RT \sum_{i=0}^{\infty} B_i(T)\rho^i, \tag{5.28}$$

where the $B_i = B_i(T)$ are referred to as the virial constants and R = the gas constant. In order that $p = p(\rho,T) \longrightarrow \rho RT$ as $\rho \longrightarrow 0$, we require that $B_0 = 1$ so that

$$p = \rho RT[\, 1 + B_1\rho + O(\rho^2)\,]. \tag{5.29}$$

Here B_1 will be referred to as the first virial coefficient. We now define a nondimensional version of this factor as

$$\overline{B} = \overline{B}(\frac{T}{T_c}) \equiv -\rho_c B_1 \tag{5.30}$$

so that

$$p = \rho RT[\, 1 - \overline{B}\,\frac{\rho}{\rho_c} + O\big(\frac{\rho}{\rho_c}\big)^2\,]. \tag{5.31}$$

Here we have chosen to rescale B_1 with a minus sign due to the fact that the first effects of intermolecular forces is to lower the pressure relative to the ideal gas value as the density is increased from zero.

The bulk modulus (5.1) is calculated to be

$$\kappa_T = \rho RT[1 - 2\overline{B}\frac{\rho}{\rho_c} + O\big(\frac{\rho}{\rho_c}\big)^2\,]. \tag{5.32}$$

At the reference density and temperature, the bulk modulus is

$$\kappa_T|_{ref} = \rho_{ref} RT_{ref}[1 - 2\overline{B}_{ref}\Delta + O(\Delta^2)\,] \tag{5.33}$$

where

$$\Delta \equiv \frac{\rho_{ref}}{\rho_c} \ll 1 \tag{5.34}$$

is the small parameter associated with the virial expansion. The quantity

$$\overline{B}_{ref} \equiv \overline{B}\big(\frac{T_{ref}}{T_c}\big). \tag{5.35}$$

To obtain the scaled bulk modulus (5.18) we evaluate (5.32) at T = T_{ref} and take the ratio of (5.32) to (5.33) yielding

$$\overline{\kappa}_T = \overline{\rho}[\, 1 - 2\overline{B}_{ref}\Delta(\overline{\rho} - 1) + O(\Delta^2)\,]. \tag{5.36}$$

The quantity (5.19) seen in our expressions for I_{x1}, I_{x3}, I_{y2} and (5.21) is found to be

$$\overline{\kappa}_{To} = \frac{1}{\overline{h}}(1 + 2\overline{B}_{ref}\Delta) - 2\overline{B}_{ref}\Delta\,\frac{1}{\overline{h}^2} + O(\Delta^2). \tag{5.37}$$

5.4 Virial Expansion of the Shear Viscosity

We now expand the shear viscosity in a virial, i.e., small density, expansion,

$$\mu = \mu(\rho, T) = \sum_{i=0}^{\infty} a_i(T)\rho^i \tag{5.38}$$

$$= a_0(T) + a_1(T)\rho + O(\rho^2). \tag{5.39}$$

In order that $\mu \longrightarrow \mu_{ideal}(T)$ as $\rho \longrightarrow 0$ we require that $a_0 \equiv \mu_{ideal}(T)$ so that (5.39) can be written

$$\mu = \mu_{ideal}[\, 1 + \widehat{a}\,\Delta\,\overline{\rho} + O(\Delta^2)\,] \tag{5.40}$$

where

$$\widehat{a} = \widehat{a}(T) \equiv \frac{a_1(T)\rho_c}{a_0(T)}. \tag{5.41}$$

We refer to a_1 as the first virial coefficient of μ and (5.41) as the scaled first virial coefficient of μ. When the viscosity is evaluated at the reference state, we have

$$\mu_{ref} = \mu_{ideal}(T_{ref})[\, 1 + \widehat{a}_{ref}\,\Delta + O(\Delta^2)\,], \tag{5.42}$$

where $\widehat{a}_{ref} \equiv \widehat{a}(T_{ref})$. For future use, we note that

$$\frac{\mu_{ref} - \mu_{ideal}(T_{ref})}{\mu_{ideal}(T_{ref})} = \widehat{a}_{ref}\,\Delta + O(\Delta^2) \ll 1. \tag{5.43}$$

The scaled viscosity (5.22) is obtained by evaluating (5.40) at T = T_{ref} and dividing the result by (5.42) to obtain

$$\overline{\mu}(\overline{\rho}, T_{ref}) = 1 + \widehat{a}_{ref}\,\Delta\,(\overline{\rho} - 1) + O(\Delta^2). \tag{5.44}$$

The quantity (5.24) appearing in (5.26) is found to be

$$\overline{\mu}_o = \overline{\mu}\big(\frac{1}{\overline{h}}, T_{ref}\big) = (1 - \widehat{a}_{ref}\,\Delta) + \widehat{a}_{ref}\,\Delta\,\frac{1}{\overline{h}} + O(\Delta^2). \tag{5.45}$$

Furthermore, the derivatives of $\overline{\mu}$ can be obtained by differentiating (5.44) to obtain

$$\frac{\partial \overline{\mu}}{\partial \overline{\rho}} = O(\Delta), \tag{5.46}$$

$$\frac{\partial^2 \overline{\mu}}{\partial \overline{\rho}^2} = O(\Delta^2). \tag{5.47}$$

Thus, (5.26) can be written

$$\begin{aligned}\int_0^1 \frac{\overline{\mu}}{\overline{h}}\, d\overline{x} &= \int_0^1 \frac{\overline{\mu}_o}{\overline{h}}\, d\overline{x} + O\big(\frac{\Delta}{\Lambda^2}\big) = \int_0^1 \frac{\overline{\mu}_o}{\overline{h}}\, d\overline{x} + o\big(\frac{1}{\Lambda^2}\big), \\ &= (1 - \widehat{a}_{ref}\,\Delta)\int_0^1 \frac{d\overline{x}}{\overline{h}} + \widehat{a}_{ref}\,\Delta \int_0^1 \frac{d\overline{x}}{\overline{h}^2} + o\big(\frac{1}{\Lambda^2}, \Delta\big),\end{aligned} \tag{5.48}$$

where (5.45) has been used.

5.5 Virial Expansions of Load, Loss and Attitude Angle

We now substitute our virial expansions of the scaled bulk modulus and viscosity in (5.14)-(5.17), (5.21), (5.48) and (5.20). We will retain only terms which are first-order in the small density expansion, i.e., those of order Δ, and only terms which are second-order in the speed number Λ, except in the case of the attitude angle where we drop all terms $o(\Lambda^{-1})$. We therefore will provide the first corrections to the $\Lambda \longrightarrow \infty$ theory of ideal gases. Note that any terms multiplied by Λ^{-2} can be evaluated in the ideal gas state, i.e., at $\Delta = 0$. Thus, the integrals (5.15)-(5.17) become

$$\begin{aligned}-\frac{I_{x1}}{2\pi} = (1 + 2\,\overline{B}_{ref}\,\Delta) &\int_0^{2\pi} \frac{\sin(\theta)}{\overline{h}^2}\frac{d\overline{h}}{d\theta}\, d\theta \\ &- 2\,\overline{B}_{ref}\,\Delta \int_0^{2\pi} \frac{\sin(\theta)}{\overline{h}^3}\frac{d\overline{h}}{d\theta}\, d\theta + O(\Delta^2),\end{aligned} \tag{5.49}$$

$$\begin{aligned}-\frac{I_{x3}}{8\pi^3} = 2\int_0^{2\pi} \frac{1}{\overline{h}}\Big(\frac{d\overline{h}}{d\theta}\Big)^2 \cos(\theta) d\theta &- \int_0^{2\pi} \frac{d^2\overline{h}}{d\theta^2}\cos(\theta)\, d\theta \\ &+ \frac{d^2\overline{h}}{d\theta^2}(0) \int_0^{2\pi} \frac{\cos(\theta)}{\overline{h}}\, d\theta + O(\Delta),\end{aligned} \tag{5.50}$$

$$\begin{aligned}-\frac{I_{y2}}{4\pi^2} = \int_0^{2\pi} \frac{1}{\overline{h}}\frac{d\overline{h}}{d\theta}\sin(\theta)\, d\theta &\\ - (4\overline{B}_{ref} + \widehat{a}_{ref})\Delta \int_0^{2\pi} \big(\frac{1}{\overline{h}^2} - \frac{1}{\overline{h}}\big)\frac{d\overline{h}}{d\theta}&\sin(\theta)\, d\theta + O(\Delta^2).\end{aligned} \tag{5.51}$$

If we now substitute the explicit expression for the film thickness (5.6) in (5.49)-(5.51), we find

$$-\frac{I_{x1}}{4\pi^2} = C_0\left[1+\overline{B}_{ref}\Delta\frac{1+3\delta-\sqrt{1+2\delta}}{1+2\delta}+O(\Delta^2)\right], \tag{5.52}$$

$$-\frac{I_{x3}}{8\pi^4} = \delta - 2C_0(3\delta+2)+O(\Delta), \tag{5.53}$$

$$-\frac{I_{y2}}{8\pi^3} = C_0\sqrt{1+2\delta}\left[1+(4\overline{B}_{ref}+\widehat{a}_{ref})C_1\Delta\right]+O(\Delta^2), \tag{5.54}$$

where the factors

$$C_0 \equiv C_0(\delta) = \frac{1+\delta-\sqrt{1+2\delta}}{\delta\sqrt{1+2\delta}} > 0, \tag{5.55}$$

$$C_1 \equiv C_1(\delta) = 1-\frac{1}{\sqrt{1+2\delta}} > 0. \tag{5.56}$$

Through substitution of (5.52)-(5.54) in (5.14) and straightforward manipulation, we then obtain the virial expansion of the load,

$$\frac{6|\mathbf{F}'|}{p_c R_i b} = 12\pi\, C_0\,\frac{\Delta}{Z_c}\frac{T_{ref}}{T_c}\Bigg[1-\overline{B}_{ref}\Delta C_{\kappa_T} + \frac{2\pi^2}{\Lambda^2}(-2+\sqrt{1+2\delta})(1+\delta)+O(\frac{\Delta}{\Lambda^2},\Delta^2,\frac{1}{\Lambda^3})\Bigg], \tag{5.57}$$

where

$$C_{\kappa_T} \equiv C_{\kappa_T}(\delta) = \frac{1+\delta+\sqrt{1+2\delta}}{1+2\delta} > 0, \tag{5.58}$$

and we have recognized that (5.33) can be rewritten as

$$\frac{\kappa_T|_{ref}}{p_c} = \frac{\Delta}{Z_c}\frac{T_{ref}}{T_c}\big[1-2\Delta\overline{B}_{ref}+O(\Delta^2)\big]. \tag{5.59}$$

Here

$$Z_c \equiv \frac{p_c}{\rho_c R T_c} = \frac{p_c V_c}{R T_c} \tag{5.60}$$

is the critical compressibility.

If we substitute (5.52) and (5.54) in (5.20) we obtain the virial approximation to the attitude angle

$$\varphi = \pi - \frac{2\pi\sqrt{1+2\delta}}{\Lambda}\Bigg[1+\frac{\mu_{ref}-\mu_{ideal}}{\mu_{ideal}}C_1 + \overline{B}_{ref}\Delta\frac{C_1}{2}(C_1+4)\Bigg]+O(\frac{\Delta^2}{\Lambda},\frac{1}{\Lambda^2}), \tag{5.61}$$

where we have used (5.43).

The expression for virial expansion of the power loss is obtained by substituting (5.7), (5.37), and (5.45) in (5.48) and (5.21) yielding

$$-\overline{P} = \frac{1}{\sqrt{1+2\delta}}\left[1 - \frac{\mu_{ref}-\mu_{ideal}}{\mu_{ideal}}\,\frac{\delta}{1+2\delta} + \frac{12\pi^2}{\Lambda^2}\,C_0\delta(1+2\delta)\right] + O(\frac{\Delta}{\Lambda^2},\Delta^2), \tag{5.62}$$

Results (5.57), (5.61), and (5.62) give the dependence of the load, attitude angle, and power loss in terms of the eccentricity (through δ), the specific gas model, the speed number, and the degree of pressurization. In the ideal gas limit, i.e., as $\Delta \longrightarrow 0$, $\mu_{ref} \longrightarrow \mu_{ideal}$, (5.57) and (5.62) become

$$\frac{6|\mathbf{F}'|}{p_c R_i b} \sim 12\pi\, C_0\, \frac{\Delta}{Z_c}\frac{T_{ref}}{T_c}\left[1 + \frac{2\pi^2}{\Lambda^2}(-2+\sqrt{1+2\delta})(1+\delta) + O(\frac{1}{\Lambda^3})\right], \tag{5.63}$$

$$-\overline{P} \sim \frac{1}{\sqrt{1+2\delta}}\left[1 + \frac{12\pi^2}{\Lambda^2}\,C_0\delta(1+2\delta) + O(\frac{1}{\Lambda^3})\right]. \tag{5.64}$$

Because $\overline{B}_{ref} > 0$ and $\mu_{ref} > \mu_{ideal}$, further inspection of (5.57) and (5.62) shows that the load and loss will always be less than that predicted by the ideal gas theory when $\Delta \neq 0$. That is, the ideal gas theory will always overpredict the value of the load and loss, at least in the near-ideal and dense gas regime.

Because the shear viscosity increases with pressurization along isotherms, result (5.62) is consistent with the observations of [27] that $|\overline{P}|$ undergoes a weak decrease as the fluid is pressurized, at least in the near-ideal and dense gas regimes. At this level of approximation, the effect of pressurization on the scaled loss (5.62) is determined by the ratio

$$\frac{\mu_{ref}}{\mu_{ideal}}$$

which [27] have pointed out tends to be nearly independent of temperature, particularly in the near-ideal and dense gas regime. This fact is illustrated in the next section as well. The independence of the scaled loss with temperature is consistent with the more comprehensive computations of [27].

In the ideal gas limit, (5.61) the attitude angle reduces to

$$\varphi \approx \pi - \frac{2\pi\sqrt{1+2\delta}}{\Lambda} + O(\frac{1}{\Lambda^2}). \tag{5.65}$$

A comparison of (5.65) to (5.61) reveals that isothermal pressurizations will increase the deviation of the attitude angle from the ideal gas result.

Once the fluid is chosen, fluid properties such as the critical pressure and temperature and the molecular weight can be obtained from widely available references; in the following examples we will use the data found in [23]. Once the degree of pressurization, i.e., ρ_{ref} and T_{ref}, is chosen, the only remaining material parameters are the scaled virial constant $\overline{B}_{ref}$ and μ_{ref}/μ_{ideal}. These parameters are computed by different approaches depending on the nature of the gas model.

If the equation of state and viscosity is determined by tabular data or is computed by using a digital property bank, the values of ρ_{ref} and T_{ref} are used to compute or interpolate the corresponding p_{ref} and μ_{ref}. The value of $\mu_{ideal}(\mathrm{T}_{ref})$ is estimated by using a sufficiently small value of ρ_{ref}/ρ_c from the tabular data or property bank. It is then a straightforward matter to compute

$$\overline{B}_{ref}\Delta \approx 1 - \frac{p_{ref}}{\rho_{ref} R T_{ref}} \quad \text{and} \quad \frac{\mu_{ref} - \mu_{ideal}(T_{ref})}{\mu_{ideal}(T_{ref})}.$$

If the equation of state and shear viscosity are modeled by explicit known formulas, the same approach as for the case of tabular data could be used. That is, we could simply compute p_{ref}, μ_{ref}, $\mu_{ideal}(\mathrm{T}_{ref})$ from ρ_{ref}, T_{ref}. Alternatively, formulas for the required parameters can be computed by expanding these explicit functions for small values of ρ/ρ_c. It is this latter approach that we will employ for the numerical calculations in the next section.

5.6 Numerical Results

For the purpose of illustration, we take the Redlich-Kwong-Soave (RKS) equation of state described in [23] and the viscosity model of Chung et al. [28, 29] as our exact gas models (EGM). The fluid is chosen to be carbon dioxide (CO_2) and the physical parameters of CO_2 were taken from Reid et al. [23].

If we expand the pressure for small density and constant temperature, we then obtain the scaled first virial coefficient for the pressure (5.30) corresponding to the RKS equation of state. The details are straightforward. In order to conserve journal space, we record only the final result here. The value of $\overline{B}$ was found to be

$$\overline{B}(T_r) = \frac{1}{Z_c}\big[k\frac{\alpha(T_r)}{T_r} - b_0\big]. \tag{5.66}$$

Internally consistent values of the nondimensional constants seen in (5.66) were found to be $\mathrm{k} = 0.427480$, $\mathrm{b}_0 = 0.08664$, $\mathrm{Z}_c = 1/3$. The reduced temperature $\mathrm{T}_r \equiv T/T_c$ and

$$\alpha(T_r) \equiv \Big[1 + (0.48 + 1.574\omega_{ac} - 0.176\omega_{ac}^2)(1 - \sqrt{T_r})\Big]^2, \tag{5.67}$$

is a dimensionless function of T_r and the acentric factor $\omega_{ac} =$ constant.

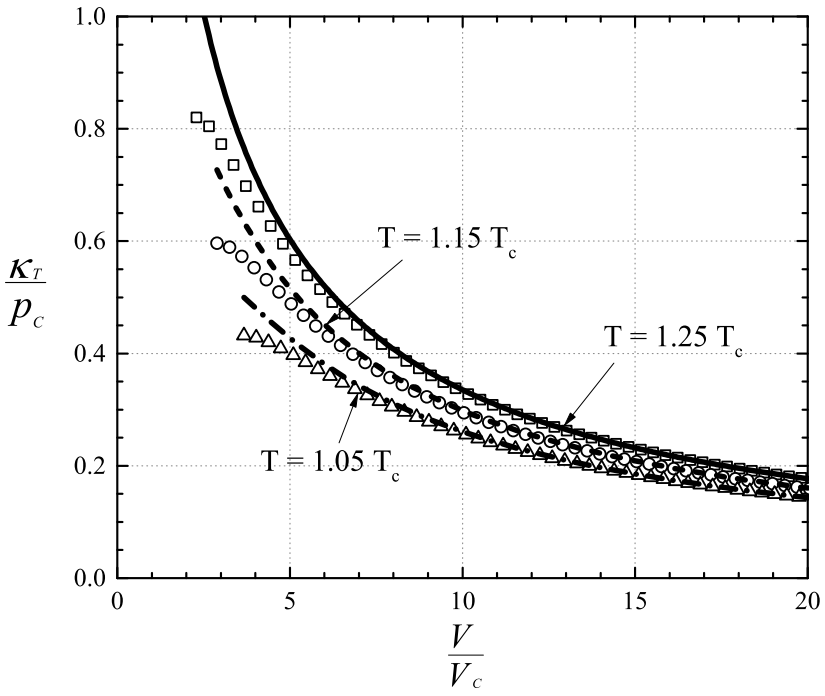

Figure 5.4: Scaled Bulk Modulus vs V/V$_c$ at T = 1.25 T$_c$, 1.15 T$_c$ and 1.05 T$_c$. The lines represent the exact bulk modulus obtained from the exact gas model (EGM) and (5.1). The symbols denote the virial expansion of the bulk modulus computed using (5.68) and (5.66).

We have plotted the scaled version of virial expansion of κ_T

$$\frac{\kappa_T}{p_c} = \frac{1}{Z_c}\frac{\rho}{\rho_c}\frac{T}{T_c}\big[1 - 2\overline{B}(\frac{T}{T_c})\frac{\rho}{\rho_c} + O\big(\frac{\rho}{\rho_c}\big)^2\big] \tag{5.68}$$

combined with (5.66) along with its exact value calculated using the EGM and (5.1) in Figure 5.4 at temperatures equal to 1.25 T$_c$, 1.15 T$_c$ and 1.05 T$_c$. The lines represent the exact κ_T; the symbols denote the virial expansion of κ_T (5.68). As V $\longrightarrow$ 0, $2\overline{B}\rho/\rho_c$ becomes O(1) such that the virial expansion is no longer valid. As a result, we will only consider the cases where $2\overline{B}\rho/\rho_c \leq 0.5$ in all that follows. Examination of Figure 5.4 reveals that the agreement is very good over most of the dense gas regime. The difference between the exact κ_T and the virial expansion of κ_T are found to be less than 5% for each temperature and V $\geq$ 5 V$_c$.

In like manner, a small density approximation is carried out for the viscosity model of Chung et al. [28, 29]. The details of this expansion are straightforward. We again only record the final result. The scaled virial coefficient for the viscosity (5.43) was found to be

$$\widehat{a} = \frac{1}{6}\left[E_6 - \frac{2E_2E_5 + 5(E_2+E_3) - E_1E_4^2}{2(E_1E_4 + E_2 + E_3)}\right], \tag{5.69}$$

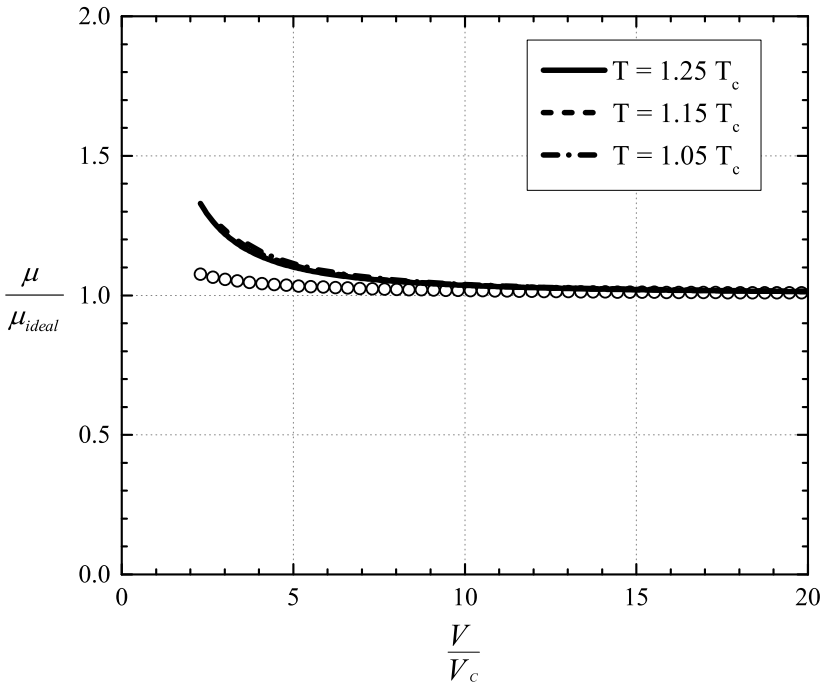

Figure 5.5: Scaled Shear Viscosity vs V/V_c at Temperatures = 1.25 T_c, 1.15 T_c and 1.05 T_c. The lines denotes the exact viscosity resulted from the viscosity model of Chung et al. [28, 29]. The symbol ◯ denote the virial expansion of viscosity computed using (5.69) and (5.70).

where the quantities E_i, i = 1 to 5, are given in [28], [29], or [23] as functions of the acentric factor, dipole moment, and association factor of the fluid in question. Thus, $\widehat{a}$ is independent of the temperature for the Chung et al. model [28]-[29].

The local form of the shear viscosity can be obtained from (5.40). The result is found to be

$$\frac{\mu(\rho,T)}{\mu_{ideal}(T)} = 1 + \widehat{a}(T)\frac{\rho}{\rho_c} + O\big(\frac{\rho}{\rho_c}\big)^2. \tag{5.70}$$

In all that follows, we take $\widehat{a}$(T) to be given by (5.69) so that $\widehat{a}$ is a constant. We have plotted this approximation to the viscosity along with that generated by the exact Chung et al. [28, 29] model for temperatures of 1.25 T_c, 1.15 T_c and 1.05 T_c in Figure 5.5. Examination of Figure 5.5 shows good agreement between the exact and the virial expansion of μ for $V \geq 5V_c$. The difference is found to be approximately 6.8% at $V = 5V_c$. Because $\widehat{a}$ = constant for the Chung et al. model, the curve corresponding to the virial expansion is the same for every isotherm. The exact solution for μ/μ_{ideal} is also seen to have only a weak variation with temperature for the temperatures and densities in Figure 5.5.

We now compare the load, loss, and attitude angle predicted by our virial approximations to the more general integral formulas (5.14)-(5.17), (5.20)-(5.21) derived by [27]. We also

Acronym	Reference	Description
REGM	[24], [25]	Numerical solution to the Reynolds equation with exact gas model.
LLEGM	(5.14)-(5.17), (5.20), (5.21)	Large Λ approximation to Reynolds equation with exact gas model.
LLV	(5.57), (5.61), (5.62)	Virial expansion applied to LLEGM
LLIG	(5.63)-(5.65)	Ideal gas approximation applied to LLEGM or LLV

Table 5.1: Acronyms and Approximations

compare the virial approximations of the load, loss, and attitude angle to those obtained with the simplification of the ideal gas theory. For context, we also compare the results based on each of these approximations to those based on numerical solutions to the exact Reynolds equation (5.8). For the convenience of the reader, we have summarized these approximations in Table 5.1.

We regard the exact solutions to be the numerical integrations of the Reynolds equation derived and validated in [24] and [25] and used by [26]-[27]. The RKS gas model and Chung, et al [28, 29] viscosity models will be employed in the integration of the Reynolds equation. A shooting method is used to solve the resultant two-point boundary value problem. The procedure for the calculation of the load and loss from the numerical solutions to the Reynolds equation is described in [27]. Checks on the tolerance for the shooting method and the resolution in the streamwise direction were carried out to ensure that the results displayed here are independent of the tolerance and number of points in $\overline{x}$. Further details regarding the solution to the exact Reynolds equation can be found in [24], [25], and [27]. We will refer to this case using the acronym REGM.

The next level of accuracy is associated with the large Λ theory of [27]. The load, loss, and attitude angle are given by (5.14)-(5.17), (5.20)-(5.21). The integrals are evaluated using Simpson's rule. Checks on the number of points have been done to ensure that any results presented here are independent of the discretization. The material functions in (5.14)-(5.17), (5.20)-(5.21) were evaluated using the RKS equation of state and the full Chung et al. [28, 29] models. This large Λ (LL) approximation using the exact gas model (EGM) will be referred to by using the acronym LLEGM.

The third set of results is based on the virial approximation scheme developed here, i.e., on results (5.57), (5.61), and (5.62) with $\overline{B}_{ref}$, $\mu_{ref}/\mu_{ideal}(\mathrm{T}_{ref})$ estimated by (5.66)-(5.67) and

(5.43) combined with (5.69). In the following, we refer to this case as the virial expansion applied to LLEGM, i.e., LLV.

Finally, we compare each of these results to those obtained in the ideal gas theory. The formulas corresponding to the ideal gas theory are given by (5.63)-(5.65). We refer to this case as ideal gas approximation applied to LLEGM or LLV and will denote this case by LLIG.

The accuracy of the virial expansions developed here will be seen by comparing the LLV results to the integral formulas on which LLEGM theory is based; that is, it provides a measure of the accuracy of the approximation of the material functions in the context of the load, loss and attitude angle. The inclusion of the results of the exact Reynolds equation, i.e., REGM, will give a measure of the total error due to the large Λ approximation and the virial approximation. The comparison of each of these theories to the ideal gas theory will give an indication of the error in the ideal gas theory at higher pressures in the context of load, loss, and attitude angle.

In these examples, we consider the unwrapped journal bearing sketched in Figure 5.3. The ratio $h_0/L = 1.989 \times 10^{-5}$ and the speed number is taken to be $\Lambda = 50$. Unless stated otherwise, $\delta = 0.5$. Throughout this study we take the reference thermodynamic state to be that at x = 0 and L.

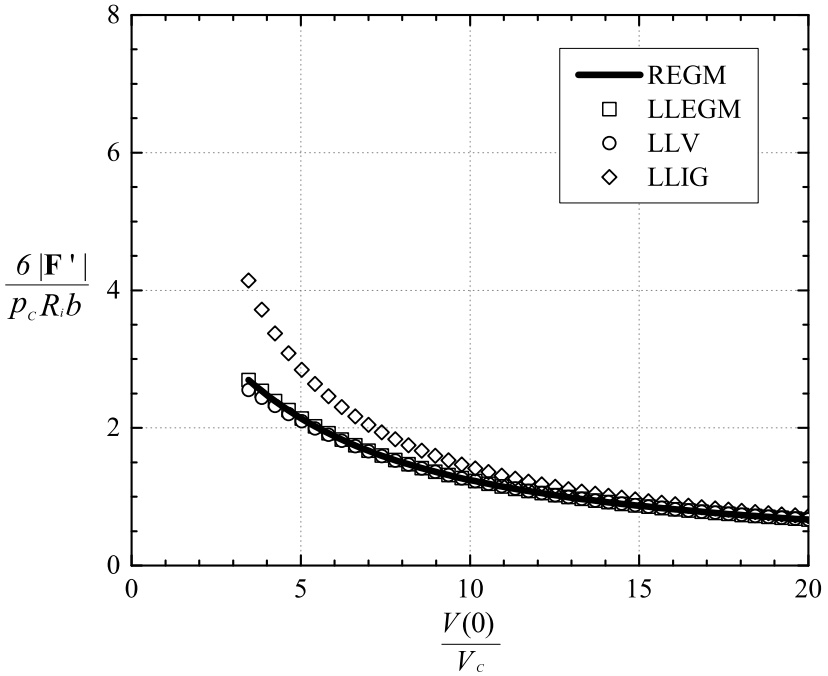

Figure 5.6: Scaled Load vs Reference Specific Volume V/V_c at $T_{ref} = 1.05\ T_c$. The speed number $\Lambda = 50$ and the parameter $\delta = 0.5$.

The variation of the scaled load at $T_{ref} = 1.05\ T_c$ and $1.25\ T_c$ with the reference specific

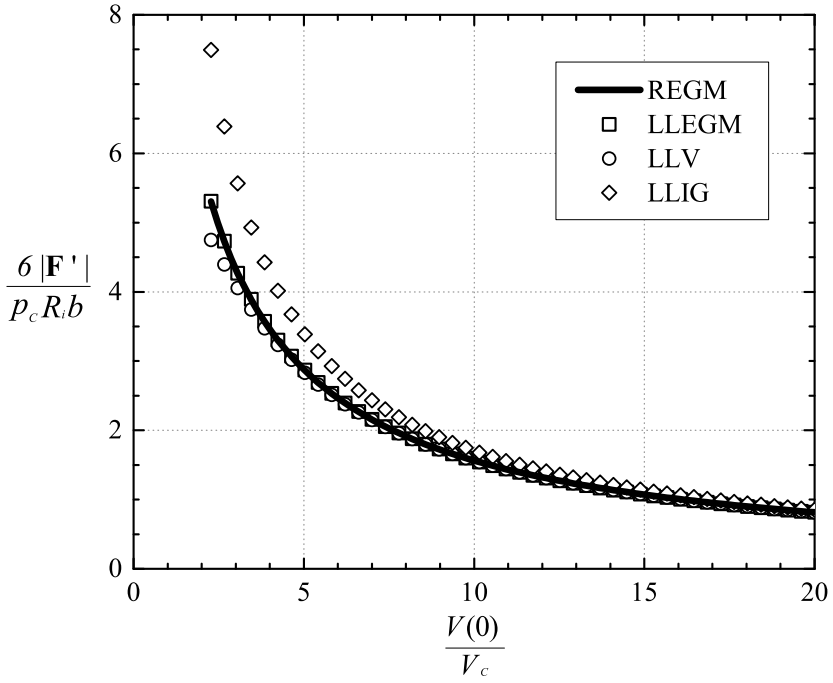

Figure 5.7: Scaled Load vs Reference Specific Volume V/V_c at $T_{ref} = 1.25\ T_c$. The speed number $\Lambda = 50$ and the parameter $\delta = 0.5$.

volume is plotted in Figures 5.6 and 5.7, respectively. In all that follows, we only present results for reference thermodynamic states having $2\overline{B}\Delta \leq 0.5$. Inspection of Figures 5.6 and 5.7 reveals that the LLV model is in excellent agreement with the LLEGM and REGM models for all the given reference thermodynamic states. As indicated in Section 5.5, the use of the ideal gas model will result in an overestimation of the load when the gas is pressurized. A comparison of Figures 5.6 and 5.7 shows that the error in the ideal gas model is larger when $T_{ref} = 1.05\ T_c$ than when $T_{ref} = 1.25\ T_c$ for fixed V_{ref}. This can be explained by the fact that the first correction term in (5.57), i.e., $\overline{B}_{ref}\Delta$, decreases as the reference temperature increases. The maximum difference between the LLV and LLIG model for the case of $T_{ref} = 1.05\ T_c$ and $1.25\ T_c$ occurs at $V_{ref} = 3.45\ V_c$ and $2.27\ V_c$, respectively, and its value is found to be 53.7% and 41.2%, respectively.

Observation of Figures 5.6 and 5.7 also indicates that the scaled load increases with the pressurization and the increase of the reference temperature. This is due to the fact that the load is dominated by the variation of the bulk modulus for fixed δ and Λ. These results are consistent with the findings of [27].

Because it was shown that the effects of the temperature on the scaled loss are insignificant [27], we have only plotted the variation of the scaled loss corresponding to the case of $T_{ref} =$

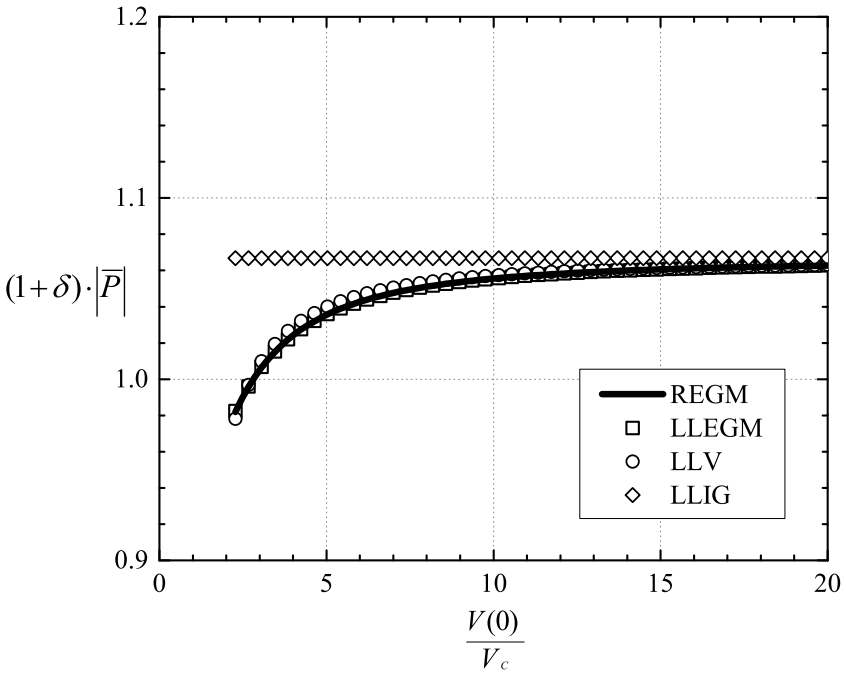

Figure 5.8: Scaled Loss vs Reference Specific Volume V(0)/V$_c$ at T$_{ref}$ = 1.25 T$_c$. The speed number $\Lambda = 50$ and the parameter $\delta = 0.5$.

1.25 T$_c$; our results are recorded in Figure 5.8. We have multiplied the scaled loss by $(1+\delta)$ in concert with the conventional practice in which the film thickness is scaled with the radial clearance. Examination of Figure 5.8 reveals that the agreement between the LLV model and the REGM and LLEGM models is seen to be excellent even at V$_{ref}$ = 2.27 V$_c$ where the fluids can be considered to be dense gases or slightly supercritical fluids. As discussed in [27], the monotone increase of the viscosity with increasing pressure or decreasing specific volume leads to the decrease of the scaled loss for fixed δ and Λ. As is clear from (5.64), the scaled loss predicted by the LLIG model remains constant with isothermal pressurization. This is due to the fact that the ideal gas viscosity is a function of the reference temperature only. Again, the LLIG model overestimates the scaled loss in the pressurized gas regimes. The maximum differences between the LLV and LLIG models are found to be 8% for the cases considered in Figure 5.8.

We note further that the loss is scaled with the zero-load loss, i.e., when $\delta = 0$. Inspection of Figure 5.8 shows that the scaled loss of ideal gases will always be larger than 1. On the other hand, because of the density dependence of the shear viscosity, the scaled loss can become ≤ 1 at higher pressures. This result is consistent with [27], but can be easily revealed by our result (5.62), at least where the virial expansion is valid.

The variation of the scaled version of the attitude angle at T$_{ref}$ = 1.25 T$_c$ is plotted as a function of the reference specific volume in Figure 5.9. Here we use the associated attitude

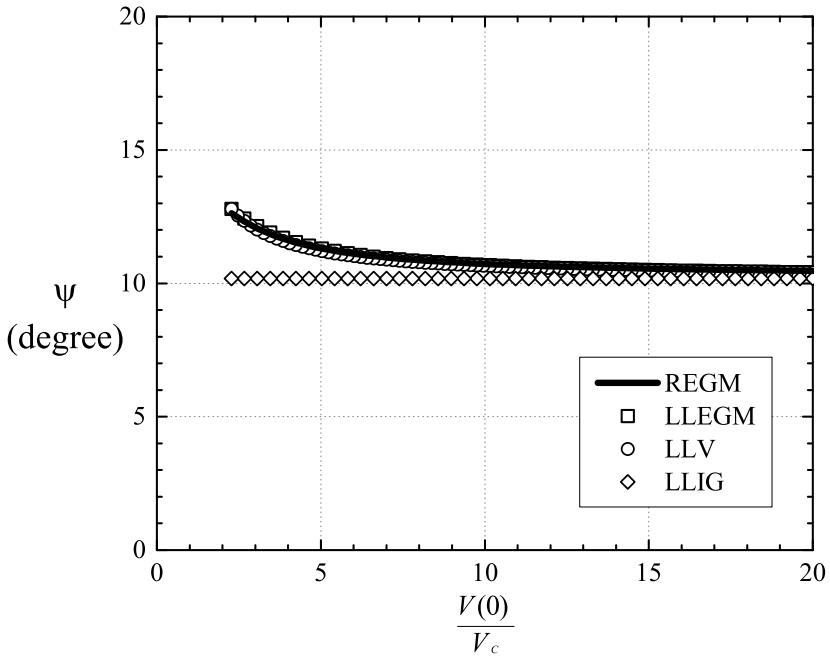

Figure 5.9: Scaled Attitude Angle vs Reference Specific Volume V(0)/V_c at T_{ref} = 1.25 T_c. The speed number $\Lambda = 50$ and the parameter $\delta = 0.5$.

angle $\psi \equiv \pi - \varphi$, i.e., the angle between the direction of the total force $\mathbf{F}'$ and the negative x′ axis seen in Figure 5.2. The agreement between the LLV, LLEGM and REGM models is seen to be excellent. The attitude angle ψ resulting from the LLV, LLEGM and REGM models increases as the reference density rises. Inspection of (5.65) reveals that ψ is dependent only on δ and Λ for ideal gases. Thus, the scaled attitude angle corresponding to the LLIG model remains constant and its value is smaller than that predicted by the LLV, LLEGM and REGM models at higher pressures. The maximum discrepancy between the LLV and LLIG models is found to be 25.6% for the reference states considered in Figure 5.9.

We also have plotted the variation of the scaled load as a function of δ for $V_{ref} = 5V_c$, 10 V_c and 15 V_c at T_{ref} = 1.05 T_c in Figure 5.10. Results obtained from the LLV, LLEGM and REGM models are found to be in excellent agreement. Inspection of Figures 5.10 reveals that the differences between the LLV and LLIG models increase with the increase of δ and reference pressure. The maximum differences between the LLV and the LLIG models at V_{ref} = $5V_c$, $10V_c$ and $15V_c$ are found to be 23.1%, 12.1% and 7.4%, respectively and occur at δ = 1.

The variation of the scaled loss is plotted against δ at T_{ref} = 1.05 T_c for V_{ref} = 10 V_c and 5 V_c in Figures 5.11 and 5.12, respectively. Examination of Figure 5.11 and 5.12 indicates that the LLV model is in very good agreement with the LLEGM and REGM models for a range of δ in both cases. The effects of the first virial correction term become more significant as δ increases for fixed pressure. The maximum discrepancy between the LLV and LLIG

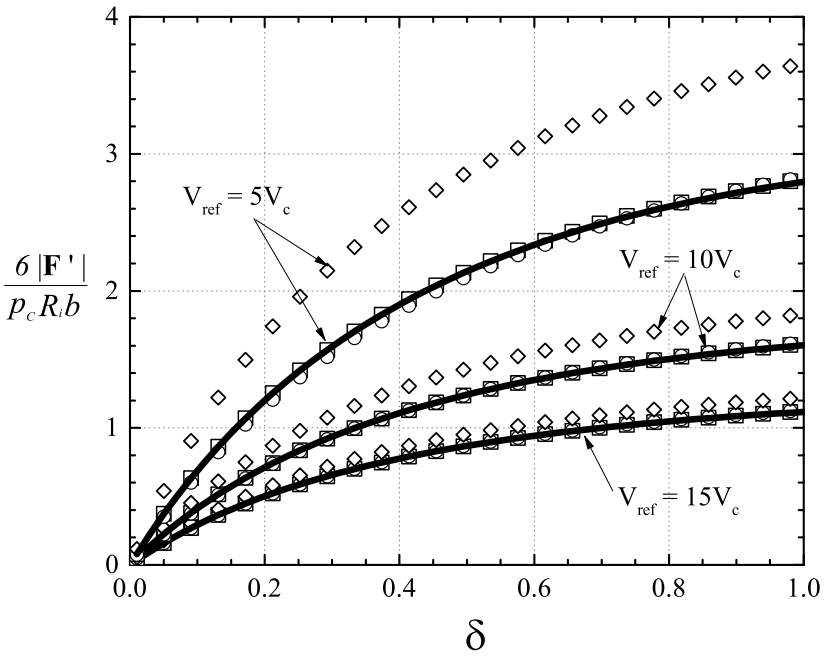

Figure 5.10: Scaled Load vs δ at V_{ref} = 5 V_c, 10 V_c and 15 V_c for T_{ref} = 1.05 T_c. The speed number $\Lambda = 50$. The solid lines represent the scaled load obtained from the REGM model; the symbols □, ◯ and ◇ denote the scaled load computed by the LLEGM, LLV and LLIG approximations, respectively.

models for the case of V_{ref} = 10 V_c and 5 V_c are found to be approximately 1% and 3%, respectively. The effects of the first virial correction on the scaled loss (5.62) seems to be smaller than that on the scaled load (5.57). This is due to the fact the variation of κ_T with the density is stronger than that of μ, as shown in Figures 5.4 and 5.5.

Inspection of 5.12 also shows that the scaled loss has a local minimum at $\delta = 0.103$ for the $V_{ref} = 5V_c$ case. In general, it is easily shown that a local minimum of $(1 + \delta)\ |\overline{P}|$ occurs when

$$\frac{\mu_{ref}}{\mu_{ideal}} - 1 = \frac{\delta(1+2\delta)}{1+\delta+\delta^2}, \tag{5.71}$$

if we consider only the lowest-order approximation in Λ, i.e, $\Lambda = \infty$, for the loss (5.62). From (5.71), it is easily shown that the minimum scaled loss of ideal gases will always be at $\delta = 0$. For pressurized gases, the location of the minimum scaled loss will depend on the ratio of μ_{ref} to μ_{ideal}. It can be shown that

$$\frac{\delta(1+2\delta)}{1+\delta+\delta^2}$$

increases monotonically from 0 to 2 as $\delta \longrightarrow \infty$. Thus, if μ_{ref}/μ_{ideal} is a constant and $\Lambda \gg 1$, a local minimum in the scaled loss, i.e., $(1 + \delta)\ |\overline{P}|$, occurs iff

$$\mu_{ref} \leq 3\, \mu_{ideal}.$$

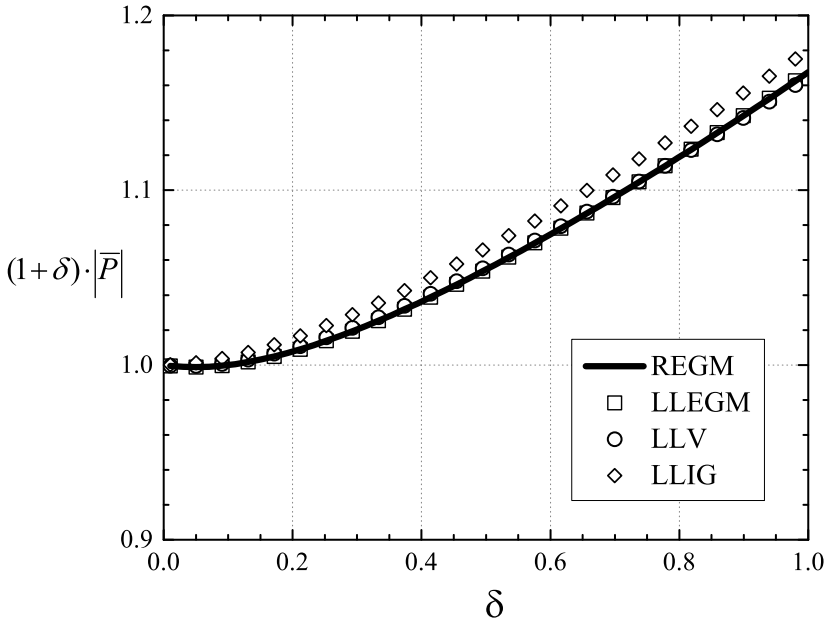

Figure 5.11: Scaled Loss vs δ at $V_{ref} = 10V_c$ and $T_{ref} = 1.05\ T_c$. The speed number $\Lambda = 50$.

We have also plotted the variation of the scaled attitude angle as a function of δ at $V_{ref} = 5\ V_c$ and $T_{ref} = 1.05\ T_c$ in Figure 5.13. Observation of Figure 5.13 reveals the good agreement between the LLV, LLEGM and REGM models, and the predicted attitude angle ψ increases as δ increases. The maximum difference between the LLV and REGM models is found to be 6.4% and occurs at $\delta = 1.0$. As is clear from (5.61), the LLIG model, on the other hand, results in underestimation of the scaled attitude angle and deviates from the LLV model by 23.1% at $\delta = 1.0$. In addition, we note that both $F_{x'}$ and $F_{y'} \longrightarrow 0$ at the same rate as δ goes to 0; this result is consistent with the findings of [30] for ideal gases.

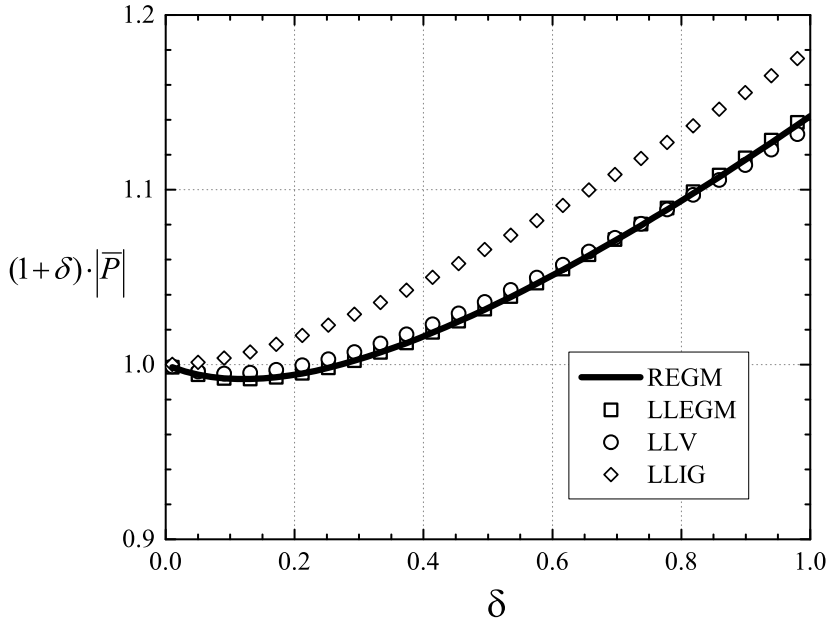

Figure 5.12: Scaled Loss vs δ at $V_{ref} = 5\ V_c$ and $T_{ref} = 1.05\ T_c$. The speed number $\Lambda = 50$.

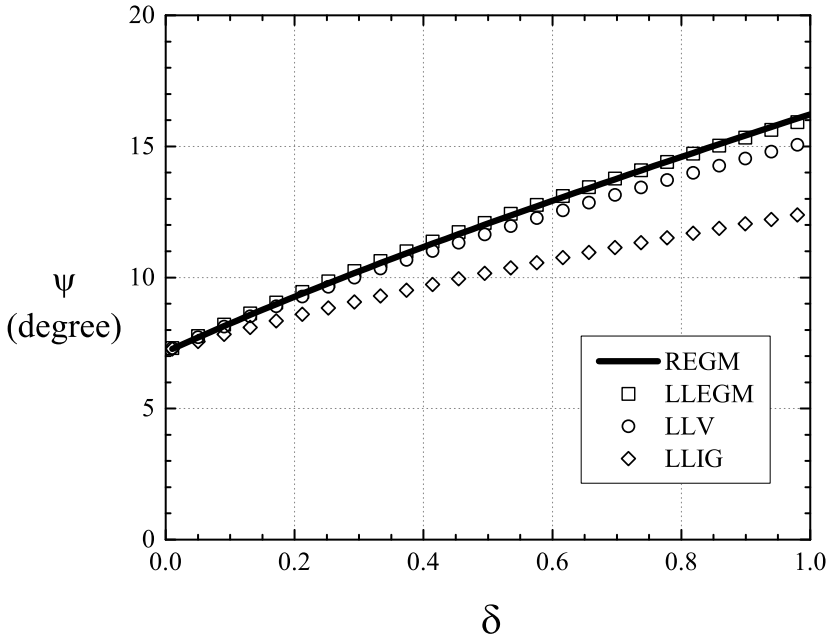

Figure 5.13: Scaled Attitude Angle ψ vs δ at $T_{ref} = 1.05\ T_c$ and $V_{ref} = 5\ V_c$. The speed number $\Lambda = 50$.

5.7 Summary

The main goal of the present study has been to provide simple explicit formulas for the load, power loss and attitude angle for moderately pressurized gases. We have applied a virial expansion, i.e., a $\rho/\rho_c \ll 1$ approximation, to the large speed number approximations developed in [27]. The general results for the load, attitude angle, and loss are given by (5.57), (5.61), and (5.62). The numerical results of Section 5.6 suggests that our virial expansions yield excellent agreement with both exact solutions to the Reynolds equation and the large Λ approximations of [27] well into the dense gas and supercritical fluid regime. For example, for CO_2 at a reference specific volume of 5 V_c and a reference temperature of 1.05 $T_c \approx 43.2$ °C, the RKS equation of state predicts a reference pressure of 0.55 $p_c \approx 40.5$ bar. Inspection of Figures 5.6 and 5.10-5.13 reveals that our approximations are quite good even at these elevated reference pressures. The results based on our simple virial expansions are also seen to be a significant improvement over those of the ideal gas theory.

Once the virial coefficients (5.30) and (5.41) are determined from experiment, tabulated data, or analytical gas models, the formulas presented here can be used to gain intuition regarding the effects of pressurization, to carry out engineering estimates, and reduce computation time in large-scale numerical studies involving moderate pressures. The approach taken here was to replace complex material functions, i.e., complex equations of state and viscosity models, with a simple approximation. Thus, virial expansions such as that employed here should be equally effective for unsteady, fully three-dimensional, and turbulent lubrication flows at moderate pressures.

Bibliography

[1] O. Reynolds. On the theory of lubrication and its application to Mr. Beauchamp Tower's experiments, including an experimental determination of the viscosity of olive oil. *Proceedings of the Royal Society of London*, 40(242-245), 191–203, 1886.

[2] O. Pinkus and B. Sternlicht. *Theory of Hydrodynamic Lubrication.* McGraw-Hill, 1961.

[3] W. A. Gross, L. A. Matsch, V. Castelli, A. Eshel, J. H. Vohr, and M. Wildmann. *Fluid Film Lubrication.* John Wiley and Sons, Inc., 1980.

[4] A. Z. Szeri. *Fluid Film Lubrication.* Cambridge University Press, 2010.

[5] B. J. Hamrock, S. R. Schmidt, and B. O. Jacobson. *Fundamentals of Fluid Film Lubrication.* CRC press, 2004.

[6] P. Johansen, D. B. Roemer, T. O. Andersen, H. C. Pedersen. On the application of Reynolds theory to thermo-piezo-viscous lubrication in oil hydraulics, In *Fluid Power and Mechatronics, 2015 IEEE International Conference. Harbin, China*, 58–62, 2015. .

[7] D. Gropper, L. Wang, T. J. Harvey. Hydrodynamic lubrication of textured surfaces: A review of modeling techniques and key findings. *Tribology International*, 94, 509–529, 2016.

[8] F. Dupuy, B. Bou-Saïd, J. Tichy. High-speed subsonic compressible lubrication. *Journal of Tribology*, 137(4), 041702, 2015.

[9] F. Dupuy, B. Bou-Saïd, M. Garcia, G. Grau, J. Rocchi, M. Crespo, J. Tichy. Tribological study of a slider bearing in the supersonic regime. *Journal of Tribology*, 138(4), 041702, 2016.

[10] Q. Chao, J. Zhang, B. Xu, Q. Wang. Discussion on the Reynolds equation for the slipper bearing modeling in axial piston pumps. *Tribology International*, 118, 140–147 2018.

[11] V. Dostal, M. J. Driscoll, and P. Hejzlar. A supercritical carbon dioxide cycle for next generation nuclear reactors. Technical report, MIT-ANP-TR-100, 2004.

[12] C. DellaCorte, K. C. Radil, R. J. Bruckner, and S. A. Howard. Design, fabrication, and performance of open source generation I and II compliant hydrodynamic gas foil bearings. *Tribology Transactions*, 51(3), 254–264, 2008.

[13] S. A. Wright, R. F. Radel, M. E. Vernon, G. E. Robert, and P. S. Pickard. Operation and analysis of a supercritical CO_2 Brayton cycle. *Sandia Report, No. SAND2010-0171*, 2010.

[14] T. M. Conboy, S. A. Wright, J. Pasch, D. Fleming, G. Rochau, and R. Fuller. Performance characteristics of an operating supercritical CO_2 Brayton cycle. *Journal of Engineering for Gas Turbines and Power*, 134(11), 111703, 2012.

[15] F. Crespi, G. Gavagnin, D. Sánchez, and G. S. Martínez. Supercritical carbon dioxide cycles for power generation: A review. *Applied Energy*, 195, 152–183, 2017.

[16] Z. C. Peng and M. M. Khonsari. On the limiting load-carrying capacity of foil bearings. *Journal of Tribology*, 126(4), 817–818, 2004.

[17] T. M. Conboy. Real-gas effects in foil thrust bearings operating in the turbulent regime. *Journal of Tribology*, 135(3), 031703, 2013.

[18] D. Kim. Design space of foil bearings for closed-loop supercritical CO_2 power cycles based on three-dimensional thermohydrodynamic analyses. *Journal of Engineering for Gas Turbines and Power*, 138(3), 032504, 2016.

[19] K. Qin. *Development and application of multiphysics simulation tools for foil thrust bearings operating with carbon dioxide.* PhD thesis, University of Queensland, 2017.

[20] E. Guenat and J. Schiffmann. Real-gas effects on aerodynamic bearings. *Tribology International*, 120, 358–368, 2018.

[21] E. W. Lemmon, M. L. Huber, and M. O. McLinden. NIST Reference fluid thermodynamic and transport properties–REFPROP. *NIST Standard Reference Database*, 23, v7, 2002.

[22] I. H. Bell, J. Wronski, S. Quoilin, and V. Lemort. Pure and pseudo-pure fluid thermophysical property evaluation and the open-source thermophysical property library CoolProp. *Industrial & Engineering Chemistry Research*, 53(6), 2498–2508, 2014.

[23] R. C. Reid, J. M. Prausnitz, B. E. Poling. *The Properties of Gases and Liquids.* McGraw-Hill, 1987.

[24] S. Y. Chien, M. S. Cramer, and A. Untaroiu. Compressible Reynolds equation for high-pressure gases. *Physics of Fluids*, 29(11), 116101, 2017.

[25] S. Y. Chien, M. Cramer, A. Untaroiu. A compressible thermohydrodynamic analysis of journal bearings lubricated with supercritical CO_2. In *ASME 2017 Fluids Engineering Division Summer Meeting. Waikoloa, HI*, paper No. FEDSM2017-69310, 2017.

[26] S. Y. Chien and M. S. Cramer. Pressure, temperature, and heat flux in high speed lubrication flows of pressurized gases. *Tribology International*, 129, 468–475, 2019.

[27] S. Y. Chien and M. S. Cramer. Load and loss for high speed lubrication flows of pressurized gases between non-concentric cylinders. *Journal of Fluid Mechanics*, 867, 1–25, 2019.

[28] T. H. Chung, L. L. Lee, K. E. Starling. Applications of kinetic gas theories and multiparameter correlation for prediction of dilute gas viscosity and thermal conductivity. *Industrial & Engineering Chemistry Fundamentals*, 23(1), 8–13, 1984.

[29] T. H. Chung, M. Ajlan, L. L. Lee, K. E. Starling. Generalized multiparameter correlation for nonpolar and polar fluid transport properties. *Industrial & Engineering Chemistry Research*, 27(4), 671–679, 1988.

[30] W. Gross, E. Zachmanoglou. Perturbation solutions for gas-lubricating films. *Journal of Basic Engineering*, 83(2), 139–144, 1961.

Chapter 6

Compressible Lubrication Flows in Thrust Bearings

The work presented in this chapter is part of an ongoing project. The contents of this chapter have not been published yet.

Attribution

The work presented in this chapter was primarily carried out by S. Y. Chien. M. S. Cramer conceived of the main idea and contributed to the development and implementation of this work.

Abstract

We present a detailed derivation of the Reynolds equation and its corresponding energy equation for three-dimensional, steady, laminar, compressible flows of single-phase Navier-Stokes fluids in thrust bearings. These equations are shown to be valid over most of the dense and supercritical gas regime except for the vicinity of the thermodynamic critical point. Numerical solutions to our Reynolds equation are obtained using a finite difference scheme for both moderate and high-speed flows.

We also develop approximate solutions to our Reynolds equation for high-speed flows through a perturbation analysis. It is found that boundary layers form on three out of four edges of the thrust pad. At the inner and outer radii of the pad, the flow is governed by a nonlinear heat equation. As the main flow leaves the pad, the flow is governed by a nonlinear relaxation equation. Two more boundary layers are required in the corners of the computational

domain in order to ensure that the end boundary layer and the boundary layers at the inner and outer radii are consistent. Last, we construct a composite solution which provides a single approximation and has the same accuracy as the individual approximations in their respective regions of validity.

6.1 Introduction

The science of thin viscous films has been developed for a wide variety of applications including the lubrication of mechanical components, the spreading of droplets, or coating processes, particle-particle interaction, and biomechanics. It is well-known that the flow dynamics in such films are governed by the Reynolds equation which, in its simplest form, is written as

$$\frac{d}{dx}\left(h^3\frac{dp}{dx}\right) = 6\mu U\frac{dh}{dx}, \tag{6.1}$$

where x is the spatial variable in the main flow direction, h = h(x) is the film thickness, p = p(x) is the fluid pressure, $\mu > 0$ is the constant shear viscosity, and U is a measure of fluid velocity in the main flow direction. Since first introduced by Osborne Reynolds [1], this equation (6.1) has formed the foundation of lubrication theory. To date many scientists and engineers have extended (6.1) to include the effects of three-dimensionality, non-newtonian fluids, unsteadiness, turbulence, phase changes and more complex configurations.

The key restrictions involved with the derivation and generalization of (6.1) are

$$\frac{h_o}{L} \ll 1, \text{ and } Re\frac{h_o^2}{L^2} \ll 1, \tag{6.2}$$

where h_o is a measure of the thickness of the fluid layer, L is a measure of length scale in the main flow direction, and Re is the Reynolds number based on U and L. The first of (6.2) requires that the fluid layer be thin compared to the length scales associated with the variations in the main flow direction. The second of (6.2) ensures that the inertia is negligible such that the shear forces balance the pressure forces.

Interest in replacing liquids with gases as lubricating fluids has been increasing with the development of advanced power systems and turbomachinery; see.e.g., [2, 3, 4, 5, 6]. The advantages of gases over liquids include the obvious weight reduction for aeronautical and space applications, the reduction of fouling due to oil leaks, and the elimination of complications due to cavitation. The shear viscosity of gases is known to be smaller than that of liquids; as a result, gas lubrication can reduce the friction losses of rotating machines. However, in order to generate the pressure required to support a given load, the speed must be higher than that in viscous liquids. Gas lubrication therefore tends to be compressible.

When ideal, i.e., low pressure, gases are of interest, the perfect gas model is used to modify the Reynolds equation (6.1) to account for the compressibility of the gas film. This approach

is found in many studies [7, 8, 9, 10, 11, 3]. Recently research has focused on lubrication with pressurized gases, i.e., gases corresponding to pressures and temperatures on the order of that of the thermodynamic critical point. These studies include those of Conboy [12], Kim [13], Dousti and Allaire [14], Qin [15], Heshmat [16], and Guenat and Schiffmann [17] who employed pure numerical schemes to solve different versions of modified Reynolds equation. Most of these studies evaluated the thermodynamic properties of pressurized gases using digital table look-ups. Examples include the NIST REFPROP database [18] used by Conboy [12], Kim [13] and Qin [15], and the CoolProp database [19] used by Guenat and Schiffmann[17]. The numerical results of Dousti and Allaire [14] used a gas model based on a linear pressure-density relation, but this model may not be valid over the full range of thermodynamic states corresponding to the dense and supercritical regime [16].

The transport and thermodynamic properties of pressurized gases, particularly supercritical fluids, are known to have a rapid and sometimes singular dependence on density and temperature. Chien et al. [20] have performed a careful analysis to examine the approximations leading to the Reynolds equation for compressible lubrication flows in pressurized gases. They have derived a general form of the Reynolds equation and corresponding temperature equation and delineated their region of validity. Besides the usual lubrication approximations, i.e., (6.2), and mild conditions on the imposed temperature difference between isothermal walls, their analysis revealed that the validity of the Reynolds equation further requires the thermodynamic states to be sufficiently far from the thermodynamic critical point. Chien et al. [20] also showed that energy convection is negligible whenever the Reynolds equation is valid.

Chien and Cramer [21, 22, 23] have derived the approximate solutions to the Reynolds and corresponding temperature equations of [20] for high-speed high-pressure lubrication flows between non-concentric cylinders. Their results provide the explicit formulas for the local values of the pressure, temperature and heat flux in terms of material functions, e.g., the viscosity, bulk modulus and thermal expansivity [21]. The approximations for global parameters including the total force and total friction loss were also developed in [22, 23]. While the numerical and analytic results of [21, 22, 23] delineate the effects of pressurization for a simple two-dimensional configuration, the complication due to the three-dimensionality of the flow has not yet been investigated in their analysis.

The goal of the present study is to examine the compressible lubrication flows in a thrust bearing for pressurized gases. The thrust bearing is commonly used in a wide variety of applications, including the automotive, marine, and aerospace industries. An example of the geometry of a thrust bearing is provided in Figure 6.1. As sketched in Figure 6.1, the thrust bearing carries the axial load of a rotating shaft. The operational portion of the bearing is an upper plate which rotates with the angular speed ω. A lower plate remains stationary and is separated from the rotating plate by a lubricating fluid. In order to generate load carrying pressure, a variation in the film thickness is required; this is provided by the series of sector-shaped pads sketched at the right of Figure 6.1. These pads vary the film thickness in the direction of rotation resulting in an increase of pressure over the background static

pressure.

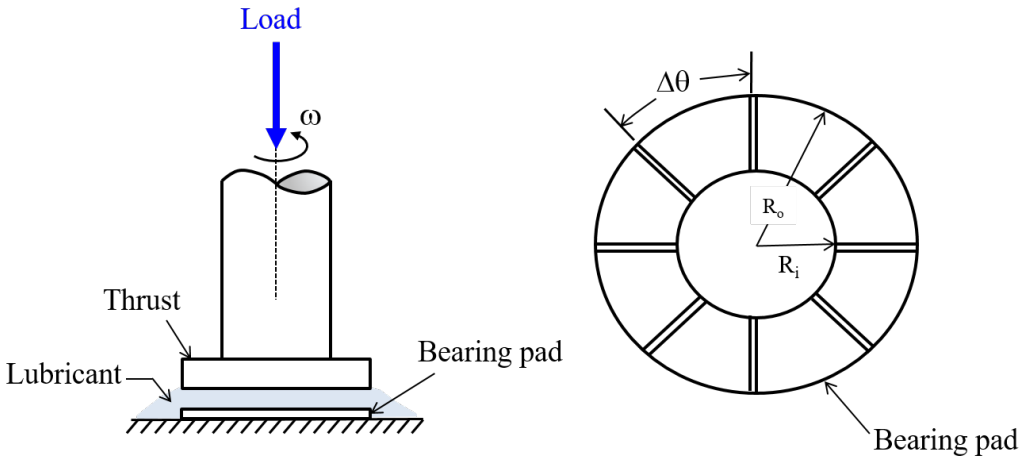

Figure 6.1: Schematic Diagram of a Thrust Bearing.

Because the flow in the thrust bearing is intrinsically three-dimensional, we aim to extend the form of the compressible Reynolds equation of [20] to include the three-dimensional effects using cylindrical polar coordinate system. The resultant Reynolds equation is found to be a nonlinear elliptic partial differential equation for the density. A numerical scheme based on the finite difference method is employed to solve this Reynolds equation. In addition, we have derived approximate solutions to the Reynolds equation valid for high speed flows. In doing so we have found that boundary layers form on three out of the four edges of the pads. At the inner and outer radii of the pad, the flow is governed by a nonlinear diffusion equation. As the main flow leaves the pad, the flow is governed by a nonlinear relaxation equation.

In the next section we describe the detailed configuration of a thrust bearing and the non-dimensionalization scheme used in this study. In Sections 6.3 and 6.4 we outline the derivation of the Reynolds equation and corresponding simplified temperature equation valid over most of the supercritical and dense gas regime. In Section 6.5 we discuss the breakdown and region of validity of our results. In Sections 6.6-6.9, we develop the approximate solutions to the derived Reynolds equation for high-speed lubrication flows. In Section 6.10 we describe the numerical scheme used to solve the Reynolds equation. The exact solution to the Reynolds equation is also presented and discussed for a range of speed numbers. In Section 6.11 we construct a composite solution and then compare the results of this approximation to the detailed numerical solutions to the Reynolds equation.

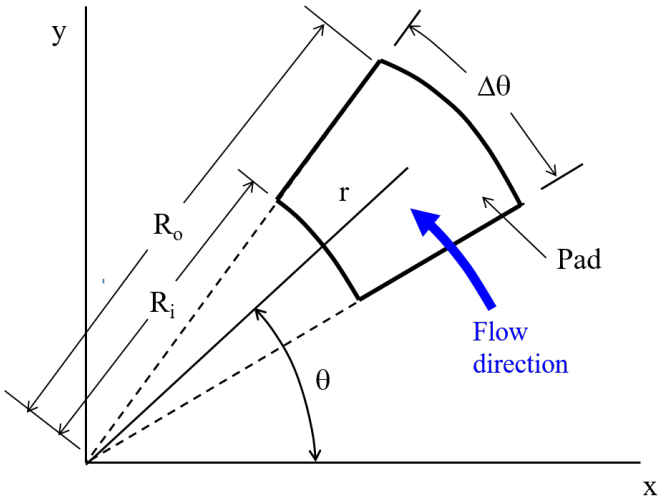

Figure 6.2: Schematic Diagram of a Thrust Bearing (Top View).

6.2 Formulation

Because of the symmetry, we consider only the single thrust pad sketched in Figure 6.2 and 6.3. We take the flow to be three-dimensional, steady, compressible, single-phase, and laminar. The body force and volumetric energy supplies are taken to be zero. We consider the pressures and temperatures to be outside of the liquid-like regime. The top view of a single thrust pad corresponding to Figure 6.1 is sketched in Figure 6.2. The rotor, stator, and the main flow lie in the x-y or r-θ plane. The radii of the inner and outer boundaries are denoted by R_i and R_o, respectively. The width of the pad is denoted as $\Delta\theta$. The side view of the thrust pad as viewed from the origin of Figure 6.2 is displayed in Figure 6.3. The rotor surface is located at $z = h_o$ = constant and has the constant speed $U = R_i\omega$ in the θ-direction where ω is the angular velocity of the rotor. The equation of the stator surface is $z = h_o f(\theta, r/L)$, where L is any reasonable measure of the length of the pad in the θ direction; throughout this study we taken $L = R_i$. The function $f(\theta, r/L)$ is any sufficiently smooth function. The gap width therefore is

$$h = h(\theta, \frac{r}{L}) = h_o(1 - f). \tag{6.3}$$

We will place the positive x-axis at the leading edge of the pad so that the pad occupies

$$R_i \leq r \leq R_o, 0 \leq \theta \leq \theta_{end}. \tag{6.4}$$

where $\Delta\theta \equiv \theta_{end}$ gives the angular width of the pad. The boundary conditions for the fluid are

$$v_r = v_\theta = v_z = 0 \text{ on } z = h_o f(\theta, \frac{r}{L}), \tag{6.5}$$

$$v_r = v_z = 0 \text{ and } v_\theta = r\omega \text{ on } z = h_o, \tag{6.6}$$

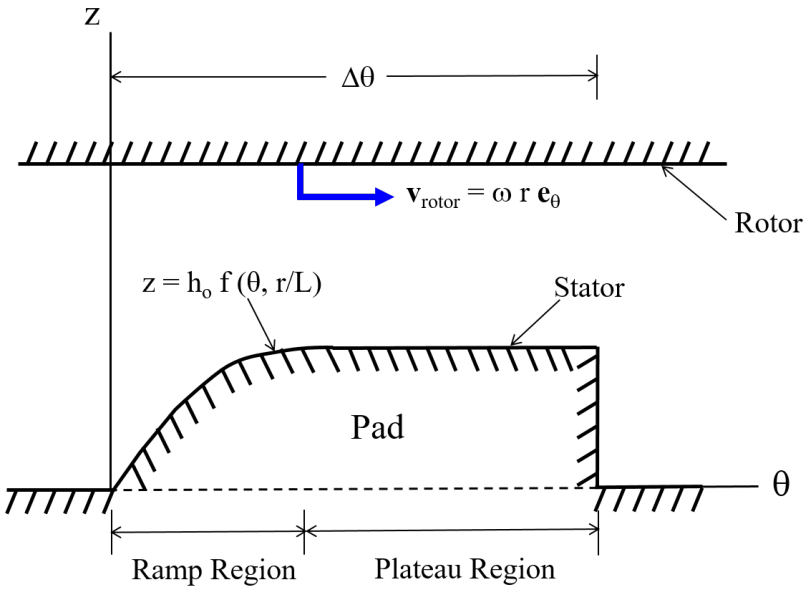

Figure 6.3: Schematic Diagram of a Thrust Bearing (Side View).

where v_r, v_θ, and v_z are the r-, θ-, and z-components of the fluid velocity. We follow previous investigation [5, 12, 15] requiring that all physical quantities have the same value at $\theta = 0$, $\theta = \theta_{end}$, r = R_i and r = R_o. Thermal boundary conditions include the isothermal-wall condition where the surfaces of the rotor and stator have fixed known temperatures, and the adiabatic-wall condition where one of the walls is taken to be adiabatic and another wall has a fixed known temperature.

The nondimensional Navier-Stokes equations in cylindrical polar coordinates can now be

written

$$\frac{1}{\overline{r}}\frac{\partial(\overline{\rho}\,\overline{r}v)}{\partial\overline{r}}+\frac{1}{\overline{r}}\frac{\partial(\overline{\rho}u)}{\partial\theta}+\frac{\partial(\overline{\rho}w)}{\partial\overline{z}}=0, \tag{6.7}$$

$$Re\frac{h_o^2}{L^2}\,\overline{\rho}(\overline{\mathbf{v}}\cdot\overline{\nabla}v-\frac{u^2}{\overline{r}})+\frac{\partial\overline{p}}{\partial\overline{r}}=\frac{\partial\overline{T}_{zr}}{\partial\overline{z}}+\frac{h_o^2}{L^2}\frac{1}{\overline{r}}\left[\frac{\partial(\overline{r}\overline{T}_{rr})}{\partial\overline{r}}+\frac{\partial(\overline{r}\overline{T}_{\theta r})}{\partial\theta}-\overline{T}_{\theta\theta}\right], \tag{6.8}$$

$$Re\frac{h_o^2}{L^2}\,\overline{\rho}(\overline{\mathbf{v}}\cdot\overline{\nabla}u-\frac{uv}{\overline{r}})+\frac{1}{\overline{r}}\frac{\partial\overline{p}}{\partial\theta}=\frac{\partial\overline{T}_{z\theta}}{\partial\overline{z}}+\frac{h_o^2}{L^2}\left[\frac{1}{\overline{r}^2}\frac{\partial(\overline{r}^2\overline{T}_{\theta r})}{\partial\overline{r}}+\frac{1}{\overline{r}}\frac{\partial\overline{T}_{\theta\theta}}{\partial\theta}\right], \tag{6.9}$$

$$Re\frac{h_o^4}{L^4}\,\overline{\rho}\,\overline{\mathbf{v}}\cdot\overline{\nabla}w+\frac{\partial\overline{p}}{\partial\overline{z}}=\frac{h_o^2}{L^2}\left[\frac{\partial(\overline{r}\overline{T}_{rz})}{\partial\overline{r}}+\frac{1}{\overline{r}}\frac{\partial\overline{T}_{\theta z}}{\partial\theta}+\frac{\partial\overline{T}_{zz}}{\partial\overline{z}}\right], \tag{6.10}$$

$$\begin{aligned}Re\frac{h_o^2}{L^2}Pr\overline{\rho}\,\overline{c_p}\overline{\mathbf{v}}\cdot\overline{\nabla}\,\overline{T}=&PrEc\left(\beta T\overline{\mathbf{v}}\cdot\overline{\nabla}\overline{p}+\overline{\Phi}\right)\\&+\frac{h_o^2}{L^2}\left[\frac{1}{\overline{r}}\frac{\partial}{\partial\overline{r}}\left(\overline{r}\overline{k}\frac{\partial\overline{T}}{\partial\overline{r}}\right)+\frac{1}{\overline{r}}\frac{\partial}{\partial\theta}\left(\frac{\overline{k}}{\overline{r}}\frac{\partial\overline{T}}{\partial\theta}\right)\right]\\&+\frac{\partial}{\partial\overline{z}}\left(\overline{k}\frac{\partial\overline{T}}{\partial\overline{z}}\right),\end{aligned} \tag{6.11}$$

where $\overline{r}=r/L$ and $\overline{z}=z/h_o$. The scaled velocity vector is denoted as $\overline{\mathbf{v}}$ and the nondimensional quantities are defined as

$$u=\frac{v_\theta}{U},\ \ v=\frac{v_r}{U}\ \text{ and }\ w=v_z\frac{L}{h_oU}. \tag{6.12}$$

The scalings for the thermodynamic pressure, density and temperature are

$$\overline{p}=(p-p_{ref})\frac{h_o^2}{\mu_{ref}UL},\ \ \overline{\rho}=\frac{\rho}{\rho_{ref}},\ \text{ and }\ \overline{T}=\frac{T-T_{ref}}{\Delta T} \tag{6.13}$$

respectively, where the subscript "ref" denotes the value of quantities evaluated at a reference thermodynamic state. Throughout this study, we take this reference state to be that at $\theta=0$. The quantity ΔT is a measure of the temperature differences occurring in the flow. The shear viscosity (μ), thermal conductivity (k) and the specific heat at constant pressure (c_p) are scaled as

$$\overline{\mu}=\frac{\mu(\rho,T)}{\mu_{ref}},\ \ \overline{k}=\frac{k(\rho,T)}{k_{ref}},\ \text{ and }\ \overline{c}_p=\frac{c_p(\rho,T)}{c_{pref}}, \tag{6.14}$$

respectively. The quantity $\beta\equiv\beta(\rho,T)$ is the thermal expansivity. The nondimensional

parameters are defined

$$Re \equiv \frac{\rho_{ref} U L}{\mu_{ref}} = \text{the Reynolds number}, \tag{6.15}$$

$$Pr \equiv \frac{\mu_{ref} c_{pref}}{k_{ref}} = \text{the Prandtl number}, \tag{6.16}$$

$$Ec \equiv \frac{U^2}{c_{pref} \Delta T} = \text{the Eckert number}. \tag{6.17}$$

The components of the nondimensional stress tensor are given by

$$\overline{T}_{rr} = 2\overline{\mu}\frac{\partial v}{\partial \overline{r}} + \overline{\lambda}(\overline{\nabla} \cdot \overline{\mathbf{v}}), \tag{6.18}$$

$$\overline{T}_{\theta\theta} = 2\overline{\mu}\left(\frac{1}{\overline{r}}\frac{\partial u}{\partial \theta} + \frac{v}{\overline{r}}\right) + \overline{\lambda}(\overline{\nabla} \cdot \overline{\mathbf{v}}), \tag{6.19}$$

$$\overline{T}_{zz} = 2\overline{\mu}\frac{\partial w}{\partial \overline{z}} + \overline{\lambda}(\overline{\nabla} \cdot \overline{\mathbf{v}}), \tag{6.20}$$

$$\overline{T}_{r\theta} = \overline{T}_{\theta r} = \overline{\mu}\left[\overline{r}\frac{\partial}{\partial \overline{r}}\left(\frac{u}{\overline{r}}\right) + \frac{1}{\overline{r}}\frac{\partial v}{\partial \theta}\right], \tag{6.21}$$

$$\overline{T}_{rz} = \overline{T}_{zr} = \overline{\mu}\left[\frac{h_o^2}{L^2}\frac{\partial w}{\partial \overline{r}} + \frac{\partial v}{\partial \overline{z}}\right], \tag{6.22}$$

$$\overline{T}_{\theta z} = \overline{T}_{z\theta} = \overline{\mu}\left[\frac{\partial u}{\partial \overline{z}} + \frac{h_o^2}{L^2}\frac{1}{\overline{r}}\frac{\partial w}{\partial \theta}\right], \tag{6.23}$$

where $\overline{\lambda} = \lambda(\rho, T)/\lambda_{ref}$ is the scaled second viscosity ($\overline{\lambda}$). The scaled stress components (6.18)-(6.23) are related to the dimensional stress components by

$$\overline{T}_{rr} = \frac{L}{\mu_{ref} U} T_{rr}, \;\; \overline{T}_{\theta\theta} = \frac{L}{\mu_{ref} U} T_{\theta\theta}, \;\; \overline{T}_{zz} = \frac{L}{\mu_{ref} U} T_{zz}; \tag{6.24}$$

$$\overline{T}_{r\theta} = \frac{L}{\mu_{ref} U} T_{r\theta}, \;\; \overline{T}_{rz} = \frac{h_o}{\mu_{ref} U} T_{rz}, \;\; \overline{T}_{\theta z} = \frac{h_o}{\mu_{ref} U} T_{\theta z}. \tag{6.25}$$

The nondimensional viscous dissipation is given by

$$\begin{aligned}\overline{\Phi} = \frac{h_o^2}{\mu_{ref} U^2}\Phi = 2\overline{\mu}\frac{h_o^2}{L^2}\Bigg[&\left(\frac{\partial v}{\partial \overline{r}}\right)^2 + \left(\frac{1}{\overline{r}}\frac{\partial u}{\partial \theta} + \frac{v}{\overline{r}}\right)^2 + \left(\frac{\partial w}{\partial \overline{z}}\right)^2 \Bigg] \\ &+ \overline{\mu}\Bigg[\frac{h_o^2}{L^2}\left(\frac{1}{\overline{r}}\frac{\partial v}{\partial \theta} + \frac{\partial u}{\partial \overline{r}} - \frac{u}{\overline{r}}\right)^2 + \left(\frac{\partial u}{\partial \overline{z}} + \frac{h_o^2}{L^2}\frac{1}{\overline{r}}\frac{\partial w}{\partial \theta}\right)^2 + \left(\frac{h_o^2}{L^2}\frac{\partial w}{\partial \overline{r}} + \frac{\partial v}{\partial \overline{z}}\right)^2 \Bigg] \\ &+ \frac{h_o^2}{L^2}\overline{\lambda}(\overline{\nabla} \cdot \overline{\mathbf{v}})^2. \end{aligned} \tag{6.26}$$

6.3 Three-Dimensional Compressible Reynolds Equation

We now apply the well-known approximation of lubrication theory, i.e., (6.2), to the exact Navier-Stokes equations (6.7)-(6.10). The results are

$$\frac{1}{\overline{r}}\frac{\partial(\overline{\rho}\,\overline{r}v)}{\partial\overline{r}}+\frac{1}{\overline{r}}\frac{\partial(\overline{\rho}u)}{\partial\theta}+\frac{\partial(\overline{\rho}w)}{\partial\overline{z}}=0, \tag{6.27}$$

$$\frac{\partial\overline{p}}{\partial\overline{r}}=\frac{\partial}{\partial\overline{z}}\left(\overline{\mu}\frac{\partial v}{\partial\overline{z}}\right)+O(Re\frac{h_o^2}{L^2},\frac{h_o^2}{L^2}), \tag{6.28}$$

$$\frac{1}{\overline{r}}\frac{\partial\overline{p}}{\partial\theta}=\frac{\partial}{\partial\overline{z}}\left(\overline{\mu}\frac{\partial u}{\partial\overline{z}}\right)+O(Re\frac{h_o^2}{L^2},\frac{h_o^2}{L^2}), \tag{6.29}$$

$$\frac{\partial\overline{p}}{\partial\overline{z}}=O(Re\frac{h_o^4}{L^4},\frac{h_o^2}{L^2})=O(\frac{h_o^2}{L^2}). \tag{6.30}$$

Inspection of (6.30) reveals that the pressure variation across the gap is negligible, i.e., $\overline{p}\approx\overline{p}(\overline{r},\theta)$ only. As a result, (6.28) and (6.29) can be integrated with respect to $\overline{z}$ at least once.

The density variation can be evaluated using the simple identity

$$\frac{d\overline{\rho}}{\overline{\rho}}=\frac{M_{ref}^2}{Re\frac{h_o^2}{L^2}}\frac{\gamma}{\overline{\rho}\,\overline{a}^2}d\overline{p}-\beta\Delta T d\overline{T}, \tag{6.31}$$

where

$$M_{ref}\equiv\frac{U}{a_{ref}}=\text{the reference Mach number}, \tag{6.32}$$

$$\gamma\equiv\gamma(\rho,T)=\text{the ratio of specific heats}, \tag{6.33}$$

$$a\equiv a(\rho,T)=\sqrt{\left.\frac{\partial p}{\partial\rho}\right|_s}=\sqrt{\left.\gamma\frac{\partial p}{\partial\rho}\right|_T}=\text{the sound speed}. \tag{6.34}$$

The variations of the density in the r- and θ-direction therefore can be written as

$$\frac{1}{\overline{\rho}}\frac{\partial\overline{\rho}}{\partial\overline{r}}=\frac{M_{ref}^2}{Re\frac{h_o^2}{L^2}}\frac{\gamma}{\overline{\rho}\,\overline{a}^2}\frac{\partial\overline{p}}{\partial\overline{r}}-\beta\Delta T\frac{\partial\overline{T}}{\partial\overline{r}}, \tag{6.35}$$

$$\frac{1}{\overline{\rho}}\frac{\partial\overline{\rho}}{\partial\theta}=\frac{M_{ref}^2}{Re\frac{h_o^2}{L^2}}\frac{\gamma}{\overline{\rho}\,\overline{a}^2}\frac{\partial\overline{p}}{\partial\theta}-\beta\Delta T\frac{\partial\overline{T}}{\partial\theta}. \tag{6.36}$$

Examination of (6.35) and (6.36) indicate that the density changes due to the temperature is proportional to $\beta\Delta T$. When one of the walls is adiabatic, the temperature difference is determined by the flow dynamics and given by

$$\Delta T=\frac{U^2}{c_{pref}}Pr. \tag{6.37}$$

As a result,

$$\beta\Delta T = \frac{\beta a_{ref}^2}{c_{pref}} \frac{U^2}{a_{ref}^2} Pr = O(G_{ref} M_{ref}^2 Pr), \tag{6.38}$$

where

$$G \equiv \frac{\beta a^2}{c_p} = \text{the Grueneisen parameter}, \tag{6.39}$$

When the isothermal wall condition is considered, we will require that the temperature difference satisfies

$$\Delta T = O(M_{ref}^2 T_{ref} \frac{G_{ref} Pr}{\beta_{ref} T_{ref}}), \tag{6.40}$$

and as a result,

$$\beta\Delta T = O(M_{ref}^2 G_{ref} Pr). \tag{6.41}$$

Because we consider all pressures and temperature outside of the liquid-like regime, $Pr = O(\beta T) = O(\gamma)$ and $G = O(1)$. That is, the scaling of the thermal expansion for both types of thermal boundary conditions, i.e., (6.38) and (6.41), are found to be $O(Pr M_{ref}^2)$. Therefore, the density changes due to the temperature can be written

$$\beta\Delta T = O(M_{ref}^2 Pr) \ll O(\gamma \frac{M_{ref}^2}{Re \frac{h_o^2}{L^2}}). \tag{6.42}$$

Therefore, the equations (6.35) and (6.36) can be rewritten as

$$\frac{1}{\overline{\rho}} \frac{\partial \overline{\rho}}{\partial \overline{r}} = \frac{M_{ref}^2}{Re \frac{h_o^2}{L^2}} \frac{\gamma}{\overline{\rho}\,\overline{a}^2} \frac{\partial \overline{p}}{\partial \overline{r}} + O(M_{ref}^2 Pr), \tag{6.43}$$

$$\frac{1}{\overline{\rho}} \frac{\partial \overline{\rho}}{\partial \theta} = \frac{M_{ref}^2}{Re \frac{h_o^2}{L^2}} \frac{\gamma}{\overline{\rho}\,\overline{a}^2} \frac{\partial \overline{p}}{\partial \theta} + O(M_{ref}^2 Pr). \tag{6.44}$$

In order that the flow be compressible we require that

$$M_{ref}^2 = O(Re \frac{h_o^2}{L^2}) = o(1). \tag{6.45}$$

Because of (6.45) and (6.40), it is easily shown that the temperature differences needs to be sufficiently small, i.e.,

$$\frac{\Delta T}{T_{ref}} = O(M_{ref}^2) = o(1). \tag{6.46}$$

when the isothermal-wall condition is imposed.

The density variation across the gap, i.e., in the z-direction, is determined by

$$\frac{1}{\overline{\rho}} \frac{\partial \overline{\rho}}{\partial \overline{z}} = \frac{M_{ref}^2}{Re \frac{h_o^2}{L^2}} \frac{\gamma}{\overline{\rho}\,\overline{a}^2} \frac{\partial \overline{p}}{\partial \overline{z}} - \beta\Delta T \frac{\partial \overline{T}}{\partial \overline{z}}, \tag{6.47}$$

where, from (6.30) and (6.45) we recognize that the first term of (6.47) is $O(\gamma\frac{h_o^2}{L^2}) = O(Pr\frac{h_o^2}{L^2}) \ll 1$ and the second term is $O(PrM_{ref}^2) = O(PrRe\frac{h_o^2}{L^2})$. We therefore conclude that the density variation across the gap is negligible, i.e.,

$$\frac{1}{\overline{\rho}}\frac{\partial\overline{\rho}}{\partial\overline{z}} = O(Pr\frac{h_o^2}{L^2}, PrRe\frac{h_o^2}{L^2}) \ll 1, \tag{6.48}$$

and we can take $\overline{\rho} = \overline{\rho}(r,\theta)$ only.

To evaluate the changes in the shear viscosity, we expand the shear viscosity in a Taylor series for T $\approx$ T_{ref}, i.e.,

$$\frac{\mu(\rho,T)-\mu(\rho,T_{ref})}{\mu_{ref}} = \frac{T_{ref}}{\mu_{ref}}\frac{\partial\mu}{\partial T}\bigg|_{\rho}\frac{\Delta T}{T_{ref}}\overline{T} + \cdots = O(M_{ref}^2) \ll 1, \tag{6.49}$$

where we used (6.46) and have recognized

$$\frac{T_{ref}}{\mu_{ref}}\frac{\partial\mu}{\partial T}\bigg|_{\rho} = O(1). \tag{6.50}$$

Hence, the variation of the shear viscosity can be taken to be dependent on density only, i.e.,

$$\mu(\rho,T) \approx \mu(\rho,T_{ref}) \approx \mu(r,\theta). \tag{6.51}$$

When the flow is away from the thermodynamic critical point, the density remains constant across the gap such that the shear viscosity is also approximately constant with respect to z. If we carry out similar analysis for the thermal conductivity, bulk modulus, and thermal expansion coefficient, we find

$$k(\rho,T) \approx k(\rho,T_{ref}) \approx k(r,\theta), \tag{6.52}$$
$$\kappa_T(\rho,T) \approx \kappa_T(\rho,T_{ref}) \approx \kappa_T(r,\theta), \tag{6.53}$$
$$\beta T(\rho,T) \approx \beta T(\rho,T_{ref}) \approx \beta T(r,\theta). \tag{6.54}$$

We now can integrate the $\overline{r}$- and θ-momentum equations, i.e., (6.28) and (6.29), twice with the boundary conditions (6.5) and (6.6). The results are

$$u = \frac{\overline{p}_\theta}{2\overline{\mu}\,\overline{r}}(\overline{z}-1)(\overline{z}-f) + \frac{\overline{r}}{1-f}(\overline{z}-f), \tag{6.55}$$
$$v = \frac{\overline{p}_{\overline{r}}}{2\overline{\mu}}(\overline{z}-1)(\overline{z}-f), \tag{6.56}$$

where

$$\overline{p}_\theta \equiv \frac{\partial\overline{p}}{\partial\theta} \quad \text{and} \quad \overline{p}_{\overline{r}} \equiv \frac{\partial\overline{p}}{\partial\overline{r}}. \tag{6.57}$$

If we substitute (6.55) and (6.56) in the mass equation (6.27) and integrate from $\overline{z}$ = f to $\overline{z}$ = 1, we then obtain

$$\frac{1}{\overline{r}}\frac{\partial}{\partial \overline{r}}\left(\frac{\overline{\rho}\,\overline{r}\overline{h}^3}{\overline{\mu}}\frac{\partial \overline{p}}{\partial \overline{r}}\right)+\frac{1}{\overline{r}}\frac{\partial}{\partial \theta}\left(\frac{\overline{\rho}\,\overline{h}^3}{\overline{\mu}\,\overline{r}}\frac{\partial \overline{p}}{\partial \theta}-6\overline{\rho}\,\overline{r}\overline{h}\right)=0. \tag{6.58}$$

where $\overline{h}$ = h/h$_o$. Examination of (6.44) and (6.43) reveals that the variations of p in r- and θ-direction can be regarded as being proportional to the variation of ρ in the r- and θ-direction, respectively, i.e.,

$$\frac{\partial p}{\partial \overline{r}} \approx \frac{\kappa_T(\rho, T_{ref})}{\rho}\frac{\partial \rho}{\partial \overline{r}}\left[1+O(M_{ref}^2)\right], \tag{6.59}$$

$$\frac{\partial p}{\partial \theta} \approx \frac{\kappa_T(\rho, T_{ref})}{\rho}\frac{\partial \rho}{\partial \theta}\left[1+O(M_{ref}^2)\right]. \tag{6.60}$$

If we substitute (6.59) and (6.60) in (6.58), we then obtain the nondimensional compressible Reynolds equation in cylindrical polar coordinates, i.e.,

$$\frac{1}{\overline{r}}\frac{\partial}{\partial \overline{r}}\left(\overline{r}\overline{h}^3\overline{\kappa}_{Te}(\overline{\rho})\frac{\partial \overline{\rho}}{\partial \overline{r}}\right)+\frac{1}{\overline{r}}\frac{\partial}{\partial \theta}\left(\frac{\overline{h}^3\overline{\kappa}_{Te}(\overline{\rho})}{\overline{r}}\frac{\partial \overline{\rho}}{\partial \theta}\right)=\Lambda\frac{\partial(\overline{\rho}\overline{h})}{\partial \theta}, \tag{6.61}$$

where the quantity κ_{Te} is the effective bulk modulus defined as

$$\kappa_{Te} \equiv \kappa_{Te}(\rho, T_{ref}) \equiv \frac{\kappa_T(\rho, T_{ref})}{\mu(\rho, T_{ref})}, \tag{6.62}$$

and the scaled version of effective bulk modulus is denoted as

$$\overline{\kappa}_{Te} \equiv \frac{\kappa_{Te}(\rho, T_{ref})}{\kappa_{Te}(\rho_{ref}, T_{ref})} = \frac{\kappa_{Te}(\rho, T_{ref})}{\kappa_{Te}|_{ref}}. \tag{6.63}$$

The effective bulk modulus gives a measure of relative importance of the local fluid stiffness to the fluid friction. The quantity

$$\Lambda \equiv \frac{6UL}{h_o^2\kappa_{Te}|_{ref}} \tag{6.64}$$

is the speed number and is regarded as a measure of flow compressibility. As mentioned in Section 6.2, we take the boundary conditions of the Reynolds equation (6.61) to be

$$\overline{\rho}=1 \quad \text{at} \quad \theta=0, \;\; \overline{r}\in\left[1,\frac{R_o}{R_i}\right], \tag{6.65}$$

$$\overline{\rho}=1 \quad \text{at} \quad \theta=\theta_{end}, \;\; \overline{r}\in\left[1,\frac{R_o}{R_i}\right], \tag{6.66}$$

$$\overline{\rho}=1 \quad \text{at} \quad \overline{r}=1, \;\; \theta\in[0,\theta_{end}], \tag{6.67}$$

$$\overline{\rho}=1 \quad \text{at} \quad \overline{r}=\frac{R_o}{R_i}, \;\; \theta\in[0,\theta_{end}]. \tag{6.68}$$

6.4 Simplified Temperature Equation

We apply the lubrication approximation (6.2) to the temperature equation (6.11). The resultant simplified temperature equation reads

$$\frac{\partial}{\partial \overline{z}}\left(\overline{k}\frac{\partial \overline{T}}{\partial \overline{z}}\right) = -PrEc\left[\beta T\left(v\frac{\partial \overline{p}}{\partial \overline{r}} + \frac{u}{\overline{r}}\frac{\partial \overline{p}}{\partial \theta}\right) + \overline{\Phi}\right] + O(Re\frac{h_o^2}{L^2}Pr, \frac{h_o^2}{L^2}), \tag{6.69}$$

where

$$\overline{\Phi} \approx \overline{\mu}\left[\left(\frac{\partial u}{\partial \overline{z}}\right)^2 + \left(\frac{\partial v}{\partial \overline{z}}\right)^2\right]. \tag{6.70}$$

When Pr $= O(1)$, i.e., in the thermodynamic states away from the critical point, we found that the convection terms are negligible. As a result, the temperature distribution is therefore determined by a balance of the conduction in the z-direction, viscous dissipation and flow work.

Due to (6.51), (6.52) and (6.54) and the fact that T $\approx$ T$_{ref}$, we found that the temperature equation can be integrated explicitly. The only function of $\overline{z}$ will be introduced by combining (6.55) and (6.56) with (6.69) and (6.70).

We now define

$$F_1 = \beta_1(r,\theta) = \beta T\frac{\partial \overline{p}}{\partial r}, \tag{6.71}$$

$$F_2 = \beta_2(r,\theta) = \frac{\beta T}{\overline{r}}\frac{\partial \overline{p}}{\partial \theta}, \tag{6.72}$$

$$A_1 = A_1(r,\theta) = \frac{\overline{p}_\theta}{2\overline{\mu}\,\overline{r}}, \tag{6.73}$$

$$A_2 = A_2(r,\theta) = \frac{\overline{p}_r}{2\overline{\mu}}, \tag{6.74}$$

$$B_1 = B_1(r,\theta) = -(1+f)\frac{\overline{p}_\theta}{2\overline{\mu}\,\overline{r}} + \frac{\overline{r}}{1-f}, \tag{6.75}$$

$$B_2 = B_2(r,\theta) = -(1+f)\frac{\overline{p}_r}{2\overline{\mu}}, \tag{6.76}$$

$$D_1 = D_1(r,\theta) = \frac{\overline{p}_\theta f}{2\overline{\mu}\,\overline{r}} - \frac{\overline{r}f}{1-f}, \tag{6.77}$$

$$D_2 = D_2(r,\theta) = \frac{\overline{p}_r f}{2\overline{\mu}} \tag{6.78}$$

such that the equations (6.55) and (6.56) can be rewritten as

$$u = A_1\overline{z}^2 + B_1\overline{z} + D_1, \tag{6.79}$$

$$v = A_2\overline{z}^2 + B_2\overline{z} + D_2. \tag{6.80}$$

The simplified temperature equation (6.69) can also be rewritten as

$$\frac{\partial}{\partial \overline{z}}\left(\overline{k}\frac{\partial \overline{T}}{\partial \overline{z}}\right) = -PrEc\left(G_1\overline{z}^2 + G_2\overline{z} + G_3\right), \tag{6.81}$$

where

$$G_1 = G_1(r,\theta) = F_1A_2 + F_2A_1 + 4\overline{\mu}(A_1^2 + A_2^2), \tag{6.82}$$
$$G_2 = G_2(r,\theta) = F_1B_2 + F_2B_1 + 4\overline{\mu}(A_1B_1 + A_2B_2), \tag{6.83}$$
$$G_3 = G_3(r,\theta) = F_1D_2 + F_2D_1 + \overline{\mu}(B_1^2 + B_2^2). \tag{6.84}$$

We note that the contribution due to the flow work are those terms with the factors E_1 and E_2. These are first two terms in (6.82)-(6.84) while other terms without the factors E_1 and E_2 are those due to the viscous dissipation.

We first consider the case where both stator and rotor surfaces have prescribed temperatures, i.e., $T = T_R$ = constant at $\overline{z} = 1$ and $T = T_S$ = constant at $\overline{z} = f$. It is easily shown that the resultant solution to (6.69) is

$$\frac{T - T_R}{\Delta T} = \frac{-Pr\ Ec}{12\overline{k}}\Bigg\{G_1\Big[\overline{z}^4 - (f+1)(f^2+1)\overline{z} + f(f^2+f+1)\Big] \tag{6.85}$$
$$+ 2G_2\Big[\overline{z}^3 - (f^2+f+1)\overline{z} + f(f+1)\Big] \tag{6.86}$$
$$+ 6G_3\Big[\overline{z}^2 - (f+1)\overline{z} + f\Big]\Bigg\} + \frac{\overline{z}-1}{f-1}, \tag{6.87}$$

where $\Delta T \equiv$T$_S$ - T$_R$ for this case.

If the stator surface, i.e., the $\overline{z}$ = f surface, is specified as an adiabatic wall and the rotor surface has a fixed temperature T_R, integration of (6.69) yields

$$\frac{T - T_R}{\frac{U^2}{2c_{pref}}} = -\frac{Pr}{12\overline{k}}\Big[G_1(\overline{z}^4 - 4f^3\overline{z} + 4f^3 - 1) \tag{6.88}$$
$$+ 2G_2(\overline{z}^3 - 3f^2\overline{z} + 3f^2 - 1) \tag{6.89}$$
$$+ 6G_3(\overline{z}^2 - 2f\overline{z} + 2f - 1)\Big], \tag{6.90}$$

where we have used (6.37). Finally, if we take the rotor to be adiabatic and $T = T_S$ at $\overline{z}$ = f, we then find

$$\frac{T - T_S}{\frac{U^2}{2c_{pref}}} = -\frac{Pr}{12\overline{k}}\Big[G_1(\overline{z}^4 - 4\overline{z} - f^4 + 4f) \tag{6.91}$$
$$+ 2G_2(\overline{z}^3 - 3\overline{z} - f^3 + 3f) \tag{6.92}$$
$$+ 6G_3(\overline{z}^2 - 2\overline{z} - f^2 + 2f)\Big]. \tag{6.93}$$

6.5 Near-Critical Region

In Section 6.3- 6.4 we have taken the pressures and temperatures to be sufficiently far from the near-critical region. When the thermodynamic state is in the vicinity of thermodynamic critical point, i.e., $\rho_{ref} = \rho_c$ and $T_{ref} = T_c$, the quantities of βT, c_p and Pr become singular [20] such that the Reynolds equation (6.61) and its corresponding simplified temperature equation (6.69) are no longer valid.

Examination of (6.28)-(6.30) reveals that the pressure will remain nearly constant in the z-direction, and the flow inertia will remain negligible in the near-critical region. However, when

$$PrRe\frac{h_o^2}{L^2} = O(1), \tag{6.94}$$

which will occur near the thermodynamic critical point, the energy convection is no longer negligible in (6.69). If we apply (6.94) to (6.48), we can further show that the variation of density in the z-direction will no longer be negligible, i.e.,

$$\frac{1}{\overline{\rho}}\frac{\partial \overline{\rho}}{\partial \overline{z}} = O(1). \tag{6.95}$$

While the shear viscosity is found to remain independent of temperature, the density variation with z will imply that $\mu = \mu(r, \theta, z)$. As a result, the integration of (6.28) and (6.29) becomes impossible. Therefore, the Reynolds equation (6.61) and its corresponding simplified temperature equation (6.69) are insufficient to describe the compressible lubrication flows when (6.94) holds. These results are consistent with the finding of [20] for a two-dimensional configuration. The region of validity of the theory given by Equation (74) and (75) in [20] is still valid for a three-dimensional thrust bearing.

6.6 Large Speed Number Approximation

In the remaining sections we will focus on solutions to the Reynolds equation (6.61). We seek approximate solutions valid for high-speed flows, i.e., flows with large speed numbers. We make the simplification that f = f(θ) only so that

$$\overline{h} = \overline{h}(\theta) = 1 - f(\theta). \tag{6.96}$$

The function $\overline{h}$ is taken to further satisfy

$$\overline{h} = 1 \quad \text{at} \quad \theta = 0 \quad \text{and} \quad \overline{r} \in [1, \delta_o], \tag{6.97}$$

$$\overline{h} = \overline{h}_{end} \leq 1 \quad \text{at} \quad \theta = \theta_{end} \quad \text{and} \quad \overline{r} \in [1, \delta_o], \tag{6.98}$$

$$\frac{d\overline{h}}{d\theta} = 0 \quad \text{at} \quad \theta = \theta_{end} \quad \text{and} \quad \overline{r} \in [1, \delta_o] \tag{6.99}$$

where $\delta_o \equiv R_o/R_i$ and $\overline{h}_{end} \equiv \overline{h}(\theta_{end})$.

We first obtain the simplest solution valid over most of the pad. We found that the first-order expansion for the scaled density can be written as

$$\overline{\rho} = \frac{1}{\overline{h}} + \frac{1}{\Lambda \overline{h} \overline{r}^2} \left(\left. \frac{d\overline{h}}{d\theta} \right|_{\theta=0} - \overline{\kappa}_{Te} (\frac{1}{\overline{h}}) \overline{h} \frac{d\overline{h}}{d\theta} \right) + O(\frac{1}{\Lambda^2}), \tag{6.100}$$

for $\Lambda \longrightarrow \infty$. Because of (6.97), we can easily show that (6.100) satisfies the boundary condition (6.65). However, (6.100) cannot satisfy the boundary conditions at $\theta = \theta_{end}$ and $\overline{r}$ = 1 and δ, i.e., (6.100) cannot satisfy (6.66)-(6.68). In order to obtain the approximations valid over the whole pad, we seek boundary layer solutions in these regions.

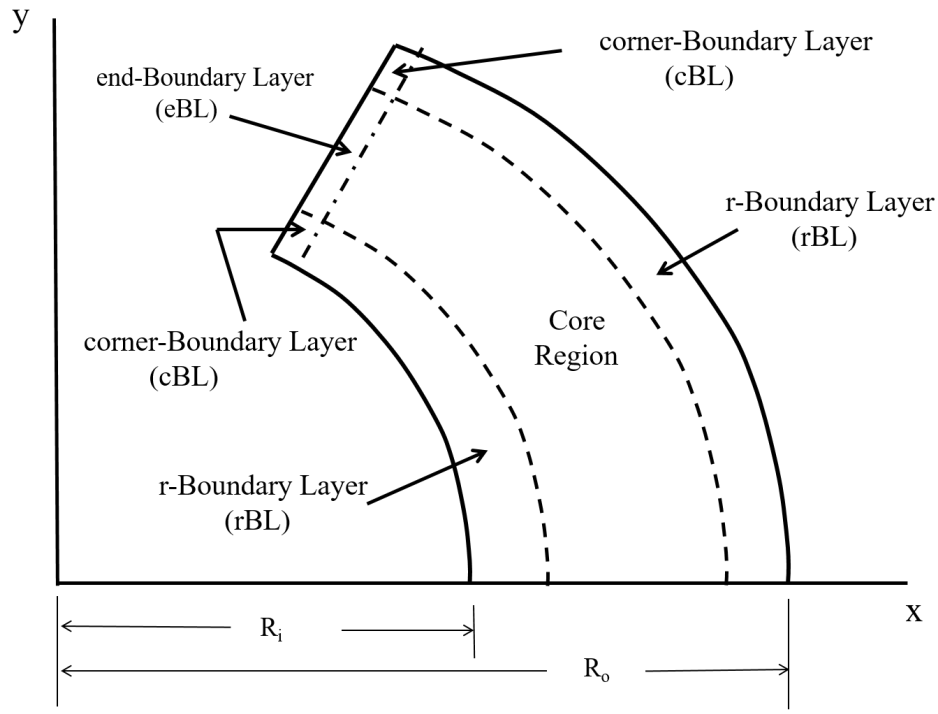

Figure 6.4: Sketch of Boundary Layers in the Thrust Bearing Problem.

The regions of interest are those sketched in Figure 6.4. The solution (6.100) is valid in the core region where $\theta = O(1)$ and $\overline{r} = O(1)$. The r-boundary layers are located at the inner and outer radii of the pad, i.e., near $\overline{r}$ = 1 and $\delta_o = \mathrm{R}_o/\mathrm{R}_i$, and can be shown to have the thickness of $\mathrm{O}(\Lambda^{-1/2})$. We will refer to the inner and outer r-boundary layers by using the acronym "rBLi" and "rBLo", respectively. The end-boundary layer is located near $\theta = \theta_{end}$, and will be referred to by using the acronym "eBL". The thickness of eBL can be shown to be $\mathrm{O}(\Lambda^{-1})$. The corner-boundary layers are in the regions where $\overline{r} - 1 = O(\Lambda^{-1/2})$,

$\delta_o - \overline{r} = O(\Lambda^{-1/2})$ and $|\theta - \theta_{end}| = O(\Lambda^{-1})$. We will refer to the inner and outer corner boundary layers by using the acronym "cBLi" and "cBLo", respectively.

In Section 6.7-6.9, we will present the lowest-order approximation in each region, i.e., rBL, eBL and cBL. In the interests of clarity, we will use a primitive matching rather than the formal Method of Matched Asymptotic Expansions (MMAE)[27, 28].

6.7 r-Boundary layers

To analyze the boundary layer flow in the rBL region, we re-scale the radial coordinate as follows:

$$\widehat{r} \equiv \sigma(\overline{r} - \delta)\sqrt{\Lambda} \Longleftrightarrow \overline{r} \equiv \delta + \frac{\widehat{r}}{\sigma\sqrt{\Lambda}}, \tag{6.101}$$

with $\widehat{r} = O(1)$, $\theta = O(1)$, and

$$\sigma = 1, \delta = 1, \quad \text{for} \quad \overline{r} \approx 1, \tag{6.102}$$

$$\sigma = -1, \delta = \delta_o, \quad \text{for} \quad \overline{r} \approx \delta_o. \tag{6.103}$$

The density in the r-boundary layers is expanded for large Λ, i.e.,

$$\overline{\rho} = \rho^{rBL}(\theta, \widehat{r}) + O(\frac{1}{\Lambda^{1/2}}), \tag{6.104}$$

where ρ^{rBL} is the lowest-order approximate density in the rBL region and the $\Lambda^{-1/2}$ in the error term is selected due to a recognition of higher order terms in the Reynolds equation.

If we substitute (6.101) and (6.104) in (6.61) and equate like powers of Λ, we found that the flow in the rBL region is governed by

$$\frac{\partial(\overline{h}\rho^{rBL})}{\partial\theta} \approx \sigma^2\overline{h}^3\frac{\partial}{\partial\widehat{r}}\left[\overline{\kappa}_{Te}(\rho^{rBL})\frac{\partial\rho^{rBL}}{\partial\widehat{r}}\right] + O(\frac{1}{\Lambda^{1/2}}), \tag{6.105}$$

which is a nonlinear parabolic partial differential equation. The boundary conditions for this equation are

$$\rho^{rBL} = 1 \quad \text{at} \quad \widehat{r} = 0, \text{ for all } 0 \le \theta < \theta_{end}, \tag{6.106}$$

$$\rho^{rBL} = 1 \quad \text{at} \quad \theta = 0, \text{ for all } \widehat{r} \ge 0. \tag{6.107}$$

Condition (6.107) acts as an "initial condition" for (6.105) in a scheme which marches in θ. Condition (6.106) is (6.67) recast in terms of (6.102) and (6.103). The final boundary condition in $\widehat{r}$ must come from a matching to the core solution (6.100). A primitive matching simply requires that ρ^{rBL} approaches the core solution as $\widehat{r} \longrightarrow \infty$, i.e.,

$$\rho^{rBL} \sim \frac{1}{\overline{h}(\theta)} + o(1) \quad \text{as} \quad \widehat{r} \longrightarrow \infty, \theta \ge 0. \tag{6.108}$$

6.8 End Boundary layer

We now turn to analyze the flow in the eBL region, i.e., the region near $\theta = \theta_{end}$, where $\overline{\rho}$ makes transition from the core solution, i.e., $\overline{\rho} \approx 1/\overline{h}_{end}$, to the boundary condition (6.66). Here, we re-scale θ as follows:

$$\widehat{\theta} \equiv \Lambda(\theta_{end} - \theta) \Longleftrightarrow \theta = \theta_{end} - \frac{\widehat{\theta}}{\Lambda}, \tag{6.109}$$

with $\widehat{\theta} = O(1)$ and $\overline{r} = O(1)$. We also expand the density in a large Λ expansion of the form:

$$\overline{\rho} = \rho^{eBL}(\widehat{\theta}, \overline{r}) + O(\frac{1}{\Lambda^2}), \tag{6.110}$$

where $\rho^{eBL} = O(1)$ is the lowest-order approximate density in the eBL region. If we expand the $\overline{h}(\theta)$ in a Taylor series near $\theta \approx \theta_{end}$, we find

$$\overline{h}(\theta) = \overline{h}_{end} + \frac{\widehat{\theta}^2}{2\Lambda^2} \frac{d^2\overline{h}}{d\theta^2}\bigg|_{\theta=\theta_{end}} + O(\frac{1}{\Lambda^3}), \tag{6.111}$$

where we have used (6.99) and (6.109).

If we substitute (6.109)-(6.111) in (6.61) and equate like powers of Λ, we find the equation for ρ^{eBL} can be written as

$$\frac{\partial \rho^{eBL}}{\partial \widehat{\theta}} \approx -\frac{\overline{h}_{end}^2}{\overline{r}^2} \frac{\partial}{\partial \widehat{\theta}} \left(\overline{\kappa}_{Te}(\rho^{eBL}) \frac{\partial \rho^{eBL}}{\partial \widehat{\theta}} \right) + O(\frac{1}{\Lambda^2}). \tag{6.112}$$

The boundary conditions corresponding to (6.112) are found to be

$$\rho^{eBL} = 1 \quad \text{at} \quad \widehat{\theta} = 0, \overline{r} \not\approx 1, \delta_o, \tag{6.113}$$

$$\rho^{eBL} \sim \frac{1}{\overline{h}_{end}} + o(1) \ \text{ as } \ \widehat{\theta} \longrightarrow \infty, \tag{6.114}$$

where the condition (6.113) is the lowest-order form of (6.66) and the condition (6.114) has again been obtained through a primitive matching to the core solution (6.100).

A first integral of (6.112) can be obtained by direct integration to yield

$$\rho^{eBL} = -\frac{\overline{h}_{end}^2}{\overline{r}^2} \overline{\kappa}_{Te}(\rho^{eBL}) \frac{\partial \rho^{eBL}}{\partial \widehat{\theta}} + B(\overline{r}), \tag{6.115}$$

where $B(\overline{r})$ is an integration function. According to (6.114), ρ^{eBL} approaches a constant as $\widehat{\theta} \longrightarrow \infty$, i.e.,

$$\frac{\partial \rho^{eBL}}{\partial \widehat{\theta}} \longrightarrow 0 \ \text{ as } \ \widehat{\theta} \longrightarrow \infty. \tag{6.116}$$

As a result, we found that

$$B(\overline{r}) = \frac{1}{\overline{h}_{end}} \tag{6.117}$$

and we can rewrite (6.112) as

$$\overline{\kappa}_{Te}(\rho^{eBL})\frac{\partial \rho^{eBL}}{\partial \widehat{\theta}} = \frac{\overline{r}^2}{\overline{h}_{end}^2}\left(\frac{1}{\overline{h}_{end}} - \rho^{eBL}\right) + o(1), \tag{6.118}$$

which is recognized as a nonlinear relaxation equation. Because $\overline{\kappa}_{Te} > 0$ and $\overline{h}_{end} < 1$, a straightforward analysis of (6.113) and (6.118) can show that ρ^{eBL} increase monotonically from 1 to $1/\overline{h}_{end}$ with increasing $\widehat{\theta}$ or decreasing θ.

6.9 Corner Boundary layers

The corner region is taken to be rectangular in shape and has the same length in the $\overline{r}$ direction as the rBL and the same width in the θ direction as the eBL, i.e.,

$$\overline{r} - \delta = O(\frac{1}{\sqrt{\Lambda}}),\ |\theta - \theta_{end}| = O(\frac{1}{\Lambda}). \tag{6.119}$$

The scaling for $\overline{r}$ and θ are therefore the same as those in the rBL and eBL, i.e.,

$$\begin{aligned} \overline{r} &\equiv \delta + \frac{\widehat{r}}{\sigma\sqrt{\Lambda}} \Longleftrightarrow \widehat{r} = \sigma(\overline{r} - \delta)\sqrt{\Lambda}, \\ \theta &\equiv \theta_{end} - \frac{\widehat{\theta}}{\Lambda} \Longleftrightarrow \widehat{\theta} = \Lambda(\theta_{end} - \theta) = O(1). \end{aligned} \tag{6.120}$$

We expand the density in the corner region for the large Λ, i.e.,

$$\overline{\rho} = \rho^{cBL}(\widehat{\theta}, \widehat{r}) + O(\frac{1}{\sqrt{\Lambda}}). \tag{6.121}$$

where ρ^{cBL} is the lowest-order approximate density in the cBL region. The expansion of $\overline{h}(\theta)$ near $\theta = \theta_{end}$, i.e., (6.111), can also be applied in the cBL. Substitution of (6.120), (6.121) and (6.111) in (6.61) yields

$$\frac{\partial \rho^{cBL}}{\partial \widehat{\theta}} = -\frac{\overline{h}_{end}^2}{\delta^2}\frac{\partial}{\partial \widehat{\theta}}\left(\overline{\kappa}_{Te}(\rho^{cBL})\frac{\partial \rho^{cBL}}{\partial \widehat{\theta}}\right) + o(1), \tag{6.122}$$

which is similar to the eBL equation, i.e., (6.112). The boundary condition for the corner boundary layer equation (6.122) is

$$\rho^{cBL} = 1 \ \text{ at } \ \widehat{\theta} = 0, \tag{6.123}$$

which corresponds to (6.66). The second boundary condition for (6.122) is obtained by a primitive matching to the rBL solutions evaluated at $\theta = \theta_{end}$. Thus,

$$\rho^{cBL} \longrightarrow \rho^{rBL}(\theta_{end}, \widehat{r}) + o(1) \text{ as } \widehat{\theta} \longrightarrow \infty. \tag{6.124}$$

We can obtain a first integral of (6.122) subject to (6.123) and (6.124) in a manner similar to that of Section 6.8. The resultant equation governing the flow in the corner boundary is

$$\overline{\kappa}_{Te}(\rho^{cBL})\frac{\partial \rho^{cBL}}{\partial \widehat{\theta}} = \frac{\delta^2}{\overline{h}_{end}^2}\left(\rho^{rBL}(\theta_{end}, \widehat{r}) - \rho^{cBL}\right) + o(1). \tag{6.125}$$

It is easily verified that the corner solution satisfying (6.123)-(6.125) also correctly matches the solution of the eBL, i.e., (6.113)-(6.118), as $\widehat{r} \longrightarrow \infty$.

6.10 Numerical Scheme for Reynolds Equation

In order to obtain the numerical solution to the compressible Reynolds equation (6.61) we impose the boundary conditions (6.65)-(6.68) and employ a numerical scheme based on the finite difference method. The fluid domain is discretized using a uniform grid with rectangular elements in r-θ space. The central difference scheme is applied to both the first and second derivatives in (6.61). The resulting system of equations is coupled with the Redlich-Kwong-Soave (RKS) equation of state described in [24] and the viscosity model of Chung et al. [25, 26]. Once discretized, the resultant system of algebraic equations was solved using a iterative linear solver provided by MATLAB. The iteration process begins with an initial guess values of $\overline{\rho}$ and continues until the average variation of $\overline{\rho}$ is less than 10^{-5}. The pressure distribution is obtained by substituting the resultant density field to the RKS equation of state.

To demonstrate the grid independence, we compared the numerical results of grids of 100, 200 and 300 elements in the r direction and 200, 400, 600, 800 and 1000 elements in the θ direction. Grid convergence was typically achieved with the grid of 200 x 800 which yields 0.01% difference in the load when compared to the grid of 300 x 1000.

In the remainder of this study, we take the configuration of the pad sketched in Figure 6.2 and 6.3 to be given by

$$\overline{h} = \begin{cases} 1 + (\overline{h}_s - 1)\sin(\frac{\pi}{2}\frac{\theta}{\theta_s}), & \text{for } 0 \le \theta \le \theta_s \\ \overline{h}_s, & \text{for } \theta_s \le \theta \le \theta_{end} \end{cases} \tag{6.126}$$

with $\overline{h}_s \equiv 1/2$, $\theta_s \equiv \pi/12$ and $\theta_{end} \equiv \pi/4$ and $\delta_o = R_o/R_i = 2$. We have plotted (6.126) as a function of θ in Figure 6.5. The region where $\overline{h}$ increases from 1 to $\overline{h}_s$ will be referred to as the ramp or ramp region. The region where $\overline{h} = \overline{h}_s =$ constant will be referred to as the

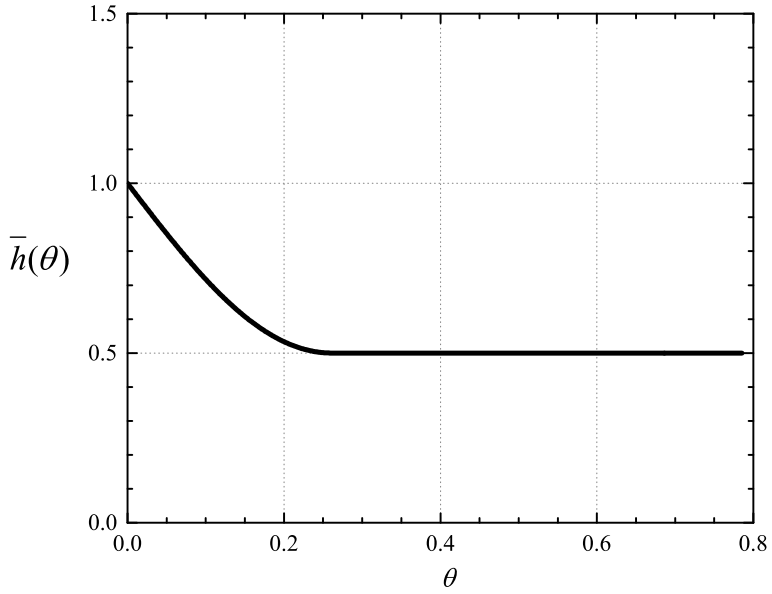

Figure 6.5: Film Thickness Function $\overline{h} \equiv \overline{h}(\theta)$.

plateau or plateau region. Unless stated otherwise, we take the reference specific volume, i.e., $V \equiv 1/\rho$, and the reference temperature to be $V_{ref} \equiv V(\theta = 0, r) = 5\ V_c$ and $T_{ref} \equiv T\ (\theta = 0, r) = 1.05\ T_c$, respectively. The pressure at these points is approximately 38.7 bar so that the thermodynamic state can be regarded as that of a dense gas or a slightly supercritical fluid. We select the fluid to be carbon dioxide (CO_2) and the physical parameters of CO_2 are taken from [24].

We have plotted the variation of the scaled density at the centerline of the pad in the r direction, i.e, at $r = 1.5R_i$, for $\Lambda = 5$, 15, 25, 35 and 45 in Figure 6.6. At $\Lambda = 5$, the scaled density is seen to increase almost linearly in the ramp and to reach its maximum value at $\theta \approx 0.24$ radians. Once the flow enters the plateau region, a slight decrease in the scaled density is seen to occur for 0.262 radians $\leq \theta \leq$ 0.71 radians. As the flow reaches the end of the pad, the scaled density gradually decreases to a value of 1. We have also plotted the variation of the scaled density at the centerline of the pad in the θ direction, i.e, at $\theta = \pi/8$ = 0.392 radians (which is located in the plateau region), for $\Lambda = 5$, 15, 25, 35 and 45 in Figure 6.7. The scaled density for the case of $\Lambda = 5$ increases from the inner and outer radii of the pad toward the center. In this case, the maximum scaled density is found to be 1.585 and located at $r = 1.575\ R_i$.

Examination of Figure 6.6 reveals that the end boundary layer begins to form as Λ increases. At $\Lambda = 15$, the slope of the curve in the ramp increases by 37% as compared to the case of $\Lambda = 5$. The maximum scaled density is found to be 1.83 for this case. In contrast with the case of $\Lambda = 5$, the scaled density remains its maximum value in the plateau region. Due to the formation of the end boundary layer, the scaled density is seen to decrease abruptly near the end of the pad. As Λ increases, the scaled density in the plateau increases and the

boundary layer near the end becomes thinner.

Inspection of Figure 6.7 shows that the increase of Λ also results in the formation of the boundary layers near the inner and outer radii of the pad. To further demonstrate this, we have also plotted the contour of the scaled density on the pad at $\Lambda = 5$, 25 and 45 in Figure 6.8a-6.8c, respectively. As predicted in Section 6.7, the thickness of the r-boundary layer is seen to decrease as Λ increases.

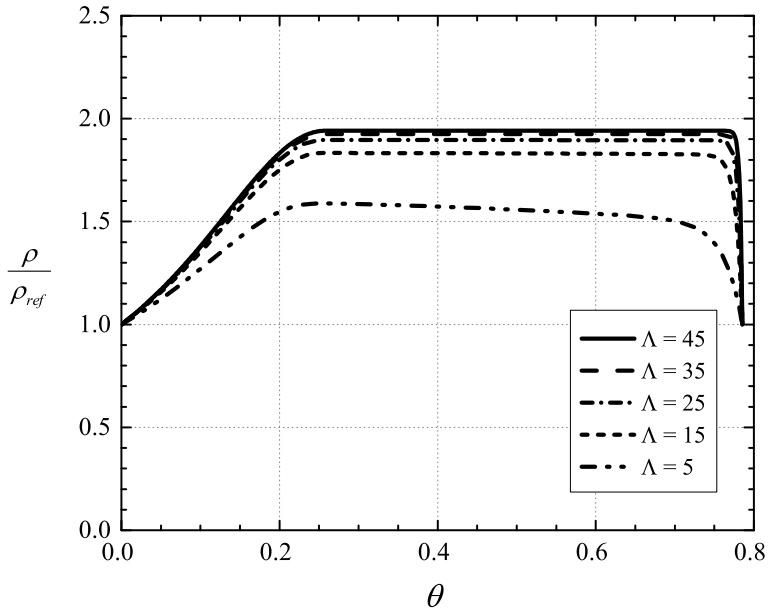

Figure 6.6: Scaled Density vs θ at r = 1.5 R_i. The reference state $V_{ref} = 5\ V_c$ and $T_{ref} = 1.05\ T_c$.

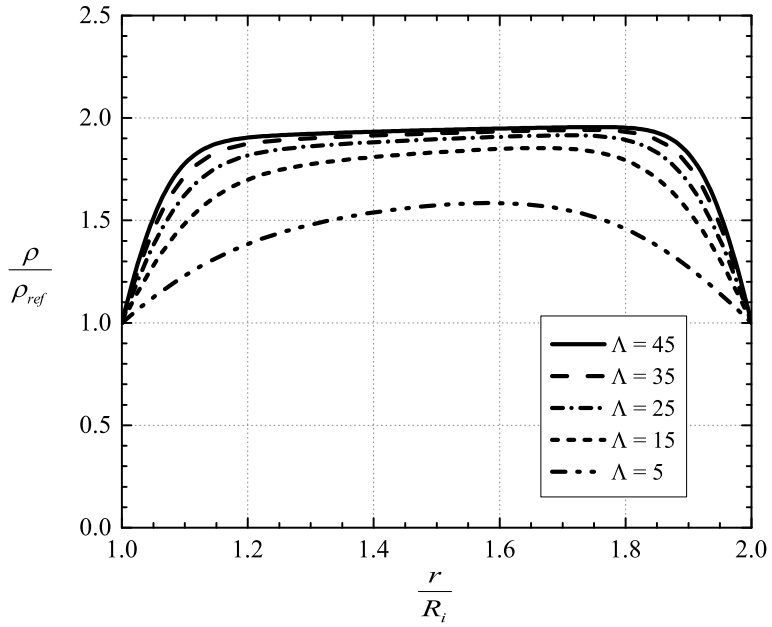

Figure 6.7: Scaled Density vs r/R_i at $\theta = \theta_{end}/2 = \pi/8$. The reference state $V_{ref} = 5\ V_c$ and $T_{ref} = 1.05\ T_c$.

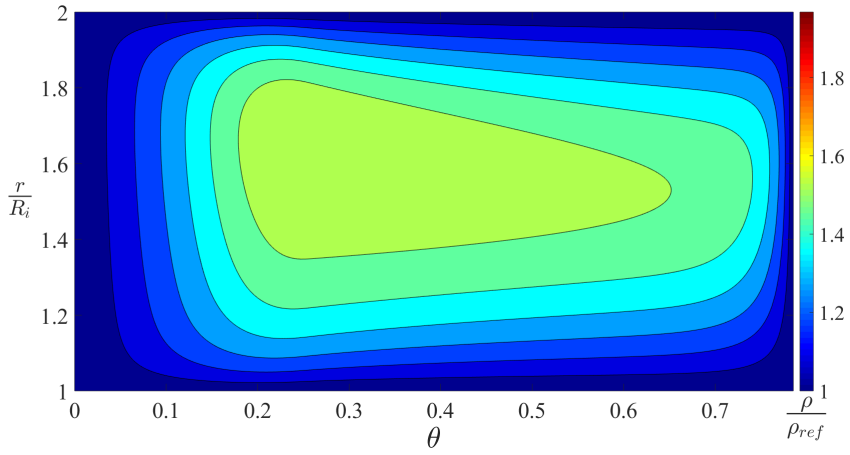

(a) $\Lambda = 5$

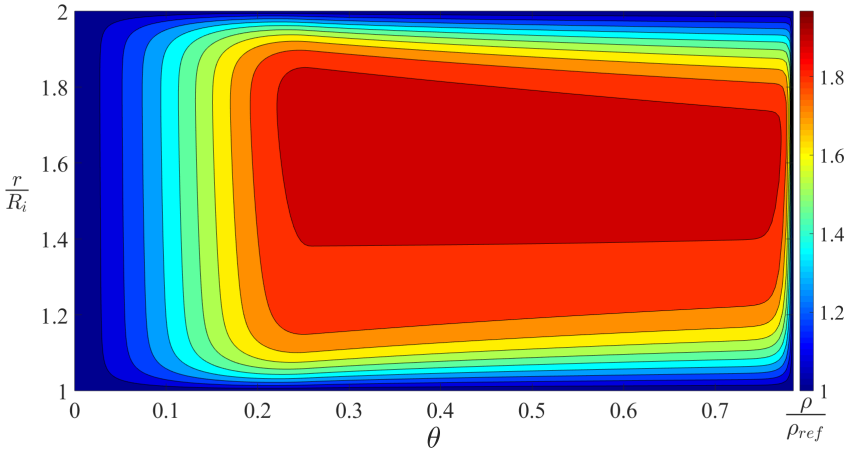

(b) $\Lambda = 25$

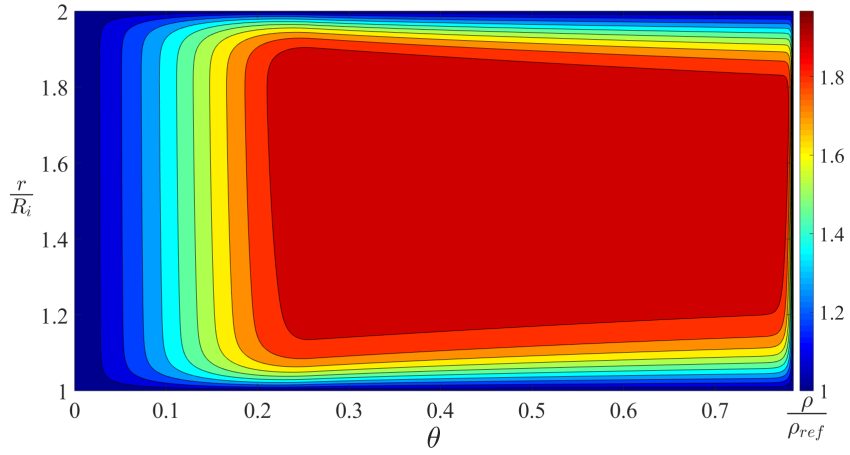

(c) $\Lambda = 45$

Figure 6.8: Distribution of Scaled Density at $V_{ref} = 5\ V_c$ and $T_{ref} = 1.05\ T_c$. Contour lines are drawn at equal intervals of $\overline{\rho}$ between 1 and 2.

6.11 Construction of a Composite Solution

The solutions derived in the previous sections comprise five boundary layer solutions and the core solution of Section 6.6. For purposes of comparison it will be convenient to combine these six solutions into a single "composite" solution. A discussion of composite solutions in the MMAE can be found in any text on perturbation methods; see, e.g., [27, 28]. The strategy is to note that the core, rBL solutions can be solved independent of the end and corner boundary layers. We then form a single composite solution which has the same accuracy as the core and rBL solutions in their respective regions. We then form a second composite solution comprised of the eBL and cBL boundary layers. The resultant composite solutions are then used to generate a single composite solution which is valid over the whole pad to the same accuracy as each solution in their respective regions.

We begin by defining the function

$$\mathscr{G}(\overline{r},\theta) \equiv \rho^{core} + \rho^{rBLi} + \rho^{rBLo} - \frac{2}{\overline{h}(\theta)}, \tag{6.127}$$

where ρ^{core} is the first-order core solution (6.100). In the language of the Method of Matched Asymptotic Expansions (MMAE), the last term in (6.127) is recognized as the matched or common part of the two boundary layers and the core. The superscripts rBLi and rBLo denote the boundary layers in the vicinity of r = R_i and R_o, respectively, that is

$$\rho^{rBLi}(\overline{r},\theta) \equiv \rho^{rBL}((\overline{r}-1)\sqrt{\Lambda},\theta), \tag{6.128}$$

$$\rho^{rBLo}(\overline{r},\theta) \equiv \rho^{rBL}((\delta-\overline{r})\sqrt{\Lambda},\theta). \tag{6.129}$$

The function $\mathscr{G}$ is the first composite solution for $\overline{\rho}$ valid in the core region and the r-boundary layers. Because

$$\widehat{r} \longrightarrow \infty \tag{6.130}$$

in the core region,

$$\rho^{rBL} \sim \frac{1}{\overline{h}(\theta)} \tag{6.131}$$

exponentially fast. Thus,

$$\mathscr{G} \sim \rho^{core} + \frac{1}{\overline{h}(\theta)} + \frac{1}{\overline{h}(\theta)} - \frac{2}{\overline{h}(\theta)} = \rho^{core} + o(\frac{1}{\Lambda}), \tag{6.132}$$

which has the same accuracy as the core solution itself.

In the rBLi, the $\widehat{r}$ corresponding to the rBLo $\longrightarrow \infty$ so that

$$\rho^{rBLo} \sim \frac{1}{\overline{h}(\theta)} \tag{6.133}$$

exponentially fast. The $\widehat{r}$ corresponding to the rBLi is of O(1) so that ρ^{rBLi} = O(1) and satisfies (6.105). Because $\overline{r} \approx 1$ in the rBLi, we can write the core solution as

$$\rho^{core} = \frac{1}{\overline{h}(\theta)} + O(\frac{1}{\Lambda}) = \frac{1}{\overline{h}(\theta)} + o(1). \tag{6.134}$$

Thus,

$$\mathscr{G} \sim \frac{1}{\overline{h}(\theta)} + o(1) + \rho^{rBLi} + \frac{1}{\overline{h}(\theta)} + o(1) - \frac{2}{\overline{h}(\theta)} = \rho^{rBLi} + o(1), \tag{6.135}$$

which has the same accuracy as the boundary layer solution in the rBLi region. Similar arguments can be made to show that $\mathscr{G} \sim \rho^{rBLo}$ + o(1) in the rBLo region.

We now consider the second composite solution, this time uniformly valid in the end boundary layer and the corner boundary layers. If we compare the relaxation equations found in Sections 6.8 and 6.9, it should be clear that

$$\overline{\kappa}_{Te}(\rho^{eBL*}) \frac{\partial \rho^{eBL*}}{\partial \widehat{\theta}} = -\frac{\overline{r}^2}{\overline{h}_{end}^2} (\rho^{eBL*} - \mathscr{G}(\overline{r}, \theta_{end})) \tag{6.136}$$

subject to

$$\rho^{eBL*} = 1 \quad \text{at } \widehat{\theta} = 0 \tag{6.137}$$

yields a solution having the same accuracy as the (6.118) and the (6.125) in their respective regions. As a verification we note that

$$\mathscr{G}(\overline{r}, \theta_{end}) = \rho^{core}(\overline{r}, \theta_{end}) + o(\frac{1}{\Lambda}) = \frac{1}{\overline{h}_{end}} + o(1) \tag{6.138}$$

in the end boundary layer, i.e., when $\overline{r}$ = O(1) and $\widehat{\theta}$ = O(1). Thus, (6.136) reduces to (6.118). In the cBLi region $\overline{r} \approx 1$ and

$$\mathscr{G}(\overline{r}, \theta_{end}) = \rho^{rBLi}(\overline{r}, \theta_{end}) + o(1) \tag{6.139}$$

in which case (6.136) reduces to (6.125) to the appropriate accuracy. Similar remarks hold for the cBLo region. Thus, ρ^{eBL*} satisfying (6.136) will be taken to be the solution valid for all $\widehat{\theta}$ = O(1) and all $1 \leq \overline{r} \leq \delta_o$.

The composite solution for the whole pad, i.e., that uniformly valid over $0 \leq \theta \leq \theta_{end}$, $1 \leq \overline{r} \leq \delta_o$ will be taken to be the "composite of the composite solutions", i.e.,

$$\overline{\rho} = \mathscr{G}(\overline{r}, \theta) + \rho^{eBL*} - \mathscr{G}(\overline{r}, \theta_{end}), \tag{6.140}$$

where the last term is recognized as the matched or common part of (6.127) and ρ^{eBL*}. Note that in the eBL* region, $\mathscr{G}(\overline{r}, \theta) \sim \mathscr{G}(\overline{r}, \theta_{end})$ + o(1) yielding $\rho \sim \rho^{eBL*}$ + o(1) as required. In the core and rBL regions, $\rho^{eBL*} \sim \mathscr{G}(\overline{r}, \theta_{end})$ + exponentially small terms so that $\overline{\rho} \sim \mathscr{G}(\overline{r}, \theta)$ + exponentially small terms as required.

The algorithm for the generation of solutions therefore is:

1. Compute ρ^{core} from (6.100) and ρ^{rBL} from (6.105)-(6.108) for all $1 \leq \overline{r} \leq \delta_o$ and $0 \leq \theta \leq \theta_{end}$.
2. Compute $\mathscr{G}(\overline{r}, \theta)$ for all $1 \leq \overline{r} \leq \delta_o$ and $0 \leq \theta \leq \theta_{end}$.
3. Compute or save $\mathscr{G}(\overline{r}, \theta_{end})$ for all $1 \leq \overline{r} \leq \delta_o$.
4. Compute ρ^{eBL*} from (6.136) and (6.137).
5. Compute $\overline{\rho}$ using (6.140).

We applied the Crank-Nicolson scheme to the nonlinear diffusion equation (6.105) and solved the resultant system of equations using a iterative linear solver by MATLAB. We continued the Crank-Nicolson iteration process until the average change in the solution was found to be less than 10^{-5}. The nonlinear relaxation equation, i.e., (6.136), is solved using the second-order Runge-Kutta method. Discretization errors were checked for all computations presented here. The difference in the load between the grids of 200 x 800 and 300 x 1000 points was less than $10^{-4}\%$.

In Figures 6.9-6.11 we have plotted the constant density contours based on our composite solution and on the exact numerical solutions of (6.61). The same scales have been used for both and the $\overline{h}(\theta)$ function is that given by (6.126). The reference state is taken to be $\mathrm{V}_{ref} \equiv \mathrm{V}(\theta = 0,\, \mathrm{r}) = 5\ \mathrm{V}_c$ and $\mathrm{T}_{ref} \equiv \mathrm{T}(\theta = 0,\, \mathrm{r}) = 1.05\ \mathrm{T}_c$ and the gas models are those described in Section 6.10. Inspection of Figures 6.9-6.11 suggests that the composite solution described above agrees well with the exact calculations for $\Lambda \geq 60$. One can observe small deviations between the composite and exact solutions in the plots corresponding to $\Lambda = 30$. The most noticeable difference is the white area in the vicinity of $\overline{r} = 1$ in Figure 6.11a; this indicates that the composite solution generates values of $\overline{\rho}$ which are < 1. To examine this discrepancy in more detail, we have plotted the variation of $\overline{\rho}$ with $\overline{r}$ at a fixed θ in Figure 6.12 for the case depicted in Figure 6.11. The value of θ chosen was $\theta = \theta_{end}/2 = \pi/8$.

Inspection of Figure 6.12 shows that the composite solution still agrees well with the exact solutions in the core region, but noticeable differences is seen in the rBL region. This is expected because the errors of the rBL solutions, i.e., (6.104), are $O(\Lambda^{-1/2})$. The maximum numerical discrepancy between the composite and exact solution is seen to be on the same order of magnitude in the rBL region. We have examined the composite solution and this mismatch is always o(1), which is within the accuracy of the boundary layer solutions themselves. As Λ increases, the error in the boundary condition decreases. This can be seen by an inspection of Figures 6.9-6.11, Figure 6.12 and Figures 6.13-6.14; the latter figures contain comparisons of the composite solution and the exact solution at the same conditions as in Figure 6.12 but for $\Lambda = 60$ and 90.

We note that the accuracy of the composite solution is quite good in the core region. Our first order core solution (6.100) captures the increase in scaled density with increasing $\overline{\rho}$. At

large Λ, the main contribution to the global properties is expected to come from this core solution so that we expect that the load and loss will be predicted to reasonable accuracy.

Inspection of Figures 6.7 and 6.12-6.14 reveals that the scaled density increases slightly between r = 1.2R$_i$ and 1.8R$_i$; this corresponds to the core region in the large Λ cases. This mild increase of the scaled density can be described by the first correction term of (6.100). As the flows enters the plateau region, i.e., $\theta_s \leq \theta \leq \theta_{end}$, $\overline{h}$ = constant and because $d\overline{h}/d\theta = 0$ the effective bulk modulus no longer affects the core solution. Because

$$\left.\frac{d\overline{h}}{d\theta}\right|_{\theta=0} < 0,$$

the scaled density in the core will increase as $\overline{r}$ increases.

Observation of Figures 6.9-6.11 also suggests that the composite solution has excellent agreement in the variation of the scaled density in the main flow direction even when $\Lambda = 30$. This can be seen more clearly by an examination of the variation of the scaled density at r = 1.5R$_i$ for $\Lambda = 30$. This variation is plotted in Figures 6.15. Because the error of the eBL solution is $O(\Lambda^{-1}) \ll O(\Lambda^{-1/2})$, any mismatches are expected to first appear in the rBL region as Λ decreases.

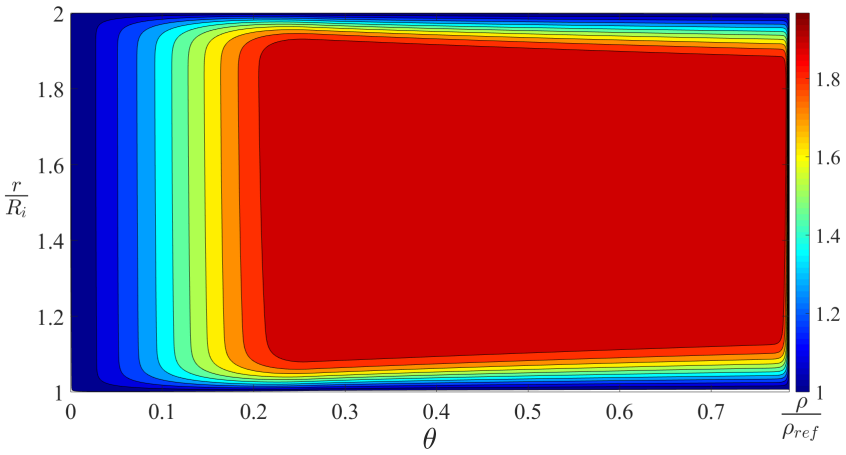

(a) Composite Solution.

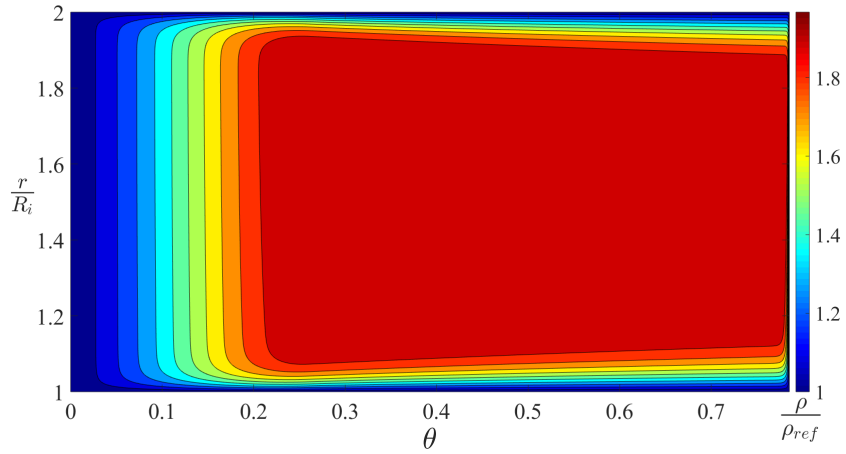

(b) Exact Reynolds Solution.

Figure 6.9: Distribution of Scaled Density at $\Lambda = 90$. The reference state $V_{ref} = 5\ V_c$ and $T_{ref} = 1.05\ T_c$. Contour lines are drawn at equal intervals of $\overline{\rho}$ between 1 and 2.

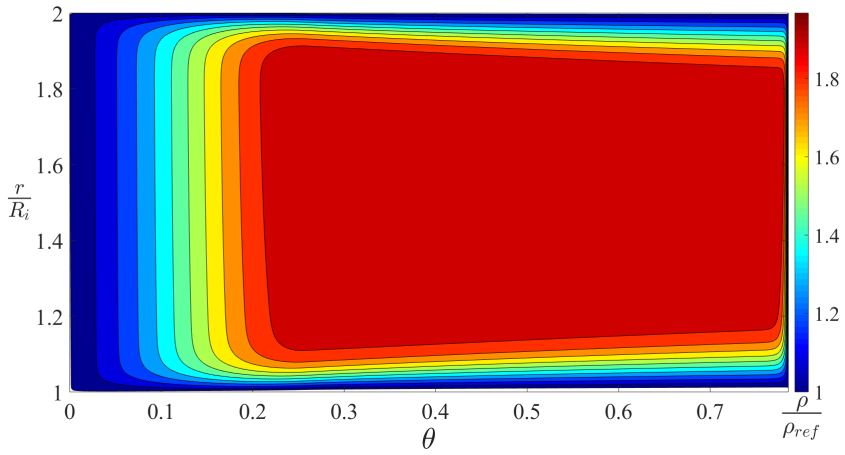

(a) Composite Solution.

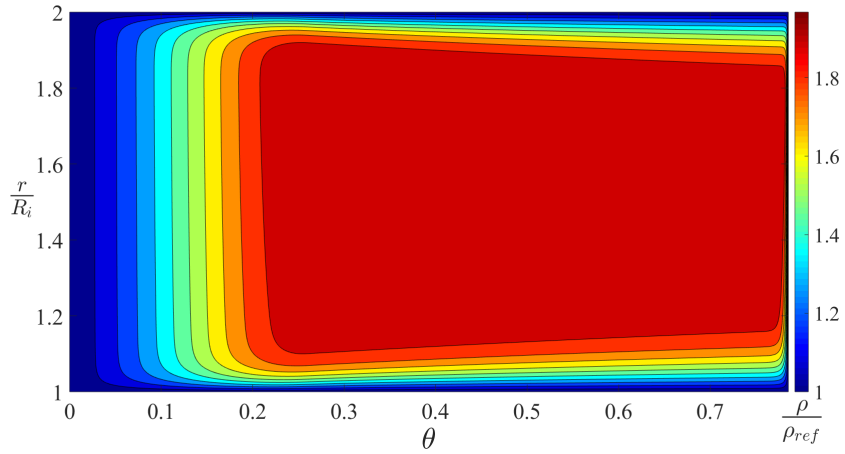

(b) Exact Reynolds Solution.

Figure 6.10: Distribution of Scaled Density at $\Lambda = 60$. The reference state $V_{ref} = 5\ V_c$ and $T_{ref} = 1.05\ T_c$. Contour lines are drawn at equal intervals of $\overline{\rho}$ between 1 and 2.

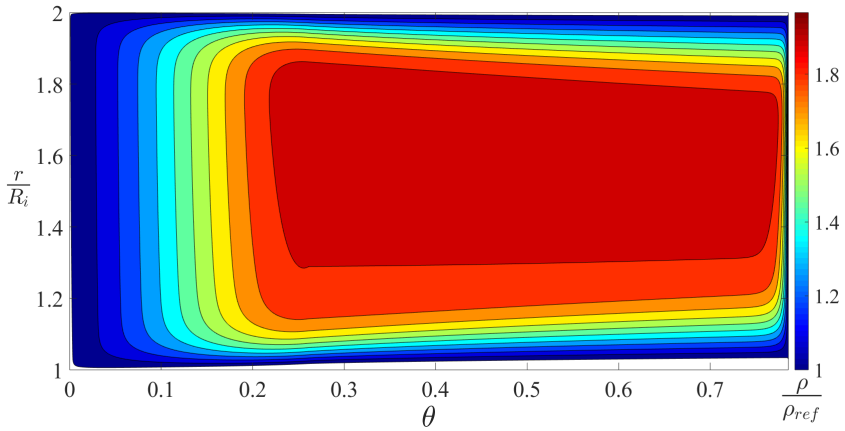

(a) Composite Solution.

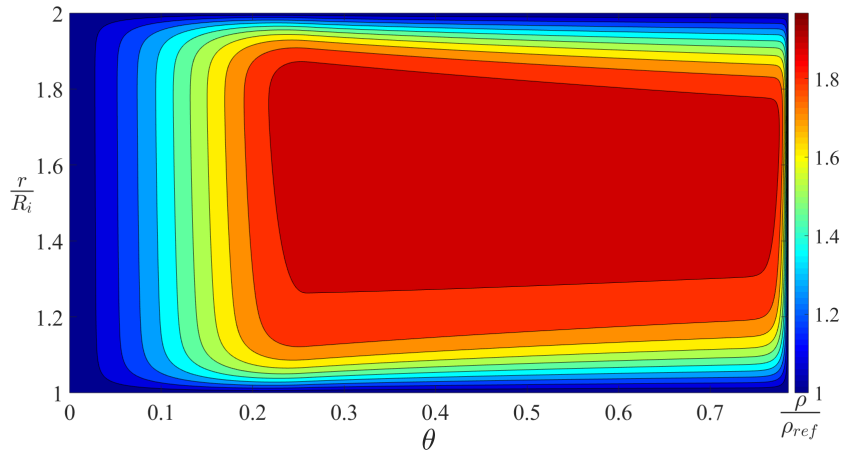

(b) Exact Reynolds Solution.

Figure 6.11: Distribution of Scaled Density at $\Lambda = 30$. The reference state $V_{ref} = 5\ V_c$ and $T_{ref} = 1.05\ T_c$. Contour lines are drawn at equal intervals of $\overline{\rho}$ between 1 and 2.

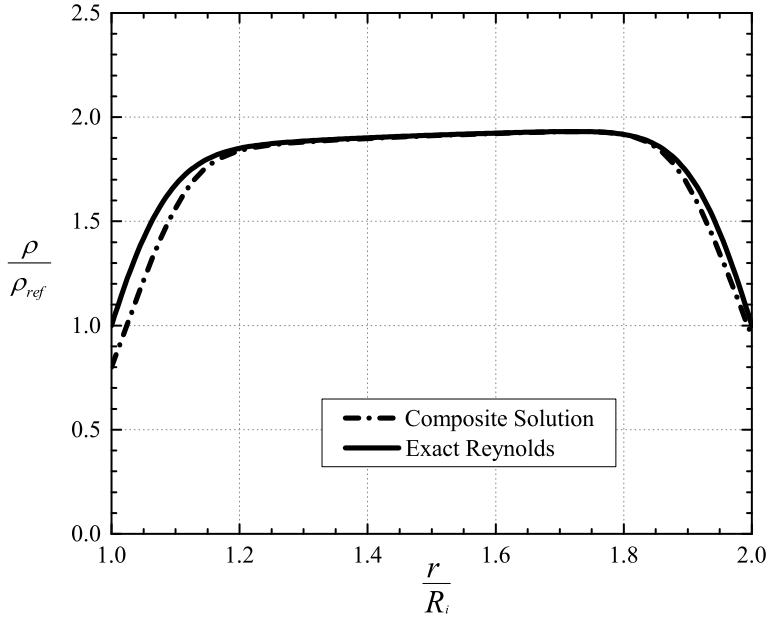

Figure 6.12: Scaled Density vs r/R_i at $\theta = \theta_{end}/2 = \pi/8$ at $\Lambda = 30$. The reference state $V_{ref} = 5\ V_c$ and $T_{ref} = 1.05\ T_c$.

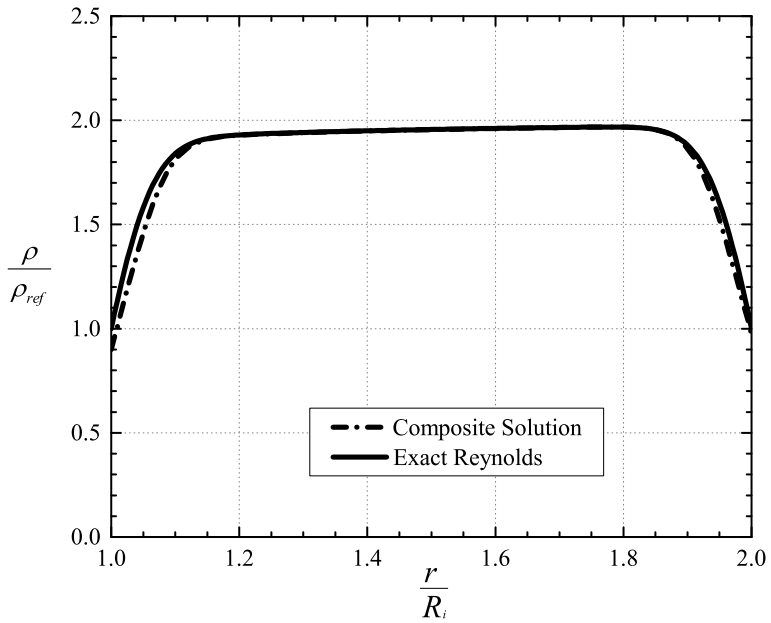

Figure 6.13: Scaled Density vs r/R_i at $\theta = \theta_{end}/2 = \pi/8$ at $\Lambda = 60$. The reference state $V_{ref} = 5\ V_c$ and $T_{ref} = 1.05\ T_c$.

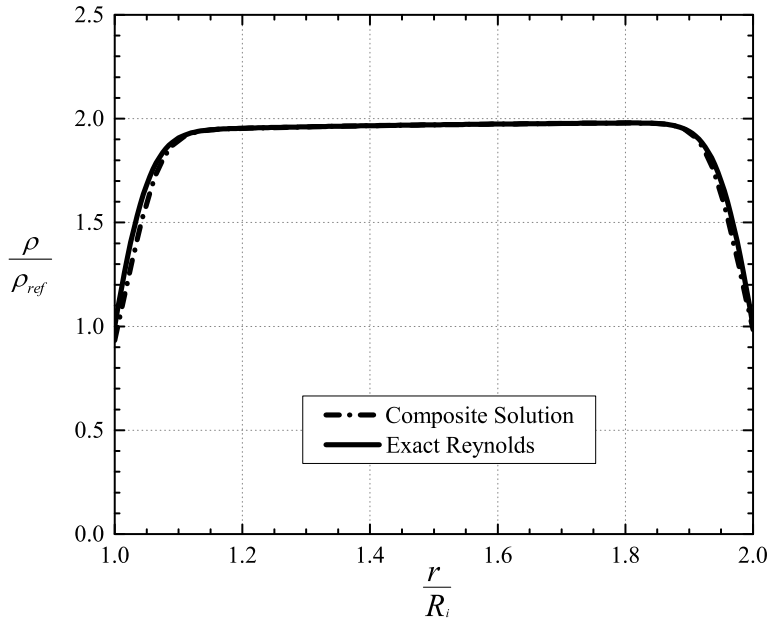

Figure 6.14: Scaled Density vs r/R_i at $\theta = \theta_{end}/2 = \pi/8$ at $\Lambda = 90$. The reference state $V_{ref} = 5\ V_c$ and $T_{ref} = 1.05\ T_c$.

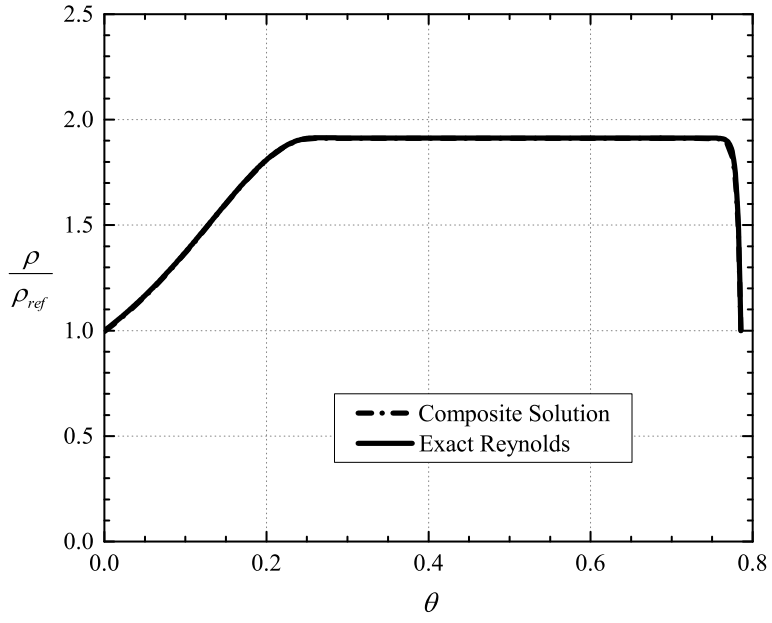

Figure 6.15: Scaled Density vs θ at r = 1.5 R_i at $\Lambda = 30$. The reference state $V_{ref} = 5\ V_c$ and $T_{ref} = 1.05\ T_c$.

6.12 Summary

In this study we present a detailed derivation of the Reynolds equation and its corresponding simplified temperature equation for a standard model of a thrust bearing. The flow is taken to be three-dimensional, steady, compressible, laminar and single-phase. The resulting Reynolds equation (6.61) is shown to be a nonlinear elliptic partial differential equation for the density.

For a two-dimensional compressible lubrication flows, the work of [20] shows that besides the typical lubrication approximation, i.e., (6.2), the validity of the Reynolds equation requires the thermodynamic state to be sufficiently far away from the thermodynamic critical point; whenever the Reynolds equation is valid, the energy convection is negligible. The present study demonstrates that these results still hold for a three-dimensional configuration.

In the course of deriving approximate solutions to the Reynolds equation for high-speed flows, we discover that the boundary layers form near the inner and outer radii as well as the end of the pad. We therefore divided the fluid domain into six regions, i.e., the core, rBLi, rBLo, eBL, cBLi and cBLo and have treated each region separately in Sections 6.7-6.9. Our analysis demonstrates that the rBLi and rBLo are governed by a nonlinear diffusion equation, i.e., (6.105), whereas the cBLi, cBLo and eBL are governed by nonlinear relaxation equations, i.e., (6.118) and (6.125).

Based on the approximate solution in each region, a composite solution is developed in Section 6.11. This composite solution provides a single approximation describing the flows in all six regions which have the same accuracy as each approximation in their respective regions. We have verified this fact analytically in Section 6.11. This composite solution is compared to the exact solutions of the (6.61) for typical values of the speed number. As Λ increases, the accuracy of our composite solution is seen to increase and for the cases considered in Figures 6.9, 6.10, 6.13,6.14 our composite solution is seen to be in excellent agreement with the exact solutions of our Reynolds equation (6.61).

Bibliography

[1] O. Reynolds. On the theory of lubrication and its application to Mr. Beauchamp Tower's experiments, including an experimental determination of the viscosity of olive oil. *Proceedings of the Royal Society of London*, 40(242-245), 191–203, 1886.

[2] V. Dostal, M. J. Driscoll, and P. Hejzlar. A supercritical carbon dioxide cycle for next generation nuclear reactors. Technical report, MIT-ANP-TR-100, 2004.

[3] C. DellaCorte, K. C. Radil, R. J. Bruckner, and S. A. Howard. Design, fabrication, and performance of open source generation I and II compliant hydrodynamic gas foil bearings. *Tribology Transactions*, 51(3), 254–264, 2008.

[4] S. A. Wright, R. F. Radel, M. E. Vernon, G. E. Robert, and P. S. Pickard. Operation and analysis of a supercritical CO_2 Brayton cycle. *Sandia Report, No. SAND2010-0171*, 2010.

[5] T. M. Conboy, S. A. Wright, J. Pasch, D. Fleming, G. Rochau, and R. Fuller. Performance characteristics of an operating supercritical CO_2 Brayton cycle. *Journal of Engineering for Gas Turbines and Power*, 134(11), 111703, 2012.

[6] F. Crespi, G. Gavagnin, D. Sánchez, and G. S. Martínez. Supercritical carbon dioxide cycles for power generation: A review. *Applied Energy*, 195, 152–183, 2017.

[7] O. Pinkus and B. Sternlicht. *Theory of Hydrodynamic Lubrication.* McGraw-Hill, 1961.

[8] W. A. Gross, L. A. Matsch, V. Castelli, A. Eshel, J. H. Vohr, and M. Wildmann. *Fluid Film Lubrication.* John Wiley and Sons, Inc., 1980.

[9] A. Z. Szeri. *Fluid Film Lubrication.* Cambridge University Press, 2010.

[10] B. J. Hamrock, S. R. Schmidt, and B. O. Jacobson. *Fundamentals of Fluid Film Lubrication.* CRC press, 2004.

[11] Z. C. Peng and M. M. Khonsari. On the limiting load-carrying capacity of foil bearings. *Journal of Tribology*, 126(4), 817–818, 2004.

[12] T. M. Conboy. Real-gas effects in foil thrust bearings operating in the turbulent regime. *Journal of Tribology*, 135(3), 031703, 2013.

[13] D. Kim. Design space of foil bearings for closed-loop supercritical CO_2 power cycles based on three-dimensional thermohydrodynamic analyses. *Journal of Engineering for Gas Turbines and Power*, 138(3), 032504, 2016.

[14] S. Dousti and P. Allaire. A compressible hydrodynamic analysis of journal bearings lubricated with supercritical carbon dioxide. In *Proceeding of Supercritical* CO_2 *Power Cycle Symposium. San Antonio, TX*, 2016.

[15] K. Qin. *Development and application of multiphysics simulation tools for foil thrust bearings operating with carbon dioxide.* PhD thesis, University of Queensland, 2017.

[16] H. Heshmat, J. F. Walton, and J. L. Cordova. Technology readiness of 5^{th} and 6^{th} generation compliant foil bearing for 10 MWE s-CO_2 turbomachiery systems. In *Proceeding of the 6^{th} International Supercritical CO_2 Power Cycles Symposium. Pittsburg, PA*, 2018.

[17] E. Guenat and J. Schiffmann. Real-gas effects on aerodynamic bearings. *Tribology International*, 120, 358–368, 2018.

[18] E. W. Lemmon, M. L. Huber, and M. O. McLinden. NIST Reference fluid thermodynamic and transport properties–REFPROP. *NIST Standard Reference Database*, 23, v7, 2002.

[19] I. H. Bell, J. Wronski, S. Quoilin, and V. Lemort. Pure and pseudo-pure fluid thermophysical property evaluation and the open-source thermophysical property library CoolProp. *Industrial & Engineering Chemistry Research*, 53(6), 2498–2508, 2014.

[20] S. Y. Chien, M. S. Cramer, and A. Untaroiu. Compressible Reynolds equation for high-pressure gases. *Physics of Fluids*, 29(11), 116101, 2017.

[21] S. Y. Chien and M. S. Cramer. Pressure, temperature, and heat flux in high speed lubrication flows of pressurized gases. *Tribology International*, 129, 468–475, 2019.

[22] S. Y. Chien and M. S. Cramer. Load and loss for high speed lubrication flows of pressurized gases between non-concentric cylinders. *Journal of Fluid Mechanics*, 867, 1–25, 2019.

[23] S. Y. Chien and M. S. Cramer. Virial approximation for load and loss in high-speed journal bearings using pressurized gases. *Fluids*, 4(1), 27, 2019.

[24] R. C. Reid, J. M. Prausnitz, B. E. Poling. *The Properties of Gases and Liquids.* McGraw-Hill, 1987.

[25] T. H. Chung, L. L. Lee, K. E. Starling. Applications of kinetic gas theories and multiparameter correlation for prediction of dilute gas viscosity and thermal conductivity. *Industrial & Engineering Chemistry Fundamentals*, 23(1), 8–13, 1984.

[26] T. H. Chung, M. Ajlan, L. L. Lee, K. E. Starling. Generalized multiparameter correlation for nonpolar and polar fluid transport properties. *Industrial & Engineering Chemistry Research*, 27(4), 671–679, 1988.

[27] A. H. Nayfeh. *Introduction to Perturbation Methods.* Wiley Interscience, 1981.

[28] M. V. Dyke. *Perturbation Methods in Fluid Mechanics.* Parabolic Press, Stanford, California, 1975.

Appendix A

Relation of Loss to Heat Transfer

In this appendix, we derive the relation between the heat transfer at the solid surfaces located at y = 0 and y = h(x) in Figure 4.3. The result is exact in the context of the approximations leading to (4.12). Chien et al. [1] have shown that the energy equation corresponding to (4.12) can be written

$$\frac{\partial \overline{q}_y}{\partial \overline{y}} = PrEc\left[\overline{\mu}\left(\frac{\partial u}{\partial \overline{y}}\right)^2 + (\beta T - 1)u\,\frac{d\overline{p}}{d\overline{x}} + u\,\frac{d\overline{p}}{d\overline{x}}\right], \tag{A.1}$$

where

$$\overline{q}_y \equiv -\overline{k}\frac{\partial \overline{T}}{\partial \overline{y}}, \tag{A.2}$$

is the scaled version of the y-component of the heat flux q_y and

$$\overline{k} \equiv \frac{k}{k_{ref}}, \tag{A.3}$$

$$Pr \equiv \frac{\mu_{ref} c_p|_{ref}}{k_{ref}}, \tag{A.4}$$

$$Ec \equiv \frac{U^2}{c_p|_{ref}\Delta T} \tag{A.5}$$

are the scaled thermal conductivity $k(\rho, T_{ref}) > 0$, Prandtl number, and Eckert number. The quantity

$$\beta = \beta(\rho, T) \equiv -\frac{1}{\rho}\,\frac{\partial \rho}{\partial T}\bigg|_p \tag{A.6}$$

is the thermal expansivity and $c_p|_{ref}$ is the specific heat at constant pressure evaluated at the reference state. As discussed by [1], ΔT is determined by the flow details yielding Pr Ec = 1 when one of the walls is adiabatic.

Because the flow is isothermal to lowest order and $\overline{\rho} \approx \overline{\rho}(\overline{x})$ only, the variables $\overline{\mu}$, βT, and $\mathrm{d}\overline{p}/\mathrm{d}\overline{x}$ can be regarded as independent of $\overline{y}$. The only $\overline{y}$ dependence will arise from the scaled velocity $\mathrm{u} = \mathrm{v}_x/\mathrm{U}$, where v_x is the x-component of the particle velocity. This scaled velocity component satisfies the approximate momentum equation

$$\frac{d\overline{p}}{d\overline{x}} \approx \frac{\partial}{\partial \overline{y}}\left(\overline{\mu}\frac{\partial u}{\partial \overline{y}}\right). \tag{A.7}$$

By combining (A.7) with (A.1) and noting that $\mathrm{u} = 1$ at $\overline{y} = 0$ and $\mathrm{u} = 0$ at $\overline{y} = \overline{h}$ we obtain the integral

$$\overline{q}_y\big|_{\overline{y}=\overline{h}} - \overline{q}_y\big|_{\overline{y}=0} + PrEc\left(\overline{\mu}\frac{\partial u}{\partial \overline{y}}\right)\Bigg|_{\overline{y}=0} = PrEc(\beta T - 1)\frac{d\overline{p}}{d\overline{x}}\int_0^{\overline{h}} u\, d\overline{y}. \tag{A.8}$$

To evaluate the last integral of (A.8) we use the solution to (A.7) subject to the no-slip conditions $\mathrm{u} = 1$ at $\overline{y} = 0$ and $\mathrm{u} = 0$ at $\overline{y} = \overline{h}$ which can be written

$$u = 1 - \left(1 + A\overline{h}^2\right)\frac{\overline{y}}{\overline{h}} + A\overline{h}^2\frac{\overline{y}^2}{\overline{h}^2}, \tag{A.9}$$

where

$$A \equiv \frac{1}{2\overline{\mu}}\frac{d\overline{p}}{d\overline{x}} = \frac{3}{\Lambda}\frac{\overline{\kappa}_{Te}}{\overline{\rho}}\frac{d\overline{\rho}}{d\overline{x}}. \tag{A.10}$$

Substitution of (A.9)-(A.10), integration, and straightforward manipulation yields

$$\overline{q}_y\big|_{\overline{y}=\overline{h}} - \overline{q}_y\big|_{\overline{y}=0} + PrEc\left(\overline{\mu}\frac{\partial u}{\partial \overline{y}}\right)\Bigg|_{\overline{y}=0} = PrEc(\beta T - 1)\frac{\overline{\mu}A}{\overline{\rho}}\left[\overline{h}\overline{\rho} - \frac{\overline{h}^3\overline{\kappa}_{Te}}{\Lambda}\frac{d\overline{\rho}}{d\overline{x}}\right]. \tag{A.11}$$

Use of (4.15) yields

$$\overline{q}_y\big|_{\overline{y}=\overline{h}} - \overline{q}_y\big|_{\overline{y}=0} + PrEc\left(\overline{\mu}\frac{\partial u}{\partial \overline{y}}\right)\Bigg|_{\overline{y}=0} = PrEc(\beta T - 1)\frac{\overline{\mu}A}{\overline{\rho}}\left[1 - \frac{1}{\Lambda}\frac{d\overline{\rho}}{d\overline{x}}(0)\right]. \tag{A.12}$$

We now integrate with respect to $\overline{x}$ from 0 to 1 and reuse (A.10) to obtain

$$\int_0^1 \left[\overline{q}_y\big|_{\overline{y}=\overline{h}} - \overline{q}_y\big|_{\overline{y}=0}\right] d\overline{x} + PrEc\,\overline{P} = \frac{3PrEc}{\Lambda}\left[1 - \frac{1}{\Lambda}\frac{d\overline{\rho}}{d\overline{x}}(0)\right]\int_0^1 \frac{\overline{\kappa}_T}{\overline{\rho}^2}\frac{d\overline{\rho}}{d\overline{x}}d\overline{x}, \tag{A.13}$$

where the definition (4.21) has been used. Because $\overline{\kappa}_T$ seen in the integral on the right hand side is a function of $\overline{\rho}$ only and our periodicity conditions require that $\overline{\rho}(0) = \overline{\rho}(1) = 1$, the fundamental theorem of calculus requires that the integral is zero yielding

$$\overline{P} = \frac{1}{Pr\ Ec}\int_0^1 \left[\,\overline{q}_y\big|_{\overline{y}=0} - \overline{q}_y\big|_{\overline{y}=\overline{h}}\,\right] d\overline{x}. \tag{A.14}$$

Result (A.14) gives a direct relation between the work done by fluid friction to the heat which must be transferred out of the channel. If friction results in a loss of mechanical energy, $\overline{P} < 0$ and the net flow of heat energy will be out of the channel. We also note that the net heat transfer out of the fluid can be obtained once the loss is computed either numerically or the approximations derived in the Section 4.3.

Chien and Cramer [2] have shown that the variation of the thermal expansion coefficient (A.6) and therefore the flow work play an important role in the variation of the local heat fluxes. However, it should be clear from (A.14) that the net heat transfer is unaffected by the value of βT and therefore the flow work. The physical reason behind this observation is that the flow work is a reversible contribution. Therefore its net effect is zero when the total energy transfer is computed. The heat transfer is due solely to the irreversible work done by the viscous dissipation.

Bibliography

[1] S. Y. Chien, M. S. Cramer, and A. Untaroiu. Compressible Reynolds equation for high-pressure gases. *Physics of Fluids*, 29(11), 116101, 2017.

[2] S. Y. Chien and M. S. Cramer. Pressure, temperature, and heat flux in high speed lubrication flows of pressurized gases. *Tribology International*, 129, 468–475, 2019.

Appendix B

Journal copyright permissions

Chapter 2 of this dissertation has appeared in the Physics of Fluid which belongs to the publishing company, American Institute of Physics (AIP). According to the copyright policies of AIP Publishing, the authors retain the right to reproduce the article in whole or in part in a thesis or dissertation written by the authors provided acknowledgment is given to the original source of publication. An acknowledgment to the original published article has been prominently placed at the beginning of chapter 2. Detailed information on the copyright policy of AIP Publishing can be found on https://publishing.aip.org/resources/researchers/rights-and-permissions/permissions/. The published article is available at: https://aip.scitation.org/doi/10.1063/1.5000827.

Chapter 3 of this dissertation has appeared in the Tribology International, which belongs to the publishing company, Elsevier. According to the copyright policies of Elsevier, the authors can use their articles, in full or in part, for inclusion in a thesis or dissertation (provided that this is not to be published commercially). Therefore, the permission to include this paper in this dissertation is granted. Detailed information on the copyright policies of Elsevier can be found at the link: https://www.elsevier.com/about/policies/copyright. The published article can be found at: https://www.sciencedirect.com/science/article/pii/S0301679X18304262.

Chapter 4 of this dissertation has appeared in the Journal of Fluid Mechanics, which belongs to the publishing company, Cambridge University Press. According to the copyright policies of Cambridge University Press, the authors retain the right to reproduce the article in whole or in part in a thesis or dissertation written by the authors provided that a full acknowledgment of the original publication, together with the copyright notice and the phrase "Reprinted with permission" are included. An acknowledgment to the original published article has been prominently placed at the beginning of chapter 4. Detailed information on the copyright policy of Cambridge can be found on https://www.cambridge.org/about-us/rights-permissions/faqs/. The published article can be found at: https://www.cambridge.org/core/journals/journal-of-fluid-mechanics/article/

load-and-loss-for-highspeed-lubrication-flows-of-pressurized-gases-between-nonconcentri
14052027F33611287625E36D7C28B4D3.

Chapter 5 of this dissertation has appeared in the Fluids, which belongs to the open access publishing company, MDPI. Therefore, no permissions are required. The published article can be found at: https://www.mdpi.com/2311-5521/4/1/27.

Chapter 6 of this dissertation has not yet appeared in any journal, and therefore, no permissions are required.